Searching for pulsars in the Galactic centre and the timing of a massive pulsar

Jompoj Wongphechauxsorn

Searching for pulsars in the Galactic centre and timing of a massive pulsar

Dissertation
zur
Erlangung des Doktorgrades (Dr. rer. nat.)
der
Mathematisch-Naturwissenschaftlichen Fakultät
der
Rheinischen Friedrich-Wilhelms-Universität Bonn

vorgelegt von
Jompoj Wongphechauxsorn
aus
Chachoengsao, Thailand

Bonn 2023

Angefertigt mit Genehmigung der Mathematisch-Naturwissenschaftlichen Fakultät der Rheinischen Friedrich-Wilhelms-Universität Bonn

Acknowledgements

At 3:00 AM, I am too anxious to sleep, but I refuse to waste any more time night-dreaming about my future. Instead, I have decided to write the most important part of my thesis: the acknowledgements.

First and foremost, I owe a debt of gratitude to David Champion, my day-to-day supervisor, without whom this thesis would not have been possible. Academic writing has never been my strong suit, and I have learned so much from him. He spent countless hours (at least 200 hours!!) discussing science and life with me. When I had lost all hope, he lifted me up.

I would also like to thank Michael Kramer, my supervisor. While Covid has limited our one-on-one interactions, every bit of our engagement has been invaluable to my PhD.

I am also grateful to my thesis advisory committee: Norbert Langer, Laura Spitler, Paulo Freire, and Robert Wharton. They provided me with invaluable advice that helped me improve over time. Special thanks to Pablo Torne, for his work on coordinating the pulsar-EHT working group and his support and advice for EHT pulsar searches.

To the rest of the FUNDI group: you know who you are! I cannot name everyone without exceeding my thesis page limit, but I would like to give a special shoutout to Marilyn Cruces for her suggestions about my life, work, and even job hunting!! Thank you, also to all those who read my thesis, provided suggestions, and even taught me how to pronounce some English words (such as "blue straggler" and "curriculum").

I would also like to acknowledge the Thai student community in Germany and Bonn, who made my life in Germany mentally and physically easier. In particular, N'Arm and P'Lily, with whom I spent most of my leisure time. There are few people in this world with whom I feel comfortable showing my weak side, and without these two, my life would be harder and sadder. And to myself, I would like to say thank you for not giving up and for continuing to fight.

Lastly, thank you for reading my thesis.

Abstract

Pulsars are rotating neutron stars that emit pulsating signals. They serve as valuable tools for studying a wide range of topics, from general relativity to the interstellar medium. The discovery of a pulsar in the Galactic centre (GC) would be particularly fascinating due to its proximity to the Sgr A*, the black hole at the centre of our Galaxy. Such a discovery could provide insights into the local environment and the nature of the black hole itself.

In the GC, up to 1000 pulsars were predicted, but thus far only six have been found, including a magnetar. One of the explanations is that the dense environment in the GC causes extreme interstellar scattering, reducing the sensitivity of pulsar surveys, particularly for short-period pulsars. To improve our sensitivity to long-period pulsars, a Fast Folding Algorithm (FFA) was used rather than the traditional Fast Fourier Transform (FFT). In this thesis, an FFA pipeline for accelerated pulsars was implemented for the first time to search for pulsars within $1°$ around GC using the data from the High Time Resolution Universe Pulsar Survey-South Low latitude. In this work, a new slow pulsar (PSR J1746−2829) was discovered with an angular distance of $\sim 0.5°$ from the GC. Follow-up observations revealed that this pulsar has properties that are usually associated with radio magnetars. Interestingly, there is another object in the GC that shows magnetar-like properties, in addition to the known magnetar. This may suggest that the GC has an anomalously large fraction of magnetars to non-recycled pulsars compared to the rest of the Galaxy.

Extreme interstellar scattering can significantly reduce the sensitivity of pulsar surveys. Fortunately, the scattering time is decreasing with the fourth power of the observing frequency. As a result, the FFA pipeline for accelerated pulsars was modified to search for a high observational frequency (230 GHz) dataset from the three most sensitive stations from the Event Horizon Telescope observations of Sgr A* in 2017. This survey is the highest frequency pulsar survey to date, leading to negligible interstellar effects. However, pulsars have a steep spectrum, making them dimmer at higher frequencies, and harder to detect. We used the FFA and FFT with acceleration search pipelines to search for pulsars in this dataset, but no new pulsars were detected. The further empirical sensitivity analysis shows that we are only sensitive to less than 2% of the known pulsar population in this search, with less sensitivity on the slow pulsars, highlighting the need for FFA searches.

Lastly, we continued the timing efforts for a massive pulsar-WD binary system, PSR J0348+0432. In this work, the timing baseline was extended from 3 to 10 years, leading to improved constraints on the orbital period decay ($\dot{P}_b$), which can be used to constrain both of the masses. We found that the $\dot{P}_b$ was significantly reduced compared to the predicted $\dot{P}_b$ from the mass measurements and orbital parameters from the previous work. I discussed various factors influencing $\dot{P}_b$, such as a possibility of this system orbiting an unseen companion.

Contents

Introduction

1.1 History of pulsars

In 1967, Antony Hewish and Jocelyn Bell discovered radio pulsations with a period of 1.34 s with a longest pulse duration of 0.016 s from the sky (Hewish et al., 1968). This source did not show any position change due to the Earth orbiting the Sun, known as stellar parallax. The lack of stellar parallax suggested that this source is located far outside the Solar system. Later, the term "pulsar" has been used to describe similar sources discovered in the sky after this discovery. Initially, the size of pulsars was estimated by the fact that the light travel time across the stars needs to be less than the pulse width (Hewish et al., 1968). For example, the first pulsar discovered by Hewish et al. (1968) must be smaller than the 0.016 light-seconds or 5000 km. Hence, pulsars have been proposed to be associated with compact objects, i.e., neutron stars (NS) (see Gold, 1968, for more details) or white dwarfs (WD) (Ostriker and Hartwick, 1968). NS and WD are both remnants of stars that collapsed into compact objects (see Section 1.2.1). While WDs have 1500 km to 3000 km radius (Shipman, 1979), NSs are estimated to be about than 20 kilometres at the time. However, the discovery of the Crab pulsar (Staelin and Reifenstein, 1968) with a pulse period of 33 ms (Lovelace et al., 1968) implies a surface velocity for this pulsar, assuming a diameter of 10000 km and a mass of 1.4 $M_\odot$, typical for a WD, to be approximately 90000000 km s^{-1}, i.e., 300% of the speed of light at its equator. Hence, it is accepted that pulsars are NSs.

To date, more than 3000 pulsars have been discovered. Currently, the fastest spinning pulsar is PSR J1748-2446ad, with a rotation period of 1.397 ms (Hessels et al., 2006) providing further constrains on the radii of the NSs. The slowest pulsar candidate (GLEAM-X J162759.5-523504.3) was found with a period of 1128s (Hurley-Walker et al., 2022). Pulsars have been found with various types of binary companions. Most of the pulsars in binary systems were discovered with WDs (Manchester et al., 2005)[1]. A small fraction ($\sim$ 8.5%) of the pulsar's companions are NS and one is even a pulsar, e.g., the double pulsar system PSR J0737−3039A/B (Burgay et al., 2003; Lyne et al., 2004). Pulsars have also been discovered with main sequence stars as a companion (see Johnston et al., 1992b, for example).

---

[1] https://www.atnf.csiro.au/research/pulsar/psrcat/ .

1.2 An introduction to pulsars and neutron stars

1.2.1 Formations

Stellar radiation is powered by nuclear fusion at its core, initially converting hydrogen to helium. This process reduces the concentration of hydrogen over time. As the radiation pressure and temperature reduces when the star uses all of its hydrogen reservoir, the inward gravitational force contracts the stellar core to maintain hydrostatic equilibrium. As the core is contracted by gravity, the temperature rises to the point where heavier element nuclear fusion begins. As helium fusion gives more energy than hydrogen fusion, the star expands and becomes a 'red-giant' until the helium at its core is depleted. This process continues throughout the star's lifetime, producing heavier nuclei (e.g., helium, carbon, and oxygen, for example) with higher nuclear binding energies. The final element produced by the thermonuclear fusion in a star is iron because it has the highest binding energy, hence iron nuclear fusion takes more energy than it can produce. However, since gravitational force is needed to re-ignite the thermonuclear fusion of heavier element, the low-mass stars will stop the thermonuclear fusion before producing iron as there is no more radiation pressure from thermonuclear fusion. If the core of the star is below approximately 1.4 $M_\odot$, the Chandrasekhar's limit (Chandrasekhar, 1931), it will collapse into a WD, compact objects that are made up of electron-degenerate matter. This will happen in most low-mass stars (M$\leq$ 8 $M_\odot$).

If the star has enough mass to produce an iron core (typically more than 8 $M_\odot$), then it will collapse. As a consequence, a supernova explosion is caused by the process of core contraction. This event is known as a core-collapse supernova (see Janka et al., 2007, for a review), where the core is compressed. The outer remained outer layers becoming a supernova remnant. This collapsed core has enough mass to overcome the electron degeneracy pressure that prevents the WDs from collapsing. Hence, the iron core is further converted into nuclear matter, primarily neutrons, giving birth to a NS (see Heger et al., 2003, for a review). The NSs are theorised to be in hydrostatic equilibrium between the gravitational pressure and neutron degeneracy pressure, i.e., Tolman-Oppenheimer-Volkoff limit (Oppenheimer and Volkoff, 1939). Furthermore, as the core of an intermediate-mass star collapses into an NS, angular momentum must be conserved, making the NSs rapidly spinning objects.

Additionally, if the core has enough mass to overcome the neutron degeneracy pressure, for a massive star (M $\geq$ 25 $M_\odot$), it will collapse into a black hole (BH) (Heger et al., 2003). A BH is an object that curves the space-times such that even light cannot escape[2].

1.2.2 Pulsar spin-down evolution

NSs are remnants of intermediate-mass stars. Those NSs that emit radio waves are known as pulsars. In this section, I will discuss a simple yet powerful model for pulsar's radio emissions. It is known as the "lighthouse model", which describes pulsars as magnetised rotating spheres, see Figure 1.1. With this model, relativistic charged particles escape from the star via the open field lines, where the magnetic fields extend beyond the light cylinder (see Figure 1.1) where the

---

[2] Therefore, it is impossible to observe the BH itself directly.
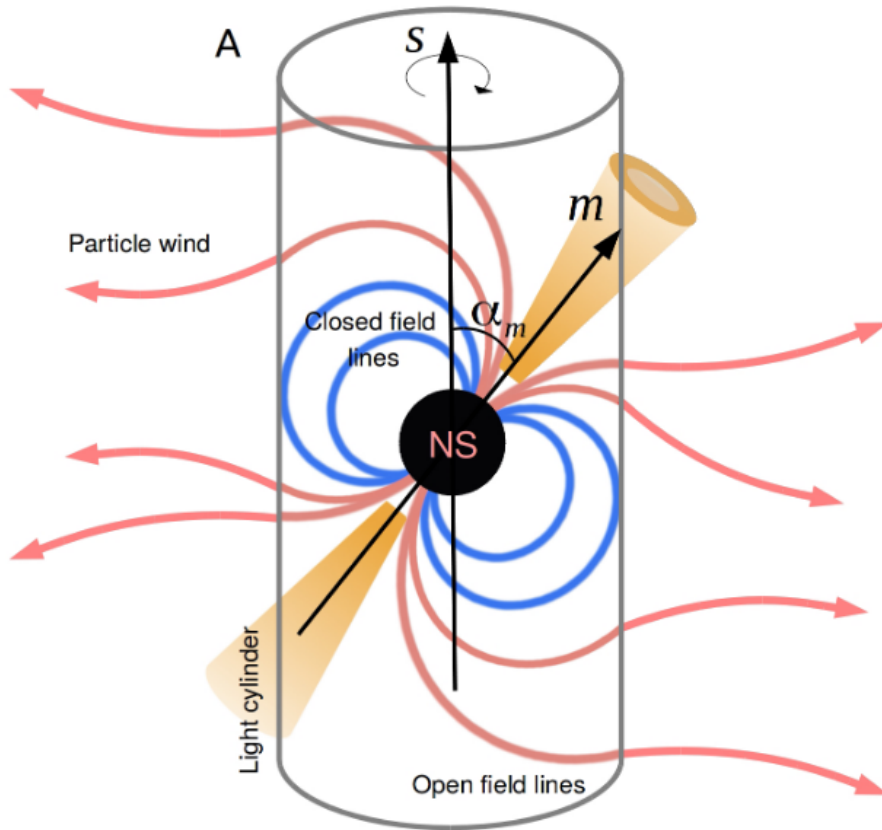
Figure 1.1: A diagram illustrating a model of the pulsars. Here, the NS is rotating around the spin axis S. The pulsar radiation beam is shown in yellow. α_m is the angle between the spin axis and the magnetic moment. Goldreich and Julian (1969) demonstrated that NSs are surrounded by a cloud of charged particles, i.e., the magnetosphere. However, the magnetosphere can co-rotate with a pulsar, like a rigid body, up to a limited distance (close-field lines) where $\Omega R \leq c$. Hence, there will be a distance where the magnetic field and particles around the pulsar exceed the speed of light, causing the field lines to extend to infinity (open field lines). In contrast, the area where the co-rotation speed matches the speed of light is known as the light cylinder radius. The charged particles can escape the star from the open field line and are theorised to generate radio emission near the magnetic poles. This explains why the radiation is aligned with the magnetic moment m. Image adapted from Porayko (2020).

magnetic fields cannot co-rotate with the star because the velocity required to co-rotate reaches the speed of light. The combination of the accelerated motion of the relativistic charged particle and pair production[3] causes a coherent radio emission in the direction of motion. As a result, if one of the magnetic poles sweep across the Earth, the observer might be able to detect the radio emission. It is worth mentioning that the radio emission mechanism model of pulsars is still not complete. The model described here is based on many works of Goldreich and Julian (1969), Sturrock (1971), Buschauer and Benford (1976), Chen and Ruderman (1993) and Graham-Smith (2003).

All the pulsars are observed with periods that are decreasing overtime (Manchester et al., 2005)[1]. The spin-down evolution of pulsars can be expressed by assuming a NS with a moment of inertia I_m and an angular velocity Ω. The rotation energy (E_{rot}) of this object is expressed as

$$E_{\text{rot}} = \frac{1}{2} I_m \Omega^2. \tag{1.1}$$

The I_m is calculated assuming that the NS is a sphere with a uniform mass distribution with an average mass and radius of pulsars, which are 1.4 $M_\odot$ and 10 km, respectively (see Özel and Freire, 2016, for details). As a result, I_m is

$$I_m = \frac{2}{5} MR^2 \simeq 10^{45} \text{g cm}^2. \tag{1.2}$$

As time passes, the pulsar's rotational energy decreases as it loses its energy through the radiation. The rate of energy loss ($\dot{E}_{\text{rot}}$) is estimated by assuming that the I_m is constant, then

$$\dot{E}_{\text{rot}} = -I_m \Omega \dot{\Omega} \simeq 3.95 \times 10^{31} \left(\frac{\dot{P}}{10^{-15} \text{ss}^{-1}} \right) \left(\frac{P}{s} \right)^{-3} \text{erg s}^{-1}. \tag{1.3}$$

If we assume that $\dot{E}_{\text{rot}}$ is carried away in the form of radiation, the rate of energy loss due to electromagnetic radiation for a spinning magnetic dipole with a misalignment α_m from the rotation pole is

$$\dot{E}_{\text{dipole}} = \frac{2}{3c^3} |m_p|^2 \Omega^4 \sin^2 \alpha_m. \tag{1.4}$$

The relation between Ω and $\dot{\Omega}$ assuming that $\dot{E}_{\text{dipole}} = \dot{E}_{\text{rot}}$ is

$$\dot{\Omega} = \frac{2|M|^2 \sin \alpha_m{}^2}{3 I_m c^3} \Omega^3. \tag{1.5}$$

As M, I_m, and α_m are assumed to be constant over time, and $\Omega = 2\pi\nu$ where ν is the rotation frequency, then Equation 1.5 can be written as

$$\dot{\nu} = -K\nu^{n_i}. \tag{1.6}$$

---

[3] Where high-energy radiations from the curvature radiation turn into electron-positron pair, producing further radiation.

where $K = \frac{2|M|^2 \sin{\alpha_m}^2}{3I_m c^3}$ and "the braking index" $n_i = 3$ for this assumption that rotation energy carried out via magnetic dipole radiation (see Lorimer and Kramer, 2012). However, as I_m, which is one of the parameters for n_i, is not directly measurable, we need to find another way to measure n_i only from observable parameters i.e., ν and $\dot{\nu}$. This can be done by differentiating Equation 1.6 which yields $\ddot{\nu} = -n_i K \dot{\nu} \nu^{n-1}$, thus n_i is measured by

$$n_i = \frac{\nu \ddot{\nu}}{\dot{\nu}^2} \tag{1.7}$$

whereas ν is the spin frequency of the pulsar, $\dot{\nu}$ and $\ddot{\nu}$ can only be obtained over a relatively long timescale, repeated pulsar observations, called pulsar timing (see Section 2.3). Typically, only a few pulsars, predominantly the young ones, have measurable $\ddot{\nu}$, limiting the number of reported n_i. The results from pulsar observations show that $0.9 \leq n_i \leq 2890$ (Hamil et al., 2015; Archibald et al., 2016; Parthasarathy et al., 2020). This means that this model might not be able to fully explain the energy loss mechanism of pulsars.

The age of the pulsars is estimated by integrating Equation 1.6 from birth period P_0 to current period P, yielding

$$T = \frac{P}{(n-1)\dot{P}} \left[1 - \left(\frac{P_0}{P} \right)^{n-1} \right].$$

Here we assumed that $n_i \neq 1$ an K is constant. After that, we assume that the energy loss is mainly from the dipole radiation and $P_0 << P$, so that the pulsar age is estimated as its characteristic age (τ_c):

$$\tau_c \equiv \frac{P}{2\dot{P}} \simeq 15.8 \left(\frac{P}{s} \right) \left(\frac{\dot{P}}{10^{-15} \, \text{s s}^{-1}} \right)^{-1} \text{Myr}, \tag{1.8}$$

assuming $n_i = 3$.

Moreover, by assuming that the spin-down of the pulsar is purely due to magnetic dipole radiation, the surface magnetic field (B_{surf}) of the pulsars can be estimated as

$$B_{\text{surf}} = \sqrt{\frac{3c^3 I P \dot{P}}{8\pi^2 R^6 \sin{\alpha_i^2}}} = 3.2 \times 10^{19} \sqrt{P \dot{P}} \, \text{G}, \tag{1.9}$$

assuming the same M, R, and I_m of pulsars as mentioned above with the magnetic pole orthogonal to the rotation pole ($\alpha_i = 90°$) (see, e.g. Lorimer and Kramer, 2012, for example).

As τ_c, B_{surf}, and $\dot{E}$ can all be estimated using only P and $\dot{P}$, the so-called $P - \dot{P}$ diagram (Figure 1.2) can be used to study pulsars properties of the pulsar population as a whole will be discussed in the next section.

1.3 Population of pulsars

In this section, we will discuss each type of pulsar as shown in Figure 1.2.

Due to the conservation of angular momentum, it is predicted that young pulsars will have
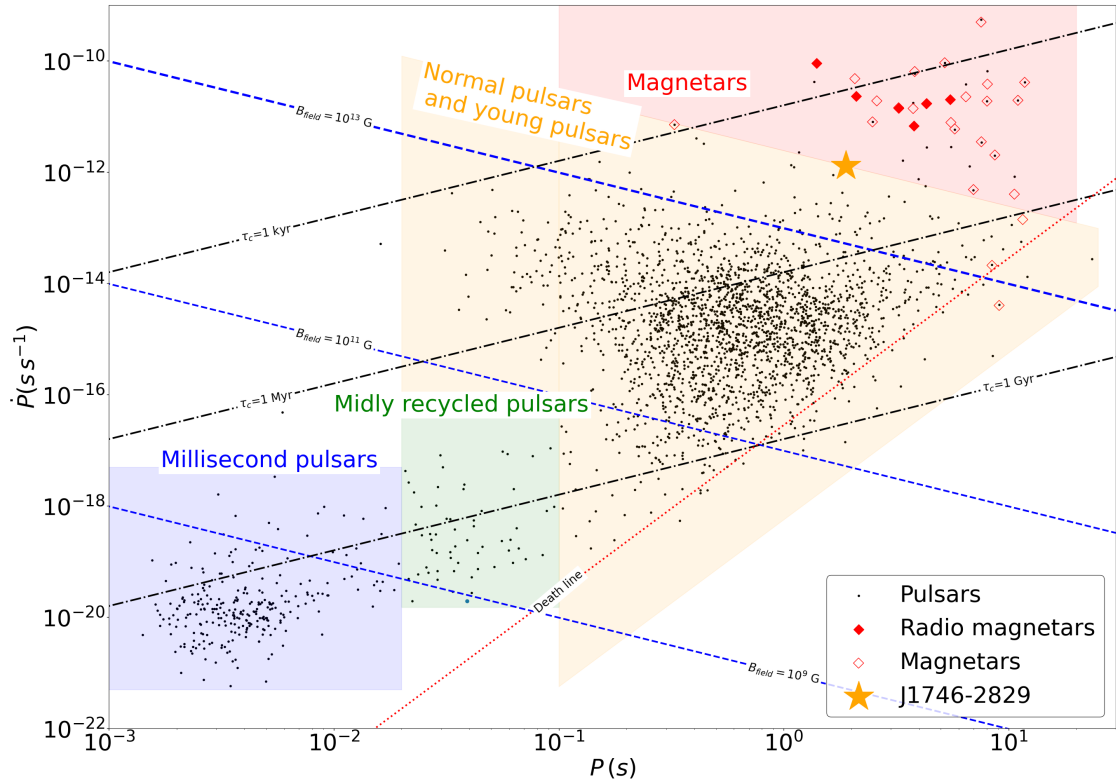
Figure 1.2: The $P - \dot{P}$ diagram. Quantities, such as B_{surf}, and τ_c, are calculated using a purely magnetic dipole braking model. The death line describes the theoretical region where the magnetic field of a pulsar cannot emit electromagnetic radiation anymore (e.g. Bhattacharya et al., 1992).

a relatively short spin period. They also have high $\dot{P}$ and are located in the upper left corner of the yellow region in the diagram. This is confirmed by the fact that many pulsars associated with supernova remnants also have low P and high $\dot{P}$ (Manchester et al., 2005)[4]. Young pulsars typically have a wide range of periods ranging from 0.01s to 10s and $\dot{P}$ greater than 10^{-15} s s^{-1}. Another common property of young pulsars is that they are occasionally reported to have a glitch, a phenomenon where the rotation period drops suddenly. Glitches are caused by the transfer of angular momentum within the NSs (e.g. Link et al., 1992). As a result, glitches can be used to investigate the structure of the NSs, which are the densest observable objects in the universe, and not well studied (see Section 1.5).

Young, energetic pulsars gradually lose their energy over time, transitioning into normal pulsars after approximately 100 kyr, located in the middle part of the diagram. This type of pulsar makes up the largest population in the diagram. The period of normal pulsars ranges from 0.1 s to a few seconds, and their τ_c ranges from 0.1 Myr to 1 Gyr. Isolated ordinary pulsars continue to gradually exhaust their E_{rot} and are eventually theorised to stop radiating photons after crossing the 'death line' in the $P - \dot{P}$ diagram (e.g. Chen and Ruderman, 1993) where the electromagnetic

---

[4] https://www.atnf.csiro.au/research/pulsar/psrcat/.

emission is stopped. The fact that we detect fewer pulsars beyond the death line essentially supports this theory. However, some pulsars can be detected beyond the death line, for instance, PSR J2144−3933, has a spin period of 8.51s with a $\dot{P}$ of $\sim 0.16 \cdot 10^{-15}$ s s^{-1} (Young et al., 1999). The detection of these pulsars beyond the death line hints that we have yet to produce a definitive model of pulsar emission. For example, Bhattacharya et al. (1992) and Chen and Ruderman (1993) predict four different death lines, depending on the NS's magnetic field structure.

Nevertheless, certain NSs that are in a binary system are capable of spin-up, and fulfil emission conditions by receiving mass and angular momentum from their companion, making the pulsar spin faster (see, e.g. Tauris et al., 2000). This process is known as *recycling*, resulting in two types of pulsars: recycled and mildly recycled. If the process is effective and long enough, the pulsars will become recycled pulsars. Due to their remarkably short observational periods, they are also addressed as millisecond pulsars (MSPs). This thesis will refer to a MSP as a pulsar with a period shorter than 20 ms. If the recycling procedure is ineffective or too short, the period of the resurrected pulsar will be slower than that of the recycled pulsars and are known as a mildly-recycled pulsars. The recycling processes are illustrated in Figure 1.3. This theory is supported by the fact that approximately 70% of pulsars with $P < 100$ ms and $\dot{P} < 10^{-15}$ s s^{-1} are found in a binary system (see Manchester et al., 2005) as well as the detection of transitional MPSs (e.g. Archibald et al., 2009).

Another type of NS that can emit radio waves is the magnetar. They are a group of NSs located in the top right part of the $P − \dot{P}$ diagram. Interestingly, most of them are not detected at radio frequencies but in a higher energy regime, i.e. X-rays and gamma rays. There are only six radio-loud magnetars out of 31 magnetar to date (Olausen and Kaspi, 2014).

Magnetars are identified with soft gamma-ray repeaters (SGR) and anomalous X-ray pulsars (AXP). These objects emit electromagnetic radiation that is brighter than the spin-down luminosity, i.e. $\dot{E}_{\text{dipole}}$. This suggests that magnetars have different energy sources than the other types of pulsars, one of which is the decay of their magnetic fields (Duncan and Thompson, 1992; Thompson and Duncan, 1995). Magnetars have spin periods ranging from 0.326 s to 12 s, with a high spin-down rate (10^{-15} s s^{-1} to 10^{-9} s s^{-1}). The large spin-down rate implies that this type of object has a high B_{surf}, hence this type of object is called a "magnetar". The slow period and high spin-down rate also imply a short life ($\sim 10^4$ years) before it crosses the death line in the $P − \dot{P}$ diagram. This might explain why only six of them have been found in radio, as it takes only a few years for them to cross the death line compared to the normal pulsars (Camilo et al., 2006; Camilo et al., 2007; Levin et al., 2010; Shannon and Johnston, 2013; Lower et al., 2020; Karuppusamy et al., 2020). They are also found to be transients, emitting radio emissions for a certain period of time (see e.g. Camilo et al., 2006; Champion et al., 2020; Lower et al., 2023). As both the normal pulsars and magnetars have long rotational periods, it is crucial to understand the difference between these objects.

It is worth mentioning that there are other objects related to pulsars that are outside the scope of this thesis. For example, Rotating radio transient (RRAT) (McLaughlin et al., 2006) and X-Ray Dim Isolated Neutron Stars (XDINS) (Treves et al., 2001). RRATs are detected with sporadic emissions. Most of them were reported with a spin period between 0.7 s to 7 s, implying that they are pulsars that do not emit radio waves that are bright enough to be detected most of the time. The XDINS are a group of nearby NSs that emit mostly X-ray pulsations. They have periods

ranging from 3s to 11s, with a small period derivative. Currently, none of XDINS has been reported with radio pulsations (Kondratiev et al., 2009b).
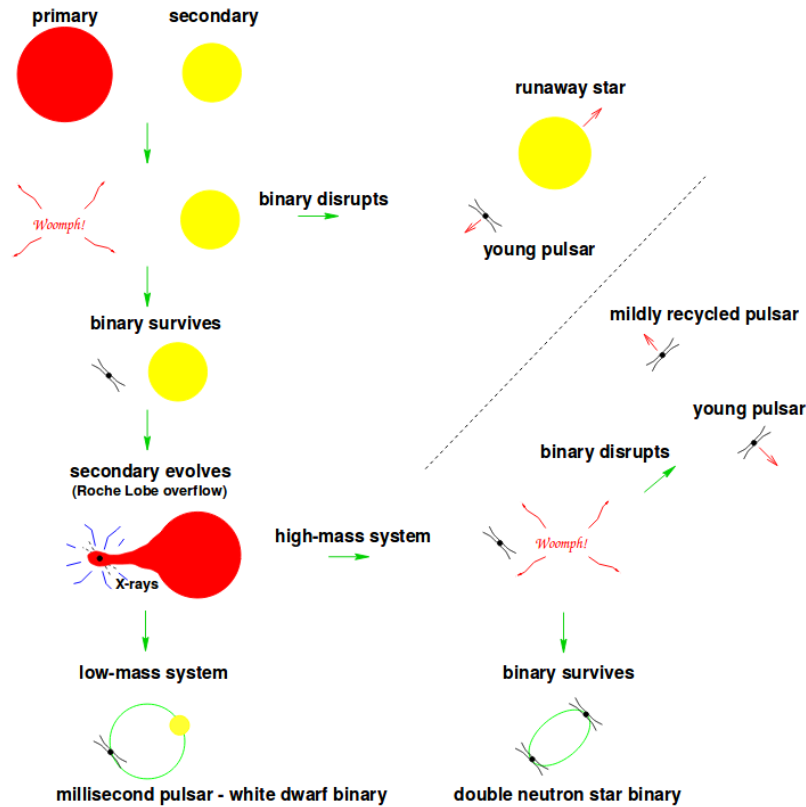
Figure 1.3: A diagram describing the recycling of a pulsar. For a binary system with a high-mass star, when the life of higher-mass star ends, it turns into a supernova. If the binary system cannot survive this process, it will be dispatched with large proper motion, i.e., changes in the position of celestial bodies. However, if the binary system survived the supernova, the companion star would continue to evolve in the binary system. In the case of a low-mass companion star, the supernova/nova at the end of its life may not have enough energy to disrupt the binary system. This process results in an almost perfectly circular orbital binary system of NS and WD. In the case of a high-mass companion, the supernova at the end of its life is enough to increase the orbit eccentricity due to the asymmetric supernova kicks (see Tauris et al., 2017). If the system can survive the supernova, it will become a highly eccentric system of two pulsars. However, if the system cannot survive the supernova, the first pulsar will be 'kicked' out of the system as a high proper motion mildly recycled pulsar and a young pulsar from the companion. Image from Lorimer (2008).

1.4 Propagation effects

As radio waves propagate through space, they are affected by the interstellar medium (ISM). In this section, I will discuss four significant effects of the ISM on the signal from pulsars; dispersion, scattering, scintillation, and Faraday rotation. In this section, we will mainly focus on how these

effects can affect the detectability of radio signals.

1.4.1 Dispersion

As the signal propagates, the ionised ISM acts like a prism with the refractive index μ_i making the electromagnetic waves have a different group velocities (v_g) depending on its frequency as

$$\mu_i = \sqrt{(1 - \frac{v_p}{f})} = \frac{v_g}{c}. \tag{1.10}$$

The plasma frequency, v_p, is defined as $v_p = \sqrt{\frac{e^2 n_e}{\pi m_e}}$ where e, m_e, and n_e are electron charge, mass, and number density, respectively. Because the velocity of the wave changes, the signal travel time over the distance L is now

$$t = \int_0^L \frac{dl}{v_g} = \frac{L}{c} + \frac{e^2 \int_0^L n_e dl}{2\pi m_e c v^2}. \tag{1.11}$$

The first term, L/c, indicates the light travel time if the space is empty ($n_e = 0$), hence the waves arrive at the Earth simultaneously, regardless of frequency. The second term describes how the pulse is delayed chromatically due to the presence of the ISM[5]. As n_e is the only variable in Equation 1.11, and we are only interested in the time delay from the light travel time in a vacuum, so Equation 1.11 can be re-written as

$$\Delta t = \frac{e^2 \text{DM}}{2\pi m_e c v^2} = 4.15 \times 10^6 \frac{\text{DM}}{v(\text{MHz})^2} \text{ ms}. \tag{1.12}$$

Where dispersion measure (DM) is defined as $\text{DM} \equiv \int_0^L n_e \cdot dl \text{ pc cm}^{-3}$. Assuming that the radio waves are emitted at multiple frequencies simultaneously. Hence, the time delay from frequencies v_1 to v_2 is written as

$$\text{DM} = \frac{\Delta t(\text{ms})}{4.150 \cdot 10^6} \cdot (v_1^{-2}(\text{MHz}) - v_2^{-2}(\text{MHz})) \text{ pc cm}^{-3}. \tag{1.13}$$

If the DM is known, then we can 'de-disperse' by subtracting the progressive time delay in each frequency band with a specific DM to the same reference frequency as shown in Figure 1.4. De-dispersion can let detection of pulsar signals, depends on DM and observing frequency, as it can recover the signal's pulsation as shown in Figure 1.4. More details about the de-dispersion and how to search for DM will be discussed in Chapter 2.
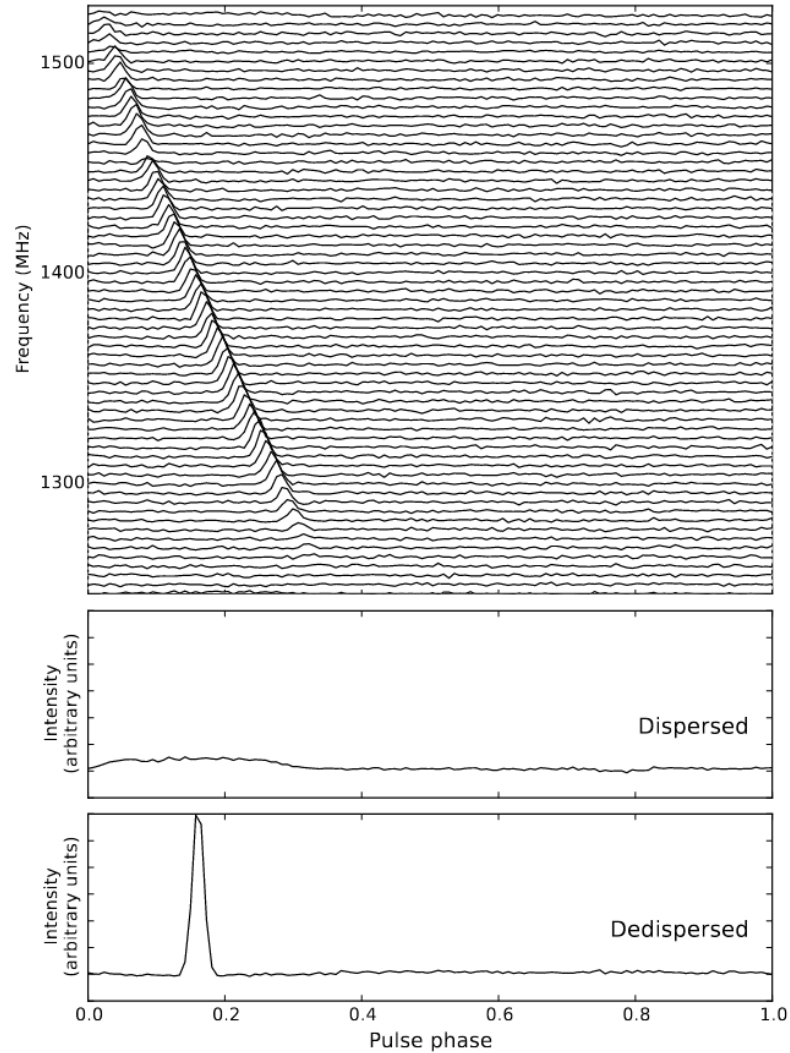
Figure 1.4: The arrival time of the signal affected by dispersion. Upper: The frequency-phase plot for PSR J1903+0135, showing the time delay that is $\propto \nu^{-2}$. Middle: The smeared integrated profile generated by direct summation of delayed pulses in all frequency channels without de-dispersion, showing no sign of pulsation. Lower: the de-dispersed integrated pulse profile, with a prominent pulsation. These plots demonstrated that, without de-dispersion, this effect reduces the detectability of the signal's pulsation, which we are searching for (see Section 2.2.1 and 2.2.2). Image from Berezina (2018).

.
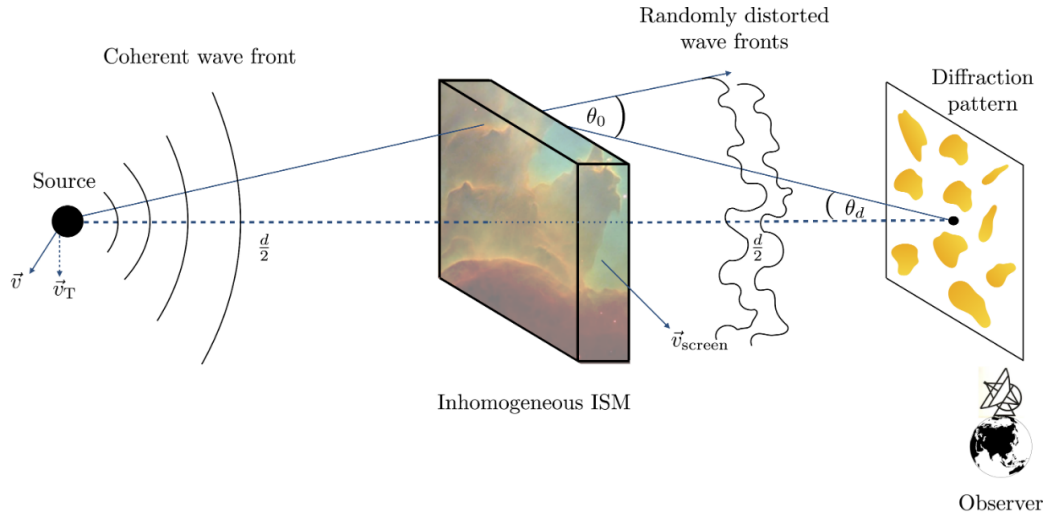
Figure 1.5: A coherence signal from a pulsar that is perturbed by the ISM, resulting in an interference pattern in pulse phase and pulse broadening. Image adapted from Lorimer and Kramer (2012) and Cruces (2021).

1.4.2 Scattering

Another propagation effect from the ionised ISM is known as scattering, which occurs due to the multi-path propagation of the signals in the ISM, as shown in Figure 1.5. This effect causes a portion of the signal to travel along for a longer duration, asymmetrically broadening the pulse. The broadening of the pulse can be modelled as a convolution of the pulse with a one-sided exponential, which analytically expressed as

$$I = I_0 e^{\frac{-t_g}{\tau_s}},$$ (1.14)

where τ_s is defined as the scattering time and t_g is the geometrical delay due to the path difference. If we consider the ISM as a thin screen with a width a_s located between the pulsar and the source with a distance of, d as shown in Figure 1.5. Then t_g is calculated from

$$t_g = \frac{\theta_0^2 \, d}{c}.$$ (1.15)

The τ_s can be computed from

$$\tau_s = \frac{\theta_d^2 \, d}{c},$$ (1.16)

where θ_d is the angular radius of the scattering disk centred around the source; in this case,

---

[5] This equation also shows that the contribution from heavier ions, such as protons, are negligible as $t \propto 1/m$.

the pulsar. In Lorimer and Kramer (2012), it is demonstrated that for a signal propagates in a turbulence screen of length a_s;

$$\theta_d = \frac{e^2}{2\pi\, m_e} \frac{\Delta n_e \sqrt{d}}{a_s\, f_{\mathrm{obs}}^2}. \tag{1.17}$$

As a result, combining Equations 1.16 and 1.17 gives the relation between τ_s and observing frequency f_{obs} as

$$\tau_s \propto f_{\mathrm{obs}}^{-\alpha_{sc}}, \tag{1.18}$$

where $\alpha_{sc} = 4$ for the thin screen scenario. This approximation also agrees well with the measurements from the multi-frequency observations of pulsars, approximately $\alpha_{sc} = 4$ (e.g. Bhat et al., 2004; Oswald et al., 2021). Moreover, since the τ_s is proportional to f_{obs}^{-4} making the scattering is expected to reduced for higher frequency observations, as shown in Figure 1.6. It is almost impossible to detect the pulsations if the scattering time is longer than the spin period of the pulsar, smearing out the pulsations. For example, the Galactic centre (GC) is expected to have a τ_s as high as 2300s (Cordes and Lazio, 2003) at the typical pulsar searching frequency, 1400 MHz. This τ_s is longer than any known period of pulsars to date (Manchester et al., 2005). Fortunately, as $\tau_s \propto f_{\mathrm{obs}}^{-\alpha_{sc}}$, the scattering can be avoided by observing at higher frequencies.

Since both dispersion and scattering are caused by the ISM and depend on, n_e and Δn_e, respectively, they are expected to be correlated. The result from the pulsar observations also shows some partial correlation between DM and τ_s, as shown in Figure1.7. This means that, if we find a pulsar with a large DM, we also somewhat expect that the signal from the pulsar will be highly scattered.

We will discuss scattering and dispersion in more detail in Chapter 3 and Chapter 4, where the GC pulsar search is discussed.

1.4.3 Scintillation

As mentioned in the previous section, the turbulence ISM causes the signal to have a multi-path propagation which causes the pulses to be chromatically delayed. In addition, it causes phase shifts in the signal, resulting in a diffraction pattern. It makes the intensity of the signal change depending on the relative position of the observer to the ISM screen, as also shown in Figure 1.5. This effect is called interstellar scintillation. It happens with pulsars that have enough change in the line of sight throughout the ISM. Thus, this effect is more substantial for the nearby pulsars (Backer, 1975).

Scintillation can increase or decrease the observed flux density of pulsars. In the first case, it means that some pulsars, even having enough luminosity, might be undetectable in some epochs. Therefore, repeated observations of the environment with high scintillation are motivated. For example, a globular cluster, 47Tuc, has been observed multiple times to search for a new pulsar with the help of this effect (e.g. Manchester et al., 1990a; Manchester et al., 1991, for examples) as it can also enhance the observed flux density of dim pulsars. Scintillation will be utilised again in Chapter 6 and 5.
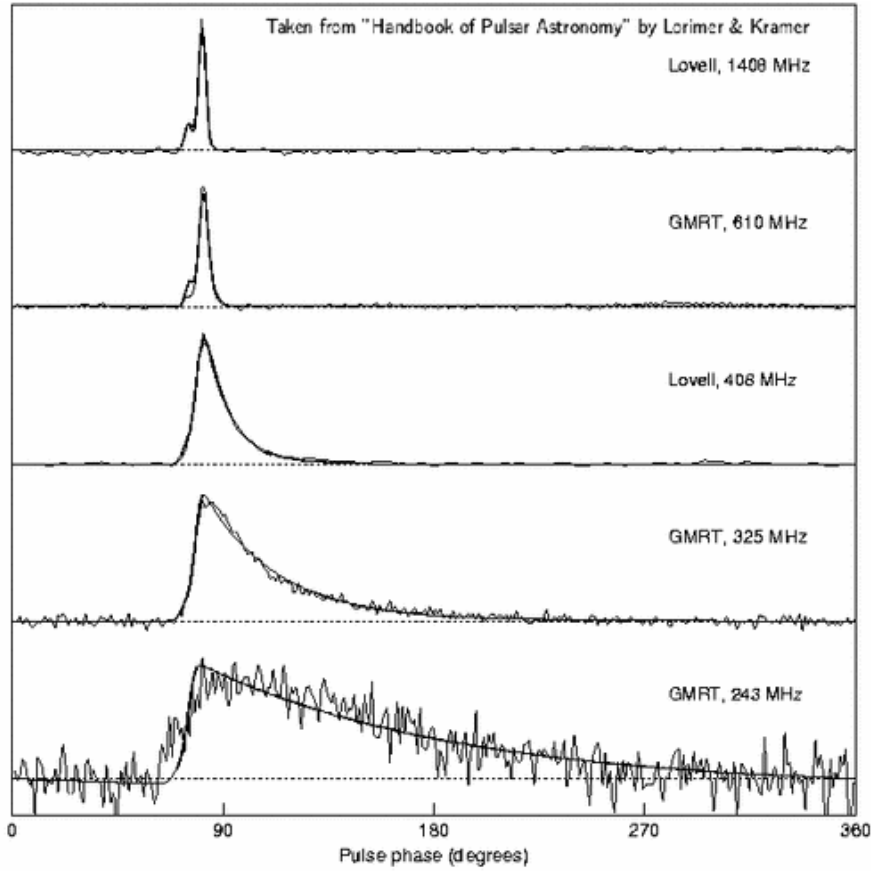
Figure 1.6: Pulse profile from the same pulsar observed at different frequencies, showing the increasing exponential decay tail at the lower frequency. The effect is enhanced at low frequencies, making the pulsar more difficult to detect (Löhmer et al., 2004).

1.4.4 Faraday rotation

In this section, I will discuss another propagation effect from the ionised ISM called Faraday rotation. This effect originates from the combination of ionised ISM and interstellar magnetic field. A naive explanation is that, as the waves propagate in the ISM, the Lorentz force makes the electrons in the ISM move perpendicular to the magnetic field. The movement of the electron rotates the polarisation angle (Ψ) of the signal, as shown in Figure 1.8. The change of Ψ can be described as

$$\Delta\Psi = \frac{0.81}{\text{rad m}^{-2}}\lambda_{\text{obs}}^2 \int_0^d n_e\, B_{||}\, dl = \text{RM}\,\lambda_{\text{obs}}^2, \tag{1.19}$$

where $B_{||}$ is the interstellar magnetic field parallel to the line of sight, and λ_{obs} is the observing wavelength. The rotation measure (RM) is defined as $0.81 \int_0^d n_e\, B_{||}\, dl$ rad m^{-2}. Typically, the RM is determined by the rate of $\Delta\Psi$ over multiple frequencies, similar to de-dispersion. Since RM is the only parameter in Equation 1.19, the intrinsic polarisation can be recovered by rotating

13
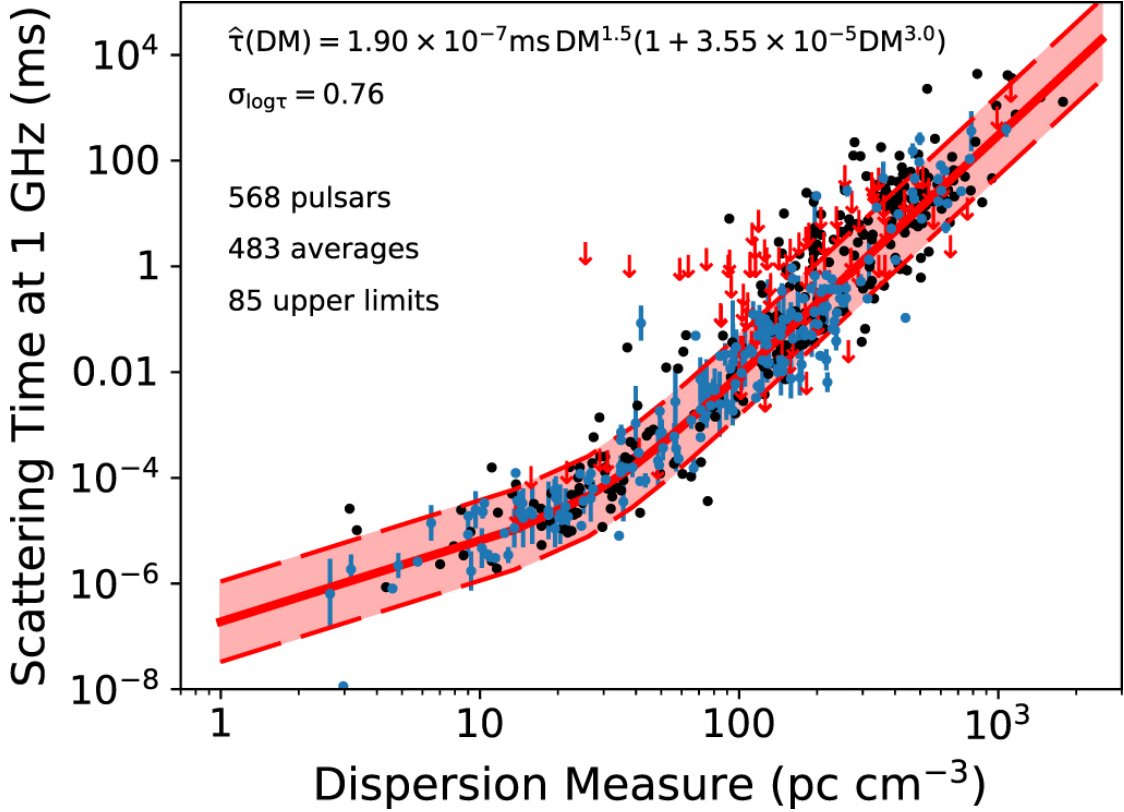
Figure 1.7: The correlation between DM and τ_s. The solid red line is the best fit function. The fact that many points are scattered from the best-fit means that there is a weak, non-linear correlation between the two effects. Image from Cordes et al. (2022).

the observed Ψ to the same reference wavelength.

As the definition of DM is $\int_0^d n_e \, dl$, the averaged magnetic field $B_{||}$ is measurable for the source with the known DM and RM as

$$B_{||} = \frac{\text{RM}}{\text{DM}} = 1.23\mu G \left(\frac{\text{RM}}{\text{rad m}^{-2}} \right) \left(\frac{\text{DM}}{\text{pc cm}^{-3}} \right) \tag{1.20}$$

Typically, Faraday rotation has no effect on the detectability of the pulsar, as the pulsar surveys usually record the data with two perpendicular polarisations summed (see Section 2). However, RMs can be used as a tool to study interstellar magnetic fields.

1.5 Applications

In this section, some pulsar applications will be discussed. I will begin with using pulsars to study the NS population, which is one of the leading applications for pulsar searches. Followed by using a pulsar as a cosmic clock, they can be used to study the surrounding space-time to study
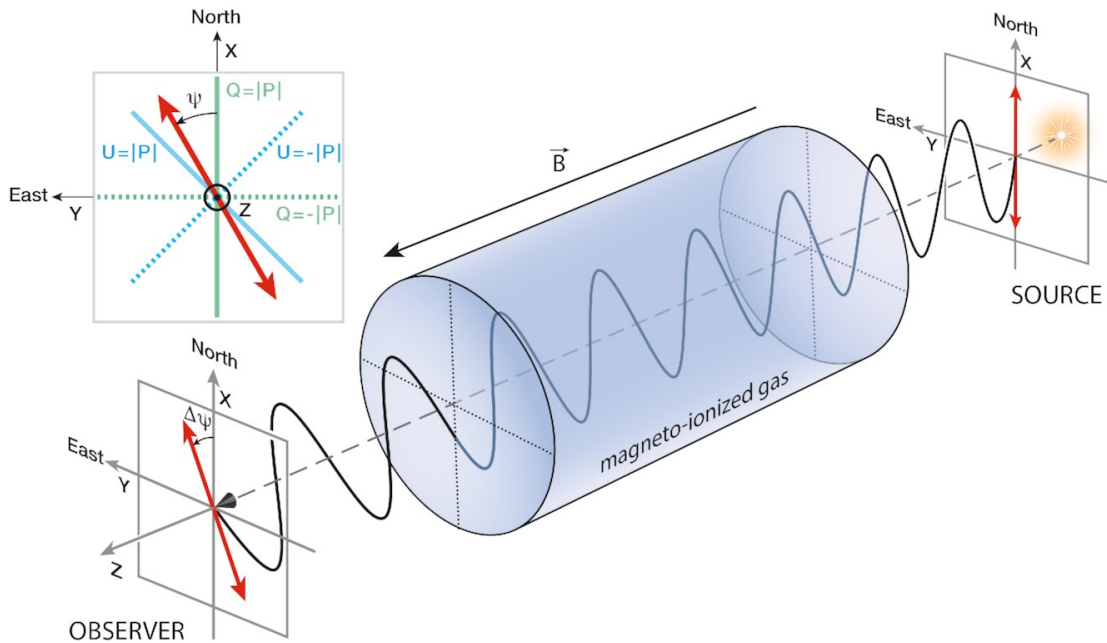
Figure 1.8: Faraday rotation, showing a light source with 100% linear polarisation along the north-south axis propagating through a cloud of magneto-ionised gas. Due to the presence of the magnetic field, the polarisation angle is rotated by $\Delta\Psi$. Image obtained from Ferrière et al. (2021).

gravitational physics. After that, pulsars are used as a tool to study dense matter, as they are the densest observable object in the universe. Lastly, some further applications of pulsars will be discussed.

1.5.1 Studying the neutron star population

As pulsars are remnants of stars, they can be used to study stellar evolution and NSs formation. For example, there are some discrepancies between the number of NSs predicted from the supernova rate and the number of discovered NSs (see Keane and Kramer, 2008, for example). This discrepancy hints that different types of pulsars (pulsars, magnetars, X-DINS, and RRATs) are various stages of NSs rather than different objects. This problem could be answered by discovering more pulsars, especially the ones that show transitional properties between two types of pulsars (Keane and Kramer, 2008). This problem also extends to the inner parsec of the Galactic centre (GC), which is expected to host around 1000 pulsars (Cordes and Lazio, 1997b; Wharton et al., 2012). However, only one magnetar has been detected (Eatough et al., 2013d; Kennea et al., 2013). The discovery of additional pulsars and NSs can tell us whether this discrepancy happened due to detectability or due to stellar formation and NS population in the GC.

1.5.2 Testing theories of gravity

Pulsars in binary systems can be used to test theories of gravity. For example, the first discovered double NS system (a binary system consisting of a pulsar and a NS), PSR B1913+16, provided the first indirect detection of gravitational wave radiation. GR predicted that the system emits gravitational waves, causing the period and orbital separation of this system will gradually shrink (Weisberg and Taylor, 2004). This prediction matched perfectly with the observation of the decay of orbital period. Furthermore, mass measurements and orbital parameters determinations of the double pulsar system, a system consisting of two pulsars, have been used to measure the best radiative test of GR's quadrupole formalism predicted by GR (Kramer et al., 2006b; Kramer et al., 2021).

The other types of binary companions of pulsars are also used as valuable tools in the study of gravity theories. For example, the strong equivalence principle predicts that the free fall of two bodies is independent of its gravitational self-energy $\propto -GM/Rc^2$. As a result, a study on the free falling of the NS-WD binaries, which have a huge difference in the gravitational self-energy, has been used to test this principle (Zhu et al., 2018).

The last type of binary companion is the pulsar-black hole binary (BH), which has not been found yet. Pulsar-BH binary can be used to study the BH in various ways. For example, there are two most important predictions from general relativity related to BHs, which are the No hair theorem (NHT) and the Cosmic censorship conjecture (CCC) (Wex and Kopeikin, 1999a; Kramer et al., 2004; Liu et al., 2012b; Liu and Eatough, 2017). Cosmic Censorship Conjecture suggests all BHs must be surrounded by event horizons, an area where even light cannot escape (Penrose, 1979) with a condition that

$$\chi \equiv \frac{c}{G} \frac{S_o}{M_o^2} \leq 1. \tag{1.21}$$

Where M_o, and S_o are the mass and spin of the BH, respectively. χ is a dimensionless spin parameter of the black hole, which is zero for non-rotating BHs. The NHT predicted that BHs with the same M_o, S_o, and electric charge are indistinguishable making the quadrupole moment (Q_o) to fulfil the condition that

$$\frac{c^4}{G^2} \frac{Q_o}{M_o^3} = -\chi^2. \tag{1.22}$$

A pulsar orbiting a BH can provide access to mass M_o, spin S_o, and quadruple moment Q_o of the BH by measuring each object's masses and determining orbital parameters (see Liu et al., 2014, and references therein). Psaltis et al. (2016b) demonstrated that by combining limits from three measurements, pulsar timing (see Chapter 2) of a typical slow pulsar, the image of the Sgr A* from Event Horizon Telescope (EHT) and the data from the star orbiting close to the BH, we can increase the confidence in Q_o and S_o as shown in Figure 1.9 leading to better constraint on CCC and NHT.

1.5.3 Testing the equation of state of dense matter

NSs are the densest observable matter in the universe. A canonical NS (uniform sphere of 1.4 $M_\odot$ and 10 km radius) has a density of approximately 5×10^{14} times greater than the density of the
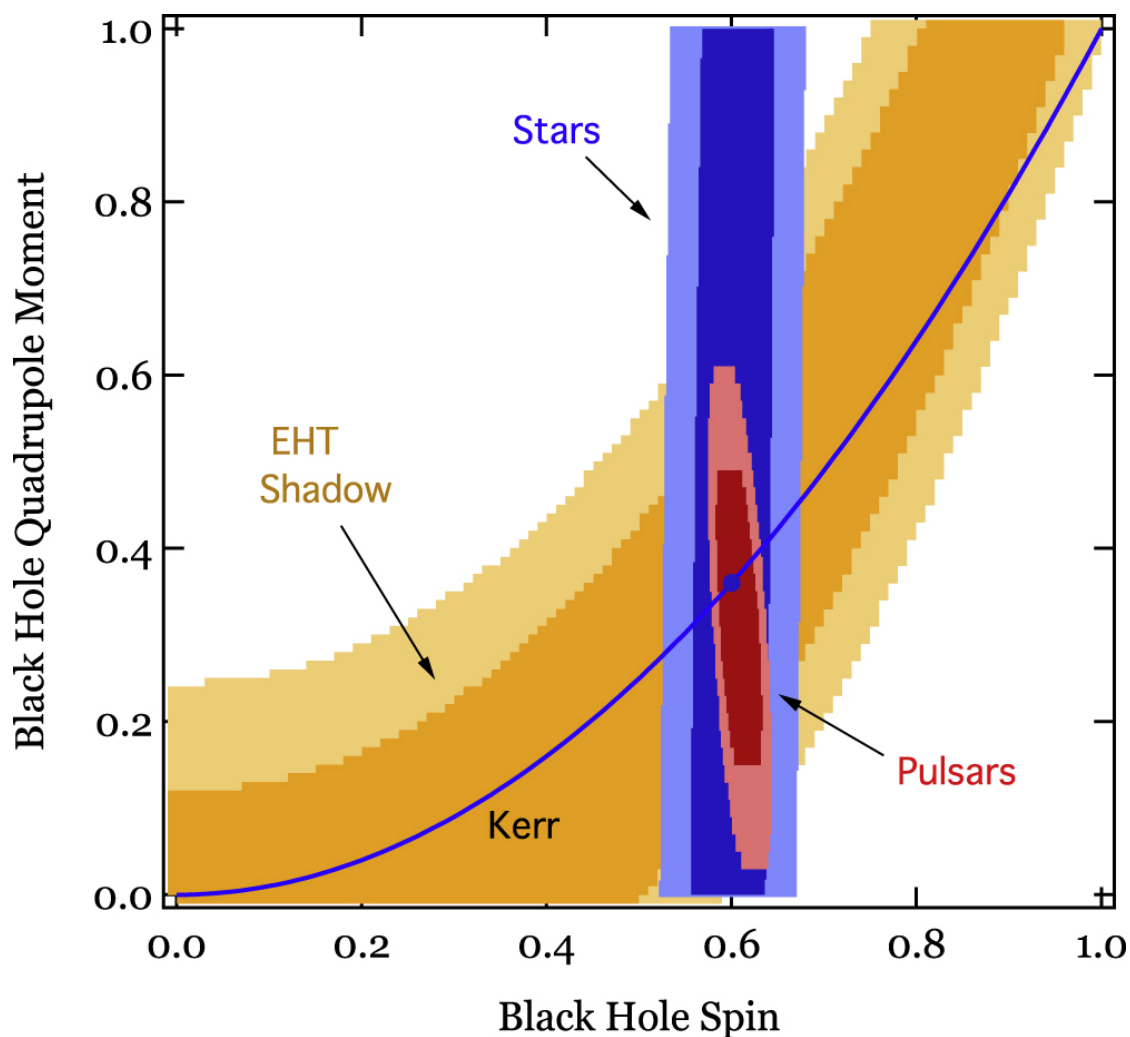
Figure 1.9: Comparison between spin and quadrupole moment of Sgr A* using three different methods. Blue: orbit of two stars near the Sgr A*, Red: timing of low-precision pulsar, and Gold: the shape of the Sgr A* shadow. The solid curve is the expected relation between both parameters for GR. Combining these measurements will increase the confidence level of the aforementioned BH properties. (Psaltis et al., 2016b).

Sun. Hence, it is impossible to create matter at these densities on Earth. As a result, studying the equation of state (EoS) of pulsars is one way to study this kind of matter. For example, each EoS predicts a different relation between the maximum mass and radius of NSs (e.g. Lattimer, 2012). Hence, measuring the mass and radius of pulsars can be used to put constraints on these EoSs.

An upper limit for radius for pulsars can be derived from the rotating period. Currently, the fastest spinning pulsar is PSR J1748−2446ad (Hessels et al., 2006), with a spin period of approximately 1.39 ms, gives an upper limit for the radius to be 16 km. However, the radii measurements are needed epically for other pulsars with relatively longer spin periods and larger

pulse widths. We can currently measure NS radii using X-ray observations of the thermal radiation of nearby NSs. Recently, the X-ray NS Interior Composition Explorer (NICER) released several more radius determinations of NSs (Riley et al., 2019a; Riley et al., 2019b; Miller et al., 2021) using a pulse profile modelling method (Bogdanov et al., 2019a; Bogdanov et al., 2019b; Bogdanov et al., 2021). These studies give the radii of the NSs ranging from 9.9 to 11.2 km.

The mass of pulsars can be evaluated from measuring the orbital parameters (see Section 2.3) for pulsars in binary systems. For example, PSR J0348+0432 (Antoniadis et al., 2013) and PSR J0740+6620 (Cromartie et al., 2019) are believed to be the first 2 $M_\odot$ class pulsars. They put the constraint on some EoSs that predict the lower maximum mass of NSs, as shown in Figure 1.10. For the lightest NS, Martinez et al. (2015) discovered a pulsar in a binary system with a relatively heavy companion ($\sim 1.1 \ M_\odot$) that is not detected with optical emission, which hints that it is likely to be an NS. This system also constrains the lower limit of the NSs masses to be $\sim 1 M_\odot$.
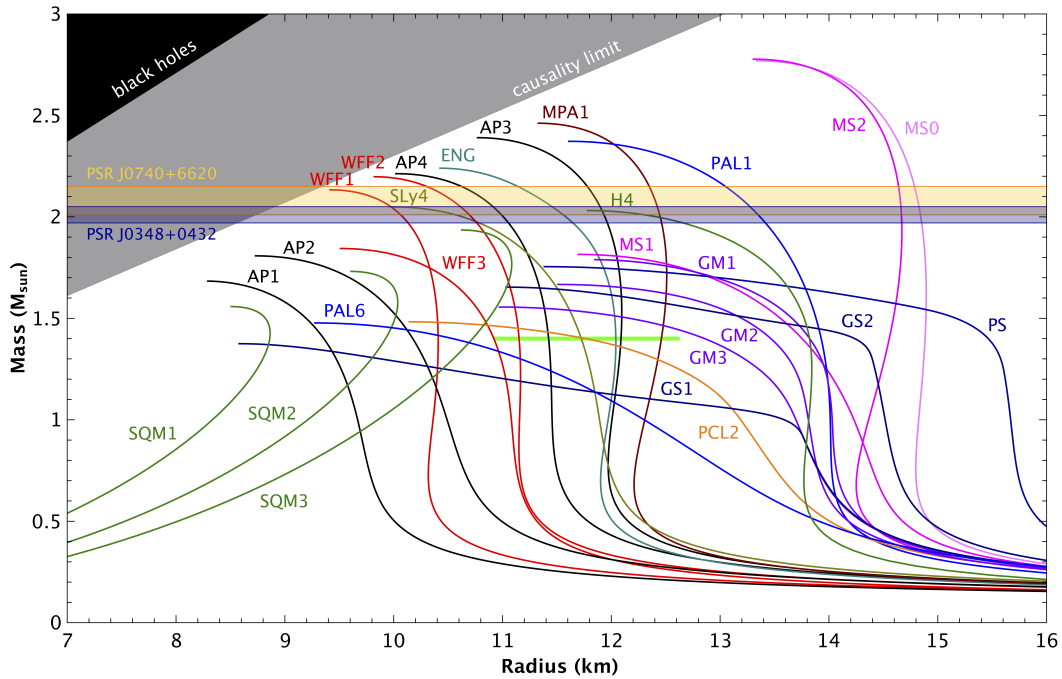
Figure 1.10: The relation between mass and radius for each EoS. The horizontal lines are the limits imposed by the two most massive pulsars. Image from N. Wex and obtained from P. Freire.

1.5.4 Further applications

Besides the aforementioned applications, pulsars can be used in many more ways. For example, pulsars are used as low-frequency stochastic gravitational wave background (GWB) detectors (see Hobbs et al., 2010; Kramer and Champion, 2013; Jenet et al., 2009, for examples), called pulsar timing arrays (PTA). One of the sources of GWBs is theorised to be the merging of two

supermassive BHs, which can be used to study the galaxy formation and galaxy merger [6]. The PTAs carry out studies for GWBs by searching for common red noise in timing residuals.

As mentioned in Section 1.4, pulsars signals are affected by the ISM. Hence, pulsars can also be used to study the ISM. For example, pulsar DM distributions have been used to study the distribution of the free electrons in the Galaxy, giving independent distant measurements[7] (Cordes and Lazio, 2002; Yao et al., 2017b). Faraday rotation distributions of pulsars are also used to probe the magnetic field structure in our Galaxy (Han et al., 2006; Noutsos et al., 2008).

1.6 Thesis outline

In the rest of the thesis, I will describe the method of radio observation and data processing for pulsar data in Chapter 2. Then I will talk about the discovery of a new pulsar from the HTRU-S LowLat survey using the FFA pipeline with acceleration search in Chapter 3. As the pulsar in the GC is expected to experience significant scattering, the only way to avoid this is to observe at a higher frequency. In Chapter 4, we will discuss the search for a pulsar orbiting around the GC using the data from the Event Horizon Telescope (EHT) that operated at 230 GHz. In Chapter 5, I will discuss the other searches using the FFA pipeline developed in this work. Moving to the study of a known pulsar. I will show you a result from the timing observation of one of the most massive pulsar PSR J0348+0428 in Chapter 6. Lastly, I will give you a conclusion for this thesis in Chapter 7.

---

[6] As it is believed that every galaxy has its own supermassive BH.

[7] For example, pulsar distant can be measured from parallax measurements (see Smits et al., 2011, and the reference therein).

Pulsar observations and discoveries

After signals from pulsars travel through the ISM and reach the radio telescope, the system at the telescope converts an analogue signal with the Analogue to Digital converter (ADC) into a digital signal that can be further analysed. Two techniques used to detect weak periodic pulses from a pulsar, known as the Fast Fourier Transform (FFT) and the Fast Folding Algorithm (FFA), will be discussed in this chapter. If this pulsar is in a binary system, its signals will suffer from Doppler shift which changes the apparent period and reduces the signal-to-noise ratio S/N of the signal, making it harder to detect. In this chapter, I will show how to mitigate both effects of dispersion and orbital motion. Later, I will also briefly discuss how to prepare the data and mitigate the effect of radio frequency interference (RFI). Furthermore, I will give a brief overview of pulsar timing, a technique to monitor and study pulsars. The chapter will conclude with a brief look back at the history of blind and targeted pulsar surveys.

2.1 Data acquisition

2.1.1 Fundamental of the radio telescopes

Two quantities that will be mentioned later in this thesis are the telescope beam Full Width Half Maximum (FWHM) and System equivalent flux density (SEFD). The FWHM is used to describe the field of view of the telescope, as a single-dish telescope points to the sky, the dish shape acts as a diffraction grating, producing an aperture power pattern or illumination pattern. This pattern is typically expressed as $\sin \theta^2/\theta$, where θ is the angular offset from the centre of the beam. This pattern has its highest sensitivity at the beam's centre and decreases as θ increases. The main beam is also surrounded by side lobes. The FWHM is twice the offset angle from the central position, where the telescope's sensitivity drops by half, as shown in Figure 2.1. The equation used to calculate the telescope's FWHM is,

$$\text{FHWM} = \frac{c}{D_{\text{tel}} \cdot f_{\text{obs}}} \text{ rad,} \tag{2.1}$$

where D_{tel} is the telescope's diameter, and f_{obs} is the observing frequency. The key message from this equation is that the bigger telescope has a smaller FWHM for a given f_{obs}. In this thesis, I

will sometimes refer to the FWHM as the beam size

SEFD is the flux density that is equivalent to system temperature (T_{sys}), i.e. the noise from the system. Hence, the lower SEFD, the more sensitive the telescope. The SEFD can be expressed as,

$$\text{SEFD} = \frac{4k_B T_{sys}}{\eta \pi D^2}. \tag{2.2}$$

Here k_B is Boltzmann's constant and η is the telescope efficiency, typically near unity, some literature also prefers to express Equation 2.2 as SEFD $= \frac{T_{sys}}{G_{tel}}$, where the telescope *gain* (G_{tel}) is

$$G_{tel} = \frac{\eta \pi D^2}{4k_B}. \tag{2.3}$$

In pulsar observations, Lorimer and Kramer (2012) demonstrated that the flux density (S) of for a signal with S/N is calculated from

$$S = \frac{\text{S/N} \cdot \text{SEFD}}{\sqrt{n_p \cdot T_{obs} \cdot \Delta f}} \sqrt{\frac{W}{P - W}}, \tag{2.4}$$

where n_p, T_{obs}, W, P are the number of polarisation channels, observation time, period, and pulse width, respectively. This equation is known as the *radiometer equation*. S is usually expressed with a unit 'Jansky' (Jy) in radio astronomy, where 1 Jy= 10^{-26} W Hz^{-1} m^{-2}.
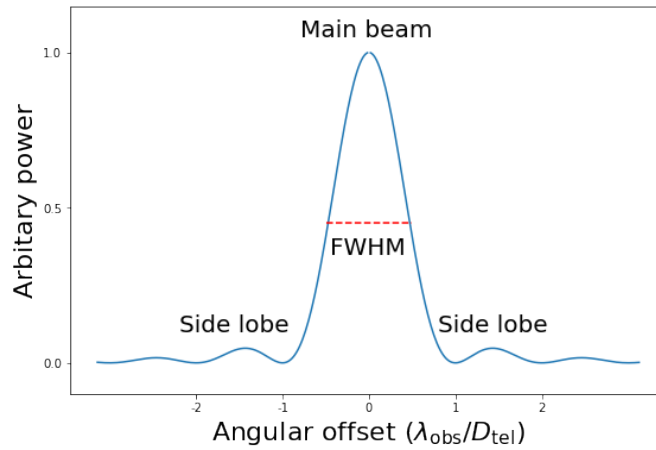
Figure 2.1: Simple radio telescope sensitivity pattern at given observation wavelength (λ_{obs}). The main beam is located between $\pm \lambda_{obs}/D_{tel}$, showing maximum sensitivity at an angular offset equal to $0°$. The FWHM is the width between two angular offsets with half the sensitivity. The *side lobe* are the position outside the main beam that show localised increase sensitivity.

2.1.2 The radio/millimetre telescope family

In this subsection, I will give a quick review of current radio telescopes worldwide that are relevant to pulsar research. Traditional radio telescopes have parabolic steerable dishes. Examples of these kinds of radio telescopes are the 64-m Parkes (Murriyang) radio telescope in Australia, the 100-m Green Bank telescope in the United States (GBT), the 100-m Effelsberg telescope (EFF), the 30-m operated by Institute for Radio Astronomy in the Millimeter Range (IRAM) in Spain, and the 50-m Large Millimeter Telescope Alfonso Serrano (LMT). Some steerable dish telescopes (Parkes, EFF, and GBT) are shown in Figure 2.2.

However, there are many alternative designs for telescopes. For instance, some telescopes have spherical and fixed reflectors. Some examples of these types of radio telescopes are the 300-m Arecibo telescope in Puerto Rico (AO) and the Five-hundred-meter Aperture Spherical radio telescope (FAST) in the People's Republic of China. An image of AO and FAST are also shown in Figure 2.2. Despite limited steerability, this type of telescope has a much larger dish, i.e. higher sensitivity.
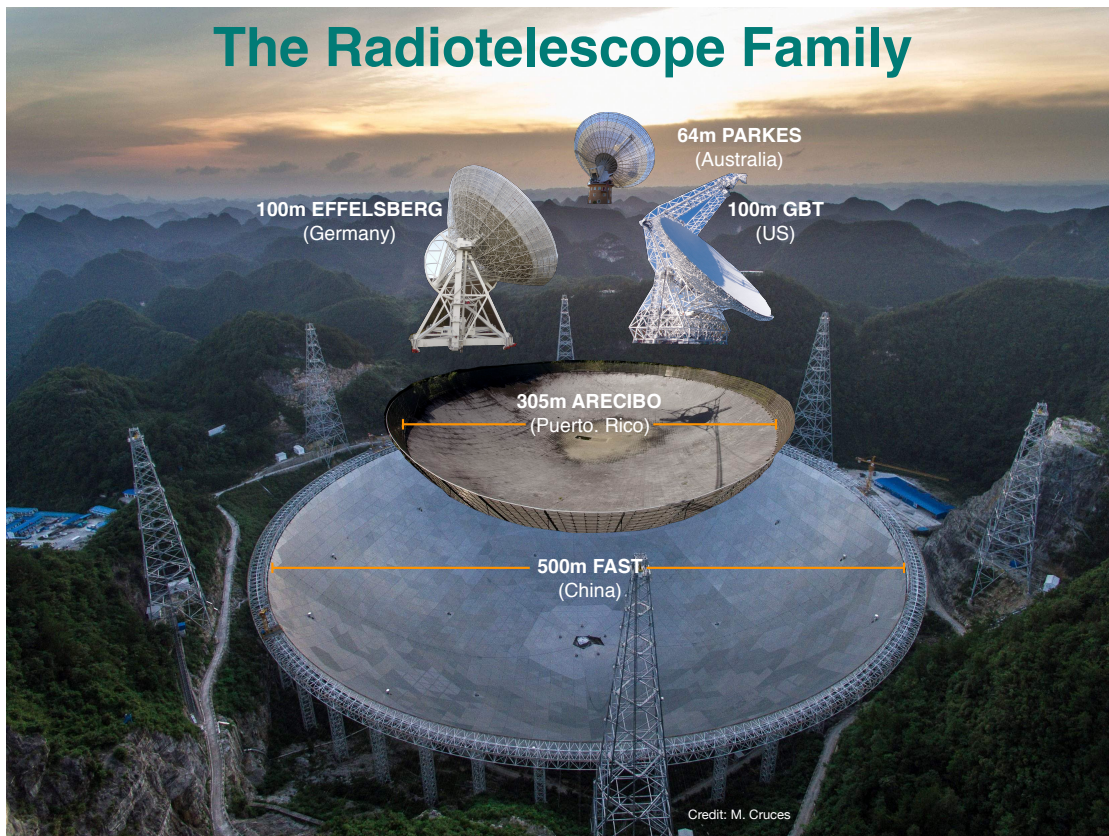
Figure 2.2: Single dish telescopes with the size to scale. Image credit M. Cruces.

In addition, some telescopes are part of an radio interferometric array, which together make up an a "synthetic telescope". This technique utilises the method of coherently combining the nyquist

sampled data from multiple telescopes. The FWHM of this "synthetic telescope" is calculated from the distance between each pair of telescopes, rather than the telescope's diameter. Typically, interferometric radio telescopes often consist of a few relatively small radio telescopes that are placed at a distance of a few metres to kilometres apart. Examples of this kind of array are include the Atacama Large Millimeter/submillimeter Array (ALMA) in Chile and the MeerKAT telescope located in South Africa. An image of the MeerKAT radio telescope array is shown in Figure 2.3.

Figure 2.3: The MeerKAT telescope is an example of a close compact telescope array. Image from SRAO.

Furthermore, telescopes can be electronically connected via a technique called Very Long Baseline Interferometry (VLBI), which joins the data of many telescopes across countries or continents. An example of the "virtual" VLBI telescope is the Event Horizon Telescope (EHT), which has enough resolution to produce images of the shadows of the BH in the centre of M87 (see Event Horizon Telescope Collaboration et al., 2019a, for example) and the Milky Way (see Event Horizon Telescope Collaboration et al., 2022a, for example). The EHT uses high-frequency observations and the most extended baseline, which is approximately the diameter of the Earth, to create such high-angular resolution images (25 μarcsec).

Each type of telescope has its strengths and weaknesses. Steerable single-dish telescopes allow more sky coverage, albeit there have size limitations. Non-steerable telescopes have fewer restrictions on the size of the dish. However, they can cover only some parts of the visible sky. Smaller telescopes have large FWHM, see Equation 2.1, cover a larger part of the sky at the same observation frequency. Furthermore, the larger telescopes have higher sensitivity. Interferometers have a better angular resolution, providing a better position uncertainty of the sky.

2.1.3 Frontends

After the signal arrives at the telescope, the antenna reflects the radio frequency (RF) to the feed horn. A simplified diagram of how the telescope frontend works is shown in Figure 2.4. Normally, the feed horn samples the signal using two orthogonally polarised feeds. Subsequently, the RF is amplified by low noise amplifiers (LNA) as soon as they reach the feed to reduce the signal's power loss in the electronic cables. Since we amplify the signal here, the LNA need to be cryogenically cooled (typically below 30 K) to reduce the self-made thermal noise. Afterwards, the signal passes to the bandpass filter (BF), which filters out any signal that has a frequency outside the desired frequency range.

The RF is then mixed with a signal from the local oscillator (LO) to down-converted the signal's frequency to an intermediate frequency (IF) as $f_{IF} = f_{RF} - f_{LO}$. Where f_{IF}, f_{RF}, and f_{LO} are IF frequency, RF frequency, and LO frequency, respectively. The RF contains the same information as the IF, but the IF contains some critical advantages over the RF. For example, as the signal losses is proportional to f_{obs}, there is lower signal loss due to the transmission for the IF, and it is more convenient for digitisation which converts from raw voltage to digital data as it has a limit on how high of a frequency it can digitize (see the next Section). This method is called the heterodyne principle (Espenschied, 1959) and is widely used in many receivers over the world. During these processes, the RF, and the IF may be amplified multiple times of times, depending on the receiver design (IF Amp. chain in Figure 2.4). Finally, the IF is transmitted via cables to the backend.

2.1.4 Backends

The backend is responsible for digitised the radio frequency (RF) signal, converting it into a digital form and stored the signal. A popular choice for this purpose in current pulsar search observations is the polyphase filterbank (PFB). Which will be discussed in this section.

After the IF is transmitted via cables to the backend, the first part of the backend converts a raw voltage inside the dynamic range to a digital number with as Analogue to Digital converter (ADC). The converted number has a range of $2^{n_{bits}}$, e.g. unsigned 4-bit data ranges from 0 to 15. However, the ADC has a limitation on the highest digitised frequency due to the Nyquist theorem (see Section 2.2.1), which states that for sampled data with the frequency range f_l to f_h, the sampling frequency needs to be more than $2f_h$. For example, it is impossible for the ADC with a sampling rate of 2 Giga-sample per second to digitise RF with a frequency range of 1.2 GHz to 1.7 GHz. This is another advantage of mixing RF down to IF started at 0 GHz with the same bandwidth (i.e., frequency range) using f_{LO} of 1.2 GHz, as the IF can be digitised with the ADC that has a sampling rate less than 2 GHz. The resulting data is known as baseband data, which is the raw data that has not yet undergone any processing and contains all of the information present in the original RF signal. The backend received a time tag from a maser clock, providing high-precision timestamps.

The digitised data are streamed to the polyphase filterbank (PFB), which normally is implemented on a Field Programmable Gate Array (FPGA). The PFB is used to perform the FFT (see Section 2.2.1 for more information) to channelise N sample of data into $N/2$ frequency channels. The data are then stored and ready for processing.
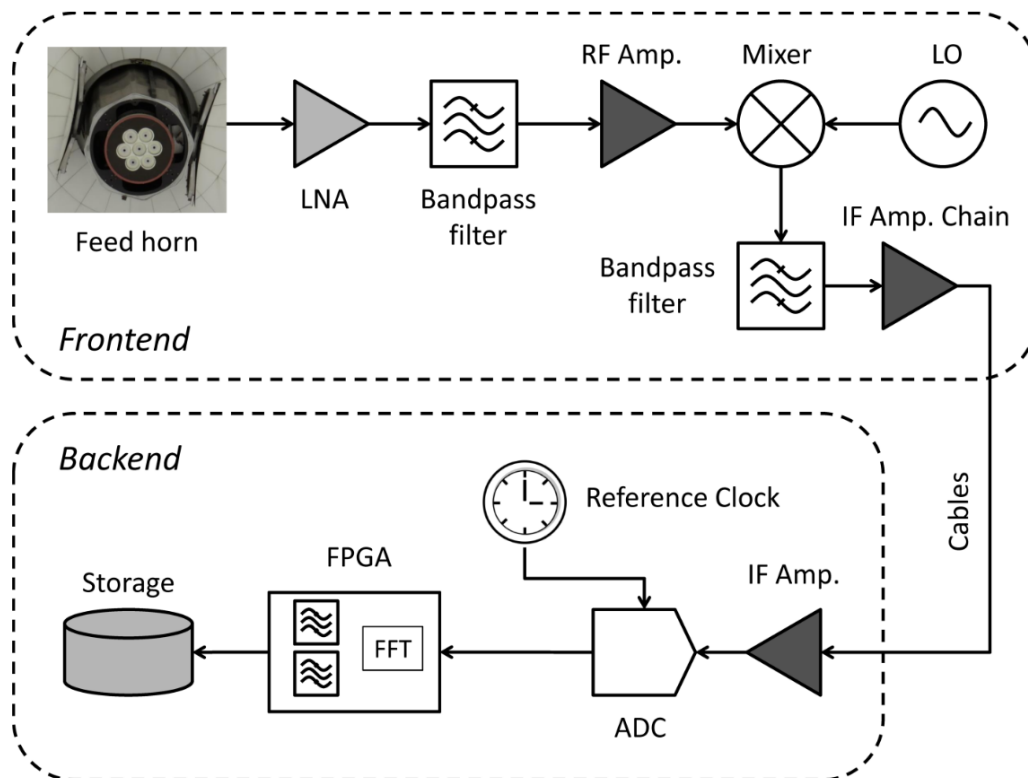
Figure 2.4: Simplify components of the radio telescope system. The frontend and backend were described in Section 2.1.3 and 2.1.4, respectively. Image taken from Cameron (2018).

2.2 Pulsar searching

In this section, the method of pulsar search will be discussed. The overall search pipeline is shown in Figure 2.6. As the signal is stored as a "**filterbank**" file, which contains frequency information through channelisation (see the previous section). The frequency information in the filterbanks file is needed to correct the frequency delay of the pulse due to the interaction with the electrons along the line of sight. This correction is known as de-dispersion that was introduced in Section 1.4.1. After de-dispersion, the data are reduced to a one channel de-disperesed **timeseries**, which are combined power in each frequency channel after de-dispersion to each DM step. Next, a binary motion of the pulsar in a binary system can reduce the pulsar's detectability, causing the period pulse period to change due to the Doppler effect. I will briefly discuss how to compensate for the period change due to binary motion and its limitations in Section 2.2.4. The technique used in this pipeline is known as time domain resampling (see Section 2.2.4), which corrects for the time advance/delay caused by the binary motion, assuming that the acceleration over T_{obs} is constant.

After mitigating all external effects, a periodic signal is searched for using various methods, including the Fast Fourier Transform (FFT) and the Fast Folding Algorithm (FFA). These methods

are discussed in more detail in Sections 2.2.1 and 2.2.2, respectively. With the possible period determined using either of these search algorithms, weak pulses can be detected by folding the timeseries. The general idea of folding is that the signal is a combination between a random noise and a signal with a specific period. If the timeseries is divided with the length of the expected period and added together, then the signal will keep increasing, as shown in Figure 2.5. As each individual single pulses of pulsars is often weaker than the noise, folding the timeseries can increase the S/N significantly, assisting the discovery of the new pulsar. The result from folding is also known as an "**archive file**" and is considered as a *pulsar candidate*, which contains pulse profile and other helpful information for pulsar candidate classification (see Section 2.2.6). To improve the sensitivity of the pipeline and data quality, radio frequency interference (RFI) needs to be mitigated. This can be done at the beginning or end of the pipeline. Each type of RFI and how to mitigate them will be discussed in Section 2.2.5. Lastly, each pulsar candidate needs to be inspected. An example of this process will be discussed in Section 2.2.6.
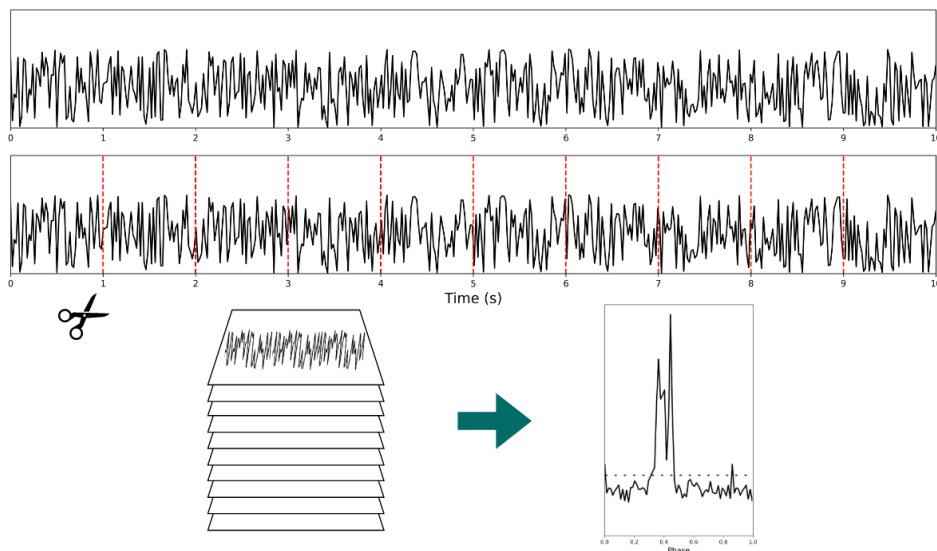
Figure 2.5: Illustration of the folding technique, where a timeseries is cut into segments of 1s long. Combining these segments together resulting in a pulse profile, confirming the presence of a 1s periodic signal. Image from Cruces (2021).

2.2.1 Pulsar searching algorithms: The Fast Fourier Transform (FFT)

The Fast Fourier Transform (FFT) is the most successful method for searching for pulsars. However, the FFT has additional drawbacks when dealing with narrow pulse pulsars. Consequently, a thorough understanding of how the FFT operates is vital to comprehending these disadvantages.

The FFT searches for periodicity in timeseries $\mathcal{T}$ with N samples. Using the Fourier transform of the $\mathcal{T}$ and analysing the Fourier power spectrum. However, because the timeseries are discrete, the Fourier transform cannot be applied directly. Instead, discrete Fourier transform (DFT) is
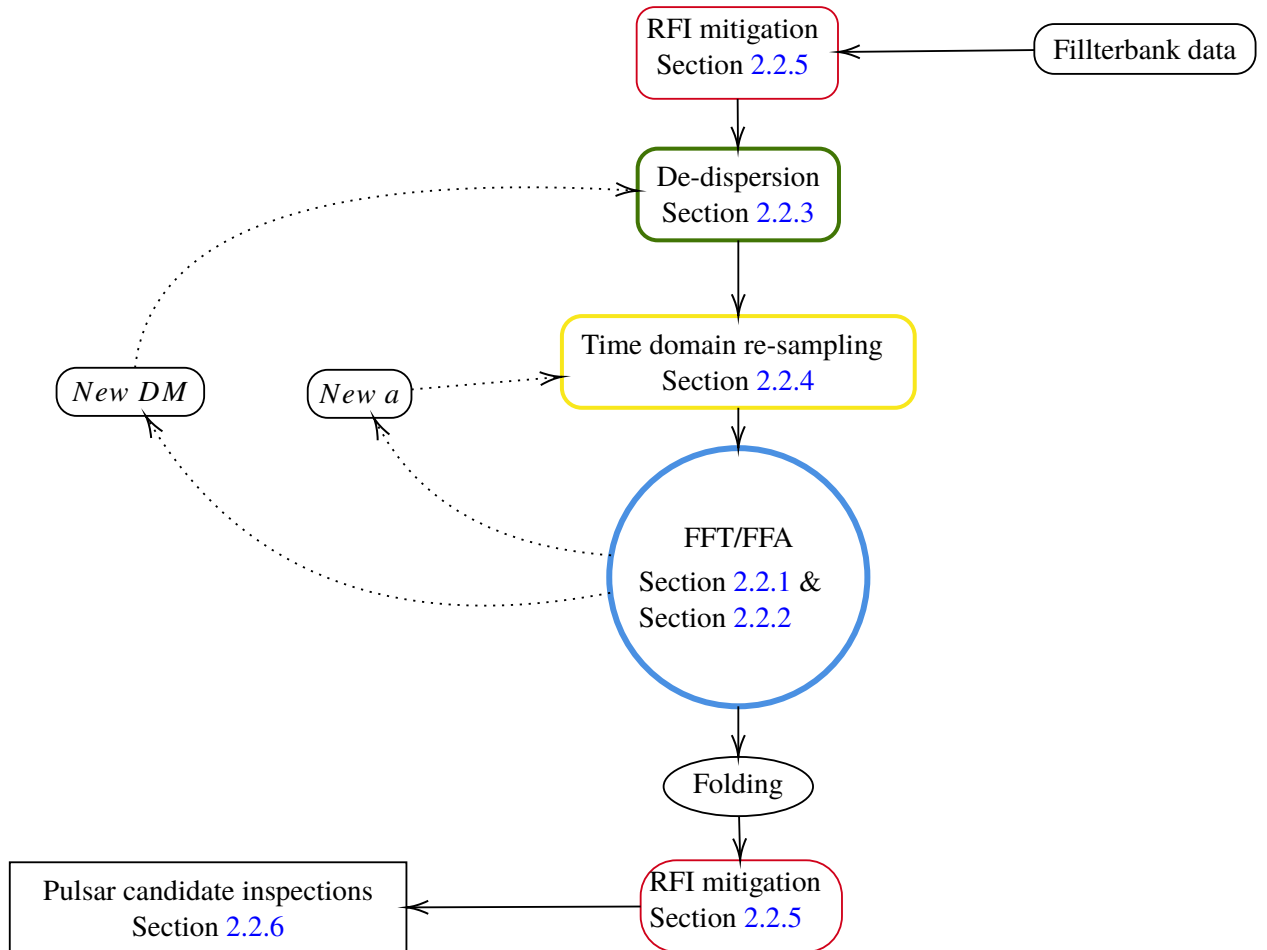
Figure 2.6: A simplified flowchart of a pulsar search pipeline. The pipeline begins by removing the RFI. Then the data is de-dispersed and resampled to the corresponding acceleration and DM, resulting in timeseries. The timeseries are then searched for the periodicity and fold to increase the S/N. The folded data turned into a pulsar candidate which will be further inspected.

used. The kth Fourier component of the DFT can be determined by,

$$\mathcal{F}_k = \sum_{j=1}^{N-1} \mathcal{T}_j exp(-2\pi ijk/N), \tag{2.5}$$

where i here is the imaginary number $i = \sqrt{-1}$ and k is the Fourier frequency. From Nyquist sampling theory, the range of frequency spectrum that can be obtained from DFT is $\frac{1}{T_{obs}} < \nu < \frac{1}{2t_{samp}}$ (Shannon, 1949). However, the DFT need a large floating-point operation, $O(N^2)$, (Cooley and Tukey, 1965), which requires a significant amount of computational resources. The optimised implementation of the DFT is known as the fast Fourier transform (FFT), which requires only $O(N\log_2(N))$ operations (Cooley and Tukey, 1965). The improvement of the FFT comes from the properties of the Fourier transform that can be written as $\mathcal{F}_{N-k} = (\mathcal{F}_k)*$, which makes the DFT symmetrical around $k = N/2$, which reduces the number of operations drastically (Cooley and Tukey, 1965). To explain this, we study a timeseries with 10^6 samples, while the DFT needs 10^{12} operations, the FFT takes only $10^6 \cdot 6\log_2 10$, which is $\sim 10^4$ times less than the former. After that, summation of the real and imaginary parts of the Fourier components ($\mathcal{P}_k = |\mathcal{F}_k^2|$). The Fourier spectrum can be used to investigate the periodicity in timeseries, as demonstrated in Figure 2.7.

Normally, most of the pulsars have a relatively narrow pulse, which means that they are only active for a few percent of their period. This active fraction of a pulsar with a period P is defined as the duty cycle, $\delta = W_p/P$ where W_p is the pulse width. To demonstrate how each pulse of a different width is manifested the Fourier spectrum, we apply the FFT to two signals with an δ of 5% and 50% as shown in Figure 2.8. This figure demonstrates that the Fourier power of a narrow pulses has more power being distributed over many harmonics ($2/P,3/P,4/P,...$). Since the frequency of the harmonics is known, the distributed power can be recovered incoherently by adding the power in each harmonic to the fundamental frequency, this method is called incoherent harmonic summing (Taylor and Huguenin, 1969) as shown in Figure 2.9. As the power is smeared over higher harmonics, there is an optimal harmonic at which the S/N is maximised before the contribution from noise becomes dominant. This optimal harmonic depends on the pulse width. Standard FFT searches often consider up to the 8th, 16th, or 32nd harmonics, depending on the pulse width. Limiting the maximum number of harmonics considered can also save computational resources.

After applying the FFT to the data, peaks in the Fourier spectrum are searched for, providing a list of significant periods. In addition, it is highly likely for a pulsar candidate to be detected multiple times in each trial for different values of the search parameters. To reduce the number of candidates, the filterbank data will be folded at each detected period and search parameters that give the highest S/N. This process is known as sifting.

Although the FFT is the most successful search method for pulsars, there are some restrictions. For instance, it has less sensitivity on the search for a long-period pulsar (defined here as a pulsar with a period greater than 1 s), as demonstrated by Kondratiev et al. (2009b).Moreover, the FFT is less sensitive to periodic signals with narrow pulse shapes because as the pulse width becomes narrower, more of the power is distributed to higher harmonics. This can exceed the harmonic
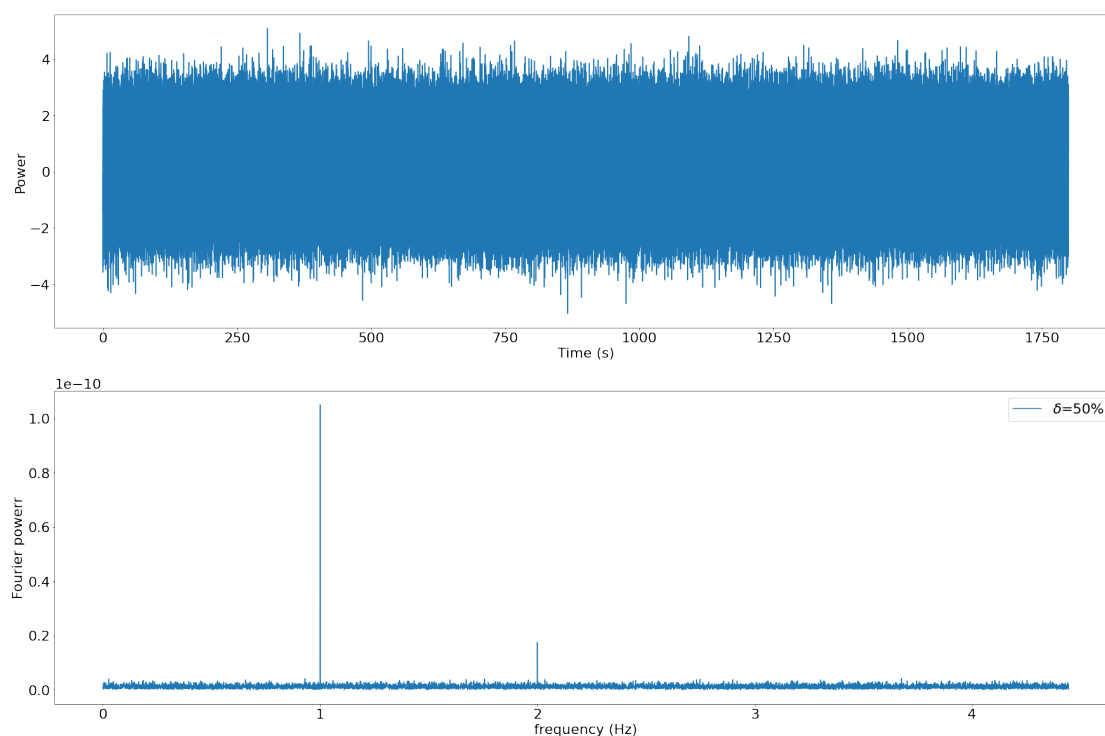
Figure 2.7: Showing how the FFT can be used to search for a periodicity. Upper: simulated timeseries are plotted between power and time. The pulsations are not visible visually in this plot. However, applying the FFT resulting in the Fourier spectrum shows a strong peak at 1-Hz, indicating a periodicity at the mentioned frequency.

summing limit. To combat this, an alternative search algorithm will be discussed in the next section.

2.2.2 Pulsar searching algorithms: The Fast Folding Algorithm (FFA)

As mentioned in the previous section, one of the last steps of the FFT searches is to fold the timeseries at each possible period with high power in the Fourier spectrum that passes the customised threshold. Folding increases the S/N because when the timeseries is divided into segments with the duration of one period, all the pulses will be in the same bins offset. After combining all segments together, the containing signals are summed, increasing the S/N by a factor of $\sqrt{N_{\text{pulses}}}$ (see Figure 2.5 for example), where N_{pulses} is the number of pulses in the data. However, if the folded period is $P + \delta P$, then the time offset will be increased linearly (see Figure 2.13 for example) and the folded S/N will be decreased. Consequently, the folding technique can be employed to search for periodicity, by identifying the period that yields the highest S/N after the fold.

However, searching by folding all possible periods is computationally expensive as it requires $O(N^2)$ operations (see e.g. Cameron et al., 2017a, and the reference therein). Following the implementation of the FFT in 1965 (Cooley and Tukey, 1965), Staelin (1969) implemented the

Figure 2.8: Results of applying the FFT to two signals with the period of 20s, i.e., 0.05 Hz with δ of 50% (Right) and 5% (Left). For the signal with δ=50% the Fourier power is concentrated in the fundamental harmonic with approximately 20% in the first harmonics. In contrast, the Fourier power from the narrow signal (δ=5%) is distributed to multiple harmonics, making the peak at the fundamental frequency less prominent.

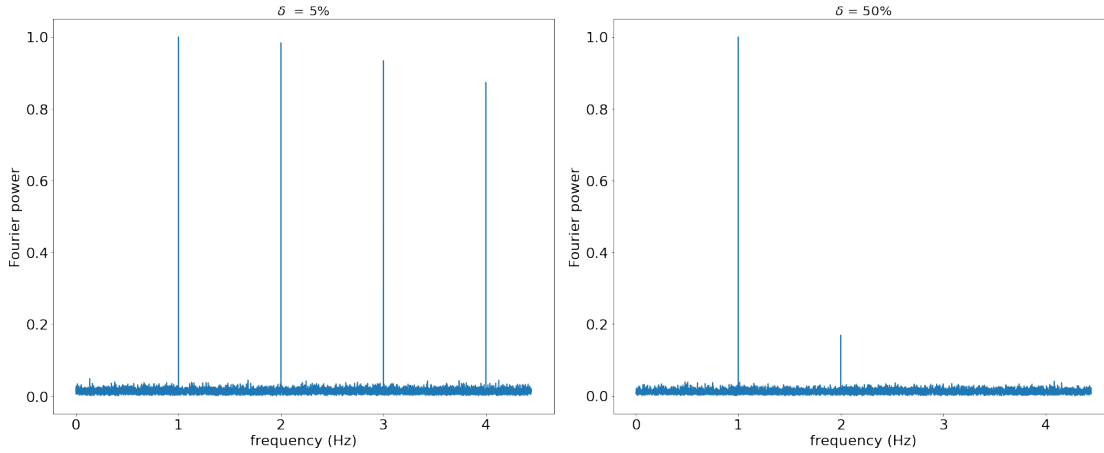Fast folding algorithm (FFA). The FFA works by splitting a timeseries ($\mathcal{T}$) into small fractions of n samples, representing the initial search period (p_0) with the condition that N/p_0 is an integer power of 2, where N is the total number of samples. After that, the data are folded with a different pulse offset rate, representing a different pulse period from p_0 to $p_0 + 1$, illustrated by each arrow in Figure 2.10.

Each time the folded profile is produced, it corresponds to fold the $\mathcal{T}$ at the period p_j, where j is to total number of bins that drifted during the T_{obs} as

$$p_j = p_0 + \frac{j}{N/p_0 - 1}. \tag{2.6}$$

Until this point, we are folding the processed data, not searching for the pulsations themselves. in order to do that, the folded profile is searched by using matched filters. The matched filter is a computational method used to search for a signal with a known shape by convolving the data with different templates. After normalisation, the template that 'best matched' the signal shape will result in the highest peak, as demonstrated in Figure 2.11. It is worth to mention that, the implementation of matched filter needs to be efficient due to the large number of operation for FFA searches.

The advantage of the FFA is that it takes only $O(N \log_2(N/n))$ operations, which is significantly less than brute force folding, leading to a shorter computational time. However, the FFA is still too computationally expensive to apply on a large-scale pulsar survey compared to the FFT with the same data length. Hence, the FFA has been used mainly on targeted searches, e.g., radio emission from known X-ray neutron stars (Crawford et al., 2009; Kondratiev et al., 2009a).

Lazarus et al. (2015) showed that the current search pipelines, using FFTs, are less sensitive to slow pulsars. Cameron et al. (2017a) made an in-depth sensitivity analysis of the FFA, showing
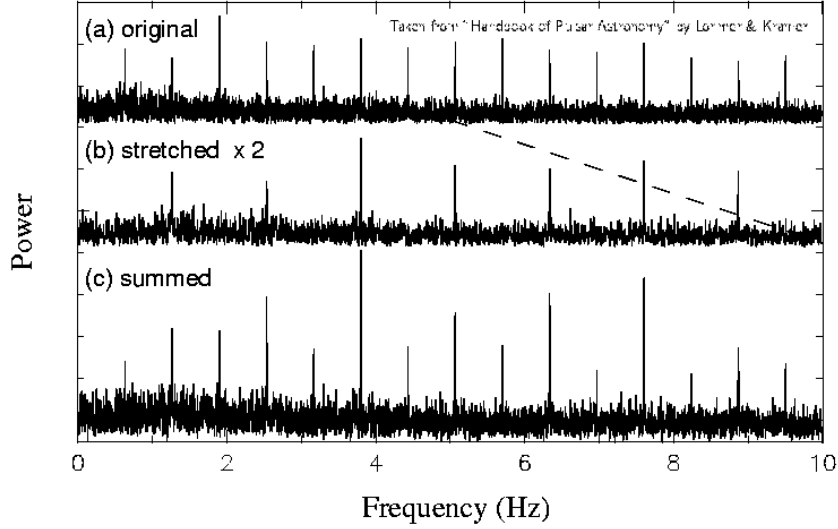
Figure 2.9: Demonstration of the applying harmonic summing by stretching the other half of the spectrum by a factor of 2 and adding that to the original spectrum. This process increases the S/N by a factor of $\sqrt{2}$. Repetition of this process will increase S/N by large factors. Images obtained from Lorimer and Kramer (2012).

that the FFA pipeline is more sensitive to the slow pulsars than the FFT, as confirmed by Parent et al. (2018). These are some niche use cases for the FFA over slow pulsars.

Recently, Morello et al. (2020a) published a new implementation of the FFA called `riptide`-FFA (rFFA). The rFFA makes use of the folding transform, illustrated in Figure 2.13. Similar to the traditional FFA, the folding transform reshapes $\mathcal{T}$ with N sample containing m cycles of pulses with a period p bins to a 2D array with m rows and p columns. If we assumed that the last pulse is drifted by s bins over the m cycle, then the folded profile is expressed by

$$p_c = \sum_{s=0}^{m-1} \mathcal{T}_{c, r+\frac{s}{m-1}r} \tag{2.7}$$

in the cth column and r^{th} row, respectively (see Figure 2.14). Hence, to search for periodicity in a range of p_0 to $p_0 + 1$, we only need to search from $s=0$ to $s = m - 1$. To further optimise the FFA, the rFFA computes the folding transform of two halves of the aforementioned two-dimensional array of $\mathcal{T}$. As shown in Figure 2.14, the $\mathcal{T}$ is divided into two blocks, called the head and the tail. Each block contains m_h and m_t rows with a condition that $m = m_t + m_h$. In both blocks, the last pulse will be drifted by i bins for the head and j bins for the tail. These drifted rates are expressed by

$$i = \left\lfloor (m_h - 1) \cdot \frac{s}{m - 1} \right\rfloor, \tag{2.8}$$

$$j = \left\lfloor (m_t - 1) \cdot \frac{s}{m - 1} \right\rfloor. \tag{2.9}$$
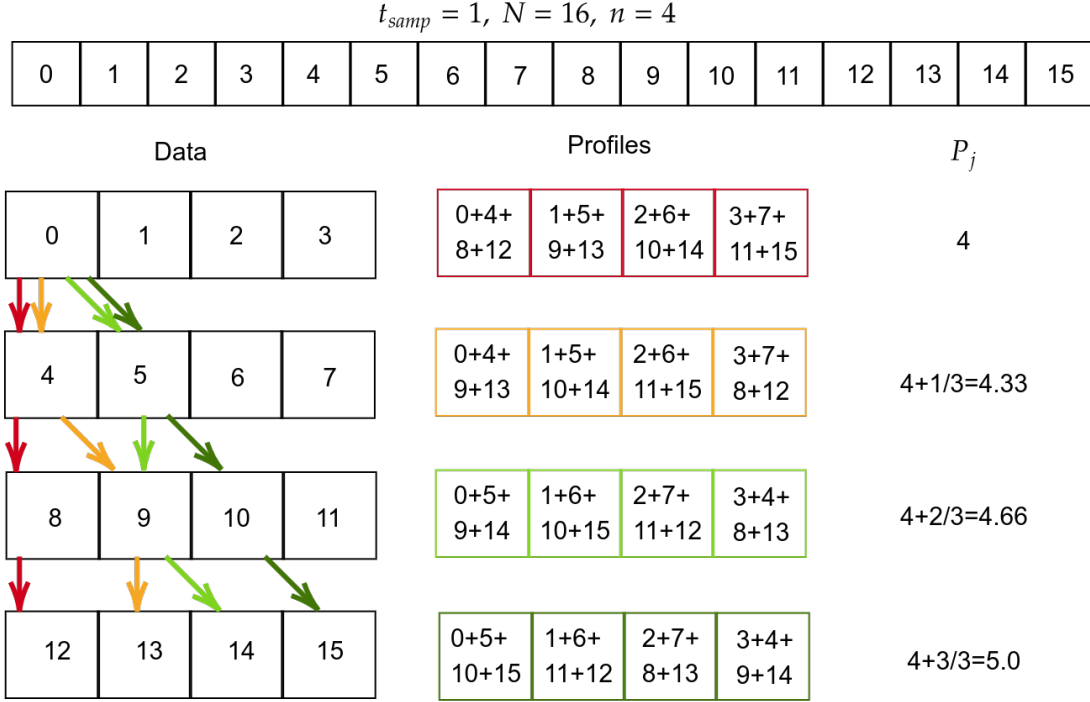
Figure 2.10: Schematic representation of the FFA that folds a $\mathcal{T}$ with $t_{\text{samp}}=1$ and $N = 16$. For this search, the period range is set to be from 4 bins to 5 bins. The FFA searches for a different period by folding the data with a different path represented by red, yellow, light green, and dark green arrows. The pulse profiles, demonstrated in each combined data point, are shown in the corresponding colour boxes.

Where $\frac{s}{m-1}$ is a total drifting rate and $\lfloor\rceil$ represents the rounding to the nearest integer. This process can be recursively repeated by further splitting the head and the tail into smaller blocks until the block size is basically one row, improving the calculation speed. The S/N for each pulse profile is determined by matched filters. After that, the combination of FFA and matched filtering yields a one-dimensional array called a periodogram that contains only the highest S/N across all trial widths and phases as a function of the trial period, as shown in Figure 2.12.

The rFFA is more efficient than the original FFA as it has a smaller input, basically each row, allowing the input to be stored in the modern CPU caches. Storing the input directly in the CPU can reduce the computational time significantly, as there is no need to transfer the data between the main memory and the CPU cache. In addition, the rFFA does not require that N has to be 2^n, unlike the original FFA. The classical FFA deals with the non-2^n samples $\mathcal{T}$ by zero-padding the data until it reaches the requirement, which increases the number of operations, leading to unnecessary increases in computational time.

Currently, the rFFA has been successfully applied to reprocess the blind pulsar surveys, namely, the SUPERB surveys (Morello et al., 2020c), the GMRT survey (Singh et al., 2022), and the HTRU survey (Chapter 3), discovering pulsars that were not detected by the FFT pipeline.
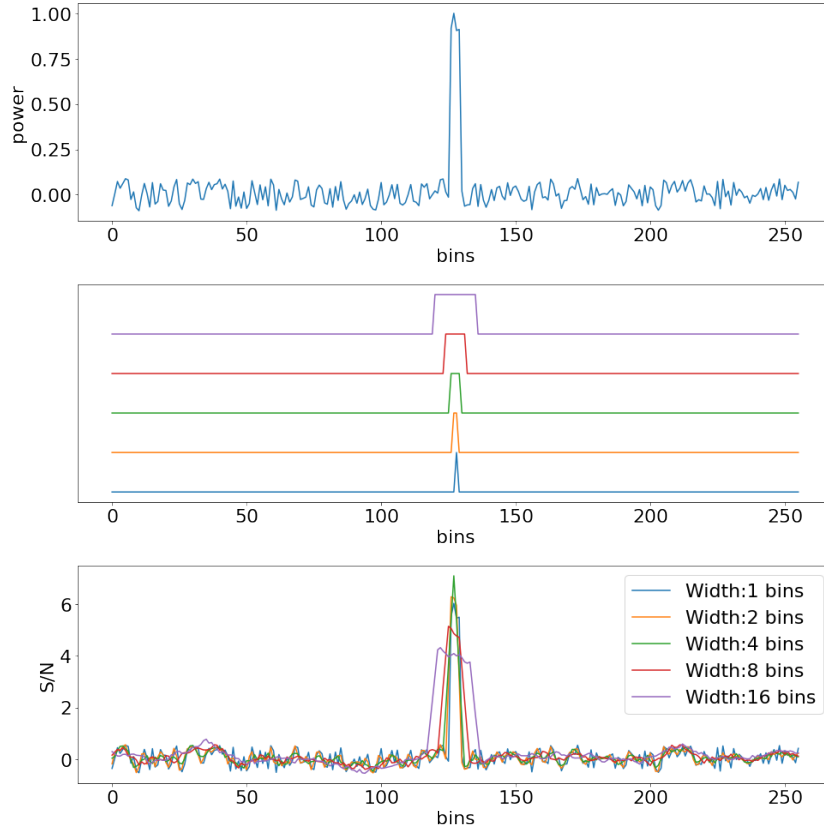
Figure 2.11: Demonstration of matched filters. Upper: A pulse profile with a 4 bins width boxcar signal. Middle: Trial boxcar function with a width of 1,2,4,8,16 bins. Lower: Results from matched filters, showing maximum S/N with 4 bins boxcar templates.

2.2.3 Pulsar data preparation: De-dispersion

As mentioned in Section 1.4.1, the signals from the pulsars are delayed chromatically due to the presence of free electrons in the ISM. The dispersion can be mitigated by subtracting the time delay in each frequency at each step DM. As a result, we still need multi-frequency data from the filterbank file, which contains both time and channelised frequency information.

If the DM is unknown before the observation, it is searched for by correcting the time delay through a range of DM values to increase S/N. To search for DM efficiently, we need to calculate the dispersion trials, which is given by

$$\text{DM}_i = 1.205 \times 10^{-7} \text{t}_{\text{samp}}(\text{ms}) \frac{\text{f}_c(\text{MHz})^3}{\Delta \text{f}(\text{MHz})} \text{pc cm}^{-3}, \tag{2.10}$$

where DM_i is the ith DM for a receiver with a bandwidth Δf at central frequency f_c (see Lorimer and Kramer, 2012, and the reference therein). The de-dispersion is done by shifting the time delay, calculated from Equation 1.12, in each frequency at each trial DM. This technique is
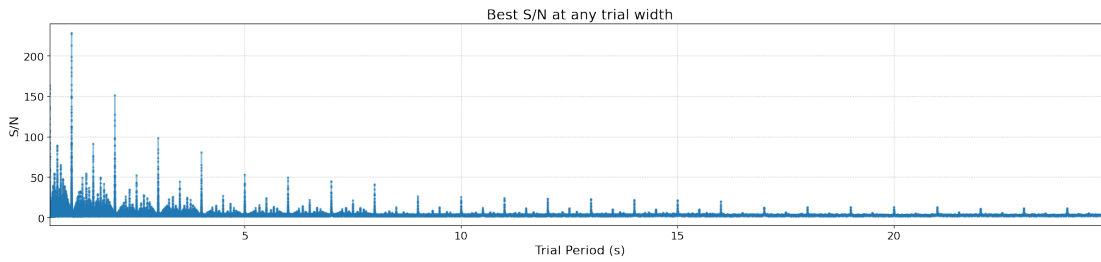
Figure 2.12: A result from applying rFFA timeseries shown in Figure 2.7 known as periodogram, showing the S/N over the period. In this periodogram, there is a strong peak at 1 s, which is the underlying periodicity in this timeseries.
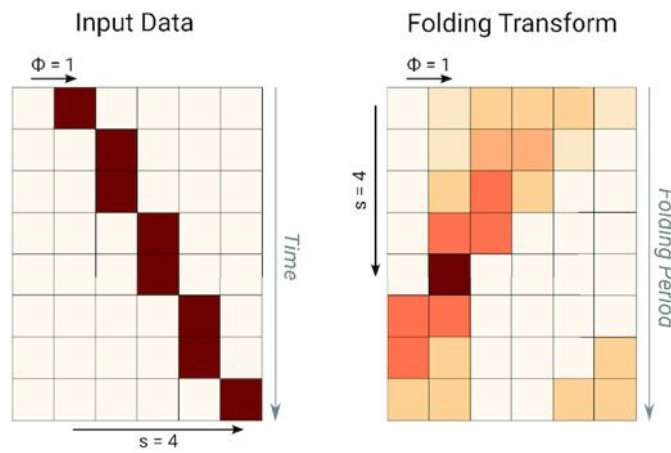
Figure 2.13: A demonstration of the folding transform, similar to Figure 2.10. In the left panel, input data is reshaped into a 2D array of 8 rows and 6 columns, where the darker colour represents a larger folded S/N. The data contain pulses with the initial phase of ϕ=1 samples and a period larger than p. As a result, the pulses drift over the whole data by 4 bins. The right panel shows the folding transform of the data, showing the highest S/N at ϕ=1 and s=4. Image from Morello et al. (2020a).

known as "incoherent de-dispersion". However, this de-dispersion method has a limitation due to the "intrachannel smearing". This effect is caused by the fact that the filterbank contains a bandwidth divided into smaller frequency channels which may contain dispersion inside each channels, broadening the pulse profile. Alternatively, the "coherent de-dispersion" technique (Hankins, 1971; Hankins and Rickett, 1975) can be used. This technique applies an FFT to the baseband data (see Section 2.1.4) and then shifts the phase of the bins in Fourier spectrum by the phase-shift expected from the DM value, which must be known before the observation. This method recovers more power of signals than the incoherence de-dispersion. The comparison between these methods is shown in Figure 2.15.

In this thesis, incoherent de-dispersion is mainly used when we search for a new pulsar or when only the filterbank data are available. For known pulsars, the coherence de-dispersion can be used to improve the sensitivity, as shown in Figure 2.15.
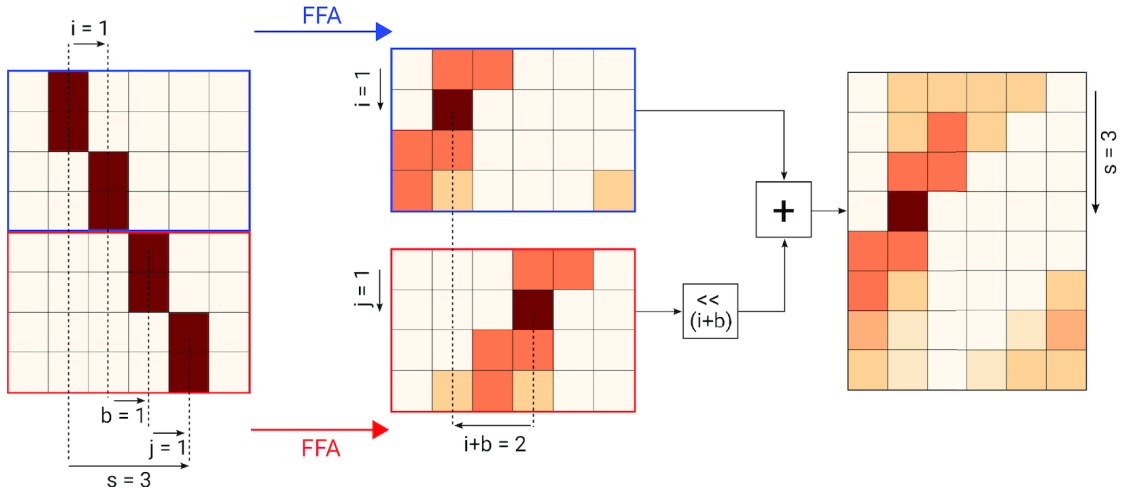
Figure 2.14: A demonstration of the segmented folding transform where the data has been divided. This process can be re-applied recursively. Image from Morello et al. (2020a).

2.2.4 Pulsar data preparation: Mitigating the effect from the binary motion

Both the FFA and FFT work on the assumption that the spin period of the observed pulsar is constant over the course of the observation. If the observed period is changing, for example due to the Doppler effect caused by the motion of a pulsar around its companion star in a binary system, the pulse power will be spread out in both the Fourier spectrum and the periodogram. This can make it more difficult to detect the periodic signal, as the power is distributed over a wider range of frequencies or periods. As a result, both are efficient only for searching for an isolated pulsar and a pulsar in a binary system with a long orbital period, where the period change through the observation is considered negligible. However, this is not the case for pulsars that have a relatively short orbital period, where the motion of the pulsar is enough to cause the rotation period to change non-linearly. For pulsars with an intrinsic period P_0 that is moving with line-of-sight velocity (v_l), due to Doppler motion, the detected period will be modulated as

$$P = P_0(1 - v_l/c), \tag{2.11}$$

where P is the apparent period. Hence, without correcting for the non-linear change [1], the period of the pulsar will drift in the periodogram, reducing the total S/N as shown in Figure 2.16.

Freire et al. (2001) demonstrated that the v_l of an object with the orbital period of P_b, eccentricity e, projected semi-major axis a_p with angular velocity Ω at time t is

$$v_l = (\frac{2\pi}{P_b})\frac{a_p}{\sqrt{(1-e^2)}}[\cos(\Omega t) + e\cos\Omega t] \tag{2.12}$$

In theory, the period drifting, where the apparent period is changing overtime, can be corrected

---

[1] A linear change in period will cause the pulse to drift linearly, changing the detected period.
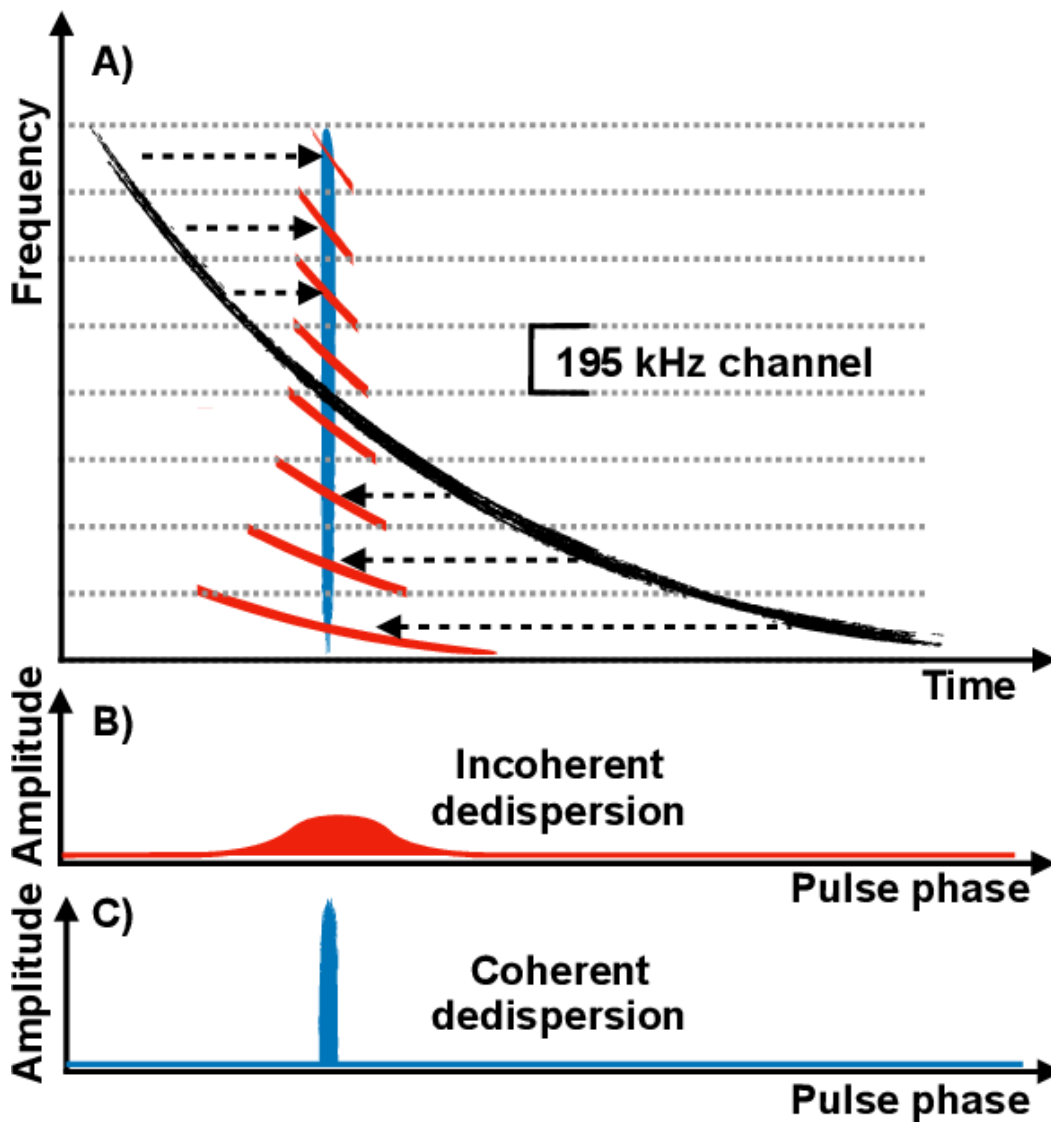
Figure 2.15: Illustration of the difference between pulsar incoherent and coherent de-dispersion. The upper plot shows the frequency-phase plot with a channel width of 195 kHz, with a highly dispersed signal in black. The result from incoherent and coherent de-dispersion is shown as the red and blue curves, respectively. The pulse profile from incoherent de-dispersion is shown in the middle plot, with a broad pulse profile. The lower plot results from coherent de-dispersion, showing more S/N and a narrower pulse profile. Image from Bondonneau et al., 2020.
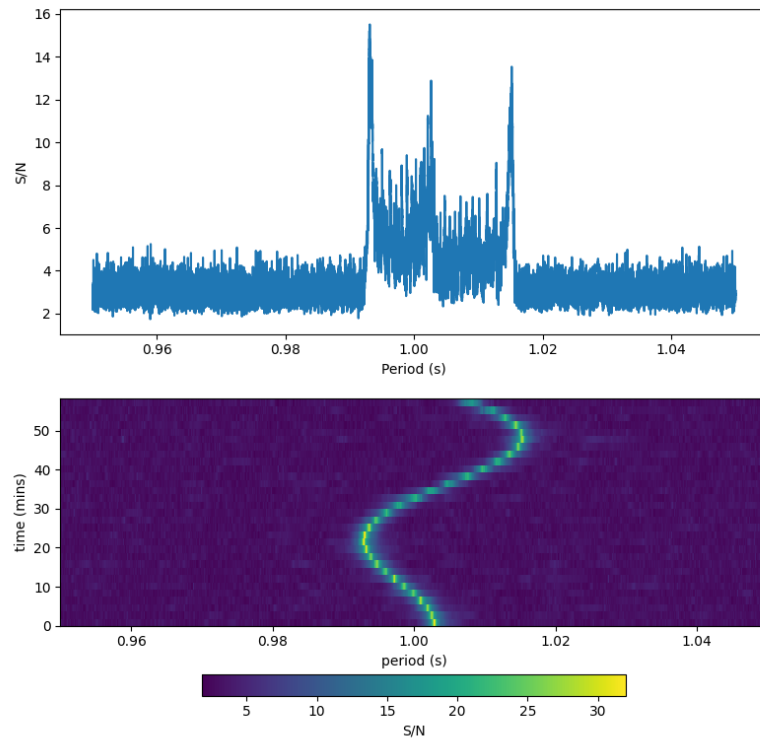
Figure 2.16: Effect of binary motion in pulsar detectability. Upper: A rFFA's periodogram from a simulated 1 s pulsar in a circular binary orbit with an orbital period of an hour. The observation was an hour long. Due to the binary motion, the apparent period of the pulsar was oscillating around 1 s peak at S/N of 16. Lower: Periodograms from segmented the whole data to 32 segments showing the period evolution over the observation. The maximum S/N from this set of periodograms is approximately 35. In most cases, the pulsar is too weak to be detected in a small segmented time. As a result, without correcting for the binary motion, a large fraction of the signal is lost. This effect also occurred for the FFT search, smearing the Fourier power spectrum, as demonstrated in Figure 6.11 in Lorimer and Kramer (2012).

by searching for five Keplerian orbital parameters (see Section 2.3): with the right orbital parameters, it can completely account for the period change due to binary motion. The search can be done by "resampling" every data point in the timeseries to match each set of orbital parameters such that the period of any pulsar would be constant (e.g. Balakrishnan et al., 2022). However, it is not computationally feasible to do that in most blind pulsar surveys. Alternatively, we can assume that the pulsar moves with a line-of-sight acceleration a and its derivative i.e. jerk j at time t, then using a Taylor series expansion which gives the first three terms as

$$v_l = v_l + a_l t + \frac{j_l t^2}{2!} + ..., \tag{2.13}$$

where v_l, a_l, and j_l is the line-of-sight velocity, acceleration, and jerk at $t = 0$. Assumed that there is no higher order derivative in v_l, then the line-of-sight travel distance (Δd_l) of the pulsar is

$$\int v_l dt = \Delta d_l = v_l t + a_l \frac{t^2}{2!} + \frac{j_l t^3}{c \, 3!}. \tag{2.14}$$

As the pulsar is moving, changing the position, the light travel time is also modulated by Δt as

$$\Delta t = \frac{v_l t}{c} + \frac{a_l t^2}{c \, 2!} + \frac{j_l t^3}{c \, 3!}. \tag{2.15}$$

To approximate Δt, the simplest approach is to assume that the pulsar is moving with a constant acceleration (a) throughout the observation time T_{obs}. Hence, the non-linear contribution from a to the pulse arrival time is,

$$\Delta t = a_l \frac{T_{\text{obs}}^2}{2 \, c}, \tag{2.16}$$

then we can resample the timeseries for each acceleration. However, this technique assumes that (a_l) is constant, limiting our shortest detectable binary period (P_b) to 10% of the observation time (T_{obs}) since a cannot be assumed to be constant for the shorter P_b. This is demonstrated in Ransom et al. (2003) and Ng et al. (2015b). Furthermore, Eatough et al. (2013a) and Ng et al. (2015b) for instance also demonstrated that, if the pulsar is bright enough, we can segment the timeseries, which reduces the 'effective' T_{obs}, as $\Delta t \propto T_{\text{obs}}^2$, leading to a larger acceleration step, reducing the number of trials. Since this technique searches for only one parameter, it is widely used in many pulsar surveys due to its relatively low computational cost, including in this work (see Chapter 3, for example).

For a short orbital period and dim pulsar, the segmented acceleration search is not effective. As a result, we can either use a bigger telescope or search for the higher-order orbital motion. An example of a higher-order search is the jerk search. This method assumes that the pulsar is moving with a constant jerk i.e. with a constant acceleration derivative, throughout T_{obs}. Thus, the non-linear contribution from a and j to the pulse arrival time is

$$\Delta t = \frac{a \, T_{\text{obs}}^2}{2 \, c} + \frac{j T_{\text{obs}}^3}{6 \, c}. \tag{2.17}$$

Each data point in the timeseries is resampled to each a and j in the desired ranges. Since we are

searching for a and j in the time domain; hence they are known as "Time domain acceleration/jerk searches".

Alternatively, for an FFT search Ransom et al. (2003) and Andersen and Ransom (2018) implemented a technique to search for the period/frequency drift in the FFT spectrum, making the corresponding Fourier peak to be broadened (see upper panel in Figure 2.16), rather than resampling in the timeseries. As a result, the a and j are corresponding to drifting Fourier bins as z and w, respectively, which are expressed by

$$a = \frac{zcP_0}{hT^2}, \tag{2.18}$$

$$j = \frac{wcP_0}{hT^3}, \tag{2.19}$$

where h is the number of harmonics. Then the Fourier domain acceleration/jerk searches can be done with matched filters of a Fourier response pattern with z, and w bins smearing. Thus, to search for acceleration and jerk, one needs to just search from the smearing bin in the range of 0 to $zmax$ and/or $wmax$ depends on each search pipeline acceleration and jerk ranges.

2.2.5 Pulsar data preparation: Radio Frequency interference (RFI) mitigation

With the rapid development in telecommunication technology, there are many sources of radio signals, e.g. mobile phones, satellites, and wireless routers. These signals are known as "radio frequency interference" (RFI). If not properly mitigated, the cumulative impact of RFI across an observation might interrupt the detection of an astrophysical signal. It also can increase the computation time of processing pipelines by increasing the number of candidates to fold and result in longer manual inspection times.

There are a few techniques for RFI mitigation, depending on how the RFI manifests in the data. Some RFI will appear in the time domain as either persistent or short live bursts, while some RFI manifests in a specific frequency range as narrowband signals, as shown in Figure 2.17. If sufficiently bright, this type of Radio Frequency Interference (RFI) can be mitigated by subtracting the median from the part of the data that is statistically different from the remainder. This process is applied to the time-domain data, resulting in a continuous time series. In the frequency domain, outliers are replaced with zeroes, which do not need to be continuous and introduce no additional noise to the data. There are a couple of methods that can further mitigate the RFI. For example, astrophysical signals experience dispersion as they travel across the interstellar medium. Hence, they need to have some amount of DM. One of the algorithms that used DM to mitigate the RFI is known as the *zero-DM filter*. However, the zero-DM filter might remove the signal from the pulsar with low-DM or long-period, as shown in Eatough et al. (2009).

Another type of radio noise, which needs to be mitigated, in the time domain is known as 'red noise', which appears as noise variation in the timeseries, mimicking low-frequency signals. This type of RFI is likely originates from slow changes in the receiver's gain and atmosphere (see Figure 2.17). The red noise is important to the search for slow pulsars. The data that suffered from the red noise can be mitigated by either scaling down the Fourier power spectrum[2] or running

---

[2] In this approach, red noise is modelled as a power law in the power spectrum, where power decreases towards higher
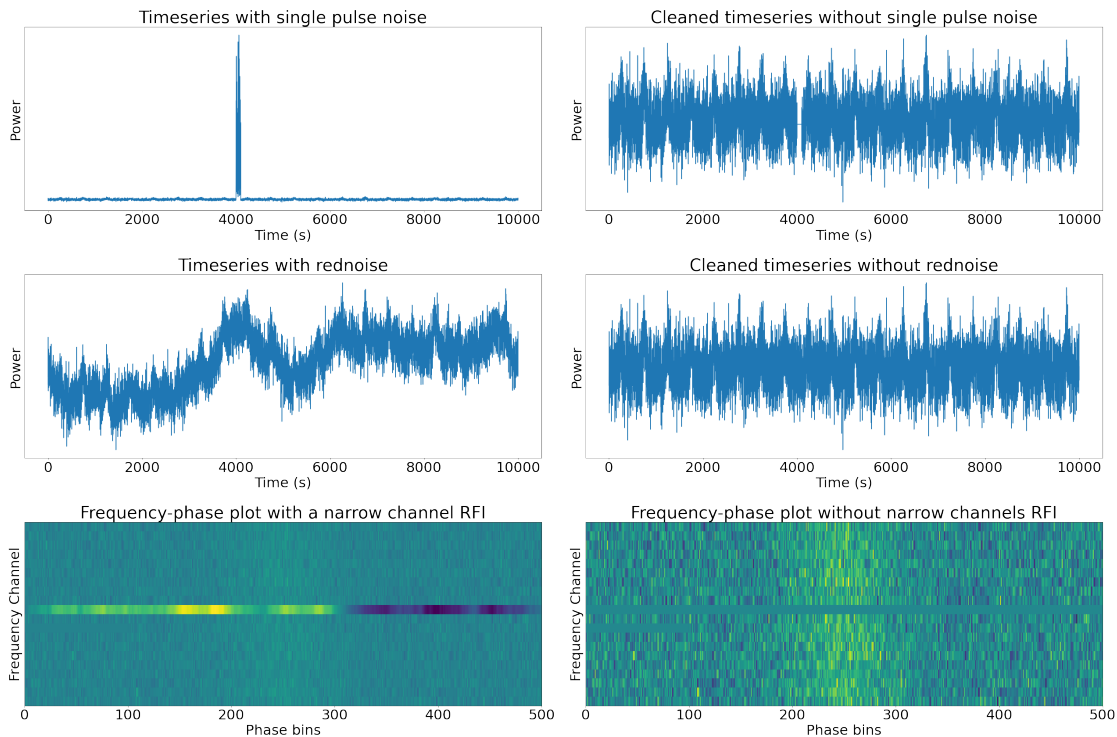
Figure 2.17: Simulated pulsar data with RFI added. The first row shows the timeseries with (left) and without (right) bursts of RFI. The second row shows the timeseries with and without red noise, where the baseline of the timeseries is slowly changing, mimicking a low-frequency signal. Lastly, the plots show the frequency-phase with and without narrowband RFI.

median subtraction. The first technique is implemented to the standard pulsar search software, i.e., PRESTO[3] and SIGPROC (Lorimer, 2011)[4], while rFFA is implemented with a running median. Singh et al. (2022) demonstrated that running median subtraction can improve the S/N in the FFA for more than 30%, which is better than scaling down the Fourier power spectrum.

These are just some examples of automated RFI and red noise mitigation, which can be implemented and applied to the data from large pulsar surveys prior to the pre-processing, which is impossible for a human to visually inspect all the candidates, which can be in the order of millions. With proper RFI mitigation, the number of candidates can be reduced by two orders of magnitude in some cases (see Chapter 3). The RFI can also be mitigated manually by zero-weighting the contaminated frequency channels and time intervals. This is mostly done after the signal is detected and folded at the corresponding period. Examples of manual RFI mitigation software are psrzap and pazi (van Straten et al., 2012b). These packages were used throughout this work.

---

frequencies. Then we can model it as a power law, and normalises the Fourier components by this model, thereby reducing the effects of the red noise in the time domain.

[3] https://github.com/scottransom/presto

[4] https://sigproc.sourceforge.net

2.2.6 Pulsar candidate inspection

After detecting periodicity, one can fold the timeseries/filterbank to obtain the folded pulse profiles. Moreover, some features of the data might be useful to distinguish the pulsar from RFI. For example, the pulsar's signal is propagated through the ISM, which causes dispersion. As a result, a plot of the S/N versus DM trail should show peaks that are not associated with a DM of 0 pc cm^{-3}. This plot is known as the DM curve. Furthermore, pulsars intrinsically emit broadband signals. Thus, the emission that is detected over the bandwidth and the pulses should be aligned in a phase-time and phase-frequency plot. Consequently, both plots are usually used to classify pulsar candidates.

There are always some exceptions. For example, a pulsar with a broad pulse profile can appear at low DM and has a peak near 0 DM, depending on the observation bandwidth. Furthermore, scintillation (see Section 1.4.3) can also cause the signal to be observed in a relatively narrow frequency range and time. Typically, the number of pulsar candidates per observation is in the order of thousands of candidates per observation. Therefore, it is almost impossible to inspect all of them as part of blind pulsar surveys, which contain more than 10000 pointings. As a result, Machine Learning and Deep Learning techniques are sometimes incorporated into candidate classifications (see Balakrishnan et al., 2021, for example).

Currently, there are two major folding software, DSPSR (van Straten and Bailes, 2011) and `prepfold`, which give the "archive file". As archive files contain folded phase, time, and frequency information. They are much smaller than the filterbank files. An example of a result from the folding is shown in Figure 2.18.

2.3 Pulsar timing

When a pulsar is discovered, its rotation period and DM are estimated from its discover parameters. The position of the newly discovered pulsar is estimated based on the telescope's pointing position, with a positional error as the telescope's FWHM (see Figure 2.1). These parameters can be used to detect the pulsar for an intermediate timescale, typically in the order of a year, i.e. the parallax motion between of this pulsar and the Earth. To account for the effect of the binary motion for the pulsar in binary systems and dispersion, high time and frequency resolution data from the "filterbank" mode is required.

In this section, we will discuss one of the most important techniques in pulsar science, called pulsar timing. More details about pulsar timing can be found in, Hobbs et al. (2006) and Edwards et al. (2006) for instance.

Pulsars in binary systems can be detected for as little as a few hours depending on the pulsar's rotational period and the orbital period of the binary system, due to the pulsar's motion in the system modulating the time of arrival (TOA) of pulses. By fitting the TOAs to a timing model that includes binary parameters, we can study the orbital parameters of the system. Pulsar timing is crucial for both detections and the scientific applications as discussed in Chapter 1.5.

This technique assumes that the integrated pulse profile of a pulsar, calculated over a few thousand to ten thousand pulses, is usually stable. (see Rathnasree and Rankin, 1995; Liu et al., 2012a, for example). The arrival time at site (t_{sat}) is measured by cross-correlating the integrated
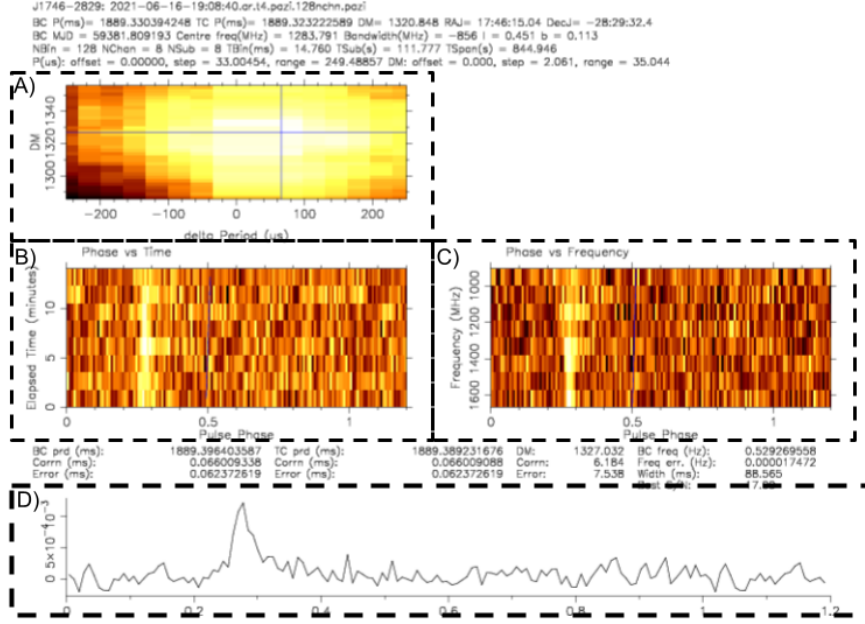
Figure 2.18: Candidate plot of PSR J1746-2829 from `pdmp`. Plot A) show DM-ΔP plane, where the brightness of the plot represents the S/N. This plot shows that this signal has a DM of 1327 $pc\,cm^{-3}$ Plot B) is the Phase vs time plot, showing a persistence signal near phase 0.3. Plot C) is the Phase vs Frequency plot showing a persistence signal in the throughout the bandwidth. Plot D) is the folded pulse profile, showing a peak near phase 0.3.

pulse profile, $P(t)$, with the pulse template, $T(t)$, to obtain the time shift (τ) as shown in Figure 6.2. A simple $T(t)$ is created by making an analytic noise-free pulse profile by fitting the profile with a combinations of Gaussian functions (see Kramer et al., 1994, for example). Then t_{sat} is calculated from $t_{sat} = t_{ref} + \tau$ when t_{ref} is a reference time of the observation for, $P(t)$ e.g., the modified Julian date (MJD) at the start of the observation.

Up to this point, t_{sat} has been referenced to the time at the observatory, which is not a rest frame with respect to the pulsar. This means that the TOAs will be affected by the Earth's motion, rotation and the location of the observatory. Therefore, we need to calculate the TOA at a reference point, such as the pulsar's commoving reference frame, in order to accurately study the pulsar's characteristics. A simplified equation used for frame transformation is

$$t_{psr} = t_{sat} + \underbrace{t_{corr} + \Delta_{R_\odot} + \Delta_{S_\odot} + \Delta_{E_\odot}}_{\text{Barycentric corrections}} + \underbrace{\Delta_{VP*} + \Delta_{DM} + \Delta_{E*}}_{\text{Interstellar corrections}} + \underbrace{\Delta_{R_B} + \Delta_{S_B} + \Delta_{E_B}}_{\text{Binary corrections}}. \qquad (2.20)$$

This equation includes three corrections, barycentric corrections, interstellar corrections, and binary motion corrections.
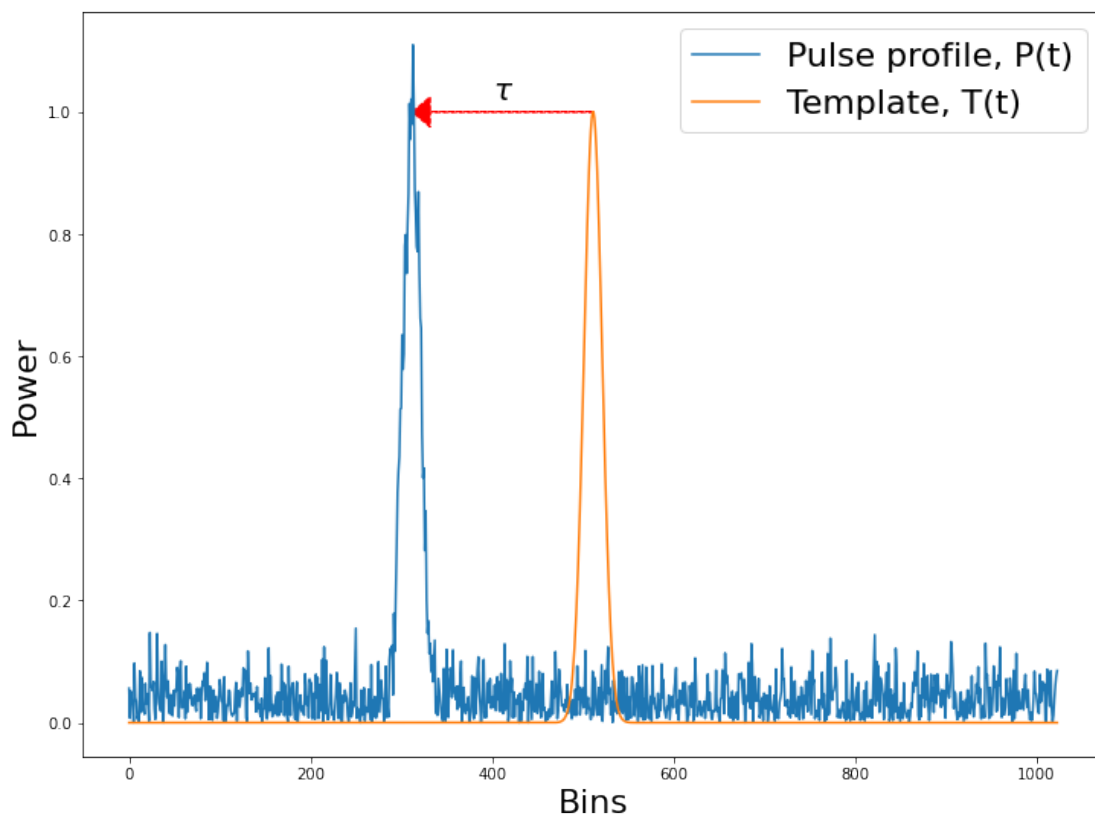
Figure 2.19: TOA extraction by computing a delay time (τ) between a noise-free template, $T(t)$, and the real pulse profile, $P(t)$. Typically, the template is centred at the first bin in the pulse profile, which serves as the reference time (t_{ref}) of the observation. However, for demonstration purposes, the template is centred in the middle of the pulse profile.

2.3.1 Barycentric corrections

First, barycentric corrections include a set of contributions which are

- t_{corr} is the observatory clock correction offset compared to a time standard, i.e. International Atomic Time (TAI).

- $\Delta_{\mathrm{R}_\odot}$ Solar System Romer delay, a light travel time difference between the observatory and the Solar System barycentre, assuming that the pulsar is located at an infinite distance.

- $\Delta_{\mathrm{S}_\odot}$ Solar System Shapiro delay (Shapiro, 1964), an additional relativistic delay caused by the space-time curvature around Solar System bodies.

- $\Delta_{\mathrm{E}_\odot}$ Solar System Einstein delay, the time dilation due to the motion of the Earth and gravitational redshift caused by objects in the solar system.

The last three terms are calculated based on accurate positions of the objects in the Solar system known as Solar System ephemeris. An up-to-date Solar System ephemeris is regularly provided
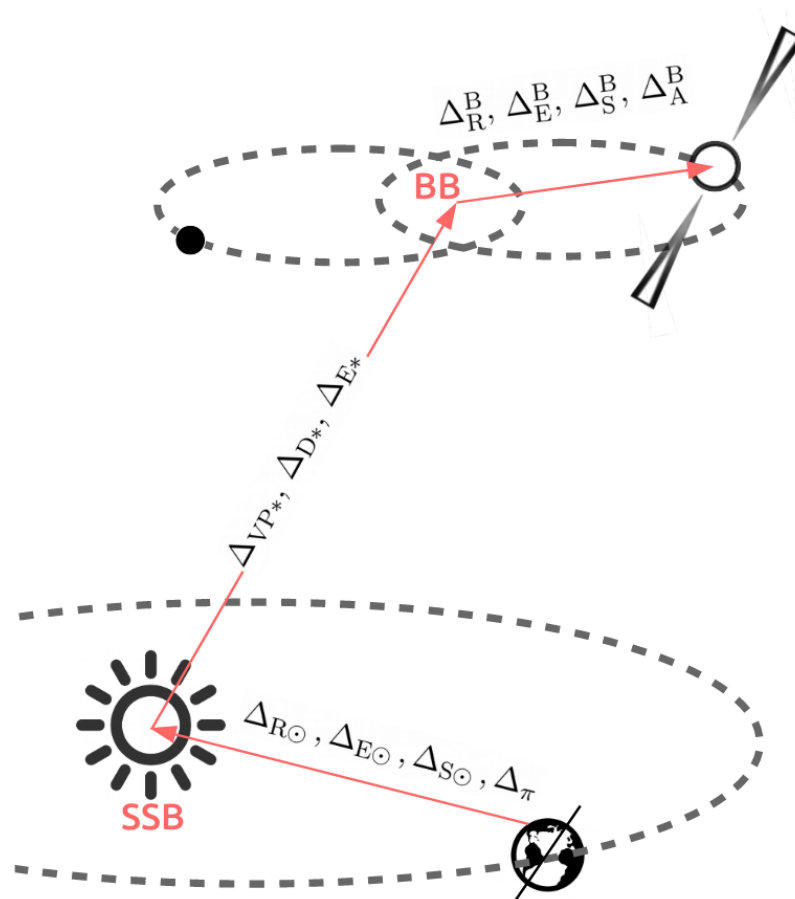
Figure 2.20: Representation of reference frame transformation in pulsar timing. First, the t_{sat} is moved to the SSB by correcting for effects from the Solar System. Then if this pulsar is an isolated pulsar, then the reference frame is transformed directly from SSB into the pulsar's frame. If the pulsar is in a binary system, then we need to transform from SSB to BB, then from BB to pulsar's frame. Image adapted from Porayko (2020).

by Jet Propulsion Laboratory (JPL) (e.g. *JPL Solar System Dynamics* 2022) and Intégrateur Numérique Planétaire de l'Observatoire de Paris (INPOP).

2.3.2 Interstellar and spatial corrections

For the interstellar corrections, there are three prominence effects which are:

- Δ_{VP_*}, the travelling time from the pulsar's reference frame to the SSB in a vacuum. Normally, it is not required to be corrected as the pulsar's distance is considered to be constant, so it appeared as a constant offset.

- Δ_{E_*}, the time dilation between SSB and pulsar's system reference frame, i.e. centre of mass for binary systems. It is also considered to be constant, as it is dependent entirely on the pulsar mass, which is assumed to be constant.

- Δ_{DM} is the frequency-dependent time-delay due to dispersion, as discussed in Section 2.2.3. Δ_{DM} is calculated Equation 1.12 at the pulsar's DM, the reference frequency, usually at ∞ MHz.

2.3.3 Binary corrections

In the same manner as the Barycentric corrections, if the pulsar is in a binary system, the Römer delay $\Delta_{\text{R}_{\text{B}}}$, Shapiro delays $\Delta_{\text{S}_{\text{B}}}$, Einstein delay $\Delta_{\text{E}_{\text{B}}}$ are used to transform the pulse arrival time to the pulsar's commoving frame.

Now $\Delta_{\text{R}_{\text{B}}}$, the light travel time between the pulsar to the binary system centre of mass (BB), with semi-major axis a_p passing through periastron at an angle ω_p from the line of sight, i.e. longitude of periastron passage and has orbital eccentricity e is expressed as

$$\Delta_{\text{R}_{\text{B}}} = a_p \sin i (\cos E - e) \sin \omega_p + a_p \sin i \sin E \sqrt{1 - e^2} \cos \omega_p. \qquad (2.21)$$

Where E is known as the eccentric anomaly, which is the angle between the periastron and the pulsar.

Most of the orbits found in nature can be considered governed by Newtonian dynamics. However, since pulsars have relatively high compactness, some pulsars have been found in a relativistic orbit where a_p are a few light seconds. The strong gravitational field in these compact binary produces observable patterns in timing residuals. Hence, a set of parameters are introduced as post-Keplerian (PK) parameters to describes these patterns. In GR (e.g. Blandford and Teukolsky, 1976a; Damour and Deruelle, 1985; Damour and Deruelle, 1986), the PK parameters for a system with a pulsar mass m_p and a companion mass m_c, with an orbital period P_b and an eccentricity e are

- Rate of periastron advance ($\dot{\omega}$): It is the rate of the periastron passage time that changes over time, which described as

$$\dot{\omega} = 3 T_{\odot}^{\frac{2}{3}} \frac{1}{1 - e^2} \left(\frac{P_b}{2\pi}\right)^{-\frac{5}{3}} (m_p + m_c)^{\frac{2}{3}}. \qquad (2.22)$$

Where $T_\odot$ is a constant value defined by; $T_\odot = \mathcal{G}\mathcal{M}_\odot c^{-3} \simeq 4.9254909$ (Prša et al., 2016).

- Orbital decay ($\dot{P}_b$): The rate of orbital period decay due to the emission of gravitational waves as

$$\dot{P}_{\rm b} = -\frac{192\pi}{5} T_\odot^{\frac{5}{3}} \left(\frac{P_{\rm b}}{2\pi}\right)^{-\frac{5}{3}} \frac{m_{\rm p} m_{\rm c}}{\left(m_{\rm p} + m_{\rm c}\right)^{\frac{1}{3}}} \left(1 + \frac{73}{24}e^2 + \frac{37}{96}e^4\right) \left(1 - e^2\right)^{-\frac{7}{2}}. \tag{2.23}$$

- Einstein delay ($\Delta_{\rm E_B}$), the delay due to the gravitational redshift due to the companion's gravity and the time dilation due to the pulsar motion:

$$\Delta_{\rm E_B} = T_\odot^{\frac{2}{3}} \left(\frac{P_{\rm b}}{2\pi}\right)^{\frac{1}{3}} \frac{m_{\rm c}\left(m_{\rm p} + 2m_{\rm c}\right)}{\left(m_{\rm p} + m_{\rm c}\right)^{\frac{4}{3}}}. \tag{2.24}$$

- Range of $\Delta_{\rm S}$ (r):

$$r = T_\odot m_c \tag{2.25}$$

- Shape of $\Delta_{\rm S}$ (s)

$$s = \sin(i) = x T_\odot^{-\frac{1}{3}} \left(\frac{P_{\rm b}}{2\pi}\right)^{-\frac{2}{3}} \frac{\left(m_{\rm p} + m_{\rm c}\right)^{\frac{2}{3}}}{m_{\rm c}}. \tag{2.26}$$

The last two parameters (r and s) are related to the same effect used to calculate, $\Delta_{\rm S}$ as

$$\Delta_{\rm S} = -2r \ln\left[1 - e\cos E - s\left(\sin\omega(\cos E - e) + \sqrt{1 - e^2}\cos\omega\sin E\right)\right]. \tag{2.27}$$

The Shapiro delay causes by the gravitational field of the companion. It is stronger if the system is edge on and expected to be maximum at superior conjunction, i.e. when the pulsar is nearly behind the companion.

As $\Delta_{\rm E_B}$ and $\Delta_{\rm S}$ can be modelled as a part of PK orbit, now we can calculate the TOA at the rest frame using Equation 2.20.

2.3.4 Creating and fitting timing model

Once we obtain the $t_{\rm psr}$, we can calculate the number of pulses from a reference time $t_{\rm ref}$ to $t_{\rm psr}$ assuming that pulsar period spin down is described by a polynomial of order k as

$$N(t_{\rm psr}) = N_{\rm ref} + \sum \frac{f_0^{(k)}}{(k+1)!}(t_{\rm psr} - t_{\rm ref})^2, \tag{2.28}$$

by doing this, we are accounting for every rotation of the pulsar.

As $t_{\rm psr}$ depends on the pulsar timing model, it can be fitted by minimising the reduced chi-square (χ^2) of the model $N(t_{\rm psr})$ to n_i, where n_i is the nearest integer to N_i. The χ^2 is calculated as

$$\chi^2 = \frac{1}{N_{\rm dof}} \sum \left(\frac{N_i(t_{\rm psr}) - n_i}{\sigma_i} \right)^2 . \tag{2.29}$$

Typically, all parameters in the timing model are fitted by a lest-square minimisation. In general, timing parameters precision increases as the data span is longer, as a tiny offset in the timing model can accumulate over time, motivating a long-term pulsar timing campaign.

Since we optimised the reduced chi-square from the predicted pulse number to the nearest pulse number, the initial timing model must be able to predict the pulse phase to the precision of less than 0.5 pulse phase. Otherwise, the nearest pulse number might be shifted by one pulse, making it harder to fit for the timing solution.

2.4 Notable pulsar surveys

2.4.1 Galactic plane pulse surveys

The discovery of the first pulsar by Hewish et al. (1968), marking the beginning of the pulsar survey era. An example for the first generation of pulsar survey was given by the first Molonglo transit survey (Large et al., 1968; Vaughan and Large, 1970; Davies et al., 1970). This survey observed at low frequencies (~ 400 MHz) and with limited bandwidth (4 MHz) and frequency resolution (2 MHz) observations using the Molonglo telescope in New South Wales, Australia, it covered approximately 330 square degrees of sky. During this initial stages of pulsar survey, the telescope's output was recorded on a chart recorder and examined manually. The sensitivity of this survey was limited due to its narrow bandwidth and short observation time, which resulted in the discovery of only 31 relatively bright pulsars (Manchester et al., 2005)[1] .One of these pulsars was PSR B0833-45, also known as the Vela pulsar, which is associated with the Vela supernova remnant.

A new era of pulsar survey began in the late 1980s with pulsar observations at a relatively high frequency (1.4 GHz), taking advantage of the reduced scattering effect from ISM (Johnston et al., 1992a; Clifton et al., 1992). However, the strength of pulsar signals typically follows a power law ($S_f \propto f^{\alpha}$), where most of the pulsars have a negative spectral index (α) with the average of -1.4 (Bates et al., 2013). As a result, the signal is expected to be weaker at high frequencies, and the observation time is also longer as S/N $\propto \sqrt{T_{\rm obs}}$ (see Equation 2.4), resulting in a longer processing time. Furthermore, as shown in Equation 2.1, the beam width is smaller at a higher frequency, causing high-frequency pulsar surveys to require more pointings than low-frequency surveys to cover the same region of the sky. The commissioning of the multibeam receiver at Parkes telescope (Staveley-Smith, 1997) opened up a new possibility for high-frequency pulsar surveys. To compensate for the disadvantage of having lower beam width from observing at high frequency, the multibeam receiver was used to observe 13 different patches of the sky simultaneously (Staveley-Smith, 1997), reducing the total observation time. The Parkes multibeam pulsar survey (PMPS) is the most successful pulsar survey in history, having discovered more than 800 known pulsars (Manchester et al., 2005)[1] The PMPS recorded pulsar signals with $t_{\rm samp}$ = 0.25ms, bandwidth of 288 MHz and frequency resolution of 3 MHz (Camilo et al., 2000b; Manchester et al., 2001), observing at 1374 MHz with $T_{\rm obs}$ of 2100s.
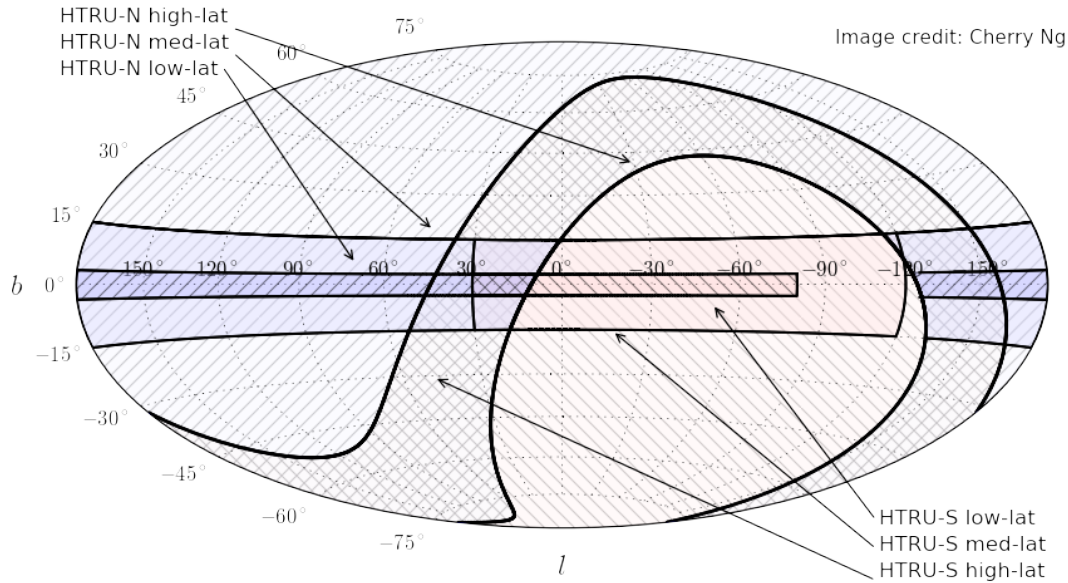
Figure 2.21: Sky coverage of all HTRU surveys, covering the whole sky. The information for each HTRU survey can be found in the texts.

The implementation of a digital spectrometer (see McMahon, 2011, for more informations) enabled high-time and frequency resolution observations. This led to the proposal of an updated version of the PMPS, known as The High Time Resolution Universe Survey (HTRU). This survey is divided into southern (HTRU-S) and northern (HTRU-N) surveys parts. The HTRU was observed with the multibeam receiver at Parkes, which is further divided into three surveys to optimise the observational time to the expected pulsar population, which concentrated in the Galactic plane. The survey observed the Galactic plane (Galactic latitude $b \pm 3°$) with a long observation time (4320 s), called HTRU-S low-lat. Then further out from the Galactic plane, there are HTRU-S mid-lat ($b \pm 15°$) and HTRU-S high-lat (DEC$\leq 10°$). The HTRU-S has a sampling time of 64 μs and a frequency resolution of 390.625 kMHz. A similar setting was applied to the HTRU-N, using the 7-beam receiver at the Effelsberg telescope, and the survey is divided into HTRU-N low latitude, mid-latitude, and high latitude. The data were also recorded with the sampling time of 54 μs and frequency resolution of 585.9 kHz. While all observations from HTRU-S were completed, the observations from HTRU-N are still ongoing. The combination of the HTRU-S and HTRU-N leads to an all-sky survey, as shown in Figure 2.21. As of now, over 240 pulsars have been discovered through the HTRU-S survey, which have significantly higher DM and lower flux densities compared to those discovered in the PMPS survey (see Balakrishnan, 2022, for example).

2.4.2 Galactic centre pulsar surveys

Another type of pulsar survey is the targeted survey. This survey searches for a pulsar in a specific location/environment in the sky. An example of the targeted searches is the Galactic centre (GC) pulsar search. As mentioned in Section 1.5, the GC is expected to host many neutron stars due to the high concentration of massive stars and star formation rate (e.g. Figer, 2003; Barnes et al., 2017). However, the GC pulsar searches are challenging, as we need to balance between pulse scattering at the GC at low-frequencies and pulsar flux reduction at high frequencies. We also need to account for the sensitivity loss due to binary motion in the case of pulsars in binary systems. As a result, even though many blind pulsar surveys have searched the GC, e.g., PMPS and HTRU-S low-lat, no pulsar associated with the GC with a projected distance of $\leq$ 100 pc, has been found. As mentioned in 1.4.2, one of the explanations why the L-band pulsar surveys are not so successful in this region is due to the interstellar scattering. The expected τ_{sc} in this region at 1400 MHz is longer than any known pulsar period, making it much harder to detect any periodicity with a period shorter than τ_{sc}. The pulsar survey must be done at a higher frequency to combat this. Such searches were conducted at 4.85, 8.5, 14.6, 18.95 GHz at Effelsberg and GBT telescopes (Kramer et al., 2000; Klein et al., 2004; Macquart et al., 2010; Eatough et al., 2021; Suresh et al., 2022). However, no new pulsars has been found from these surveys.

Johnston et al. (2006b) conducted a targeted survey at 3.1 and 8.5 GHz using the Parkes telescope and discovered two pulsars toward the GC. Then, Deneva (2010) also found three more pulsars within 1° from the GC using the GBT telescope at 2 GHz. It is worth pointing out that all five pulsars near the GC show the same characteristics: long period, high DM and RM, of which the latter are expected from the dense environment in the GC (see Appendix 1).

Subsequently, a radio-loud magnetar was discovered with only 0.1 pc from the GC due to the follow-up of an X-ray pulsation near the GC. This pulsar can be detected up to 291 GHz (Torne et al., 2017), motivating pulsar search in ultra-high frequency. For example, Torne et al. (2021) used the IRAM-30m telescope for GC searches at 84 and 156 GHz while Liu et al. (2021a) also searched for pulsars at 86 GHz with the ALMA telescope.

As the pulsar in the GC might be highly variable and rapidly changing in observed flux density due to it being in a tight binary orbit or being a transient pulsar, e.g. magnetars, another approach for the GC search is to conduct a repetitive search at the GC. Eatough et al. (2021) used the Effelsberg telescope at 4.85, 8.35, 14.6, and 18.95 GHz for pulsar searches. As these searches observed the GC for a multiple epoch, it is also sensitive to the sporadic pulsar's population, e.g., RRAT and magnetars. However, until this point, no new pulsar from the GC has been found.

These are examples of the targeted pulsar search, in which we can optimise our resources, e.g., observational time, observational frequency, and computational time to the pulsar population expected in the targeted region. In Chapter 5, I will discuss a few targeted searches with the FFA.

The High Time Resolution Universe Pulsar Survey – XVIII. The reprocessing of the HTRU-S Low Lat survey around the Galactic centre using a Fast Folding Algorithm pipeline for accelerated pulsars (Summary)

This chapter is a summary of the article titled "The High Time Resolution Universe Pulsar Survey – XVIII. The reprocessing of the HTRU-S Low Lat survey around the Galactic centre using a Fast Folding Algorithm pipeline for accelerated pulsars" that appears in MNRAS (Wongphechauxsorn et al., 2024). The original manuscript is included in Appendix A. This work is permitted for re-publication on a non-exclusive basis. As the first author, I conducted a portion of the follow-up observations with the Parkes telescope and all observations with the Effelsberg telescope. I also analysed the data which including timing analysis, flux density measurements, and spectral index. Finally, I prepared the manuscript for this work.

The full author list is J. Wongphechauxsorn, D. J. Champion, M. Bailes, V. Balakrishnan, E. D. Barr, M. C. i Bernadich, N. D. R. Bhat, M. Burgay, A. D. Cameron, W. Chen, C. M. L. Flynn, A. Jameson, S. Johnston, M. J. Keith, M. Kramer, C. Ng, A. Possenti, R. Sengar, R. M. Shannon, B. Stappers, W. van Straten.

3.1 Summary

As discussed in Section 2.4, the Galactic Centre (GC) is one of the most interesting regions in our Galaxy, due to its dense environment of matter and magnetic fields around the supermassive black hole, Sgr A* . A pulsar in the GC can be used to test the predictions of General Relativity, including the No Hair Theorem and the Cosmic Censorship Conjecture (Wex and Kopeikin, 1999b; Kramer et al., 2004; Liu and Eatough, 2017).

Despite the prediction that there could be thousands of active radio pulsars in the inner parsec of the Galaxy (Wharton et al., 2012), only 6 pulsars have been detected within one square degree

around the GC (Johnston et al., 2006b; Deneva et al., 2009a; Eatough et al., 2013b). This is likely due to the challenges posed by the dense GC environment, which affects the detectability of pulsars through serve scattering (Cordes and Lazio, 2003). As the scattering time is proportional to f^{-4}, pulsar surveys at higher frequencies (Kramer et al., 2000; Klein et al., 2004; Liu et al., 2021a; Torne et al., 2021; Eatough et al., 2021), were motivated.

In this work, a different approach was used, by searching for pulsars using the FFA, which is more sensitive to long-period pulsars. The long period pulsars are less affected by scattering, even at the typical frequency (1400 MHz) for pulsar searches.

The existing data from the Southern High Time Resolution Universe Survey low-latitude (HTRU-S LowLat) within one degree of the GC were selected. As mentioned in Section 2.4, the long observation time of the LowLat (4320 s) improves sensitivity toward the slow pulsars, as more pulses were recorded during the observation (Keith et al., 2010).

Since the FFA searches for a specific range of periodicity, searching for periodicity of P with N_{bins} will give the folding bins of $t_{\text{bins}} = N_{\text{bins}}/P$ which make the DM step size (ΔDM) and acceleration step size (Δa) to be

$$\Delta\text{DM} = 1.205 \cdot 10^{-4} \frac{N_{\text{bins}}}{P(s)} \frac{f_c^3}{\Delta f} \text{pc cm}^{-3},\qquad(3.1)$$

$$\Delta a = 8c \frac{P}{N_{\text{bins}}T_{\text{obs}}^2} \text{ m s}^{-2}.\qquad(3.2)$$

To search for a longer period, the data are downsampled while keeping the same N_{bins}, causing the ΔDM and Δa to be larger, reducing the number of redundancy trials.

In this work, the search period range was 0.6 s to 430 s. The N_{bin} was chosen to be 128 for every period range. The maximum DM was set to be 4000 pc cm^{-3} which is approximately equivalent to the DM at the edge of the Galaxy with a line-of-sight directly through the GC, according to the YMW16 (Yao et al., 2017a). The acceleration range was set to be $\pm$ 128 m s^{-2}, which corresponds to a pulsar of mass $1.4 M_\odot$, with a companion mass up to $37 M_\odot$ in a 12-hour orbital period (see Ng et al., 2015a, for calculations). With these parameter ranges, the optimisation implemented in this work reduced the number of acceleration and dispersion trials by 86%.

All known pulsars detected by the previous FFT processing were detected, as well as a missing pulsar that had slipped through the previous FFT analysis. By comparing the S/N from the FFT to the S/N from the FFA, we found that the FFA pipeline has greater sensitivity than the FFT pipeline in the searched parameter range.

We discovered a slow pulsar (spin period of 1.889 s) with a relatively high dispersion measure (DM) of 1309 $\pm$ 1.7 pc cm^{-3}, located $\sim$ 0.5 $^\circ$ from the GC. Follow-up observations revealed that this pulsar has an unusually flat spectrum ($\alpha = -0.9$) as demonstrated in Figure 3.1, has a high flux density variability, and a period derivative of $\sim$ 1.3 $\times 10^{-12}$ s s^{-1} (see Figure 3.2), corresponding to a surface magnetic field (B_{field}) of $\sim$ 5.2 $\times 10^{13}$ G. This pulsar is either a magnetar or a high B_{field} pulsar, making it the third such object out of seven pulsars located less than 0.5° from the GC[1] which may be hinting at an abnormally large fraction on Magnetar-like objects in the GC.

---

[1] Including the Galactic centre magnetar, and PSR J1746-2850
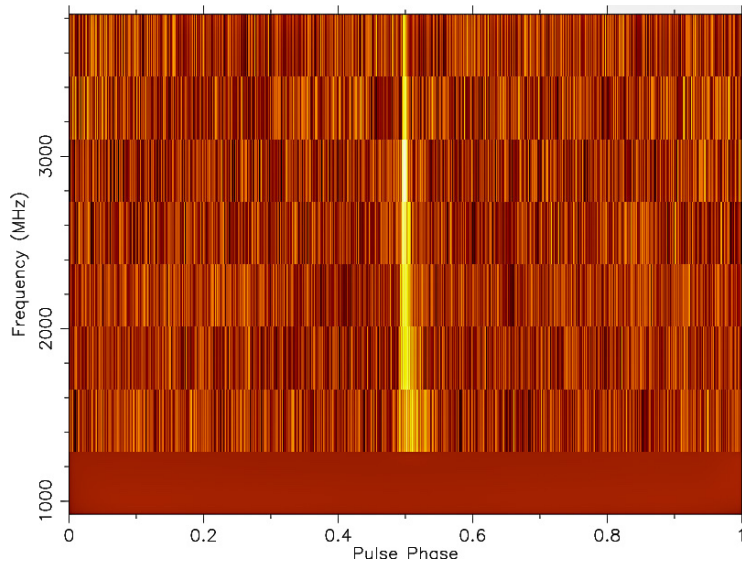
Figure 3.1: The frequency vs pulse-phase plot of PSR J1746−2829. The plot shows a frequency-phase plot from an 82-minute observation with the UWL receiver, containing 8 channels and 128 bins.
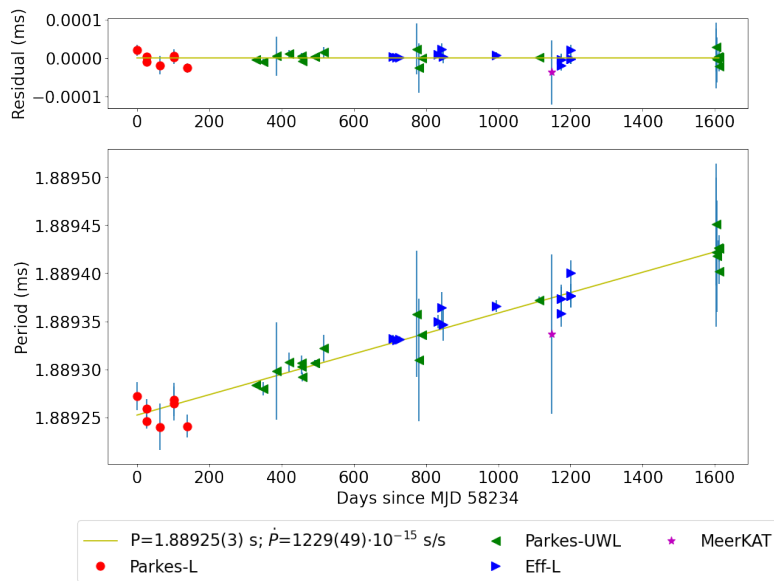

Figure 3.2: The barycentric spin period evolution of PSR J1746−2829. The spin period of this pulsar can be described by a simple linear function ($P(t) = \dot{P}t + P_0$).

A search for pulsars around Sgr A* in the first Event Horizon Telescope dataset using the FFA pipeline

This chapter presents my contribution to the article titled "A search for pulsars around Sgr A* in the first Event Horizon Telescope dataset using the FFA pipeline" that is published in the Astrophysical Journal (APJ, Torne et al., 2023). As one of the main contributors, I developed the FFA search pipeline to test the sensitivity and search for pulsars in this dataset. Additionally, I contributed to the preparation of the manuscript, specifically the sections related to the FFA searches.

4.1 Motivation

The Event Horizon Telescope (EHT) Collaboration has been studying supermassive black holes (SMBHs) at the centres of galaxies through millimetre interferometric imaging with angular resolution of μarcsec. One of the results is a comparison between the SMBH shadows seen for M87 and Sgr A* with synthetic images from general relativistic magnetohydrodynamic (GRMHD) simulations and general relativistic ray tracing, which provides a new way to measure the properties of black holes and test theories of gravity in the strong-field regime (e.g. Event Horizon Telescope Collaboration et al., 2019b; Event Horizon Telescope Collaboration et al., 2022b). The results from the two EHT images of M87* and Sgr A* agree with the prediction of the rotating black hole in general relativity (Psaltis et al., 2020).

Binary radio pulsar systems are other extremely useful tools for testing of gravity in the strong-field regime (e.g. Wex and Kramer, 2020a). Pulsar-WD and pulsar-NS binaries have already been discovered. However, the discovery of another type of compact companion, the black hole, in a binary system with a pulsar has yet to be discovered. Discovering a pulsar-BH binary would enable the measurement of the black hole's spin and quadrupole moment. Additionally, a pulsar orbiting Sgr A* could yield further information about stellar populations and dark matter in the region, along with insights into the magnetoionic plasma. (Psaltis et al., 2016a; Weinberg et al., 2005; Eatough et al., 2013c; Schnitzeler et al., 2016; Desvignes et al., 2018).

Table 4.1: Description of the observations and data used in this work, which were recorded at three stations (ALMA, IRAM and LMT) with 2-GHz bandwidth centred at 229.1 and 227.1, GHz. The columns indicate the EHT station, effective single dish diameter D_s, effective beam FWHM, central observing frequency f_{obs}, total bandwidth (Δf), number of frequency channels (n_{ch}), initial sampling time (t_{samp}), total time span of the dataset constructed for the pulsar search, and net integration time on Sgr A*. The difference between the total time span and net integration time is due to various factors such as the time for observations of calibrators, only the net integration time on Sgr A* is used for the search sensitivity analysis.

Station	D_S	FWHM	ν_{obs}	$\Delta \nu$	n_{ch}	$t_{samp}^{\ddagger}$	Total time span (hr)			Net time on Sgr A* (hr)		
	(m)	(arcsec)	(GHz)	(GHz)		(μs)	Apr. 6	Apr. 7	Apr. 11	Apr. 6	Apr. 7	Apr. 11
ALMA	74	0.72	228.1	3.75	64	8	4.6	10.2	3.6	2.1	4.6	1.9
LMT	50 (32.5[†])	11.1	228.1	4.00	32	8	5.7	6.4	3.6	2.4	3.0	1.7
IRAM 30 m	30	10.3	228.1	4.00	32	8	-	3.2	-	-	1.1	-

[†]The effective equivalent diameter during the 2017 observations.

As mentioned previously, despite the predictions of many pulsars in the GC, only six radio pulsars have been detected within 50 pc of Sgr A* (Johnston et al., 2006a; Deneva et al., 2009b). One of the explanations of the lack of pulsars in the GC is the multipath propagation, due to the scattering, which can reduce the S/N of radio pulsations (Cordes and Lazio, 1997a). Since the scattering is proportional to f_{obs}^4, one solution is to search for pulsars at mm and sub-mm wavelengths, where multipath scattering can be avoided. However, pulsars typically have steep spectra, leading them to have low flux density at higher frequencies. In this work, we searched for a pulsar located close to Sgr A* with the data from the EHT 2017 observation campaign, aiming to discover pulsars that orbiting Sgr A* and have flat/inverted spectra making them brighter in the higher observing frequencies.

4.2 Data collection and conversion

The EHT was used to conduct an observational campaign in April 2017, where three nights were dedicated to observing Sgr A*. The participating telescopes included the Atacama Large Millimeter/submillimeter Array (ALMA), the Large Millimeter Telescope Alfonso Serrano (LMT), the IRAM 30m telescope, the James Clerk Maxwell Telescope, the Submillimeter Array, the Submillimeter Telescope, and the South Pole Telescope. The data collected during these observations were recorded with 2-bit sampling at 32 Gbps in two 2-GHz bands centred at 229.1 and 227.1 GHz.

We chose to analyse data only from the three most sensitive telescopes in the EHT 2017 observations, which were ALMA, LMT, and IRAM 30m. While ALMA has the highest sensitivity, its field of view is limited to 1-2 arcsec, which limits its sky coverage. LMT and IRAM 30m, both single-dish telescopes with a field of view of approximately 10 arcsec, are used to suplement the sky coverage of ALMA while maintaining acceptable sensitivities. The total length of the tracks on Sgr A* for these three telescopes varied from 5 to 10 hr.

The voltage data was converted into filterbank files, using the software MPIvdif2psrfits[1]. This tool is an upgraded version of the original toolkit developed under the ALMA Pulsar Mode

---

[1] https://github.com/xuanyuanstar/MPIvdif2psrfits

Project[2] and has parallel processing capability using the OpenMPI library.

The final product contains a timeseries of four Stokes parameters with a time resolution of 8μs and 32-bit float samples. These were created separately for the high and low parts of the frequency band. The frequency resolution was retained as 62.5 MHz for the ALMA data and 125 MHz for the LMT and IRAM 30m data. The data from ALMA results in two filterbanks of 32 channels each, while data from the LMT and IRAM 30m results in two 16-channel filterbanks each, giving a total of 32 frequency channels.

The ALMA data were processed to remove noise features introduced by the array phasing cycle. The process included visual inspection of each scan to identify the phasing features, replacing the data within two-second windows around the first broad feature (and every 18.192s thereafter) with the mean level of the timeseries, and using a moving window to clip negative narrow spikes. The slow variations in the mean power level were also removed with a running-fit filter, and the timeseries were normalized by their standard deviation. The individual scans were then concatenated into a single continuous filterbank file for each sub-band, and the low and high sub-bands were spliced into one file with the full 4 GHz of bandwidth.

The IRAM 30 m telescope data were also affected by noise features, including a strong pulsation in the timeseries with a period of 5 ms and regular power drop-offs. To reduce the impact of these noise features on the analysis, the data were first zero-weighted in a few Fourier bins centred on the 210.7 Hz signal and 1 Hz signal. All samples were substituted with the median of the remaining data. Despite these steps, some scans still showed additional noise characteristics, so five scans (corresponding to 0.72 hr) were flagged and excluded from the search. The final data were concatenated by padding the gaps with the mean level, and spliced into a two-channel filterbank file.

The LMT data also shows periodicities related to the local receiver, with the strongest signals at 1.2 Hz (likely due to the cryogenic refrigeration cycle) and 185 Hz (of unknown origin). There are also power drop-offs present, but less frequent than in the ALMA and IRAM 30m data. To reduce these undesired effects, the data are first cleaned by zero-weighting the strongest peaks in the Fourier domain, then using a moving window of 10 s to clip power-drops and replace them with the median value. The mean power level variations are minimized using a running-fit filter with a window of 10 s. Some scans still showed clear artefacts after cleaning and were flagged and excluded from the search. The cleaned scans of each frequency sub-band are then concatenated into a single filterbank file and spliced into a two-frequency channel filterbank

4.3 The FFA pipeline

The search for pulsars near Sgr A* was conducted using two independent pipelines: a Fourier-domain search and an FFA search. As mentioned in Chapter 2, the Fourier-domain search is a widely used and effective method used for discovering pulsars with a variety of spin parameters. The FFA is particularly good at detecting long-period pulsars with narrow pulse profiles. The FFT pipeline is divided into two parts; the FFT_1 aims to search for highly accelerated pulsars (`zmax` of 1200), while the FFT_2 aims towards finding less accelerated pulsars with high jerk (`zmax` of 300

---

[2] http://hosting.astro.cornell.edu/research/almapsr/

and `wmax` of 900). This `zmax` and `wmax` can be used to correct the line-of-sight motion of any pulsar orbiting the Sgr A* down to an orbital periods of 2.5 yr in a circular orbit, as demonstrated in Section 2.2.4.

In addition, the data were searched for single-pulse transients such as pulsar giant pulses, Rotating Radio Transients (RRATs), and Fast Radio Bursts (FRBs). In this thesis, I will focus only on the FFA pipeline.

We used the AFFA pipeline implemented in Chapter 3 to search for signals with the period range of 1s to 1025s. We folded using 128 bins, making this pipeline sensitive to duty cycles as low as 1%[3]. The acceleration range was chosen to be capable of detecting pulsars with accelerations up to ±50 m s^{-2}. Furthermore, we did not need a jerk search for a system with a jerk up to approximately 2.6×10^{-5} m s^{-3} without any jerk search. This acceleration and jerk are equivalent to a `zmax` of 1400 and a `wmax` of 10 for a 1-s pulsar in the Fourier domain acceleration search pipeline with N_h = 32 and T_{obs} of 4.5 hr, making these search parameters equivalent to the FFT$_1$ pipeline. The Δa = 0.07 m s^{-2} in this work is calculated from Equation 3.2 using T_{obs} of 4.6 hrs.

To search for even narrower duty cycles, the pipeline was repeated with 512 bins and no acceleration, allowing for the detection of pulsars with duty cycles greater than 0.19%. All candidates with a S/N ratio of 6 or higher were visually inspected.

At this observing frequency (230 GHz), there is no need to search for any dispersion as the DM step size ΔDM calculated from Equation 3.1 using 512 bins for 1s is approximately 4×10^{11} pc cm^{-3}, which is larger than the expected DM from the GC (Cordes and Lazio, 2002).

4.4 Results and discussion

4.4.1 Results

The FFA pipeline was applied to three datasets collected with the ALMA, the LMT, and IRAM 30m telescopes. In the ALMA data, 3044 candidates were produced, with the strongest candidate appearing with a period of 18.2 s. However, the candidate and its harmonics likely originated from residual contamination from a known 18.2-s phasing feature. In the LMT data, 300 candidates were produced, but most of them showed repetitions of the pulse, indicating that they were locally produced. In the IRAM 30m data, the pipeline produced over 16000 candidates; a relatively strong candidate was discovered at 3.000 s, meaning that it is produced locally. A summary of the number of candidates per station and epoch can be found in Figure 4.2, representing visually the spin periods of the FFA candidates.

The results from the FFT and the single pulse searches pipeline also show no promising candidate. The spin periods of the candidates per station per epoch for the FFT pipeline is shown in Figure 4.2. It is worth pointing out that, the candidates from the FFT pipeline have a period up to a few seconds which matches perfectly with the minimum period from the FFA pipeline, showing the ability of the FFA to cover the period where the FFT is less sensitive.

---

[3] less than 7% of known pulsars have a lower duty cycle (Manchester et al., 2005)[1],
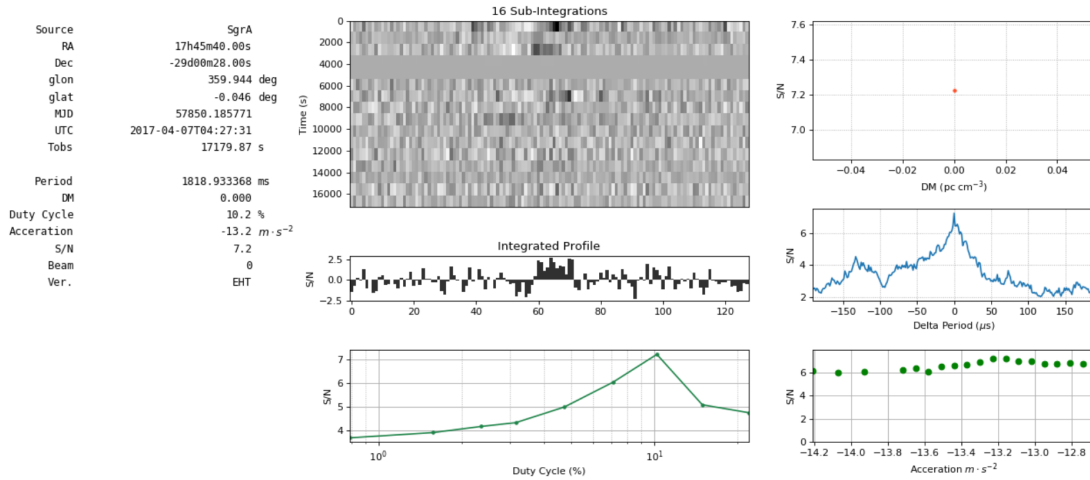
Figure 4.1: The strongest candidate from ALMA using the FFA$_1$ pipeline with a period similar to the phasing feature.

4.4.2 Sensitivity

There are several potential contributing factors to the non-detection of new pulsars in this search, including the typically steep spectrum of radio pulsars and the large distance to the centre of our Galaxy. One important factor in determining the possible success of a pulsar search is the sensitivity of the observing system. This is usually quantified by the minimum detectable mean flux density of a pulsar, S_{min}, given a certain set of observational and pulsar properties.

The FFA and FFT methods have similar sensitivity in theory, as stated in Morello et al. (2020b). In reality, the search efficiency factor ($\mathcal{E}$) is used to characterise the theoretical sensitivity difference between the two methods and is determined by the number of harmonics summed and the duty cycle of the pulsar for FFT. For those signals with duty cycle of 2%, 5%, and 10%, and a summation of up to 32 harmonics, $\mathcal{E}$ is approximately 0.65, 0.76, and 0.83, respectively. Assuming $\mathcal{E}_{FFA} = 0.93$, the FFA search is theoretically more sensitive than the FFT search by a factor of 1.4, 1.2, and 1.1, respectively.

The radiometer equations are known to be significantly overestimate the realistic sensitivity of a pulsar search in practice. This is especially true for slow pulsars with a large duty cycle, where instrumental red noise is prominent in the data (Lazarus et al., 2015; Liu et al., 2021b). Therefore, a more accurate estimation is typically obtained empirically by injecting synthetic pulsar signals of varying flux densities into real data, conducting the search, and determining the minimum detectable flux density.

We estimated the search sensitivity in practice by injecting artificial signals into the real data. Our results indicate that the practical sensitivities for fast-spinning pulsars with periods in the range of $P = 1 - 10$ ms are approximately 0.02 mJy, 0.4 mJy, and 1 mJy for the ALMA, LMT, and IRAM 30-meter telescopes, respectively. However, the sensitivity is roughly an order of magnitude worse for slow pulsars with periods in the range of P from 1 s to 10 s as shown in Figure 4.3. Our results indicate that the sensitivity of our current observations is still low, and that
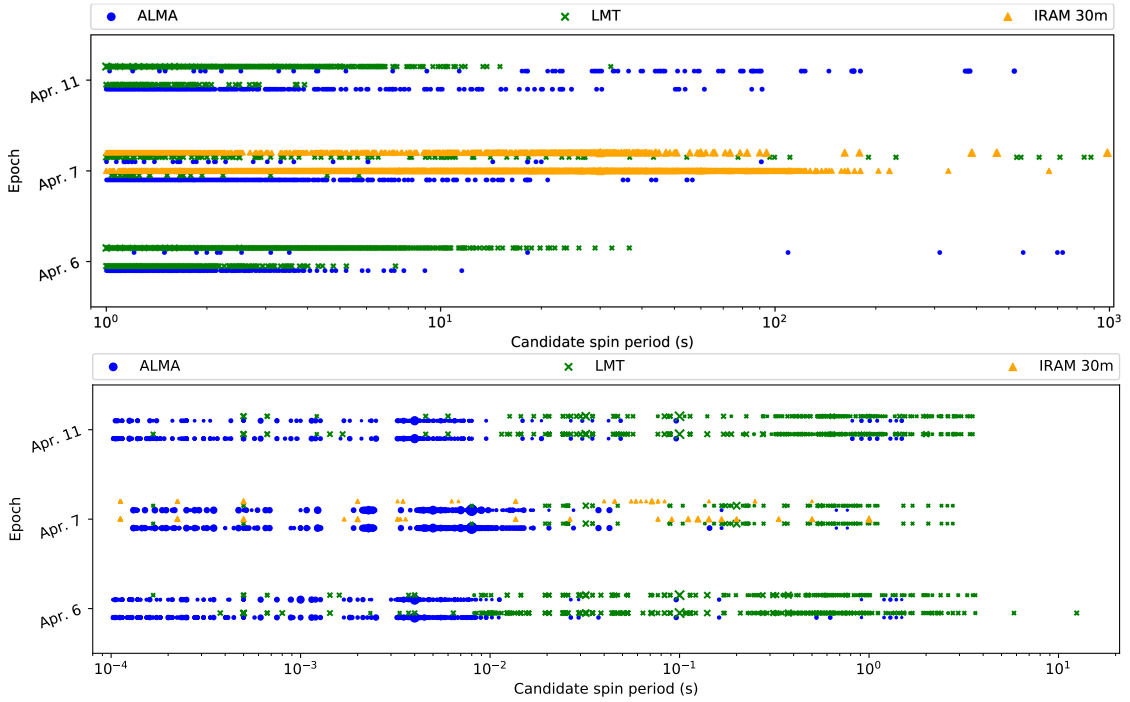
Figure 4.2: Period-Epoch-S/N plots. For the FFA pipeline, only the candidates with a S/N greater than 6 are plotted. While we used σ larger than 2 from sifting.py. For each epoch, two groups of markers corresponding to each pipeline are plotted. The candidates from ALMA, LMT, and the IRAM 30 m telescope are represented in blue circles, green crosses, and orange squares, respectively. The size of the marker is proportional to the σ, a similar significant measurement from `presto`, and S/N ratio values, for the Fourier-domain and FFA cases, respectively. None of the candidates is a convincing pulsar signal after the visual inspection of their candidate evaluation plots, as produced by our searching pipelines. The black arrows in the top panel indicate the P = 0.5 ms candidate, the only periodicity present in all datasets and related to a locally-generated signal at $\nu = 2000$ Hz.

the lack of discoveries does not necessarily mean that pulsars do not exist in the covered areas. It is possible that there are still pulsars present in these areas that simply emit below our current detection thresholds.

Subsequently, we calculate how many pulsars from the simulated population in the GC would be detectable with the actual sensitivity, given the flux density limits of the observations. The pseudo-luminosity of those pulsars was obtained from PSRCAT(Manchester et al., 2005)[1] .Then we performed a Monte Carlo simulations with 10000 executions to obtain the average percentage of the detectable population for each station. The results indicate that the percentage of detectable pulsars can decrease by $\sim 50 - 60\%$ when using aforementioned empirically-derived sensitivity limits compared to the theoretical ones. This sensitivity loss is significant and is caused by the noise characteristics, which are far from showing the Gaussian statistics that were assumed in the radiometer equation. We would like to point out that, these search mainly target flat-spectrum pulsars such as radio magnetars, and probing a frequency space where certain emission models include possible emission boosts e.g. inverse Compton scattering (Blandford and Scharlemann,

1976), making certain pulsars potentially visible in higher observational frequency.

4.4.3 Population of pulsar in the GC

The non-detection from this survey can be used to estimate the population of pulsars in the GC. To estimate the number of pulsars in the GC, we used Equation 32 in Wharton et al. (2012),

$$N_{psr} = f_b f_\nu \tau \beta_{SN}, \tag{4.1}$$

where f_b is the beaming fraction that was fixed to be 0.2. f_{nu} is the fraction of pulsars that were born in the region of interested and are still retained there, which is ≤ 0.1. τ is the pulsar radio lifetime. β_{SN} is the core collapsed supernova rate, i.e. the birth rate of NS. For the inner 20 pc, the β_{SN} is estimated by assuming that the plasma in the GC was heated by supernovae (Muno et al., 2004), which is 10^{-5} to 10^{-3} per year. This estimation shows that there should be ~ 2 to 600 non-recycled pulsars in the GC. As a result, the expected number of pulsars (N_{det}) can be calculated from, $N_{det} = N_{psr} f_{det}$ which are ≤ 12. However, since the FWHM of each telescope covered only a fraction of the projected distance from the GC, we expect the number of pulsars in each beam to be significantly fewer, depending on the distribution of pulsars in the inner GC.

Similarly, the population of recycled pulsars can be calculated by assuming the age of MSPs to be $\tau_{re} \sim 10^{10}$ yrs yielding $N_{re} \simeq 10^3 N_{psr} f_{re}$ when f_{re} is the fraction of pulsars recycled to MSP, which is assumed to be 0.1 by Wharton et al. (2012). As a result, the expected number of recycled pulsars in the GC for this scenario is 60000. Since this work observed at 230 GHz, the expected scattering time even from the strong scattering model (Cordes and Lazio, 2003) is $\sim 10^{-7}$s. As a result, we expect to encounter no scattering at this observing frequency. However, given that we are not sensitive to any recycled pulsars as shown in Figure 4.3, it is possible that the GC might be dominated by the recycled pulsars.

However, there is already one magnetar (PSR J1745−2900) located 0.1pc away (Eatough et al., 2013b). Magnetars have emission lifespans 10^{-3} times shorter than normal pulsars before crossing the death lines. Assuming the same f_b, f_ν, β_{SN} (meaning that all core-collpased supernova in the GC resulting in magnetars) and that we are sensitive to all magnetars as they have flat spectra (meaning that we should detect all of them in this work $f_{det}=1$), the expected number of magnetar in the GC is ~ 1 which is in agreement with the detection of PSR J1745−2900. It might mean that the GC might host more magnetars over normal pulsar.

Another possibility is that that geodetic precession of pulsars due to the spin-orbit coupling with their companion could move their emission beams in and out of our line of sight, making them undetectable, especially if the timescale is comparable to the observation making the pulsar to beamed towards the Earth for a fraction of the observation time, reducing the sensitivity (Kramer, 1998; Desvignes et al., 2019). Liu et al. (2012c) calculated the geodetic precession timescale for a pulsar orbiting around Sgr A*, showing that for P_B of one year, the geodetic precession timescale is at the order of a decade. As the FFA$_1$ are only sensitive up to this the orbital period of 1 year, any pulsar with this type of orbit should have the geodetic precession timescale significantly less than the observation time.

In conclusion, since pulsars are generally having steep spectra, it makes them harder to detect at the higher frequencies. However, we need to observe them at higher frequency to avoid
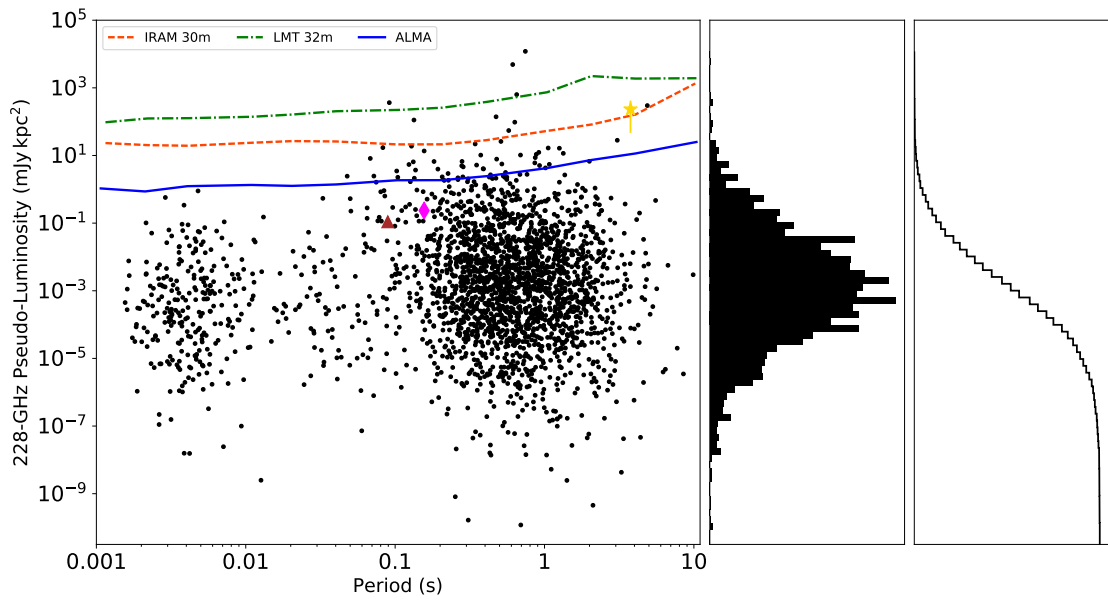
Figure 4.3: Simulated pulsar luminosity at 228GHz (black dots) overlaid with telescope-specific minimum detectable luminosity (lines). ALMA, LMT, and IRAM 30m telescope limits are represented by blue, green, and orange dashed lines respectively. The luminosities of PSR J1745-2900, Vela pulsar, and PSR B0355+54 are marked with yellow, brown, and pink symbols respectively. The middle and right charts show luminosity distribution and cumulative luminosity distribution histograms, respectively.

scattering broadening. In this work, we perform pulsar searches at 230 GHz, the highest observing frequency for pulsar search to date, which can entirely ignore any effects from ISM that can reduce the detectability (both dispersion and scattering). The analysis on the empirical sensitivity demonstrated that we are not uniformly sensitive to all period of pulsars even without scattering effects. In the future, the search in the lower frequency (2-50 GHz) with higher sensitivity will be useful to constraint the population of the recycled pulsars in the GC.

Pulsar searches with the FFA: Other sources

In Chapter 3, an acceleration search was implemented for the FFA pipeline for the first time. In this chapter, I will apply the aforementioned pipeline to various types of radio observations to search for new pulsating objects. All data analyse were performed on MPIfR's *Hercules* cluster at the Max-Planck Computing and Data Facility (MPCDF) in Garching, Germany.

5.1 A white dwarf with a strong magnetic field

5.1.1 Background

Pulsars are proven to be rotating NSs due to their small radii (~10 km, see Chapter 1). However, there will always be a question whether another type of compact object, e.g. the WDs, can emit pulsar-like emission at radio frequencies. Currently, there is only one radio pulsar-like WD known as AR Scorpii, which has a spin period of 118.2 s (Marsh et al., 2016) and located 116 pc from our Solar system. The radio continuum flux density at L-band was obtained from the FIRST 21-cm radio survey (Becker et al., 1995) and found to be 8 mJy. The reason behind the lack of detection for this kind of object could be due to its low intrinsic population, flux density or the lack of radio survey sensitivity toward long period pulsations. Therefore, discovery of additional radio pulsar-like WDs would greatly enhance our understanding of the radio emission properties.

The WD SDSSJ125230.93-023417.72 is a particularly promising candidate for radio pulsations. It has a strong magnetic field of 5 MG[1] and a 317-s periodic optical emission (Reding et al., 2020). The high surface magnetic field (B_{surf}) of this WD suggests that it could produce pulsar-like radio emissions. Additionally, the distant measurements from parallax using Gaia data release 2 (Luri et al., 2018) indicate that this source is located 77.26±0.67 pc away from Earth and has no companion. At this distance and position, the expected dispersion measure (DM) predicted from the YMW16 model (Yao et al., 2017b) is 0.8146 pc cm^{-3}.

---

[1] Only ~13% of the WDs have B_{field} more than 0.1 MG (Ferrario et al., 2020)

5.1.2 Observations, Analysis, and Results

The WD was observed using the central beam of the 21cm multibeam receiver and the PFFTS backend at the Effelsberg telescope to record the filterbank, i.e. search mode data. The observations were recorded at a central frequency of 1360 MHz with 240 MHz bandwidth and 54.61 μs sampling time. This system was observed at two epochs, 5th of April 2020 and 19th of April 2020, each epoch has an observation length of one hour. Since this candidate is expected to have a low DM, making it harder to distinguish from RFI, the data from the other beams that were stored from the observation on 19th of April 2020[2].

Since this system is located at a high Galactic latitude ($\sim$60°) which had never been searched with a long observation time (> 30 mins), we extended our search parameters to include an unexpected detection a pulsar that is not associated with this source. The search utilised the AFFA pipeline described in Chapter 3, with a search period range from 1.0 s to 400.0 s using 1024 folding bins. The DM range was 0 to 100 pc cm^{-3} with a $\pm$64 m s^{-2} acceleration range. The candidates with an S/N of $\geq$ 7 were examined visually. There was no evidence of a pulsar-like signal. According to the radiometer equation, the S/N of 7.0 is equivalent to a flux density of $\sim$ 0.035 mJy at Effelsberg. Compared to the luminosity ($L = S \cdot d^2$) distribution of pulsars[3], all known pulsars are brighter than this limit, 6.34$\times$10^{-5} mJy kpc (Manchester et al., 2005)[1] as demonstrated in Figure 5.1.

If this object has the same continuum flux as the only known pulsar-WD (AR Scorpii), this object would have a flux density of $\sim$ 16 mJy at 1400 MHz (Marsh et al., 2016). As a result, we can conclude that this object has no AR Scorpii-like emission.

However, this candidate could have a different emission mechanism from AR Scorpii allowing fainter emission. Another explanation for the non-detection is possible high instrumental red-noise from the system temperature varying over time, reducing the sensitivity towards long period signals as shown in Chapter 4. Finally, while this object may emit like a pulsar, it is possible that the radio beam is not directed towards the Earth

5.2 47 Tucanae

5.2.1 Background

Globular clusters are dense, gravitationally bonded groups of hundreds of thousands to millions of stars. Studies of the relation between luminosity and temperature of these stars demonstrated that they were born at nearly the same time and have the age of 10 to 13 billion years. Recycled pulsars in globular clusters emit radio emissions for much longer than non-recycled pulsars. These clusters host a significant proportion (33%) of known pulsars, making them a 'Space Jurassic Park' for discovering old population pulsars. Therefore, if we were to discover a slow pulsar within a globular cluster, it would likely be the result of a minor channel of neutron star formation e.g. acceleration induced collapsed of a WD (Grindlay and Bailyn, 1988). Until now, only a

---

[2] For details about multibeam RFI mitigation, see Ng (2014)

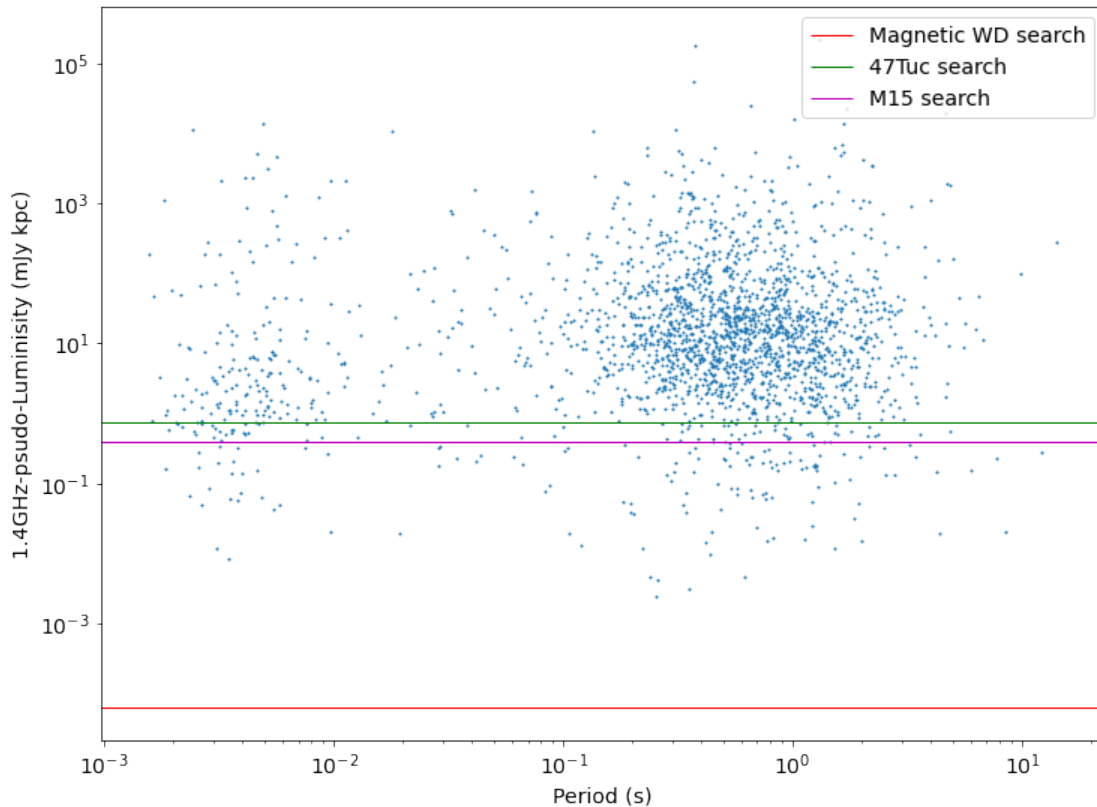[3] most of them have the distant (d) estimated from DM.

Figure 5.1: Luminosity at 1.4 GHz vs Period plot of the known pulsars (blue dots), with the theoretical sensitivity limits on the highly magnetized WD, 47Tuc, and M15 searches plotted in red,green, and magenta lines respectively.

few slow pulsars[4] have been discovered in globular clusters. For example, PSR B1718−19 an eclipsing slow (rotation period of 1 s) pulsar-WD binary was discovered in the direction of NGC 6342. Initially, the association between this pulsar and the cluster could not be confirmed since it is the only pulsar in that direction. Later, the association between this pulsar and the cluster was confirmed by the discovery of a 2-ms pulsar with the similar DM in the same direction from Transients and Pulsars with MeerKAT (TRAPUM) survey [5].

47 Tucanae (hereafter 47 Tuc) is a massive globular cluster located at a distance of 4.45 kpc from the Earth (Chen et al., 2018). Its position near the south celestial pole makes it circumpolar for telescopes located in the Southern Hemisphere, including the Parkes and MeerKAT telescopes. Searches of this cluster have led to the discovery of 29 pulsars, many of which exhibit fast spin periods ranging from 2 ms to 8 ms (Manchester et al., 1990b; Manchester et al., 1991; Robinson et al., 1995; Camilo et al., 2000a; Pan et al., 2016; Ridolfi et al., 2021)[6]. The 47Tuc also displays

---

[4] Pulsars with a rotation period longer than 1s.

[5] http://trapum.org/discoveries/

[6] See https://www3.mpifr-bonn.mpg.de/staff/pfreire/GCpsr.html for the up-to-date number.

a large degree of scintillation (Freire et al., 2003). On one hand, this scintillation can enhance the brightness of a dim pulsar, making it easier to discover, on the other hand, it also makes the discovery and follow-up observations of these pulsars more challenging as the pulsar could be detected only when the pulsar is scintillating up.

For this work, I will present results of searching 96.5 hr of 47 Tuc search-mode observations from the Parkes telescope with the AFFA pipeline.

5.2.2 Observations, Analysis, and Results

To search for pulsars in the 47 Tuc, we selected 10 of Parkes archival observations that have an observation time longer than 1.0 hr, with an average range of $\sim$ 10 hours that are in search mode and are available on the MPIfR archive server. These observations were observed with the Parkes Multi-Beam receiver (PMB) at the central frequency of 1389.75 and, 256 MHz bandwidth, with t_{samp} of 80 μs. The data were segmented into 15 mins chunks to improve the sensitivity to binary pulsars while taking advantage of possible scintillation (approximately 15 mins for this cluster). This resulted in a total observation length of 96.5 hr.

The search was divided into three ranges, the first search was aimed at detecting the known pulsars in the system with the FFA. As a result, a search pipeline was employed to search for a fast pulsar in the period range of 0.002s to 0.1s by folding with 26 bins, assuming a duty cycle of 30% for MSP. The data were de-dispersed from 0 to 40 pc cm^{-3} with an acceleration range of $\pm$ 16 m s^{-2}. This dispersion range was enough to cover the DM of this cluster, $\sim$ 24.4 pc cm^{-3}. To search for a slow pulsar within the period range of 0.1s to 90s, the 128 folding bins were employed. Given that the complexity of the FFA with acceleration searches decreases with the search period range, this allows us to explore a broader range of parameters. Hence, the data were de-dispersed from 0 to 40 pc cm^{-3} with an acceleration range of $\pm$ 128 m s^{-2}. Furthermore, to be sensitive to the population of isolated narrow-pulse pulsars with δ < 1%, we performed a non acceleration search with a search period range of 1.0s to 90.0s. All the pipelines employed the limiting S/N at 7.0.

The detection of PSR J0023-7203J from the first pipeline is shown in Figure 5.2, confirming that the pipeline is working for this dataset. The second pipeline found no new candidate, while the third pipeline resulted in only one recurrent candidate with a period of approximately 7 s. This candidate was also detected at multiple epochs. Examples of the detection of this candidate at MJD 51860.666 and 51809.369 are shown in Figure 5.3. The flux density of this candidate is stronger in the lower part of the observation band as shown in Figure 5.4 hinting that this candidate has a steep spectrum. However, this candidate was detected with a low DM, given that the pulse width of this candidate is approximately 20 ms, leading to a poor DM discrimination at this observing frequency (the DM needs to be larger than 21 pc cm^{-3} to smear the signal of this candidate more than one folding bin, see Equation 3.1.). If not extraterrestrial, this candidate might be local generated noise, and we may need another telescope to rule out that possibility. Observing with a receiver with a broader bandwidth or at the lower frequencies will also lead to a better constraint on the DM of this candidate.

This search is the first time that the acceleration search with FFA has been used to search for a slow pulsar in 47Tuc. The equivalent radio flux density of a repeating signal periodic signal with S/N of 7 with δ of 1% observed with the central beam of the PMB (Gain = 0.7 K Jy^{-1}) with 15
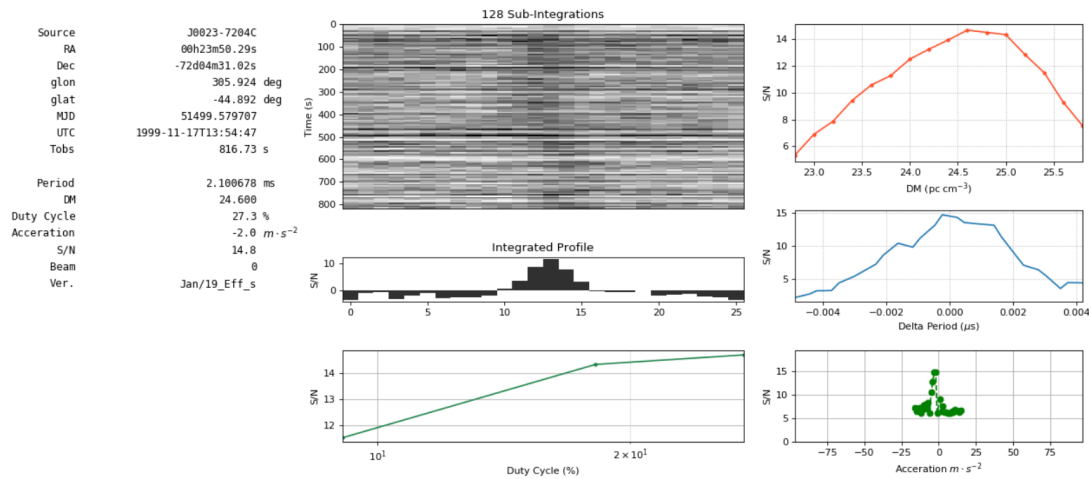
Figure 5.2: Detection of PSR J0023-7203J, the fastest pulsar in 47Tuc. The detection of this pulsar proves that the AFFA pipeline can search for this kind of pulsar if computational resources are available.

mins T_{obs} and T_{sys} of 30 K is 0.044 mJy. This limiting flux density[7] allows us to detect more than 90% of the current pulsar population, as shown in Figure 5.1. We searched more than 95 hours of data allowing us to be able to detect those pulsars that might have boosted the flux density by scintillation, which allows us to be more sensitive than we expected over the detectability threshold. The study on the S/N ratio distribution from scintillation in 47 Tuc was reported by Freire et al. (2000). This work can be used to estimate the probability distribution function of the scintillation amplification factor, which can further constrain the population for this search.

5.3 A search for pulsars in M15

5.3.1 Background

M15 has a higher stellar density than 47Tuc and known as a core-collapsed cluster. Due to its dense environment, the stellar interaction rate in this cluster is expected to be higher than non core-collapsed cluster. This leads to an increased number of close encounters and interaction between stars, which can cause the central region of the cluster to become much denser. The high interactions rate can be seen from the fact that more isolated pulsars and exotic systems, which could be results from such stellar interactions, have been detected (Verbunt and Freire, 2014). For example, of the 9 pulsars in M15, one of them, PSR B2127+11A, has a rotational period longer than 100ms [8].

For this work, we searched about 20 min of M15 search mode observations from the Arecibo telescope using the FFA pipeline.

---

[7] Utilizing the distance to 47Tuc.

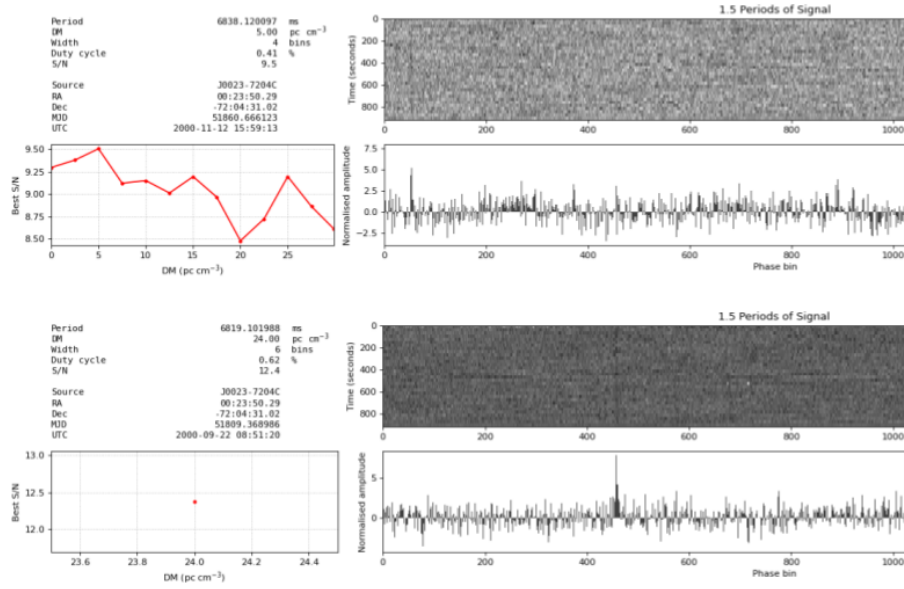[8] see https://www3.mpifr-bonn.mpg.de/staff/pfreire/GCpsr.html

Figure 5.3: Only pulsar candidate from the third pipeline. Upper: The candidate plot from MJD 51860. Lower: The candidate plot from MJD 51809.

5.3.2 Observations, Analysis, and Results

We used archival data obtained from the 305-m Arecibo telescope. The observation was done on MJD 58911 (3$^{\text{rd}}$ March 2020) using the PUPPI backend with the central frequency of 1390 MHz and total bandwidth of 700 MHz.

The data were masked with `rfifind`, then de-dispersed with a DM step size of 0.18 pc cm^{-3} from 0 to 70 pc cm^{-3}. This DM range is enough to cover the DM of any known pulsars in the cluster and allow us to compare the S/N at DM = 0 pc cm^{-3} to any specific DM. The DM step size was calculated from the DM that can delay the pulse arrival time for this receiver by 2 ms, which is equal to the pulse width assuming the pulse width of 1 folding bin of 128 profile bins, corresponding to ∼ 1%.

Due to the superb sensitivity of the Arecibo telescope, the data were originally observed with a 4-minute integration time, with 5 segments, i.e. sub integrations (20 minutes in total). Following the acceleration step size calculated in Chapter 3, the acceleration step size is 162 m s^{-2} for a 1 s pulsar with 0.5% pulse width. This acceleration is comparable to that of a 1 s pulsar orbiting 9 M$_\odot$ companion with 40 minutes orbital period. As a result, there is no need for acceleration search for this work. Despite the short observation time, the radiometer equation shows that the flux density limit of this search is 3.6 μJy using a telescope gain of 10 K/Jy and a system temperature of 30 K[9].

For this work, we applied the non-acceleration FFA pipeline to each segment. All candidates with the S/N more than 7.0 were inspected visually. The most prominent, candidate has a period

---

[9] For a pulsar with δ=1%.

6819.31ms_Cand: 51809.5122917/1_47T060_1.dd15.fil/1_1_47T060_1.dd15_6819.31ms_Cand.pfd.pazi
BC P(ms)= 6819.543835868 TC P(ms)= 6819.548322397 DM= 30.688 RAJ= 00:00:00.00 DecJ= 00:00:00.0
BC MJD = 51809.523990 Centre freq(MHz) = 1390.000 Bandwidth(MHz) = 256 l = 96.337 b = −60.189
NBin = 256 NChan = 16 NSub = 16 TBin(ms) = 26.639 TSub(s) = 56.064 TSpan(s) = 897.024
P(us): offset = 0.00000, step = 202.51966, range = 3240.31459 DM: offset = 0.000, step = 16.324, range = 538.683

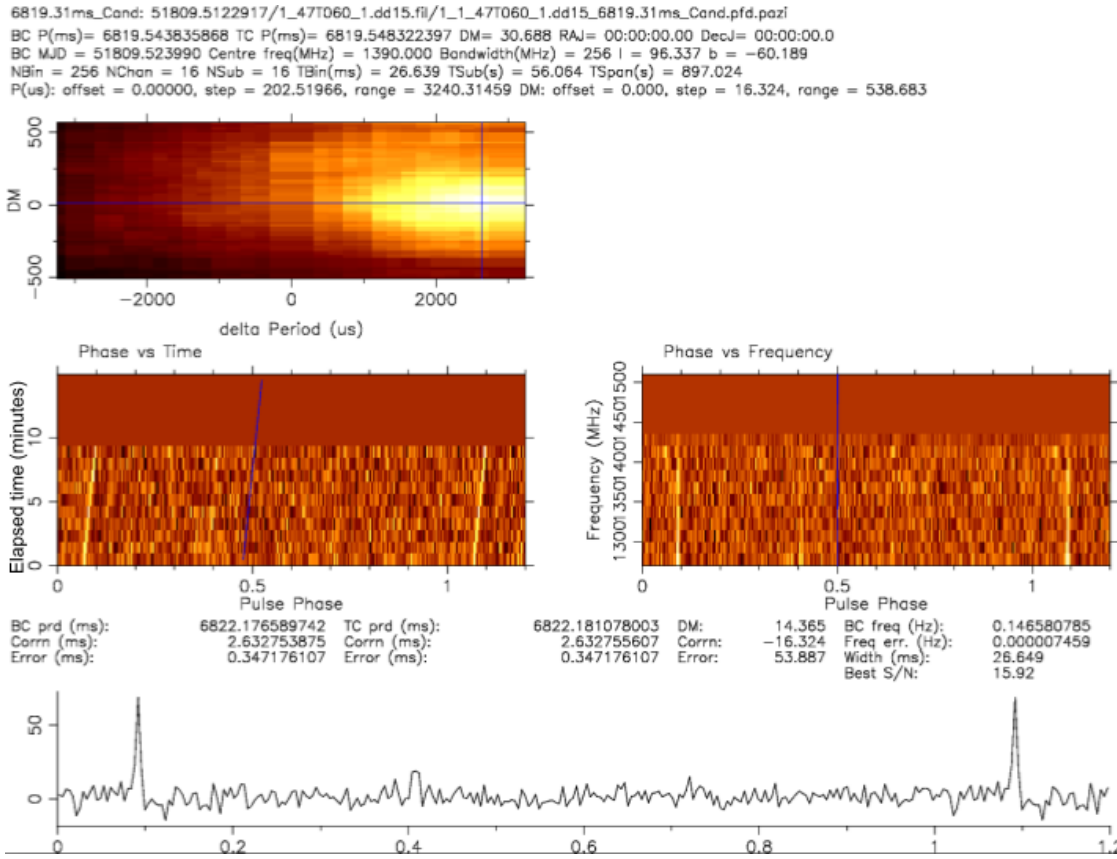|						
BC prd (ms):	6822.176589742	TC prd (ms):	6822.181078003	DM:	14.365	BC freq (Hz):	0.146580785
Corrn (ms):	2.632753875	Corrn (ms):	2.632755607	Corrn:	−16.324	Freq err. (Hz):	0.000007459
Error (ms):	0.347176107	Error (ms):	0.347176107	Error:	53.887	Width (ms):	26.649
						Best S/N:	15.92

Figure 5.4: Candidate plot from folding the search mode data from MJD 58109 with DSPSR and optimised with pdmp. The phase-frequency plot shows that this pulsar has a broad band emissions.

of 110 ms which is the period of the slow pulsar in this globular cluster as shown in Figure 5.5. No new pulsar was detected. With the aforementioned flux density limit, this search could detect more than 93% of the current pulsar population[10], as shown in Figure 5.1.

5.4 Conclusion

We employed the FFA pipeline to probe various datasets for pulsars, including a WD-pulsar candidate, a core-collapsed globular cluster (M15), and a non-core-collapsed globular cluster (47 Tuc). While discovering an additional WD-pulsar candidate can be used to explore new types of objects, discovering a slow pulsar in a globular cluster can lead to a study on alternative formation mechanisms for NSs. No pulsations were observed in the search for the WD pulsar. By applying the FFA to Parkes archival data from 47 Tuc and Arecibo data from M15, we were able to identify known pulsars and potential pulsar candidates that require additional study.

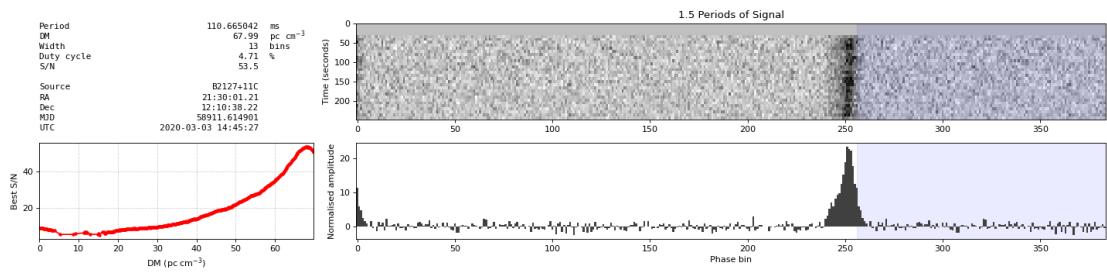[10] Using the distance of this cluster of 10.45 kpc (McNamara et al., 2004).

Figure 5.5: Detection of B2127+11A in the first segment of the data with the FFA pipeline.

Orbital period decay of PSR J0348+0432

6.1 Introduction

PSR J0348+0432 is a recycled pulsar with a white dwarf (WD) companion, discovered by Lynch et al. (2013) in the Green Bank Telescope 350 MHz Drift-scan Survey. This binary system has a short orbital period (2.46 hrs) and a highly circular orbit (e $\sim 10^{-5}$). Later, Antoniadis et al. (2013) (hereafter A13) used optical spectroscopy observations of the WD companion and pulsar timing to calculate the mass ratio (q) of 11.7 ± 3, and then measured the surface gravity (g) from the shape of the spectral lines[1], with the finite-temperature mass-radius relation for low mass WDs (van Kerkwijk et al., 2005) to determine the m_c to be 0.172 ± 0.003 $M_\odot$. Combining these two constraints yielded a mass estimate for the pulsar (m_p) of 2.01 ± 0.04 $M_\odot$, showing that PSR J0348+0432 was the most massive pulsar known at the time (Antoniadis et al., 2013).

A13 used a three-year pulsar timing campaign that included observations from the 100-m Green Bank, Arecibo 300-m, and 100-m Effelsberg telescopes. This observational campaign also detected the orbital period decay ($\dot{P}_b$) of 273 ± 45 fs s^{-1}. $\dot{P}_b$ is one of the Post-Keplerian parameters, which may originate from orbital energy loss due to the emission of gravitational waves. The $\dot{P}_b$ measured from a radio pulsar timing was in a good agreement with the $\dot{P}_b$ predicted from General Relativity (GR), $\sim$250 fs s^{-1} using m_p and m_c determined in A13. Later, PSR J0740+6620, a radio pulsar-WD binary was discovered with a pulsar mass (m_p) of 2.07±0.08 $M_\odot$ (Cromartie et al., 2020; Fonseca et al., 2021), these pulsars are among the most massive known NSs and provide further constraints on the equation of state for dense matter at supra-nuclear densities (e.g. Lattimer, 2012; Özel and Freire, 2016)

A13 used a short timing baseline to study this system. The uncertainty of measured $\dot{P}_b$ is proportional to the timing baseline length (T) as $T^{-5/2}$, making the extension of the timing baseline crucial for accurately measuring the $\dot{P}_b$. Furthermore, improving the measured $\dot{P}_b$ uncertainty can be used to further test gravity theories, as most of them predict additional $\dot{P}_b$ terms from GR (see Wex, 2014; Wex and Kramer, 2020b, for reviews). In this work, we present timing results from more than 10 years of data, obtained using three telescopes, to further constrain the measured $\dot{P}_b$ of this system.

---

[1] $g \equiv \frac{Gm_c}{R_c^2}$, where m_c is the WD mass and R_c is the WD radius.

6.2 Observations and Data analysis

In this study, we initially used the previous data presented in A13 from the Green Bank Telescope (GBT) and Arecibo observatory with the Wideband Arecibo Pulsar Processor (WAPP) backends (Dowd et al., 2000) at the L-band (1400 MHz). These Arecibo data were obtained with the Puerto Rico Ultimate Pulsar Processing Instrument (PUPPI) backend also centred at 1400 MHz after MJD 56185. While the WAPPs were capable of recording data up to 4×100 MHz bandwidth, the PUPPI backend had a wider effective bandwidth of 580 MHz (1150-1730 MHz), and coherently de-dispersion enabled (see Section 2.2.3), which provided a better timing precision. PUPPI also recorded in fold mode with polarisation information, facilitating additional exploration of this pulsar's polarisation characteristics. Therefore, the data from the PUPPI backend were used after MJD 56185.

To reduce radio frequency interference (RFI) in the data, we employed various automated RFI mitigation software packages, including COASTGUARD (Lazarus et al., 2016) and CLFD (Morello et al., 2019). In addition, we manually removed any remaining RFI using PAZI (van Straten et al., 2012a). After that, the data were folded using the pulsar ephemeris from A13.

To preserve frequency information, the PUPPI data were divided into 4 subbands with a sub-integration time of 5 minutes. The profile of the brightest observation was used as a template to extract time-of-arrivals (TOAs). As the pulse profile does not evolve significantly across the observed frequency (see Figure 6.1), a frequency scrunched pulse profile was used for 2D (frequency-phase) TOA extraction. This enhances sensitivity to chromatic phenomena, such as changes in dispersion. Furthermore, some observations were corrupted by various factors, such as backend faults, calibration issues, strong RFI, or strong interstellar scintillation, which caused the pulsar signal to become faint or disappear. These corrupted observations were removed, resulting in 10357 TOAs with a weighted timing uncertainty of less than 6 μs, with 6267 TOAs from the WAPPs before MJD 56185 and 187 TOAs from GBT data used in A13.

As the pulse profile does not evolve significantly across the observed frequency (see Figure 6.1), a frequency scrunched pulse profile was used for 2D (frequency-phase) TOA extraction. This enhances sensitivity to chromatic phenomena, such as changes in dispersion. Furthermore, some observations were corrupted by various factors, such as backend faults, calibration issues, strong RFI, or strong interstellar scintillation, which caused the pulsar signal to become faint or disappear. These corrupted observations were removed, resulting in 10357 TOAs with a weighted timing uncertainty of less than 6 μs, with 6267 TOAs from the WAPPs before MJD 56185 and 187 TOAs from GBT data used in A13.

The Effelsberg telescope was used in A13 and the telescope has been used to continue the timing of PSR J0348+0432 since with the L-band receiver. In this work, the RFI in the data were cleaned in a way similar to the Arecibo data. After that, the TOAs from the Effelsberg telescope data were extracted similarly by creating a noise-free pulse profile template by combining cleaned observations from 2018 to May 2020. We then calibrated the polarisation using a reference noise diode, which was observed before each observation of the pulsar. This calibration observation was used to correct differential phase and amplitude offsets introduced by the receiver. As the Effelsberg telescope has lower sensitivity than the Arecibo telescope, we applied the template matching method to the frequency-scrunched data with 10-minute sub-integrations per TOA.
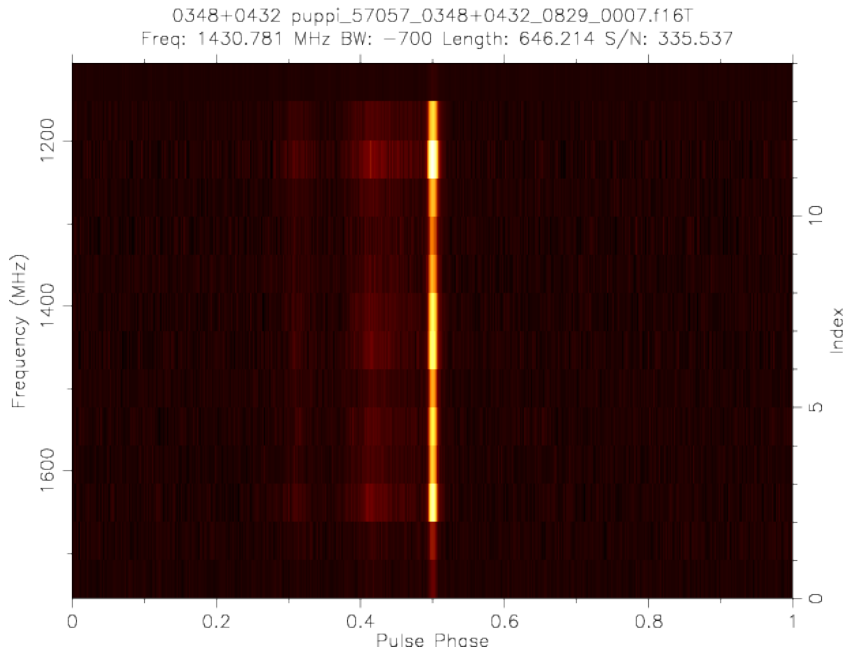
Figure 6.1: A frequency-phase plot of PSR J0348+0342, recorded via the PUPPI backend at the Arecibo Observatory, shows no evidence of pulse profile evolution across frequencies. The profile also rotated such that the emission's peak is located at pulse phase 0.5.

Using this method, we obtained 383 TOAs with a timing uncertainty of less than 13 μs after removing corrupted observations.

To make each TOAs from each instrument to refer to the same longitude of the binary orbit, we aligned all the peaks of the radio emission at phase 0.50 (see Figure 6.1). This is especially important to the measurements of $\dot{P}_b$ (see Guo et al., 2021, for more information).

Subsequently, we connected all the TOAs by fitting for any time jumps between the different instruments, extending the radio timing baseline from 3.66 to 10.2 years. The final dataset includes a total of, 28489 TOAs.

6.3 Timing solution

The previous results indicate that this pulsar has a nearly circular orbit, meaning that it has a small eccentricity (e) leading to an uncertain longitude of periastron (ω) and time of periastron passage (T_0). As these parameters (e, ω, T_0) are highly correlated with each other for a highly circular orbit, we used the ELL1 model (Lange et al., 2001) to describe the orbit with the time of ascending node (TASC), $\eta \equiv e \sin \omega$, and $\kappa \equiv e \cos \omega$. To analyse the TOAs, the TEMPO[2] software package was used. The range, and the shape of the Shapiro delay (s and r respectively), and the rate of periastron advance ($\dot{\omega}$) were kept fixed to the numbers reported in A13 because m_c, m_p, i are better constrained from the optical spectroscopic observations, with r,s and $\dot{\omega}$ being calculated

---

[2] https://tempo.sourceforge.net/

from m_c, m_p, i. The full-timing solution is shown in Table 6.1 with the residual from the ELL1 model with the masses from Antoniadis et al. (2013) in Figure is shown 6.2. The result shows the weighted root-mean-square of the residuals of 5.11 μs.
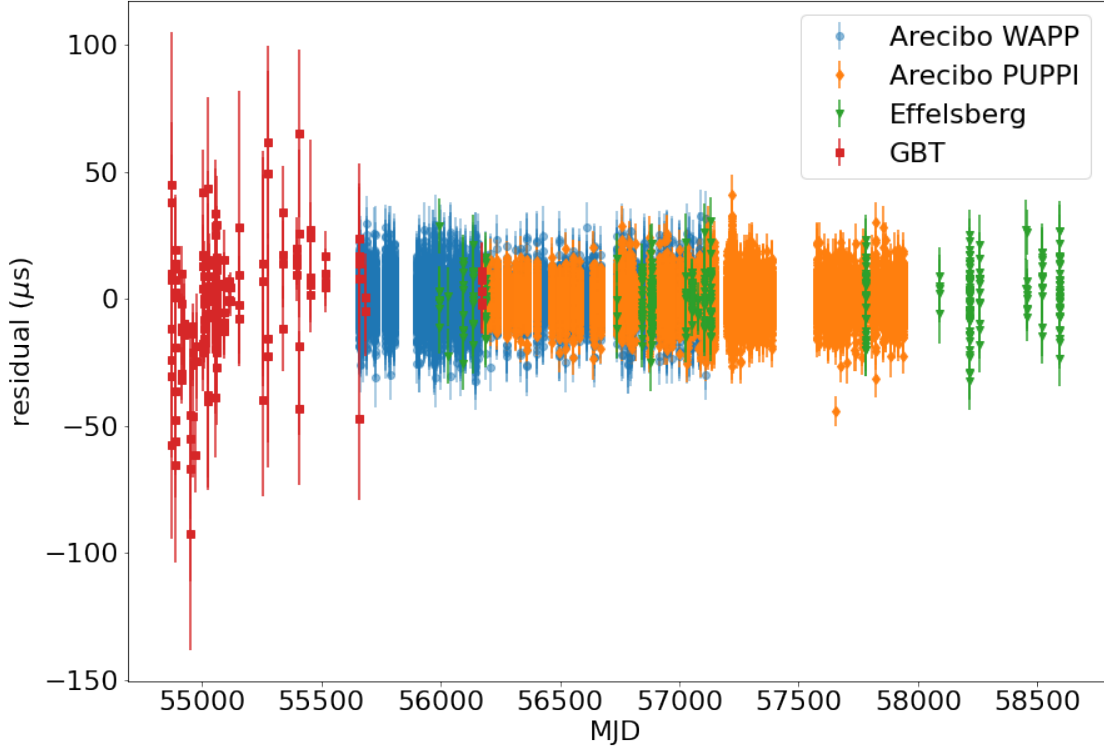

Figure 6.2: Residuals of the TOAs from the GBT (red rectangles), Arecibo with the WAPP backend (blue circles), Arecibo with the PUPPI backend (orange diamonds), and the Effelsberg telescope (green triangles) fitted to an ELL1 model.

6.4 Discussion

As previously shown in Table 6.1, our expanded timing baseline resulted in a smaller $\dot{P}_b$ than predicted in A13 by approximately 60 fs s^{-1}. We also detected a significant second spin frequency derivative (8σ). In this section, we will demonstrate the stability of the measured $\dot{P}_b$ as the timing baseline grows longer, then we will explore a possible higher order orbital period decay. After that, we will model kinematic contributions to $\dot{P}_b$ to calculate the intrinsic $\dot{P}_b$, and compare that to the predicted $\dot{P}_b$ from the mass measurements and orbital parameters in A13. We will then discuss possible explanations for the excess $\dot{P}_b$. Lastly, assuming that the measured $\dot{P}_b$ from this work is constant and given purely by GR, we will estimate possible masses of the NS and WD.

Table 6.1: Timing solutions for PSR J0348+0432 using the ELL1 model with companion mass and orbital inclination from the previous work, using the ELL1 model with fitted masses from Section 6.4.5 and using the BTX model (see Section 6.4.2).

Pulsar	ELL1	ELL1 fitted masses	BTX
Proper Motion in α, μ_α (mas yr^{-1})	4.37(1)	4.36(1)	4.37(1)
Proper Motion in δ, μ_δ (mas yr^{-1})	0.64(4)	0.65(4)	0.66(4)
Parallax (mas)	0.4700	0.4240	0.4700
Spin Frequency, f (s^{-1})	25.5606365914501(2)	25.5606365914501(2)	25.5606365914495(1)
1st Spin Frequency derivative, $\dot{f}$ (Hz s^{-2})	$-1.57294(4)\times10^{-16}$	$-1.57294(4)\times10^{-16}$	$-1.57330(2)\times10^{-16}$
2nd Spin Frequency derivative, $\ddot{f}$ (Hz s^{-3})	$-5.1(6)\times10^{-28}$	$-5.0(6)\times10^{-28}$	$3.5(3)\times10^{-28}$
Reference Epoch (MJD)	55900.000000	55900.000000	55900.000000
Start of Timing Data (MJD)	54873.750	54873.750	54873.750
End of Timing Data (MJD)	58593.673	58593.673	58593.673
Dispersion Measure, DM (pc cm^{-3})	40.4926(5)	40.4926(5)	40.4929(5)
Solar System Ephemeris	DE405	DE405	DE405
Terrestrial Time Standard	UTC(NIST)	UTC(NIST)	UTC(NIST)
Time Units	TDB	TDB	TDB
Number of TOAs	28489	28489	28489
Residuals RMS (μs)	5.11	5.10	5.13
χ^2	37347.19	37347.19	37736.32
reduced χ^2	1.3121	1.3121	1.3257
Binary Parameters			
Binary Model	ELL1	ELL1	BTX
Projected Semi-major Axis, x_p (lt-s)	0.14097963(4)	0.14097974(4)	0.14098087(4)
Orbital Eccentricity, e	–	–	0.0000039985
Longitude of Periastron, ω (deg)	–	–	283.373310811800
Epoch of passage at Periastron, T_0 (MJD)	–	–	57126.0104732100
First Laplace-Lagrange parameter, η	$-2.2(5)\times10^{-6}$	$-2.0(5)\times10^{-6}$	–
First Laplace-Lagrange parameter, κ	$2.1(5)\times10^{-6}$	$2.0(5)\times10^{-6}$	–
Epoch of passage at Ascending Node, T_{asc} (MJD)	57125.929850329(6)	57125.929850329(6)	–
Rate of periastron advance, $\dot{\omega}$ (deg yr^{-1})	14.9000000	13.4000000	–
Orbital Period, P_b (days)	0.1024240609014(10)	0.1024240609015(10)	–
Orbital Period derivative, $\dot{P}_b$ (10^{-12} s s^{-1})	$-0.199(2)$	$-0.199(2)$	–
Orbital Frequency, f_b (s^{-1})	–	–	$1.13001515189(2)\times10^{-4}$
1st Orbital Freq. derivative, $f_b^{(1)}$ (s^{-2})	–	–	$2.26(4)\times10^{-21}$
2nd Orbital Freq. derivative, $f_b^{(2)}$ (s^{-3})	–	–	$5(3)\times10^{-30}$
3rd Orbital Freq. derivative, $f_b^{(3)}$ (s^{-4})	–	–	$3.4(8)\times10^{-37}$
$\sin i$,	0.64	0.68	0.64
Companion Mass, m_c (M$_\odot$)	0.173	0.146	0.173

6.4.1 Validity of the $\dot{P}_{\rm b}$ measurement

To validate our $\dot{P}_b$ measurement, we investigated the $\dot{P}_{\rm b}$ evolution as the timing baseline increased. To accomplish this, we initially replicated the $\dot{P}_{\rm b}$measurements reported in A13 by using only the TOAs obtained before MJD 56200, and subsequently fit the timing model with `TEMPO` using the ELL1 model and the exact parameters employed in the aforementioned work. We then utilised the timing model developed in our study to fit the same set of TOAs. To examine the $\dot{P}_{\rm b}$ evolution, we performed `TEMPO` fits with the new timing model each time we extended the timing baseline by 180 days. Our results with the same MJD range, depicted in Figure 6.3, reveal that the $\dot{P}_{\rm b}$ obtained from this work is still comparable to both the $\dot{P}_{\rm b}$ predicted from GR and observed from A13. However, as the timing baseline grew longer, the measured $\dot{P}_{\rm b}$ approached its current value with greater precision, indicating the current $\dot{P}_{\rm b}$ is stable. Note that, the $\dot{P}_{\rm b}$ measured from all the TOAs in this work is only $\sim 1.6\sigma$ from the $\dot{P}_{\rm b}$ measured from A13.
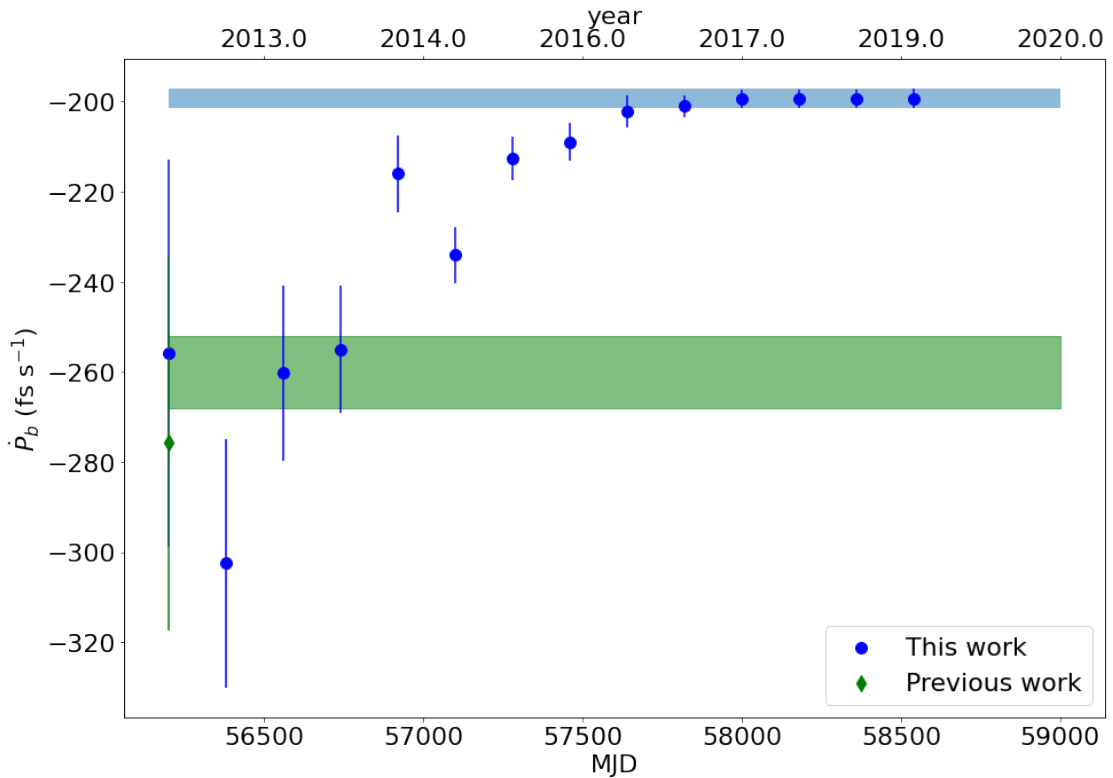

Figure 6.3: Evolution of $\dot{P}_{\rm b}$ as a function of timing baseline. The green diamond represents $\dot{P}_{\rm b}$ obtained from the timing model from A13, while the blue dots represent the results from our study. As the timing baseline increases (each point represents 180 days of additional timing baseline), the measured $\dot{P}_{\rm b}$ from both studies agreed with each other at the same range of MJD. Furthermore, as the timing baseline is extended, the $\dot{P}_{\rm b}$ converge to the current value, hinting the stability of the current $\dot{P}_{\rm b}$. The green and blue bars represent the 1-σ intervals of $\dot{P}_{\rm b}$ predicted from A13 and measured in this work, respectively.

To obtain a more precise constraint on $\dot{P}_b$, we computed the χ^2 value across a range of $\dot{P}_{\rm b}$using

the ELL1 model in `TEMPO`. Subsequently, we estimated the probability (p) of the measured $\dot{P}_\mathrm{b}$ using

$$p \propto e^{\frac{\chi^2_{\min} - \chi^2}{2}}, \tag{6.1}$$

as described in Splaver et al. (2002). We utilised cubic spline interpolation of p to estimate the probability distribution function (PDF) for $\dot{P}_b$, which resulted in a value of $199.3^{+1.2}_{-1.2}$ fs s^{-1}.
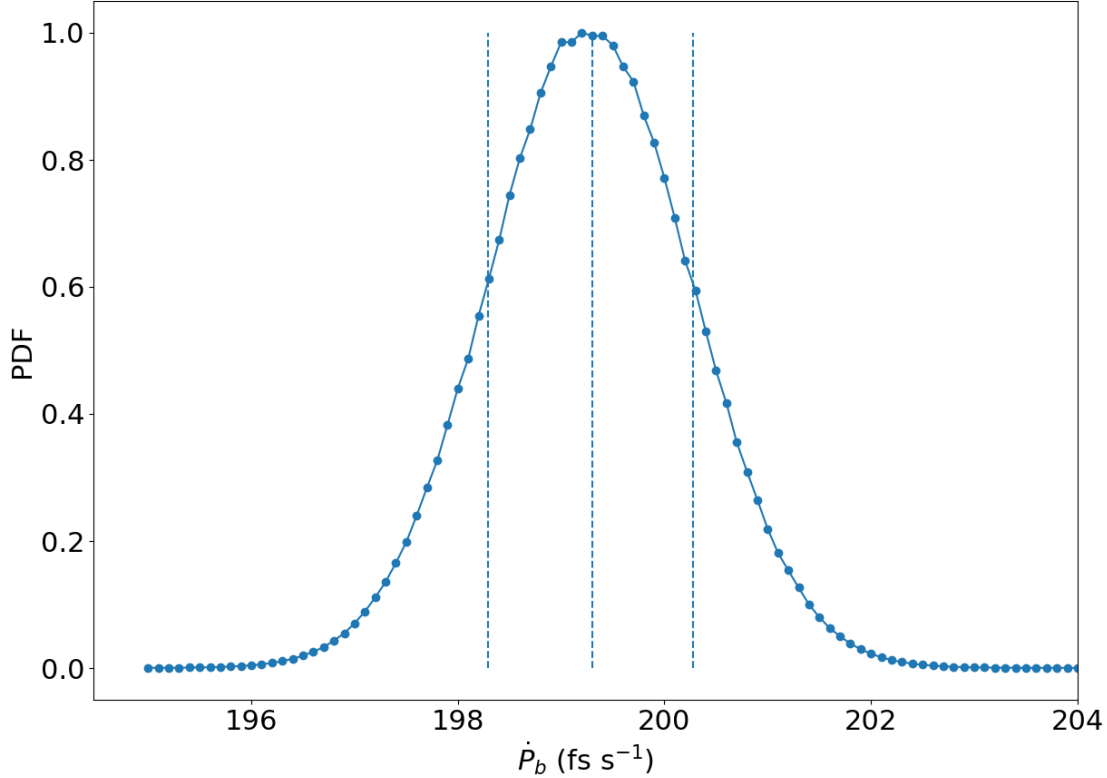

Figure 6.4: The probability density function of the measured $\dot{P}_b$ derived from `TEMPO` χ^2 using ELL1 model. Each dot represents χ^2 over different $\dot{P}_b$ from `TEMPO` fit. The curve shows the interpolated function. The dashed lines show the 1-σ uncertainty range and the median.

6.4.2 Higher order orbital period decay

To verify whether $\dot{P}_b$ is constant (as suggested by the parabolic curve), we applied the BTX model, a re-implementation of BT model (Blandford and Teukolsky, 1976b) that is possible to model to higher order derivatives of the orbital frequency [3], to model the same set of TOAs and searched for higher-order orbital frequency derivatives, e.g. second and third order orbital frequency derivatives (FB2 and FB3 respectively) using `TEMPO`. Our timing analysis indicated

---

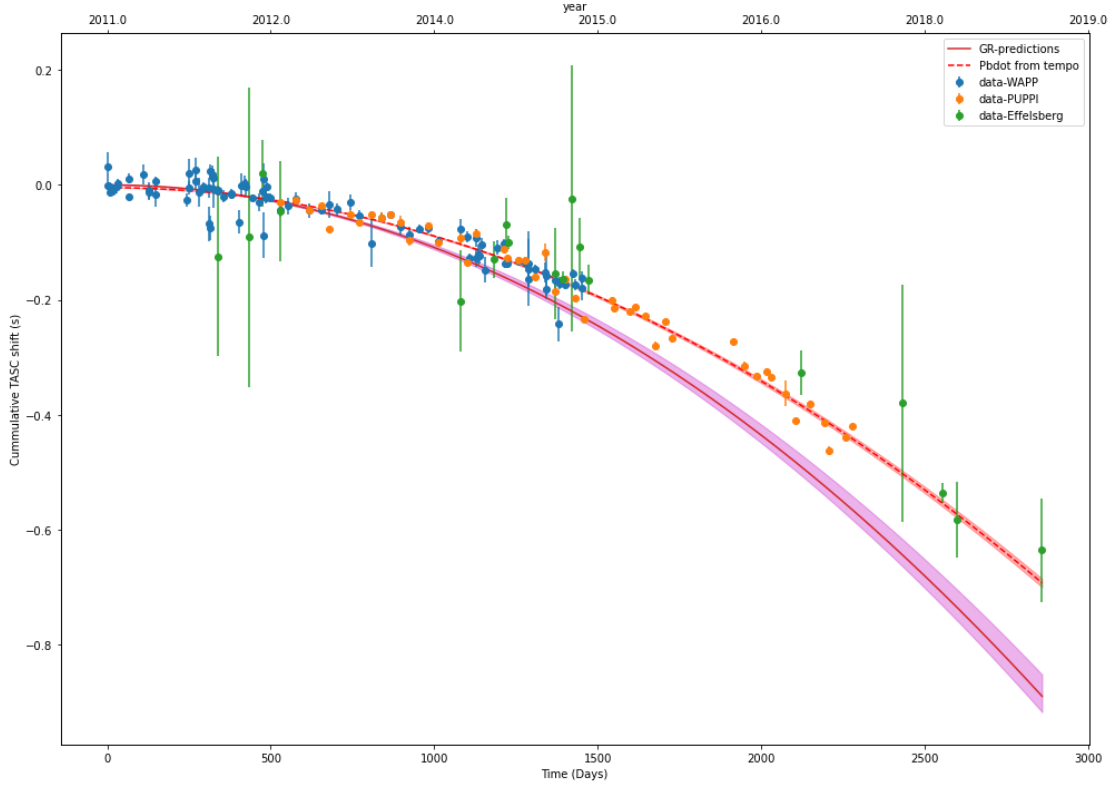[3] See https://tempo.sourceforge.net/ref_man_sections/binary.txt for details

Figure 6.5: Plot of time of assenting node (TASC) shift over time. The red solid line shows the prediction of TASC shift over time from GR, assuming the same masses as reported in A13 started from the first WAPP TOA (MJD 55996). The dashed-line shows the predictions of TASC shift from the $\dot{P}_b$ measured in this work, the red and orange bands indicating 1-σ interval.

that FB2 and FB3 are $5 \pm 3 \times 10^{-30}$ Hz s^{-3} and $3.4 \pm 0.8 \times 10^{-37}$ Hz s^{-3}, respectively, indicating that there is no significant second order orbital period derivative and a marginal detection of the third order orbital period derivative.

To further investigate the $\dot{P}_b$, we fit the data from each epoch of each backend for TASC with TEMPO using the ELL1 binary model, while setting $\dot{P}_b$ to zero. Only epochs containing more than 20 TOAs and exhibiting a reduced χ^2 less than 3 were selected. The results from the TASC fits for each epoch are presented in Figure 6.5, along with the predicted TASC shift based on the prediction from A13 and this measurement using all the data. The results indicate that the TASC shifts following the parabolic shape agrees with a constant $\dot{P}_b$ without any higher order variation.

6.4.3 Intrinsic orbital period decay

A non-zero $\dot{P}_b$ is predicted from GR due to the energy loss from gravitational wave emission. The $\dot{P}_b$ according to gravitation waves radiation of a binary system with an orbital period of P_b

with an eccentricity e can be calculated from

$$\dot{P}_{\mathrm{b}}^{\mathrm{GR}} = -\frac{192\pi}{5} \left(\frac{P_{\mathrm{b}}}{2\pi T_{\odot}}\right)^{-\frac{5}{3}} \frac{m_{\mathrm{p}} m_{\mathrm{c}}}{\left(m_{\mathrm{p}} + m_{\mathrm{c}}\right)^{\frac{1}{3}}} f(e), \tag{6.2}$$

where $T_{\odot}$ is a solar mass parameter in time unit while the masses are dimensionless quantities expressed relative to the solar mass, see Section 2.3.3 and Prša et al. (2016), with

$$f(e) = \left(1 + \frac{73}{24}e^2 + \frac{37}{96}e^4\right)\left(1 - e^2\right)^{-\frac{7}{2}}, \tag{6.3}$$

which is approximately 1 for this system. Using the masses reported in A13, the predicted $\dot{P}_{\mathrm{b}}^{\mathrm{GR}}$ is -260 ± 8 fs s^{-1}.

However, there are kinematic contributions that can alter the observed orbital period decay ($\dot{P}_{b}^{\mathrm{obs}}$) from the intrinsic $\dot{P}_{\mathrm{b}}^{\mathrm{int}}$, which can be calculated from

$$\dot{P}_{\mathrm{b}}^{\mathrm{int}} = \dot{P}_{b}^{\mathrm{obs}} - \dot{P}_{b}^{\mathrm{Gal}} - \dot{P}_{b}^{\mathrm{Shk}} - \dot{P}_{b}^{\dot{m}}. \tag{6.4}$$

Where $\dot{P}_{b}^{\mathrm{Shk}}, \dot{P}_{b}^{\dot{m}}$, and $\dot{P}_{b}^{\mathrm{Gal}}$ are contributions from the Shklovskii effect (Shklovskii, 1970), the mass loss in both objects (Jeans, 1924; Jeans., 1925) and the difference of Galactic accelerations between the binary and the Solar System (Damour and Taylor, 1991a; Nice and Taylor, 1995; Lazaridis et al., 2009) respectively. $\dot{P}_{b}^{\mathrm{GR}}$ is the orbital period decay predicted from GR (Damour and Taylor, 1991b).

The Shklovskii effect (Shklovskii, 1970) can change observed $\dot{P}_{b}^{\mathrm{obs}}$ by

$$\left(\frac{\dot{P}_{b}^{\mathrm{Shk}}}{P_{b}}\right) = \frac{(\mu_{\alpha}^2 + \mu_{\delta}^2)d}{c}, \tag{6.5}$$

where $\dot{P}_{b}^{\mathrm{Shk}}$ is the contribution from the Shklovskii effect to $\dot{P}_{\mathrm{b}}$, while μ_{α} and μ_{δ} are the proper motion in direction of RA and DEC respectively and d is the distance of this pulsar[4].

An orbital period decay can be caused by the mass loss in both objects (e.g. Jeans, 1924; Jeans., 1925) as

$$\left(\frac{\dot{P}_{b}^{\mathrm{m}}}{P_{b}}\right) = -2\frac{\dot{m}_p + \dot{m}_c}{M_{\mathrm{tot}}}. \tag{6.6}$$

The pulsar mass loss rate can be estimated by the energy loss from the loss in rotational kinetic energy ($\dot{E}_{\mathrm{rot}} = \dot{m}_{\mathrm{p}} c^2$) which leads to

$$\dot{P}^{\dot{m}} = \frac{8\pi^2 G}{T_{\odot} c^5} \frac{I_p}{M_{\mathrm{tot}}} \frac{\dot{P}}{P^3} P_{\mathrm{b}} = 7.0 \pm 1.4 \times 10^{-4} \mathrm{fs\ s}^{-1}. \tag{6.7}$$

Where the canonical pulsar moment of inertia (I_{p}) was used (10^{38} kg m^2) (Özel and Freire, 2016).

---

[4] The distance used in this work was obtained from Antoniadis (2020).

For the WD mass loss, the dominant process originates from a fraction of energy (F) from relativistic particle winds emitted by the pulsar, which induce evaporation on the WD's surface. For relativistic winds to cause evaporation of the WD, the particles at the surface must achieve sufficient velocity (v) to escape the star, defined as $v^2/2 \geq \frac{Gm_c}{R_c}$.

Assuming isotropic relativistic particle winds reach the WD with a radius of R at the semi-major axis a, the upper limit for the WD mass loss rate, based on energy conservation, is defined by:

$$\dot{E}F = \frac{1}{2}\dot{m}_c v^2,\tag{6.8}$$

where $F = R^2/4a^2$. For this work, we used F=0.00074 as shown in A13, which gives $\dot{m}_c/m_{tot} < 5.4 \times 10^{-21}$ s^{-1} and $\dot{P}^{\dot{m}_c} < 0.04$ fs s^{-1}.

Furthermore, the difference in Galactic acceleration between the binary and the Solar System can also affect the observed $\dot{P}_b^{obs}$. The contribution of this effect is given by Damour and Taylor (1991a), Nice and Taylor (1995) and Lazaridis et al. (2009) as

$$\frac{\dot{P}_b^{Gal}}{P_b} = -\frac{\Theta_0^2}{R_0 c}\left(\cos l + \frac{\beta}{\beta^2 + \sin^2 l}\right)\cos b$$
$$- \left(2.27 z_{kpc} + 3.68\left(1 - e^{-4.3 z_{kpc}}\right)\right)|\sin b|.\tag{6.9}$$

Where $\beta \equiv (d/R_o)\cos b - \cos l$ and $z_{kpc} \equiv |d \sin b|$. θ_0 is the Galactic rotation velocity which is 240.5 ± 41 km s^{-1} and R_0 is the distance to the GC which is 8.28 (GRAVITY Collaboration et al., 2021).

As shown in Table 6.2, contributions from $\dot{P}_b^{Gal}, \dot{P}_b^{Shk}, \dot{P}_b^{\dot{m}}$ are negligible compared to $\dot{P}_b^{obs}$. Upon conducting a detailed analysis of these contributions regarding distance, we discover that the distance estimation would need to be off by a factor of two to make these contributions greater than the current level of uncertainty, as illustrated in Figure 6.6. Combining all of the kinematic contributions using Equation 6.4 led to $\dot{P}_b^{int}$ of -198 $\pm$ 2 fs s^{-1}.

Comparing the $\dot{P}_b^{int}$ to $\dot{P}_b^{GR}$ lead to the excess orbital period decay ($\dot{P}_b^{xs} \equiv \dot{P}_b^{int} - \dot{P}_b^{GR}$) of 62 $\pm$ 8 fs s^{-1}, which is highly significant (30σ) compared to $\dot{P}_b^{GR}$.

6.4.4 Possible explanations for $\dot{P}_b^{xs}$

In the previous subsection, we evaluated the validity of the measured $\dot{P}_b$. In this section, we consider various scenarios that could potentially lead to a significant $\dot{P}_b^{xs}$ of 62 $\pm$ 8 fs s^{-1}.

In A13, the mass ratio was calculated using the semi-amplitude of the radial velocity modulation of the WD (K_{wd}) and the pulsar (K_{psr}), respectively. This ratio is represented as $q = K_{wd}/K_{psr}$. We explored the impact of the uncertainty of the mass ratio on the predicted $\dot{P}_b$ and found that the uncertainty of q would need to be 20 times larger than the current uncertainty to yield a predicted $\dot{P}$b that agrees within 1-σ with the $\dot{P}$b reported in this work. Consequently, it is unlikely that q is the cause of $\dot{P}_b^{xs}$.

As alternative theories of gravity predict additional contributions to $\dot{P}_b$, i.e., $\dot{P}_b^{xs} \leq 0$, the $\dot{P}_b$ discrepancy in this work is unlikely to be due to an incorrect gravity theory.
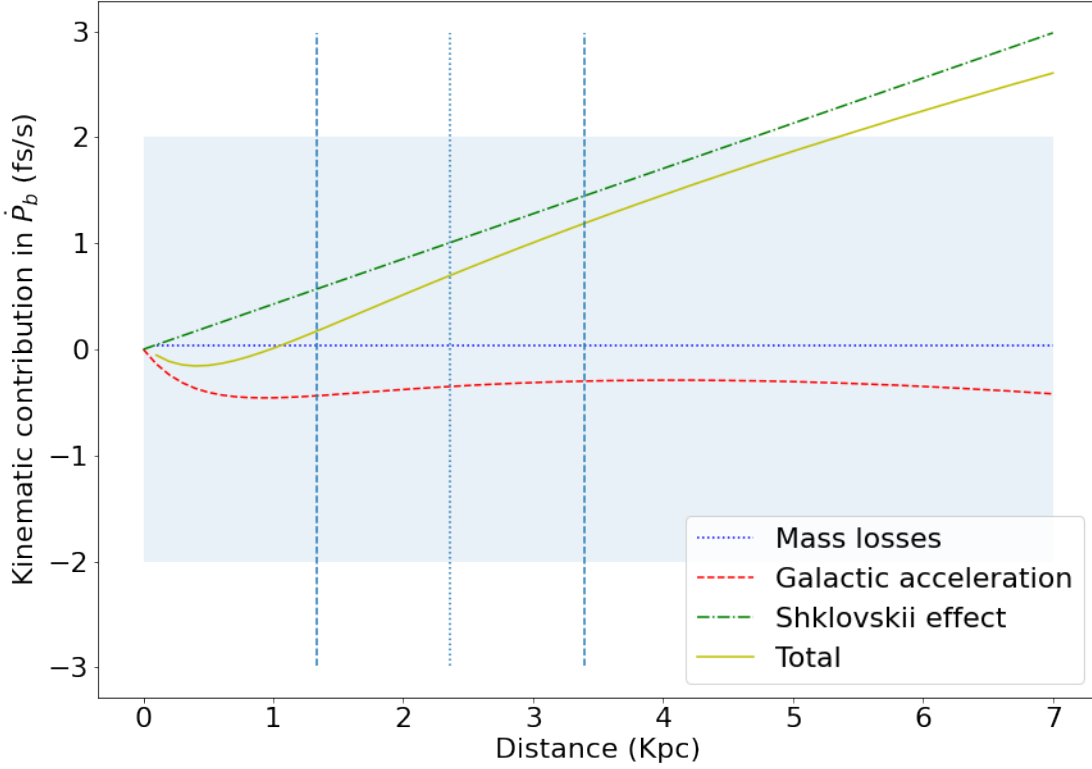
Figure 6.6: The kinematic contribution to $\dot{P}_b$ over distance. The yellow solid curve shows the combined kinematic contribution to the observed orbital decay, $\dot{P}_b$, as a function of distance to the pulsar. The red dashed, green dash-dotted, and blue dotted lines correspond to individual contributions from Galactic acceleration, assuming no contributions arise from errors in R_0 and θ_0, proper motion of the system, and mass losses, respectively. Please note that mass loss is not dependent on distance, so it is represented as a constant value. The blue area represents the current level of uncertainty in $\dot{P}_b$. The vertical dashed lines and dotted indicate the 1-σ distance and mean distance obtained from Antoniadis (2020) respectively.

Another possible explanation for this $\dot{P}_b$ discrepancy is that this system might be in a hierarchical triple system. The acceleration ($\dot{v}$) from a nearby object can also affect the first observed spin period derivative ($\dot{P}_{\text{int}}$) as

$$\frac{\dot{v}}{c} = \frac{\dot{P}_b^{\text{xs}}}{P_b} = \frac{\dot{P}_{\text{int}} - \dot{P}_{\text{obs}}}{P_0}. \tag{6.10}$$

As a result, the expected $\dot{P}_{\text{int}}$ is $-3 \pm 4 \times 10^{-20}$ s s^{-1}. Which still predicted a non-zero $\dot{P}_{\text{int}}$ of up to 10^{-20} s s^{-1} which is possible for recycled pulsars.

Since we also detect a significant $\ddot{P}$ for this pulsar (from a significant measurement of second spin frequency derivative, F2), it is possible that the $\ddot{P}$ could be originated from the motion of this binary system around the third body. Furthermore, the jerk ($\ddot{v}$) affected both of $\ddot{P}$ and $\ddot{P}_b$ as

$$\frac{\ddot{v}}{c} = \frac{\Delta \ddot{P}_b}{P_b} = \frac{\ddot{P}_{\text{int}} - \ddot{P}_{\text{obs}}}{P_0}. \tag{6.11}$$

Table 6.2: A comparison of the observed orbital period decay ($\dot{P}_b^{\mathrm{obs}}$) and orbital period decay predictions from General Relativity ($\dot{P}_b^{\mathrm{GR}}$) using masses from A13. $\dot{P}_{\mathrm{b}}$ contribution from Shklovskii Effect ($\dot{P}_b^{\mathrm{shk}}$), Galactic acceleration ($\dot{P}_b^{\mathrm{Gal}}$), and mass loss from the pulsar ($\dot{P}^{\dot{m}_P}$) and the white dwarf ($\dot{P}^{\dot{m}_c}$). This table highlights that the combined effects of Shklovskii, Galactic acceleration, and mass losses on orbital period decay rates are still smaller than the uncertainty in our measurements. The intrinsic orbital period decay ($\dot{P}_{\mathrm{b}}^{\mathrm{int}}$) is calculated from Equation 6.4 and the excess orbital period decay ($\dot{P}_b^{\mathrm{xs}}$) from $\dot{P}_b^{\mathrm{GR}}$ to $\dot{P}_{\mathrm{b}}^{\mathrm{int}}$ is also shown.

Contributions	fs s^{-1}
$\dot{P}_{\mathrm{b}}^{\mathrm{obs}}$	-199 ± 2
$\dot{P}_{\mathrm{b}}^{\mathrm{shk}}$	1.0 ± 0.4
$\dot{P}_{\mathrm{b}}^{\dot{m}_P}$	7.0 ± 1.4 ×10^{-4}
$\dot{P}_{\mathrm{b}}^{\dot{m}_c}$	0.04
$\dot{P}_{\mathrm{b}}^{\mathrm{Gal}}$	-0.4 ± 0.2
$\dot{P}_{\mathrm{b}}^{\mathrm{int}}$	-198 ± 2
$\dot{P}_{\mathrm{b}}^{\mathrm{GR}}$	-260 ± 8
$\dot{P}_{\mathrm{b}}^{\mathrm{xs}}$	62 ± 8

Assuming that the $\ddot{P}$ is dominated by the additional orbital motion, the expected FB2 is $\sim 10^{-33}$ s^{-3}, which is 3 orders of magnitude smaller than the FB2 measured from this work ($\sim 10^{-30}$ s^{-3}) using the BTX model. This indicates that we are not sensitive to this anomalous motion with FB2 yet. However, this higher order spin period derivative could also originate from red noise processes in the rotation of the pulsar; further study on red spin-noise is needed.

To investigate whether it is possible to discover this system in the future, we assume that this system exists in an edge-on circular orbit characterised by an orbital period T and semi major axis a. The observed orbital period ($\dot{P}_{\mathrm{b}}^{\mathrm{obs}}$) of this pulsar-WD system will be affected by the Doppler effect as

$$\dot{v} = \frac{c\dot{P}_{\mathrm{b}}^{\mathrm{xs}}}{\dot{P}_{\mathrm{b}}^{\mathrm{obs}}}, \qquad (6.12)$$

which is $\sim 2 \times 10^{-9}$ m s^{-2}. Then the gravitational acceleration $\dot{v}$ from this orbit is

$$\dot{v} = \frac{GM_{\mathrm{tot}}}{a^2}. \qquad (6.13)$$

As a result, a can be calculated from

$$a = \sqrt{\frac{GM_{\mathrm{tot}}}{\dot{v}}}. \qquad (6.14)$$

Given that the total mass of this possible triple system has to be larger than $m_{\mathrm{c}} + m_{\mathrm{p}}$ which is 2.18 $M_{\odot}$, the minimum orbital radius is 0.04 light year. With the minimum orbital radius, T can be

calculated from Kepler's 3$^{\text{rd}}$ law as

$$T^2 = \frac{4\pi^2}{GM_{\text{tot}}}a^3, \tag{6.15}$$

which gives the minimum T_{min} of 86000 yr. If this is true, this third object could be a planet, a gas cloud, or an unseen star.

6.4.5 Possible new mass measurements

In this section, we assume that the $\dot{P}_{\text{b}}^{\text{int}}$ measured in this work is constant, given by GR without mass losses and acceleration from a nearby object. Then the corresponding pulsar mass m_{p} and WD mass m_{c} can be calculated from the mass ratio q reported in A13 and $\dot{P}_{\text{b}}^{\text{int}}$. We employed the Markov Chain Monte Carlo (MCMC) algorithm using the `EMCEE` module (Foreman-Mackey et al., 2013). We defined a prior distribution on m_{p} and m_{c}, with upper limits of 3 $M_{\odot}$ and 2 $M_{\odot}$, respectively. The posterior samples are shown in Figure 6.7. The results show that m_{c} and m_{p} are estimated to be 0.1466 ± 0.001 $M_{\odot}$ and 1.71 ± 0.01 $M_{\odot}$, respectively. The measured masses led to $\sin i = 0.68 \pm 0.19$. As $m_{\text{p}}, m_{\text{c}}$ and i were kept as fixed values when determining the timing model, we re-analysed the TOAs based on the new values of $m_{\text{p}}, m_{\text{c}}$ and i and found no significant change in the new fitted timing model.

In A13, the surface gravity-temperature fit of the WD has revealed a high surface temperature ($\sim$ 10000 K), indicating that the WD has not yet fully cooled. As the pulsar has a large characteristic age of $\sim$ 2 Gyr, if the WD was born at approximately the same time as the pulsar, this will poses a conundrum, as WDs are expected to cool rapidly ($\sim$ Myr) over time. To maintain a high surface temperature after such a long time, a WD must have a thick hydrogen envelope, which can ignite the hydrogen burning. These type of WD must have a mass greater than 0.16 M$_{\odot}$, as demonstrated in A13. Moreover, this new m_c is significantly less than reported in A13, resulting in a significantly larger radius, $\sim$ 0.2 $R_{\odot}$ (extrapolated linearly from Figure 2 in the Supporting Online Material of A13). This combination of radius and mass give a new g ($\sim$ 5 $\log_{10}[\text{cm s}^{-1}]$) which is significantly contradicts the measured surface gravity g in A13 (6.035 ± 0.092 $\log_{10}[\text{cm s}^{-1}]$). Lastly, this radius is comparable to its Roche lobe (Eggleton, 1983), i.e., a region where matter is gravitationally bound to the star. If this is the case, and if the star is larger than its Roche lobe, it will begin to transfer mass to the NS. This process will disrupt the quadratic nature of the orbital period decay from GR (see e.g. Shaifullah et al., 2016). As a result, under the assumption that the WD was born $\sim$ 2 Gyr ago i.e. the pulsar's characteristic age, then it is unlikely that the mass of the WD will be less than 0.16 M$_{\odot}$.

6.5 Conclusions

We presented a new measurement of $\dot{P}_b$ for PSR J0348+0432 using 10.2 years of pulsar timing, -199 ± 2 fs s^{-1}. Although 1.6-sigma consistent with the value presented in paper I, it is substantially lower than the prediction of general relativity for the orbital decay of the system based on the masses derived in that paper, $\dot{P}_{\text{b}}^{\text{GR}} = -260 \pm 8$ fs s^{-1}; the difference relative to the prediction (62 fs s^{-1}) is highly significant.
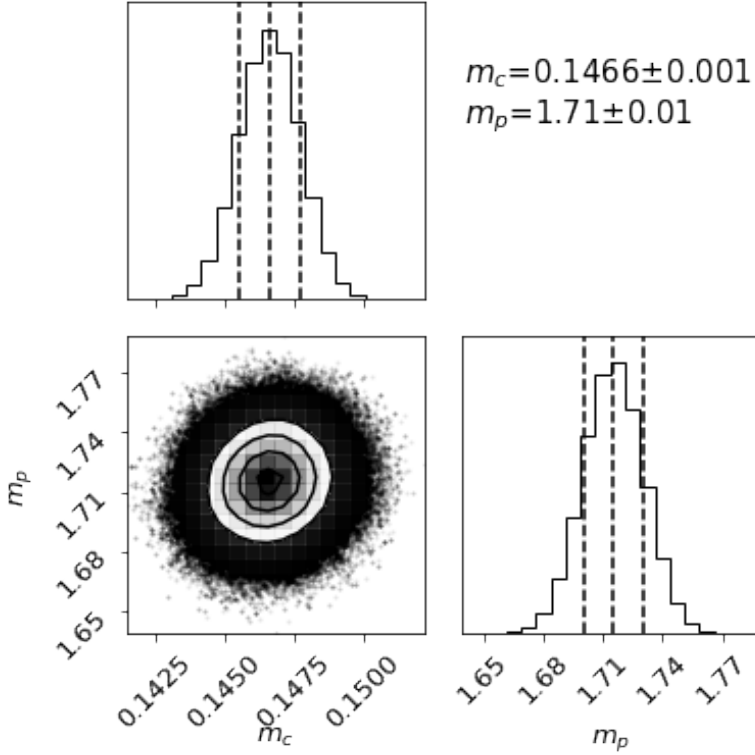
Figure 6.7: Two dimensional marginalised posterior distributions of m_c and m_p in $M_\odot$ from MCMC. The black, dashed lines represent 1-σ credible regions.

We investigated in detail the causes for this: first, we verified the robustness of our results. We reproduced the results obtained in A13, finding similar values of $\dot{P}_b$ for the same data set used earlier. As we extend the timing baseline, the measured $\dot{P}_b$ converges to its current value, and remains stable. We have looked for variations in the $\dot{P}_b$, also finding it is stable with time: the times of ascending node vary quadratically with time, as one should expect from a purely linear change of the orbital period with time. Furthermore, we found no significant second order orbital frequency derivative and a marginal detection of the third orbital frequency derivative. We conclude therefore that our measurement is robust and stable, with no clear signs of $\dot{P}_b$ changing with time.

We then looked for possible explanations for this difference. The total kinematic contributions to $\dot{P}_b$ are still smaller than the uncertainty of the current $\dot{P}_b$, implying no significant contributions from these effects to the $\dot{P}_b^{\text{obs}}$. We discussed possible additional contributions to $\dot{P}_b$. One possibility is that the system is being accelerated by a nearby mass, possibly from a third component in a hierarchical triple system with a long orbital period. This hypothesis has some mild support from the detection of a second spin frequency derivative, which could reflect a change in the acceleration of the system. However, the latter could be due to timing noise instead .

Lastly, assuming that the current $\dot{P}_b^{\text{int}}$ is purely due to GR orbital decay, we obtain the pulsar and the white dwarf masses to be 1.71±0.01 and 0.1466±0.001 $M_\odot$, respectively. These lower

masses contradict all WD atmospheric models, including all those used in A13.

The difference between the observed and predicted variation of the orbital period is not likely to be caused by a deviation in GR: in most alternative theories of gravity, there are additional contributions to the emission of gravitational waves that would amplify, not decrease (as observed), the absolute value of the orbital decay.

Conclusion and future work

Due to the large distance of pulsars[1], individual pulses from pulsars are typically too weak to be directly detected. Therefore, the periodicity of the signal is used to increase its significance by combining the data at a specific period. The Fast Fourier Transform (FFT) is widely used to search for periods, but it has less sensitivity towards narrow pulse pulsars even after compensating the loss of power through harmonic summing (Lazarus et al., 2015; Cameron et al., 2017b; Morello et al., 2020a). One of the alternative methods to search for periodicity is the Fast Folding Algorithm (FFA) (Staelin, 1969). However, due to its high computational cost in comparison to the FFT searches, FFT searches are more widely used.

Pulsar timing is a method used to study pulsars. It involves counting each rotation of the pulsar and measuring small changes in the arrival time of pulses of radiation compared to a predictive model. In the case of a pulsar having one or more companions, pulsar timing is also instrumental in investigating the orbital and post-Keplerian parameters of the (relativistic) binary system. Notably, these parameters are theory-independent. They can be combined to measure the masses of each object in the system, providing a valuable opportunity to further study and validate theories of gravity.

The last chapter of this thesis will summarise the findings from pulsar searches and pulsar timing from this work. This section will discuss possible future studies of pulsars, which could lead to new discoveries in the field.

7.1 Pulsar searches

The first part of this thesis describes searches for pulsars orbiting the supermassive black hole (Sgr A*) at the Galactic Center (GC), specifically focusing on those within an angular radius of $1°$ from Sgr A*. A pulsar-black hole binary can be used to determine the mass and spin of the black hole, which would yield a test of gravity theories. However, the dense environment at the GC causes the pulses to be broadened. This effect is known as interstellar scattering, which broadens the arrival time proportional to $f_{\rm obs}^{-4}$. This can result in the pulsations being completely smeared out, making it difficult to detect this pulsar. As demonstrated by Cordes and Lazio (2003), the

---

[1] The nearest pulsar located ∼300 light years from the Earth(Manchester et al., 2005)[1],

scattering broadening time at the GC can be as large as 2300 s at 1400 MHz, which is longer than the period of any known pulsar to date. To overcome this challenge, higher observing frequencies have been used to avoid the scattering. Despite numerous attempts to search for a pulsar in the GC, only six pulsars have been discovered within 0.5° of the GC (Johnston et al., 2006b; Deneva, 2010; Torne et al., 2017; Torne et al., 2021; Liu et al., 2021a; Eatough et al., 2021), including the Galactic Centre magnetar PSR J1745-2900, located 0.1 kpc away (Eatough et al., 2013b). Studies of the scattering broadening of J1745-2900 suggest that the scattering time at the GC is of the order of seconds (Spitler et al., 2013), providing motivation that slow pulsars may be detected with typical pulsar survey observation frequencies (1.4 GHz, see Section 2.4).

In Chapter 3, we used the FFA to search for slow pulsars in the GC using data from the HTRU-S low-latitude observations. This survey has the longest observation time among the HTRU surveys, leading to more pulses in the data. In this work, we searched for the pulsar with a spinning period ranging between 0.6 s to 430 s. With the duty cycle larger than approximately 1%, the optimisation on DM and acceleration search step size allow us to be sensitive up to DM of 4000 pc cm^{-3} and an acceleration range of ± 128 m s^{-2}. This acceleration range is comparable to a motion from a pulsar orbiting up to 37 $M_\odot$ companion with an orbital period longer than approximately 12 hr. The FFA pipeline was optimised for acceleration and de-dispersion step size, resulting in a reduction in the number of trials for the HTRU-S low-latitude observation. This pipeline is called AFFA throughout this thesis.

During the analysis of HTRU-S low-latitude data, we discovered a new slow pulsar (with a period of 1.89 s) located 0.5° from the GC. The follow-up observations using the Parkes, Effelsberg, and MeerKAT telescopes confirmed that this pulsar has high timing noise, a flat spectrum[2], $\alpha = -0.9$ ±1, and a high surface magnetic field ($\sim 5 \times 10^{-13}$ G). These properties are consistent with highly magnetised neutron stars, such as magnetars. However, this pulsar lacked other typical features of magnetars, such as pulse profile variations, high linear polarization fraction, and persistent high-energy emissions, such as X-rays. The high surface magnetic field suggests that this pulsar may be one of the transitional population from magnetars to pulsars. This pulsar also has a high dispersion measure (1309 ± 2 pc cm^{-3}), long scattering time (67 ms at 1000 MHz), and relatively large rotation measure (-743± 14 rad m^{-2}) which can be used to probe the magneto-ionic environment around the GC. Interestingly, this pulsar is the second pulsar near the GC with magnetar-like properties, the first being PSR J1746-2850 (Dexter et al., 2017), with one magnetar discovered in the GC (PSR J1745-2900). If both J1746-2829 and J1746-2850 are magnetars, it would be unusual to find three magnetars within a region of one degree. This is because magnetars have a much shorter lifetime for emitting radio waves compared to normal pulsars, and are less likely to be detected due to their transient nature.

Subsequently, we modified the AFFA pipeline to search for high-frequency data (230 GHz) from the Event Horizon Telescope (EHT) at the Galactic Centre in 2017, as described in Chapter 4. This survey is the highest frequency pulsar survey to date. The data used in this work were selected from the three most sensitive stations: ALMA, LMT, and IRAM 30 m telescope. The search period range was from 1 s to 1025 s and was capable of detecting a pulsar orbiting the Sgr A* with an orbital period in the order of years and longer. The results from the FFT, FFA, and single pulse searches showed no significant detections. However, the practical sensitivity

---

[2] Assuming that $S_f \propto f^\alpha$

limits, as determined from injecting simulated pulsar signals with various fluxes, showed that the limiting sensitivity for fast rotating pulsars (periods between 1 ms and 10 ms) was 0.02 mJy, 0.4 mJy, and 1 mJy for ALMA, LMT, and IRAM 30m telescopes, respectively. For slow pulsars with periods greater than 1 s, the limiting sensitivity was much higher, implying a lack of sensitivity towards slow pulsars regardless of the search algorithm used. This lack of sensitivity is because most pulsars have a power-law spectrum ($S \propto f_{\mathrm{obs}}^{-\alpha}$) with $\alpha \sim 1.6$ for most pulsars (Bates et al., 2013; Jankowski et al., 2018). Thus, the lack of detection does not imply the lack of pulsars around the Sgr A*.

In Chapter 5, the AFFA pipeline was applied to different datasets, including a white dwarf (WD) pulsar candidate, a core-collapsed globular cluster (M15), and a non core-collapsed globular cluster (47 Tuc). The search for a WD pulsar shows radio pulsations. However, this candidate is just one of the highly magnetised WD (Ferrario et al., 2020), which suggests that further searches are needed to understand the emission mechanism behind the radio emission from this type of object. However, the red noise caused by the instrument might makes it challenging to detect these long-period pulsations. To address this, further investigation can be conducted by injecting long-period signals into real data with instrumental red noise and studying the sensitivity loss.

For pulsars in globular clusters, the main formation of neutron stars does not favour the detection of young pulsars in these clusters due to its old population; discovering a pulsar in these systems can provide valuable information on alternative NS formations, such as accretion-induced collapse of WDs (Grindlay and Bailyn, 1988). Moreover, the exotic environments of globular clusters, especially the core-collapsed clusters. These clusters have a high interaction rate, making them an ideal place to search for slow pulsars in binary systems, as the pulsar might not be fully recycled. The AFFA was applied to approximately 100 hr of Parkes archival data from 47 Tuc, which was sensitive to 90% of the known pulsar population. This resulted in the detection of the known pulsar (PSR J0023-2703J) in the cluster and a pulsar candidate with a long period of 7 s. Further investigation is needed to confirm this candidate pulsar. For M15, which is a core-collapsed cluster, the data from the Arecibo telescope was used, which was sensitive to 93% of the pulsar population. Due to a short observation time of 4 min, no acceleration searches were required. This search resulted in no new pulsars being detected.

7.2 Pulsar timing

In Chapter 6, we discussed another aspect of pulsar research, the timing of a relativistic binary system. Our focus in this study was PSR J0348+0432, a pulsar discovered in the Green Bank Telescope 350 MHz Drift-scan survey (Lynch et al., 2013). The mass of this pulsar had been estimated to be $2.01 \pm 4\ M_\odot$ by Antoniadis et al. (2013) using optical spectroscopy of its white dwarf companion and pulsar timing, making this the most massive pulsar at the time. This system, along with other massive pulsars such as PSR J0740+6620 (Cromartie et al., 2020), has been used to constrain the equation of state for neutron stars (e.g. Özel and Freire, 2016). Antoniadis et al. (2013) also reported an orbital period decay ($\dot{P}_{\mathrm{b}}$) of 273 ± 45 fs s^{-1}, which agreed with the expected $\dot{P}_{\mathrm{b}}$ due to the system radiating gravitational waves, predicted from the General Relativity theory.

To enhance our understanding of the mass of this pulsar, the timing baseline was extended from

approximately 4 yr to approximately 10 yr using data from the Green Bank Telescope, Arecibo Telescope, and Effelsberg Telescope as the uncertainty in $\dot{P}_b$ scales as $T^{-5/2}$ when T is the timing baseline. Our results indicate that this system has a significantly lower $\dot{P}_b$ than predicted by GR using the masses reported in Antoniadis et al. (2013). We examined scenarios that may significantly impact the $\dot{P}_b$ measurements, such as acceleration of the pulsar by nearby objects. Long-term observations of this system can help to eliminate this possibility. If this measured is intrinsic, without higher order variation and purely from GR, combining the new $\dot{P}_b$ value and the mass ratio from previous work (q=11.7±0.03) led to new masses for the pulsar and the WD of 1.71 ±0.01 $M_\odot$ and 0.1466 ± 0.001 $M_\odot$, respectively. The errors here are purely statistical and do not represent systematic errors.

The discrepancy between our results and the WD mass estimate obtained through optical observations suggests that a more in-depth understanding of this system can be gained by observing its WD spectrum with a newer spectrograph, such as `Xshooter` at the Very Large Telescope (VLT) (Vernet et al., 2011).

7.3 Future works

7.3.1 GC pulsar searches

Our work on this thesis has placed constraints on the population of NSs in the GC, particularly non-recycled pulsars for which the FFA is more sensitive. Macquart et al. (2010) proposed that the GC might be dominated by recycled pulsars due to the high interaction rate in the GC. This could lead to a higher rate of binary star system formation, and the recycled pulsars' low spin-down energy could allow them to emit radio signals for a longer time, similar to what is seen in globular clusters, where only a few non-recycled pulsar has been detected. However, the results from Dexter and O'Leary (2014), Dexter et al. (2017), and this work (see Chapter 3) suggest the possibility that the GC might instead be dominated by magnetars as have shown transient radio emissions, making them difficult to detect. This could explain the non-detection of pulsars in many surveys despite some survey (e.g. Macquart et al., 2010) has enough sensitivity to detect the bright known recycled pulsars in the GC. To further study this, we need to enhance survey sensitivity, especially towards recycled pulsars. To improve the sensitivity of this survey, one can search for pulsars using data with broader bandwidth. For example, the EHT 2018 campaign recorded a bandwidth of 2 times larger than in 2017 campaign, leading to $\sqrt{2}$ improvement for the sensitivity. GC pulsar searches in the relatively lower frequency (less than 86 GHz) will be sensitive to larger fraction of population, but risking for higher scattering broadening. In the future, the new instruments, e.g. the MeerKAT S-band (2.6 GHz, Barr, 2018) and ALMA Band 1 receiver (35-50 GHz, Huang et al., 2016) will provide us with more sensitivity for pulsar searches in the GC while suffering from less scattering than previous searches at the lower frequencies.

Alternatively, instead of focusing on observations at higher frequencies, the implementation of new scattering mitigation techniques could be explored. One such method could potentially involve the search for scattered pulse profiles. For instance, one of the last steps in FFA searches is to apply matched filters to the pulse profile to evaluate the S/N. Currently, all the implementations of the FFA uses boxcar function as the trial filter. Morello et al. (2020a) demonstrated that the

deviation from the pulse profile to the filter can decrease the detected S/N. It is possible to use the other function such as boxcar convolved with exponential decay to search for pulsars in the GC where the scattering is expected to be significant. By using a template that is more similar to the pulse shape, (Morello et al., 2020a) demonstrated that the S/N can be improved.

7.3.2 Slow pulsar searches and acceleration searches with FFA

The increase in the number of ultra-long period pulsars (P > 10 s), with the discovery of the 23.5 s pulsar (Tan et al., 2018), the 76 s pulsar (Caleb et al., 2022), and the 1050 s pulsar candidate (Hurley-Walker et al., 2022), sparked interest in exploring the population of long period pulsars as these slows pulsars can be used to prove our understanding to NSs population in our Galaxy. According to Beniamini et al. (2022), approximately 100 pulsars with ultra-long periods (P>10s) are expected to be detected by the MeerKAT surveys. As the FFT is less sensitive to slow pulsars, the use of FFA and other methods, e.g. use snapshot images from interferometers (see Caleb et al., 2022, for example) for pulsar searches, should be an area of interest in the future.

Furthermore, the FFA could still be further improved. For example, Equation 2.17 demonstrated that the jerk search step size (j) can be calculated by,

$$ j = 6 \frac{c t_{\mathrm{bin}}}{T_{\mathrm{obs}}^3}. \tag{7.1} $$

Where t_{bin} is the time width equivalence of one folding bin. Since the FFA is folding each period range separately, it would be possible to optimise the step size to template bank searches (e.g. Balakrishnan et al., 2022).

7.3.3 Pulsar science with Thai National Radio Telescope

The Thai National Radio Telescope (TNRT) is a 40 m steerable dish located at the Huay Hong Krai Royal Development Study Centre in Chiang Mai, Thailand (latitude $18°51'52''$, longitude $99°13'01''$ E, 450m above sea level). It is capable of observing a wide range of radio frequencies (1 to 115 GHz). Since mid-2022, the TNRT is in the commissioning phase and is expected to be fully operational soon. Owing to its unique location and scheduling flexibility, the TNRT is a perfect tool for exploring the dynamic radio sky, including pulsars (Jaroenjittichai et al., 2022). For instance, one of the key scientific objectives of the TNRT is to search for sporadic emitting pulsars, such as RRATs, intermittent pulsars, and magnetars. The strategy is to make repeated observations as frequently as possible using the L-band receiver with an 800 MHz bandwidth, resulting in a sensitivity limit of 0.35 mJy with a 120 s observation time. With a beam area of 0.11 square degrees at the L-band, it can observe a large part of the Galactic plane (-60°<l<60°, -3°<b<3°) within nine days of observation. Discovering more sporadic pulsars can lead to a better understanding of the pulsar emission mechanism (see e.g. Kramer et al., 2006a). Since these pulsars are discovered with a long rotation period, the FFA pipeline developed in this thesis will play a key role in this search.

7.4 Closing remarks

In conclusion, this thesis highlights the importance of both pulsar searching and timing in order to improve our understanding of pulsars. The arrival of the relative new facilities including more sensitive telescope e.g., MeerKAT, FAST, and Square Kilometre Array (SKA) and better receiver technology such as ultra wide band and phased array receiver will allow us to be closer to discovering exotic systems such as pulsar-black hole binaries and relativistic binary pulsars. I look forward to a future filled with new discoveries and insights into the radio transient universe.

Bibliography

Andersen, B. C. et al. (2018), *A Fourier Domain "Jerk" Search for Binary Pulsars*, The Astrophysical Journal **863** L13, ISSN: 0004-637X, (visited on 31/10/2022) (cit. on p. 40).

Antoniadis, J. (2020), *Gaia Pulsars and Where to Find Them in EDR3*, Research Notes of the American Astronomical Society **4** 223, ISSN: 2515-5172, (visited on 06/01/2023) (cit. on pp. 79, 81).

Antoniadis, J. et al. (2013), *A Massive Pulsar in a Compact Relativistic Binary*, Science **340** 1233232, (visited on 09/05/2022) (cit. on pp. 18, 71, 74, 89, 90).

Archibald, A. M. et al. (2009), *A Radio Pulsar/X-ray Binary Link*, Science **324** 1411, ISSN: 0036-8075, (visited on 06/07/2023) (cit. on p. 7).

Archibald, R. F. et al. (2016), *A High Braking Index for a Pulsar*, Astrophys. J. **819** L16 (cit. on p. 5).

Backer, D. C. (1975), *Interstellar Scattering of Pulsar Radiation. I. Scintillation.*, Astronomy and Astrophysics, vol. 43, no. 3, Oct. 1975, p. 395-404. **43** 395, ISSN: 0004-6361, (visited on 18/05/2022) (cit. on p. 12).

Balakrishnan, V. (2022), *Novel Search Techniques to Detect Pulsar Black Hole Binaries in Radio Observations*, Thesis: Universitäts- und Landesbibliothek Bonn, (visited on 12/05/2022) (cit. on p. 49).

Balakrishnan, V. et al. (2021), *Pulsar Candidate Identification Using Semi-Supervised Generative Adversarial Networks*, Monthly Notices of the Royal Astronomical Society **505** 1180, ISSN: 0035-8711, (visited on 26/11/2022) (cit. on p. 42).

Balakrishnan, V. et al. (2022), *Coherent Search for Binary Pulsars across All Five Keplerian Parameters in Radio Observations Using the Template-Bank Algorithm*, Monthly Notices of the Royal Astronomical Society **511** 1265, ISSN: 0035-8711, (visited on 31/10/2022) (cit. on pp. 39, 91).

Barnes, A. T. et al. (2017), *Star Formation Rates and Efficiencies in the Galactic Centre*, Monthly Notices of the Royal Astronomical Society **469** 2263, ISSN: 0035-8711, (visited on 02/11/2022) (cit. on p. 50).

Barr, E. D. (2018), *An S-band Receiver and Backend System for MeerKAT*, **337** 175, (visited on 10/02/2023) (cit. on p. 90).

Bates, S. D. et al. (2013), *The Pulsar Spectral Index Distribution*, Monthly Notices of the Royal Astronomical Society **431** 1352 (cit. on pp. 48, 89).

Becker, R. H. et al. (1995), *The FIRST Survey: Faint Images of the Radio Sky at Twenty Centimeters*, The Astrophysical Journal **450** 559, ISSN: 0004-637X, (visited on 25/01/2023) (cit. on p. 63).

Beniamini, P. et al. (2022), *Evidence for an Abundant Old Population of Galactic Ultra Long Period Magnetars and Implications for Fast Radio Bursts*, (visited on 08/01/2023) (cit. on p. 91).

Berezina, M. (2018), *Pulsar Searching with the Effelsberg Telescope*, Thesis: Universitäts- und Landesbibliothek Bonn, (visited on 12/05/2022) (cit. on p. 10).

Bhat, N. D. R. et al. (2004), *Multifrequency Observations of Radio Pulse Broadening and Constraints on Interstellar Electron Density Microstructure*, Astrophys. J. **605** 759 (cit. on p. 12).

Bhattacharya, D. et al. (1992), *On the Decay of the Magnetic Fields of Single Radio Pulsars.*, Astronomy and Astrophysics, Vol. 254, p. 198-212 (1992) **254** 198, ISSN: 0004-6361, (visited on 01/06/2022) (cit. on pp. 6, 7).

Blandford, R. D. et al. (1976), *On the Scattering and Absorption of Electromagnetic Radiation with Pulsar Magnetospheres.*, Monthly Notices of the Royal Astronomical Society **174** 59, ISSN: 0035-8711, (visited on 01/06/2023) (cit. on p. 60).

Blandford, R. et al. (1976a), *Arrival-Time Analysis for a Pulsar in a Binary System.*, The Astrophysical Journal **205** 580, ISSN: 0004-637X, (visited on 15/05/2023) (cit. on p. 46).

– (1976b), *Arrival-Time Analysis for a Pulsar in a Binary System.*, The Astrophysical Journal **205** 580, ISSN: 0004-637X, (visited on 06/01/2023) (cit. on p. 77).

Bogdanov, S. et al. (2019a), *Constraining the Neutron Star Mass-Radius Relation and Dense Matter Equation of State with NICER. I. The Millisecond Pulsar X-Ray Data Set*, The Astrophysical Journal **887** L25, ISSN: 0004-637X, (visited on 09/06/2022) (cit. on p. 18).

Bogdanov, S. et al. (2019b), *Constraining the Neutron Star Mass-Radius Relation and Dense Matter Equation of State with NICER. II. Emission from Hot Spots on a Rapidly Rotating Neutron Star*, The Astrophysical Journal **887** L26, ISSN: 0004-637X, (visited on 09/06/2022) (cit. on p. 18).

Bogdanov, S. et al. (2021), *Constraining the Neutron Star Mass-Radius Relation and Dense Matter Equation of State with NICER. III. Model Description and Verification of Parameter Estimation Codes*, The Astrophysical Journal **914** L15, ISSN: 0004-637X, (visited on 09/06/2022) (cit. on p. 18).

Bondonneau, L. et al. (2020), *Pulsars with NenuFAR: Backend and Pipelines*, (cit. on p. 37).

Burgay, M. et al. (2003), *An Increased Estimate of the Merger Rate of Double Neutron Stars from Observations of a Highly Relativistic System*, Nature **426** 531, ISSN: 0028-0836, (visited on 25/09/2022) (cit. on p. 1).

Buschauer, R. et al. (1976), *General Theory of Coherent Curvature Radiation.*, Monthly Notices of the Royal Astronomical Society **177** 109, ISSN: 0035-8711, (visited on 12/05/2023) (cit. on p. 4).

Caleb, M. et al. (2022), *Discovery of a Radio-Emitting Neutron Star with an Ultra-Long Spin Period of 76 s*, Nature Astronomy **6** 828, ISSN: 2397-3366, (visited on 09/01/2023) (cit. on p. 91).

Cameron, A. D. et al. (2017a), *An Investigation of Pulsar Searching Techniques with the Fast Folding Algorithm*, **468** 1994, arXiv: 1703.05581 [astro-ph.IM] (cit. on pp. 30, 31).

Cameron, A. et al. (2017b), *An Investigation of Pulsar Searching Techniques with the Fast Folding Algorithm*, Monthly Notices of the Royal Astronomical Society **468** 1994 (cit. on p. 87).

Cameron, A. D. (2018), *Innovative Pulsar Searching Techniques*, Thesis: Universitäts- und Landesbibliothek Bonn, (visited on 12/05/2022) (cit. on p. 26).

Camilo, F. et al. (2000a), *Observations of 20 Millisecond Pulsars in 47 Tucanae at 20 Centimeters*, The Astrophysical Journal **535** 975, ISSN: 0004-637X, (visited on 25/01/2023) (cit. on p. 65).

Camilo, F. et al. (2007), *1E 1547.0-5408: A Radio-emitting Magnetar with a Rotation Period of 2 Seconds*, The Astrophysical Journal **666** L93, ISSN: 0004-637X, (visited on 25/09/2022) (cit. on p. 7).

Camilo, F. et al. (2000b), "The Parkes Multibeam Pulsar Survey", *International Astronomical Union Colloquium*, vol. 177, Cambridge University Press 3 (cit. on p. 48).

Camilo, F. et al. (2006), *Transient Pulsed Radio Emission from a Magnetar*, Nature **442** 892, ISSN: 0028-836, (visited on 25/09/2022) (cit. on p. 7).

Champion, D. et al. (2020), *High-Cadence Observations and Variable Spin Behaviour of Magnetar Swift J1818.0-1607 after Its Outburst*, **498** 6044, arXiv: 2009.03568 [astro-ph.HE] (cit. on p. 7).

Chandrasekhar, S. (1931), *The Maximum Mass of Ideal White Dwarfs*, The Astrophysical Journal **74** 81 (cit. on p. 2).

Chen, K. et al. (1993), *Pulsar Death Lines and Death Valley*, The Astrophysical Journal **402** 264 (cit. on pp. 4, 6, 7).

Chen, S. et al. (2018), *Distances to the Globular Clusters 47 Tucanae and NGC 362 Using Gaia DR2 Parallaxes*, The Astrophysical Journal **867** 132, ISSN: 0004-637X, (visited on 25/01/2023) (cit. on p. 65).

Clifton, T. et al. (1992), *A High-Frequency Survey of the Galactic Plane for Young and Distant Pulsars*, Monthly Notices of the Royal Astronomical Society **254** 177 (cit. on p. 48).

Cooley, J. W. et al. (1965), *An Algorithm for the Machine Calculation of Complex Fourier Series*, Mathematics of Computation **19** 297, ISSN: 00255718, 10886842, JSTOR: 2003354 (cit. on pp. 29, 30).

Cordes, J. M. et al. (1997a), *Finding Radio Pulsars in and beyond the Galactic Center*, **475** 557, eprint: astro-ph/9608028 (cit. on p. 56).

– (2002), *NE2001.I. A New Model for the Galactic Distribution of Free Electrons and Its Fluctuations*, arXiv e-prints astro, (visited on 28/10/2022) (cit. on pp. 19, 58).

Cordes, J. M. et al. (2022), *Redshift Estimation and Constraints on Intergalactic and Interstellar Media from Dispersion and Scattering of Fast Radio Bursts*, The Astrophysical Journal **931** 88, ISSN: 0004-637X, (visited on 12/06/2023) (cit. on p. 14).

Cordes, J. M. et al. (1997b), *Finding Radio Pulsars in and beyond the Galactic Center*, **475** 557, arXiv: astro-ph/9608028 (cit. on p. 15).

– (2003), *NE2001. II. Using Radio Propagation Data to Construct a Model for the Galactic Distribution of Free Electrons*, arXiv preprint astro-ph/0301598, arXiv: astro-ph/0301598 (cit. on pp. 12, 52, 61, 87).

Crawford, F. et al. (2009), *UPPER LIMITS ON PULSED RADIO EMISSION FROM THE 6.85 s X-RAY PULSAR XTE J0103–728 IN THE SMALL MAGELLANIC CLOUD*, ApJ **696** 574, ISSN: 0004-637X, (visited on 24/06/2022) (cit. on p. 31).

Bibliography

Cromartie, H. T. et al. (2020), *Relativistic Shapiro Delay Measurements of an Extremely Massive Millisecond Pulsar*, Nature Astronomy **4** 72, ISSN: 2397-3366, (visited on 02/07/2022) (cit. on pp. 71, 89).

Cromartie, H. T. et al. (2019), *A Larger-than-2-Solar-Mass Pulsar in NANOGrav: Leveraging Shapiro Delay to Constrain the Neutron Star Equation of State*, **2019** T09.002, (visited on 19/05/2022) (cit. on p. 18).

Cruces, M. (2021), *The Transient Radio Sky: Pulsars and Fast Radio Bursts*, Thesis: Universitäts- und Landesbibliothek Bonn, (visited on 12/05/2022) (cit. on pp. 11, 27).

Damour, T. et al. (1985), *General Relativistic Celestial Mechanics of Binary Systems. I. The Post-Newtonian Motion.*, Ann. Inst. Henri Poincaré Phys. Théor **43** 107, (visited on 15/05/2023) (cit. on p. 46).

– (1986), *General Relativistic Celestial Mechanics of Binary Systems. II. The Post-Newtonian Timing Formula.*, Ann. Inst. Henri Poincaré Phys. Théor **44** 263, (visited on 15/05/2023) (cit. on p. 46).

Damour, T. et al. (1991a), *On the Orbital Period Change of the Binary Pulsar PSR 1913+16*, The Astrophysical Journal **366** 501, ISSN: 0004-637X, (visited on 22/04/2023) (cit. on pp. 79, 80).

– (1991b), *On the Orbital Period Change of the Binary Pulsar PSR 1913+16*, The Astrophysical Journal **366** 501, ISSN: 0004-637X, (visited on 09/05/2022) (cit. on p. 79).

Davies, J. G. et al. (1970), *Five New Pulsars*, Nature **227** 1123 (cit. on p. 48).

Deneva, J. S. et al. (2009a), *Discovery of Three Pulsars from a Galactic Center Pulsar Population*, **702** L177, arXiv: 0908.1331 [astro-ph.SR] (cit. on p. 52).

– (2009b), *Discovery of Three Pulsars from a Galactic Center Pulsar Population*, **702** L177, arXiv: 0908.1331 [astro-ph.SR] (cit. on p. 56).

Deneva, J. S. (2010), *Elusive Neutron Star Populations: Galactic Center and Intermittent Pulsars*, PhD thesis: Cornell University, United States (cit. on pp. 50, 88).

Desvignes, G. et al. (2018), *Large Magneto-Ionic Variations toward the Galactic Center Magnetar, PSR J1745-2900*, **852**, L12 L12, arXiv: 1711.10323 [astro-ph.HE] (cit. on p. 55).

Desvignes, G. et al. (2019), *Radio Emission from a Pulsar's Magnetic Pole Revealed by General Relativity*, Science **365** 1013, ISSN: 0036-8075, (visited on 18/02/2023) (cit. on p. 61).

Dexter, J. et al. (2017), *A Transient, Flat Spectrum Radio Pulsar near the Galactic Centre*, Monthly Notices of the Royal Astronomical Society **468** 1486, ISSN: 0035-8711, (visited on 10/02/2023) (cit. on pp. 88, 90).

Dexter, J. et al. (2014), *The Peculiar Pulsar Population of the Central Parsec*, ApJ **783** L7, ISSN: 2041-8205, 2041-8213, arXiv: 1310.7022 [astro-ph], (visited on 14/02/2023) (cit. on p. 90).

Dowd, A. et al. (2000), *WAPP — Wideband Arecibo Pulsar Processor*, **202** 275, (visited on 17/12/2022) (cit. on p. 72).

Duncan, R. C. et al. (1992), *Formation of Very Strongly Magnetized Neutron Stars-Implications for Gamma-Ray Bursts*, The Astrophysical Journal **392** L9 (cit. on p. 7).

Eatough, R. P. et al. (2009), *An Interference Removal Technique for Radio Pulsar Searches*, Monthly Notices of the Royal Astronomical Society **395** 410, ISSN: 0035-8711, (visited on 31/10/2022) (cit. on p. 40).

Eatough, R. P. et al. (2013a), *A Coherent Acceleration Search of the Parkes Multibeam Pulsar Survey – Techniques and the Discovery and Timing of 16 Pulsars*, Monthly Notices of the Royal Astronomical Society **431** 292, ISSN: 0035-8711, (visited on 05/01/2023) (cit. on p. 39).

Eatough, R. P. et al. (2013b), *A Strong Magnetic Field around the Supermassive Black Hole at the Centre of the Galaxy*, **501** 391, arXiv: 1308.3147 [astro-ph.GA] (cit. on pp. 52, 61, 88).

– (2013c), *A Strong Magnetic Field around the Supermassive Black Hole at the Centre of the Galaxy*, **501** 391, arXiv: 1308.3147 [astro-ph.GA] (cit. on p. 55).

Eatough, R. P. et al. (2021), *Multi-Epoch Searches for Relativistic Binary Pulsars and Fast Transients in the Galactic Centre*, **507** 5053, arXiv: 2108.05241 [astro-ph.HE] (cit. on pp. 50, 52, 88).

Eatough, R. et al. (2013d), *A Strong Magnetic Field around the Supermassive Black Hole at the Centre of the Galaxy*, Nature **501** 391 (cit. on p. 15).

Edwards, R. T. et al. (2006), *TEMPO2, a New Pulsar Timing Package - II. The Timing Model and Precision Estimates*, Monthly Notices of the Royal Astronomical Society **372** 1549, ISSN: 0035-8711, (visited on 04/09/2022) (cit. on p. 42).

Eggleton, P. P. (1983), *Aproximations to the Radii of Roche Lobes.*, The Astrophysical Journal **268** 368, ISSN: 0004-637X, (visited on 14/07/2023) (cit. on p. 83).

Espenschied, L. (1959), *Discussion of "A History of Some Foundations of Modern Radio-Electronic Technology"*, Proc. IRE **47** 1253, ISSN: 0096-8390, (visited on 22/06/2022) (cit. on p. 25).

Event Horizon Telescope Collaboration et al. (2019a), *First M87 Event Horizon Telescope Results. I. The Shadow of the Supermassive Black Hole*, **875**, L1 L1 (cit. on p. 24).

Event Horizon Telescope Collaboration et al. (2019b), *First M87 Event Horizon Telescope Results. IV. Imaging the Central Supermassive Black Hole*, **875**, L4 L4 (cit. on p. 55).

Event Horizon Telescope Collaboration et al. (2022a), *First Sagittarius A* Event Horizon Telescope Results. I. The Shadow of the Supermassive Black Hole in the Center of the Milky Way*, **930**, L12 L12 (cit. on p. 24).

Event Horizon Telescope Collaboration et al. (2022b), *First Sagittarius A* Event Horizon Telescope Results. VI. Testing the Black Hole Metric*, **930**, L17 L17 (cit. on p. 55).

Ferrario, L. et al. (2020), *Magnetic Fields in Isolated and Interacting White Dwarfs*, Advances in Space Research **66** 1025, ISSN: 02731177, arXiv: 2001.10147 [astro-ph], (visited on 26/01/2023) (cit. on pp. 63, 89).

Ferrière, K. et al. (2021), *The Correct Sense of Faraday Rotation*, Monthly Notices of the Royal Astronomical Society **507** 4968, ISSN: 0035-8711, (visited on 18/05/2022) (cit. on p. 15).

Figer, D. F. (2003), *Massive Stars and The Creation of Our Galactic Center*, Astronomische Nachrichten Supplement **324** 255, (visited on 08/09/2022) (cit. on p. 50).

Fonseca, E. et al. (2021), *Refined Mass and Geometric Measurements of the High-mass PSR J0740+6620*, The Astrophysical Journal **915** L12, ISSN: 0004-637X, (visited on 22/04/2023) (cit. on p. 71).

Foreman-Mackey, D. et al. (2013), *Emcee: The MCMC Hammer*, Publications of the Astronomical Society of the Pacific **125** 306, ISSN: 0004-6280, (visited on 21/05/2023) (cit. on p. 83).

Freire, P. C. et al. (2001), *Determination of the Orbital Parameters of Binary Pulsars*, Monthly Notices of the Royal Astronomical Society **322** 885, ISSN: 0035-8711, (visited on 15/05/2023) (cit. on p. 36).

Freire, P. C. et al. (2003), *Further Results from the Timing of the Millisecond Pulsars in 47 Tucanae*, Monthly Notices of the Royal Astronomical Society **340** 1359, ISSN: 0035-8711, (visited on 25/01/2023) (cit. on p. 66).

Freire, P. C. C. et al. (2000), *Pulsars in 47 Tucanae*, PhD thesis: ProQuest Dissertations & Theses, ISBN: 9781392022870 (cit. on p. 67).

Gold, T. (1968), *Rotating Neutron Stars as the Origin of the Pulsating Radio Sources*, Nature **218** 731 EP (cit. on p. 1).

Goldreich, P. et al. (1969), *Pulsar Electrodynamics*, The Astrophysical Journal **157** 869, ISSN: 0004-637X, (visited on 22/10/2022) (cit. on pp. 3, 4).

Graham-Smith, F. (2003), *The Radio Emission from Pulsars*, Rep. Prog. Phys. **66** 173, ISSN: 0034-4885, (visited on 22/10/2022) (cit. on p. 4).

GRAVITY Collaboration et al. (2021), *Improved GRAVITY Astrometric Accuracy from Modeling Optical Aberrations*, Astronomy and Astrophysics **647** A59, ISSN: 0004-6361, (visited on 17/05/2023) (cit. on p. 80).

Grindlay, J. E. et al. (1988), *Birth of Millisecond Pulsars in Globular Clusters*, Nature **336** 48, ISSN: 1476-4687, (visited on 25/01/2023) (cit. on pp. 64, 89).

Guo, Y. J. et al. (2021), *PSR J2222-0137. I. Improved Physical Parameters for the System*, Astronomy and Astrophysics **654** A16, ISSN: 0004-6361, (visited on 22/04/2023) (cit. on p. 73).

Hamil, O. et al. (2015), *Braking Index of Isolated Pulsars*, Phys. Rev. **D91** 063007 (cit. on p. 5).

Han, J. L. et al. (2006), *Pulsar Rotation Measures and the Large-Scale Structure of the Galactic Magnetic Field*, The Astrophysical Journal **642** 868, ISSN: 0004-637X, (visited on 28/10/2022) (cit. on p. 19).

Hankins, T. (1971), *Microsecond Intensity Variations in the Radio Emissions from CP 0950*, The Astrophysical Journal **169** 487 (cit. on p. 35).

Hankins, T. et al. (1975), *Methods in Computational Physics Volume 14—Radio Astronomy*, Aca-demic Press, New York 55 (cit. on p. 35).

Heger, A. et al. (2003), *How Massive Single Stars End Their Life*, The Astrophysical Journal **591** 288, ISSN: 0004-637X, (visited on 21/10/2022) (cit. on p. 2).

Hessels, J. W. T. et al. (2006), *A Radio Pulsar Spinning at 716 Hz*, Science **311** 1901 (cit. on pp. 1, 17).

Hewish, A. et al. (1968), *Observation of a Rapidly Pulsating Radio Source*, Nature **217** 709 EP (cit. on pp. 1, 48).

Hobbs, G. B. et al. (2006), *TEMPO2, a New Pulsar-Timing Package - I. An Overview*, Monthly Notices of the Royal Astronomical Society **369** 655, ISSN: 0035-8711, (visited on 04/09/2022) (cit. on p. 42).

Hobbs, G. et al. (2010), *The International Pulsar Timing Array Project: Using Pulsars as a Gravitational Wave Detector*, Class. Quantum Grav. **27** 084013, ISSN: 0264-9381, (visited on 25/09/2022) (cit. on p. 18).

Huang, Y. D. (et al. (2016), *The Atacama Large Millimeter/Sub-Millimeter Array Band-1 Receiver*, **9911** 99111V, (visited on 10/02/2023) (cit. on p. 90).

Hurley-Walker, N. et al. (2022), *A Radio Transient with Unusually Slow Periodic Emission*, \nat **601** 526 (cit. on pp. 1, 91).

Janka, H. .-.-T. et al. (2007), *Theory of Core-Collapse Supernovae*, Physics Reports **442** 38, ISSN: 0370-1573, (visited on 21/10/2022) (cit. on p. 2).

Jankowski, F. et al. (2018), *Spectral Properties of 441 Radio Pulsars*, Monthly Notices of the Royal Astronomical Society **473** 4436, ISSN: 0035-8711, (visited on 03/03/2023) (cit. on p. 89).

Jaroenjittichai, P. et al. (2022), *Sciences with Thai National Radio Telescope*, arXiv: `2210.04926 [astro-ph]`, (visited on 14/07/2023) (cit. on p. 91).

Jeans, J. H. (1924), *Cosmogonic Problems Associated with a Secular Decrease of Mass*, Monthly Notices of the Royal Astronomical Society **85** 2, ISSN: 0035-8711, (visited on 06/01/2023) (cit. on p. 79).

– (1925), *The Effect of Varying Mass on a Binary System*, Monthly Notices of the Royal Astronomical Society **85** 912, ISSN: 0035-8711, (visited on 06/01/2023) (cit. on p. 79).

Jenet, F. et al. (2009), *The North American Nanohertz Observatory for Gravitational Waves*, (visited on 25/09/2022) (cit. on p. 18).

Johnston, S. et al. (2006a), *Discovery of Two Pulsars towards the Galactic Centre*, **373** L6, eprint: `astro-ph/0606465` (cit. on p. 56).

Johnston, S. et al. (1992a), *A High-Frequency Survey of the Southern Galactic Plane for Pulsars*, Monthly Notices of the Royal Astronomical Society **255** 401 (cit. on p. 48).

Johnston, S. et al. (1992b), *PSR 1259-63: A Binary Radio Pulsar with a Be Star Companion*, The Astrophysical Journal **387** L37, ISSN: 0004-637X, (visited on 25/09/2022) (cit. on p. 1).

Johnston, S. et al. (2006b), *Discovery of Two Pulsars towards the Galactic Centre*, **373** L6, arXiv: `astro-ph/0606465` (cit. on pp. 50, 52, 88).

JPL Solar System Dynamics (2022), https://ssd.jpl.nasa.gov/, (visited on 03/09/2022) (cit. on p. 46).

Karuppusamy, R. et al. (2020), *Detection of Pulsed Radio Emission from New Magnetar Swift J1818.0-1607*, The Astronomer's Telegram **13553** 1, (visited on 25/09/2022) (cit. on p. 7).

Keane, E. F. et al. (2008), *On the Birthrates of Galactic Neutron Stars*, Monthly Notices of the Royal Astronomical Society **391** 2009, ISSN: 0035-8711, (visited on 16/05/2022) (cit. on p. 15).

Keith, M. J. et al. (2010), *The High Time Resolution Universe Pulsar Survey - I. System Configuration and Initial Discoveries*, **409** 619, arXiv: `1006.5744 [astro-ph.HE]` (cit. on p. 52).

Kennea, J. et al. (2013), *SWIFT DISCOVERY OF A NEW SOFT GAMMA REPEATER, SGR J1745–29, NEAR SAGITTARIUS A*, The Astrophysical Journal Letters **770** L24 (cit. on p. 15).

Klein, B. et al. (2004), "Pulsar Searches at Effelsberg", *Young Neutron Stars and Their Environments*, ed. by F. Camilo et al., vol. 218, "" 133 (cit. on pp. 50, 52).

Kondratiev, V. I. et al. (2009a), *New Limits on Radio Emission from X-ray Dim Isolated Neutron Stars*, **702** 692, arXiv: `0907.0054 [astro-ph.GA]` (cit. on p. 31).

Kondratiev, V. et al. (2009b), *New Limits on Radio Emission from X-Ray Dim Isolated Neutron Stars*, The Astrophysical Journal **702** 692 (cit. on pp. 8, 29).

Kramer, M. et al. (1994), *Geometrical Analysis of Average Pulsar Profiles Using Multi-Component Gaussian FITS at Several Frequencies. I. Method and Analysis.*, Astronomy and Astrophysics Suppl., Vol. 107, p.515-526 (1994) **107** 515, ISSN: 0365-0138, (visited on 03/09/2022) (cit. on p. 43).

Kramer, M. et al. (2000), *The Effelsberg Search for Pulsars in the Galactic Centre*, **202** 37, (visited on 07/07/2023) (cit. on pp. 50, 52).

Kramer, M. et al. (2004), *Strong-Field Tests of Gravity Using Pulsars and Black Holes*, **48** 993, arXiv: `astro-ph/0409379` (cit. on pp. 16, 51).

Kramer, M. et al. (2006a), *A Periodically Active Pulsar Giving Insight into Magnetospheric Physics*, Science **312** 549, ISSN: 1095-9203 (cit. on p. 91).

Kramer, M. et al. (2006b), *Tests of General Relativity from Timing the Double Pulsar*, Science **314** 97, arXiv: `astro-ph/0609417` (cit. on p. 16).

Kramer, M. et al. (2021), *Strong-Field Gravity Tests with the Double Pulsar*, Phys. Rev. X **11** 041050, ISSN: 2160-3308, arXiv: `2112.06795 [astro-ph, physics:gr-qc]`, (visited on 16/05/2022) (cit. on p. 16).

Kramer, M. (1998), *Determination of the Geometry of the PSR B1913+16 System by Geodetic Precession*, The Astrophysical Journal **509** 856, ISSN: 0004-637X, (visited on 18/02/2023) (cit. on p. 61).

Kramer, M. et al. (2013), *The European Pulsar Timing Array and the Large European Array for Pulsars*, Classical and Quantum Gravity **30** 224009, ISSN: 0264-9381, (visited on 25/09/2022) (cit. on p. 18).

Lange, C. et al. (2001), *Precision Timing Measurements of PSR J1012+5307*, Monthly Notices of the Royal Astronomical Society **326** 274, ISSN: 00358711, 13652966, (visited on 26/05/2022) (cit. on p. 73).

Large, M. I. et al. (1968), *Pulsar Search at the Molonglo Radio Observatory*, Nature **220** 753 (cit. on p. 48).

Lattimer, J. M. (2012), *The Nuclear Equation of State and Neutron Star Masses*, Annual Review of Nuclear and Particle Science **62** 485, ISSN: 0163-8998, (visited on 16/05/2022) (cit. on pp. 17, 71).

Lazaridis, K. et al. (2009), *Generic Tests of the Existence of the Gravitational Dipole Radiation and the Variation of the Gravitational Constant*, Monthly Notices of the Royal Astronomical Society **400** 805, ISSN: 0035-8711, (visited on 22/04/2023) (cit. on pp. 79, 80).

Lazarus, P. et al. (2016), *Prospects for High-Precision Pulsar Timing with the New Effelsberg PSRIX Backend*, Mon. Not. R. Astron. Soc. **458** 868, ISSN: 0035-8711, 1365-2966, arXiv: `1601.06194 [astro-ph]`, (visited on 06/01/2023) (cit. on p. 72).

Lazarus, P. et al. (2015), *Arecibo Pulsar Survey Using ALFA. IV. Mock Spectrometer Data Analysis, Survey Sensitivity, and the Discovery of 40 Pulsars*, The Astrophysical Journal **812** 81 (cit. on pp. 31, 59, 87).

Levin, L. et al. (2010), *A Radio-loud Magnetar in X-ray Quiescence*, The Astrophysical Journal **721** L33, ISSN: 0004-637X, (visited on 25/09/2022) (cit. on p. 7).

Link, B. et al. (1992), *Pulsar Glitches as Probes of Neutron Star Interiors*, Nature **359** 616 (cit. on p. 6).

Liu, K. et al. (2012a), *Profile-Shape Stability and Phase-Jitter Analyses of Millisecond Pulsars*, Monthly Notices of the Royal Astronomical Society **420** 361, ISSN: 0035-8711, (visited on 05/01/2023) (cit. on p. 42).

Liu, K. et al. (2012b), *Prospects for Probing the Spacetime of Sgr A* with Pulsars*, **747**, 1 1, arXiv: `1112.2151 [astro-ph.HE]` (cit. on p. 16).

– (2012c), *Prospects for Probing the Spacetime of Sgr A* with Pulsars*, The Astrophysical Journal **747** 1, ISSN: 0004-637X, (visited on 18/02/2023) (cit. on p. 61).

Liu, K. et al. (2014), *Pulsar–Black Hole Binaries: Prospects for New Gravity Tests with Future Radio Telescopes*, Monthly Notices of the Royal Astronomical Society **445** 3115, ISSN: 0035-8711, (visited on 18/05/2022) (cit. on p. 16).

Liu, K. et al. (2017), *Few and Far Between*, Nature Astronomy **1** 812 (cit. on pp. 16, 51).

Liu, K. et al. (2021a), *An 86 GHz Search for Pulsars in the Galactic Center with the Atacama Large Millimeter / Submillimeter Array*, **914**, 30 30, arXiv: `2104.08986 [astro-ph.HE]` (cit. on pp. 50, 52, 88).

– (2021b), *An 86 GHz Search for Pulsars in the Galactic Center with the Atacama Large Millimeter / Submillimeter Array*, **914**, 30 30, arXiv: `2104.08986 [astro-ph.HE]` (cit. on p. 59).

Löhmer, O. et al. (2004), "The Frequency Evolution of Interstellar Pulse Broadening from Radio Pulsars", *How Does the Galaxy Work?*, ed. by E. J. Alfaro et al., Astrophysics and Space Science Library, Dordrecht: Springer Netherlands 327, ISBN: 978-1-4020-2620-1 (cit. on p. 13).

Lorimer, D. R. (2011), *SIGPROC: Pulsar Signal Processing Programs*, Astrophysics Source Code Library ascl:1107.016, (visited on 22/02/2023) (cit. on p. 41).

Lorimer, D. R. (2008), *Binary and Millisecond Pulsars*, Living Rev. Relativ. **11** 8, ISSN: 1433-8351, (visited on 01/06/2022) (cit. on p. 8).

Lorimer, D. R. et al. (2012), *Handbook of Pulsar Astronomy*, Handbook of Pulsar Astronomy, by DR Lorimer, M. Kramer, Cambridge, UK: Cambridge University Press, 2012 (cit. on pp. 5, 11, 12, 22, 32, 34, 38).

Lovelace, R. V. E. et al. (1968), *Pulsar NP 0532 Near Crab Nebula*, International Astronomical Union Circular **2113** 1, ISSN: 0081-0304, (visited on 06/07/2023) (cit. on p. 1).

Lower, M. E. et al. (2020), *Spectropolarimetric Properties of Swift J1818.0-1607: A 1.4 s Radio Magnetar*, The Astrophysical Journal **896** L37, ISSN: 0004-637X, (visited on 25/09/2022) (cit. on p. 7).

Lower, M. E. et al. (2023), *The 2022 High-energy Outburst and Radio Disappearing Act of the Magnetar 1E 1547.0-5408*, The Astrophysical Journal **945** 153, ISSN: 0004-637X, (visited on 11/07/2023) (cit. on p. 7).

Luri, X. et al. (2018), *Gaia Data Release 2. Using Gaia Parallaxes*, Astronomy and Astrophysics **616** A9, ISSN: 0004-6361, (visited on 26/01/2023) (cit. on p. 63).

Lynch, R. S. et al. (2013), *The Green Bank Telescope 350 MHz Drift-scan Survey II: Data Analysis and the Timing of 10 New Pulsars, Including a Relativistic Binary*, The Astrophysical Journal **763** 81, ISSN: 0004-637X, (visited on 09/05/2022) (cit. on pp. 71, 89).

Lyne, A. G. et al. (2004), *A Double-Pulsar System: A Rare Laboratory for Relativistic Gravity and Plasma Physics*, Science **303** 1153, ISSN: 0036-8075, (visited on 12/05/2023) (cit. on p. 1).

Macquart, J. .-.-P. et al. (2010), *A High-frequency Search for Pulsars within the Central Parsec of Sgr A**, The Astrophysical Journal **715** 939, ISSN: 0004-637X, (visited on 07/07/2023) (cit. on pp. 50, 90).

Manchester, R. N. et al. (1990a), *A 5.75-Millisecond Pulsar in the Globular Cluster 47 Tucanae*, Nature **345** 598, ISSN: 1476-4687, (visited on 18/05/2022) (cit. on p. 12).

Manchester, R. N. et al. (1990b), *A 5.75-Millisecond Pulsar in the Globular Cluster 47 Tucanae*, Nature **345** 598, ISSN: 0028-0836, (visited on 25/01/2023) (cit. on p. 65).

Manchester, R. N. et al. (1991), *Discovery of Ten Millisecond Pulsars in the Globular Cluster 47 Tucanae*, Nature **352** 219, ISSN: 0028-0836, 1476-4687, (visited on 18/05/2022) (cit. on pp. 12, 65).

Manchester, R. N. et al. (2005), *The Australia Telescope National Facility Pulsar Catalogue*, The Astronomical Journal **129** 1993 (cit. on pp. 1, 4, 6, 7, 12, 48, 58, 60, 64, 87).

Manchester, R. et al. (2001), *The Parkes Multibeam Pulsar Survey: I. Observing and Data Analysis Systems, Discovery and Timing of 100 Pulsars*, arXiv preprint astro-ph/0106522, arXiv: astro-ph/0106522 (cit. on p. 48).

Marsh, T. R. et al. (2016), *A Radio Pulsing White Dwarf Binary Star*, Nature **537** 374, ISSN: 0028-0836, 1476-4687, arXiv: 1607.08265 [astro-ph], (visited on 19/05/2022) (cit. on pp. 63, 64).

Martinez, J. G. et al. (2015), *PULSAR J0453+1559: A DOUBLE NEUTRON STAR SYSTEM WITH A LARGE MASS ASYMMETRY*, ApJ **812** 143, ISSN: 0004-637X, (visited on 26/10/2022) (cit. on p. 18).

McLaughlin, M. A. et al. (2006), *Transient Radio Bursts from Rotating Neutron Stars*, Nature **439** 817, ISSN: 0028-0836, (visited on 28/10/2022) (cit. on p. 7).

McMahon, P. L. (2011), *Adventures in Radio Astronomy Instrumentation and Signal Processing*, arXiv: 1109.0416 [astro-ph], (visited on 05/01/2023) (cit. on p. 49).

McNamara, B. J. et al. (2004), *The Dynamical Distance to M15: Estimates of the Cluster's Age and Mass and of the Absolute Magnitude of Its RR Lyrae Stars*, The Astrophysical Journal **602** 264, ISSN: 0004-637X, (visited on 25/01/2023) (cit. on p. 69).

Miller, M. C. et al. (2021), *The Radius of PSR J0740+6620 from NICER and XMM-Newton Data*, The Astrophysical Journal **918** L28, ISSN: 0004-637X, (visited on 09/06/2022) (cit. on p. 18).

Morello, V. et al. (2019), *The High Time Resolution Universe Survey XIV: Discovery of 23 Pulsars through GPU-accelerated Reprocessing*, Monthly Notices of the Royal Astronomical Society **483** 3673, ISSN: 0035-8711, 1365-2966, arXiv: 1811.04929 [astro-ph], (visited on 06/01/2023) (cit. on p. 72).

Morello, V. et al. (2020a), *Optimal Periodicity Searching: Revisiting the Fast Folding Algorithm for Large-Scale Pulsar Surveys*, **497** 4654, arXiv: 2004.03701 [astro-ph.IM] (cit. on pp. 32, 35, 36, 87, 90, 91).

– (2020b), *Optimal Periodicity Searching: Revisiting the Fast Folding Algorithm for Large-Scale Pulsar Surveys*, **497** 4654, arXiv: 2004.03701 [astro-ph.IM] (cit. on p. 59).

Morello, V. et al. (2020c), *The SUrvey for Pulsars and Extragalactic Radio Bursts - IV. Discovery and Polarimetry of a 12.1-s Radio Pulsar*, **493** 1165, arXiv: 1910.04124 [astro-ph.HE] (cit. on p. 33).

Muno, M. P. et al. (2004), *Diffuse X-Ray Emission in a Deep Chandra Image of the Galactic Center*, ApJ **613** 326, ISSN: 0004-637X, (visited on 17/02/2023) (cit. on p. 61).

Ng, C. et al. (2015a), *The High Time Resolution Universe Pulsar Survey - XII. Galactic Plane Acceleration Search and the Discovery of 60 Pulsars*, **450** 2922, arXiv: 1504.08000 [astro-ph.HE] (cit. on p. 52).

Ng, C. et al. (2015b), *The High Time Resolution Universe Pulsar Survey–XII. Galactic Plane Acceleration Search and the Discovery of 60 Pulsars*, Monthly Notices of the Royal Astronomical Society **450** 2922 (cit. on p. 39).

Ng, C. W. Y. (2014), *Pulsar Searching and Timing with the Parkes Telescope*, Thesis: Universitäts- und Landesbibliothek Bonn, (visited on 12/05/2022) (cit. on p. 64).

Nice, D. J. et al. (1995), *PSR J2019+2425 and PSR J2322+2057 and the Proper Motions of Millisecond Pulsars*, The Astrophysical Journal **441** 429, ISSN: 0004-637X, (visited on 22/04/2023) (cit. on pp. 79, 80).

Noutsos, A. et al. (2008), *New Pulsar Rotation Measures and the Galactic Magnetic Field*, Monthly Notices of the Royal Astronomical Society **386** 1881, ISSN: 0035-8711, (visited on 28/10/2022) (cit. on p. 19).

Olausen, S. A. et al. (2014), *The McGill Magnetar Catalog*, Astrophys. J. Suppl. **212** 6 (cit. on p. 7).

Oppenheimer, J. R. et al. (1939), *On Massive Neutron Cores*, Physical Review **55** 374, ISSN: 1536-6065, (visited on 21/10/2022) (cit. on p. 2).

Ostriker, J. P. et al. (1968), *Rapidly Rotating Stars.IV. Magnetic White Dwarfs*, The Astrophysical Journal **153** 797, ISSN: 0004-637X, (visited on 28/08/2022) (cit. on p. 1).

Oswald, L. S. et al. (2021), *The Thousand-Pulsar-Array Programme on MeerKAT - V. Scattering Analysis of Single-Component Pulsars*, Monthly Notices of the Royal Astronomical Society **504** 1115, ISSN: 0035-8711, (visited on 12/05/2023) (cit. on p. 12).

Özel, F. et al. (2016), *Masses, Radii, and the Equation of State of Neutron Stars*, Annual Review of Astronomy and Astrophysics **54** 401, ISSN: 0066-4146, (visited on 07/05/2022) (cit. on pp. 4, 71, 79, 89).

Pan, Z. et al. (2016), *Discovery of Two New Pulsars in 47 Tucanae (NGC 104)*, Monthly Notices of the Royal Astronomical Society **459** L26, ISSN: 0035-8711, (visited on 25/01/2023) (cit. on p. 65).

Parent, E. et al. (2018), *The Implementation of a Fast-Folding Pipeline for Long-Period Pulsar Searching in the PALFA Survey*, arXiv preprint arXiv:1805.08247, arXiv: `1805.08247` (cit. on p. 32).

Parthasarathy, A. et al. (2020), *Timing of Young Radio Pulsars - II. Braking Indices and Their Interpretation*, Monthly Notices of the Royal Astronomical Society **494** 2012, ISSN: 0035-8711, (visited on 06/07/2023) (cit. on p. 5).

Penrose, R. (1979), "Singularities and Time-Asymmetry.", *General Relativity: An Einstein Centenary Survey*, ed. by S. W. Hawking et al. 581 (cit. on p. 16).

Porayko, N. K. (2020), *Probing the Interstellar Medium and Dark Matter with Pulsars*, Thesis: Universitäts- und Landesbibliothek Bonn, (visited on 12/05/2022) (cit. on pp. 3, 45).

Prša, A. et al. (2016), *Nominal Values for Selected Solar and Planetary Quantities: IAU 2015 Resolution B3*, The Astronomical Journal **152** 41, ISSN: 0004-6256, (visited on 17/05/2023) (cit. on pp. 47, 79).

Psaltis, D. et al. (2016a), *A Quantitative Test of the No-Hair Theorem with Sgr A* Using Stars, Pulsars, and the Event Horizon Telescope*, **818**, 121 121, arXiv: `1510.00394 [astro-ph.HE]` (cit. on p. 55).

Psaltis, D. et al. (2016b), *A Quantitative Test of the No-hair Theorem with Sgr A* Using Stars, Pulsars, and the Event Horizon Telescope*, The Astrophysical Journal **818** 121, ISSN: 0004-637X, (visited on 16/05/2022) (cit. on pp. 16, 17).

Psaltis, D. et al. (2020), *Gravitational Test beyond the First Post-Newtonian Order with the Shadow of the M87 Black Hole*, **125**, 141104 141104, arXiv: `2010.01055 [gr-qc]` (cit. on p. 55).

Ransom, S. M. et al. (2003), *A New Search Technique for Short Orbital Period Binary Pulsars*, The Astrophysical Journal **589** 911, ISSN: 0004-637X, (visited on 31/10/2022) (cit. on pp. 39, 40).

Rathnasree, N. et al. (1995), *On the Approach to Stability of Pulsar Average Profiles*, The Astrophysical Journal **452** 814, ISSN: 0004-637X, (visited on 03/09/2022) (cit. on p. 42).

Reding, J. S. et al. (2020), *An Isolated White Dwarf with 317 s Rotation and Magnetic Emission*, The Astrophysical Journal **894** 19 (cit. on p. 63).

Ridolfi, A. et al. (2021), *Eight New Millisecond Pulsars from the First MeerKAT Globular Cluster Census*, Monthly Notices of the Royal Astronomical Society **504** 1407, ISSN: 0035-8711, (visited on 25/01/2023) (cit. on p. 65).

Riley, T. E. et al. (2019a), *A NICER View of PSR J0030+0451: Millisecond Pulsar Parameter Estimation*, The Astrophysical Journal **887** L21, ISSN: 0004-637X, (visited on 09/06/2022) (cit. on p. 18).

– (2019b), *A NICER View of PSR J0030+0451: Millisecond Pulsar Parameter Estimation*, The Astrophysical Journal **887** L21, ISSN: 0004-637X, (visited on 09/06/2022) (cit. on p. 18).

Robinson, C. et al. (1995), *Millisecond Pulsars in the Globular Cluster 47 Tucanae*, Monthly Notices of the Royal Astronomical Society **274** 547, ISSN: 0035-8711, (visited on 25/01/2023) (cit. on p. 65).

Schnitzeler, D. H. F. M. et al. (2016), *Radio Polarimetry of Galactic Centre Pulsars*, **459** 3005, arXiv: `1604.05322 [astro-ph.GA]` (cit. on p. 55).

Shaifullah, G. et al. (2016), *21 Year Timing of the Black-Widow Pulsar J2051-0827*, Monthly Notices of the Royal Astronomical Society **462** 1029, ISSN: 0035-8711, (visited on 10/05/2022) (cit. on p. 83).

Shannon, C. (1949), *Communication in the Presence of Noise*, Proceedings of the IRE **37** 10, ISSN: 2162-6634 (cit. on p. 29).

Shannon, R. M. et al. (2013), *Radio Properties of the Magnetar near Sagittarius a* from Observations with the Australia Telescope Compact Array.*, Monthly Notices of the Royal Astronomical Society **435** L29, ISSN: 0035-8711, (visited on 25/09/2022) (cit. on p. 7).

Shapiro, I. I. (1964), *Fourth Test of General Relativity*, Physical Review Letters **13** 789, ISSN: 0031-9007, (visited on 03/09/2022) (cit. on p. 44).

Shipman, H. L. (1979), *Masses and Radii of White-Dwarf Stars. III. Results for 110 Hydrogen-Rich and 28 Helium-Rich Stars.*, The Astrophysical Journal **228** 240, ISSN: 0004-637X, (visited on 19/10/2022) (cit. on p. 1).

Shklovskii, I. S. (1970), *Possible Causes of the Secular Increase in Pulsar Periods.*, Soviet Astronomy **13** 562, ISSN: 0038-5301, (visited on 06/01/2023) (cit. on p. 79).

Singh, S. et al. (2022), *The GMRT High Resolution Southern Sky Survey for Pulsars and Transients – III: Searching for Long Period Pulsars*, arXiv: 2206.00427 [astro-ph], (visited on 13/06/2022) (cit. on pp. 33, 41).

Smits, R. et al. (2011), *Prospects for Accurate Distance Measurements of Pulsars with the Square Kilometre Array: Enabling Fundamental Physics*, A&A **528** A108, ISSN: 0004-6361, 1432-0746, (visited on 01/12/2022) (cit. on p. 19).

Spitler, L. G. et al. (2013), *PULSE BROADENING MEASUREMENTS FROM THE GALACTIC CENTER PULSAR J1745–2900*, ApJL **780** L3, ISSN: 2041-8205, (visited on 11/02/2023) (cit. on p. 88).

Splaver, E. M. et al. (2002), *Probing the Masses of the PSR J0621+1002 Binary System through Relativistic Apsidal Motion*, The Astrophysical Journal **581** 509, ISSN: 0004-637X, (visited on 22/04/2023) (cit. on p. 77).

Staelin, D. H. (1969), *Passive Remote Sensing at Microwave Wavelengths*, Proceedings of the IEEE **57** 427 (cit. on pp. 30, 87).

Staelin, D. H. et al. (1968), *Pulsating Radio Sources near the Crab Nebula*, Science **162** 1481, ISSN: 0036-8075, (visited on 06/07/2023) (cit. on p. 1).

Staveley-Smith, L. (1997), *Hi Multibeam Survey Techniques*, Publications of the Astronomical Society of Australia **14** 111 (cit. on p. 48).

Sturrock, P. A. (1971), *A Model of Pulsars*, The Astrophysical Journal **164** 529, ISSN: 0004-637X, (visited on 22/10/2022) (cit. on p. 4).

Suresh, A. et al. (2022), *4-8 GHz Fourier-domain Searches for Galactic Center Pulsars*, The Astrophysical Journal **933** 121, ISSN: 0004-637X, (visited on 07/07/2023) (cit. on p. 50).

Tan, C. M. et al. (2018), *LOFAR Discovery of a 23.5 s Radio Pulsar*, ApJ **866** 54, ISSN: 0004-637X, (visited on 11/02/2023) (cit. on p. 91).

Tauris, T. M. et al. (2017), *Formation of Double Neutron Star Systems*, ApJ **846** 170, ISSN: 0004-637X, (visited on 26/10/2022) (cit. on p. 8).

Tauris, T. M. et al. (2000), *Formation of Millisecond Pulsars with Heavy White Dwarf Companions: Extreme Mass Transfer on Subthermal Timescales*, ApJ **530** L93, ISSN: 0004-637X, (visited on 26/10/2022) (cit. on p. 7).

Taylor, J. et al. (1969), *Two New Pulsating Radio Sources*, Nature **221** 816 (cit. on p. 29).

Thompson, C. et al. (1995), *The Soft Gamma Repeaters as Very Strongly Magnetized Neutron Stars - I. Radiative Mechanism for Outbursts*, Monthly Notices of the Royal Astronomical Society **275** 255, ISSN: 0035-8711, (visited on 07/06/2022) (cit. on p. 7).

Torne, P. et al. (2017), *Detection of the Magnetar SGR J1745-2900 up to 291 GHz with Evidence of Polarized Millimetre Emission*, **465** 242, arXiv: 1610.07616 [astro-ph.HE] (cit. on pp. 50, 88).

Torne, P. et al. (2021), *Searching for Pulsars in the Galactic Centre at 3 and 2 Mm*, **650**, A95 A95, arXiv: 2103.16581 [astro-ph.HE] (cit. on pp. 50, 52, 88).

Torne, P. et al. (2023), *A Search for Pulsars around Sgr A* in the First Event Horizon Telescope Data Set*, The Astrophysical Journal **959** 14, ADS Bibcode: 2023ApJ...959...14T, ISSN: 0004-637X, URL: https://ui.adsabs.harvard.edu/abs/2023ApJ...959...14T (visited on 14/01/2024) (cit. on p. 55).

Treves, A. et al. (2001), *The Magnificent Seven: Close-by Cooling Neutron Stars?*, arXiv: `astro-ph/0011564`, (visited on 28/10/2022) (cit. on p. 7).

van Kerkwijk, M. H. et al. (2005), *Optical Studies of Companions to Millisecond Pulsars*, **328** 357, (visited on 24/04/2023) (cit. on p. 71).

van Straten, W. et al. (2011), *DSPSR: Digital Signal Processing Software for Pulsar Astronomy*, Publications of the Astronomical Society of Australia **28** 1, ISSN: 1323-3580, (visited on 15/05/2023) (cit. on p. 42).

van Straten, W. et al. (2012a), *Pulsar Data Analysis with PSRCHIVE*, arXiv: `1205.6276 [astro-ph]`, (visited on 06/01/2023) (cit. on p. 72).

van Straten, W. et al. (2012b), *Pulsar Data Analysis with PSRCHIVE*, Astronomical Research and Technology **9** 237, ISSN: 1672-7673, (visited on 04/11/2022) (cit. on p. 41).

Vaughan, A. E. et al. (1970), *Five New Pulsars*, Nature **225** 167 (cit. on p. 48).

Verbunt, F. et al. (2014), *On the Disruption of Pulsar and X-ray Binar Ies in Globular Clusters*, Astronomy and Astrophysics **561** A11, ISSN: 0004-6361, (visited on 07/07/2023) (cit. on p. 67).

Vernet, J. et al. (2011), *X-Shooter, the New Wide Band Intermediate Resolution Spectrograph at the ESO Very Large Telescope*, A&A **536** A105, ISSN: 0004-6361, 1432-0746, (visited on 11/05/2022) (cit. on p. 90).

Weinberg, N. N. et al. (2005), *Stellar Dynamics at the Galactic Center with an Extremely Large Telescope*, **622** 878, arXiv: `astro-ph/0404407` (cit. on p. 55).

Weisberg, J. M. et al. (2004), *Relativistic Binary Pulsar B1913+ 16: Thirty Years of Observations and Analysis*, arXiv preprint astro-ph/0407149, arXiv: `astro-ph/0407149` (cit. on p. 16).

Wex, N. et al. (1999a), *Frame Dragging and Other Precessional Effects in Black Hole Pulsar Binaries*, **514** 388, arXiv: `astro-ph/9811052` (cit. on p. 16).

– (1999b), *Frame Dragging and Other Precessional Effects in Black Hole Pulsar Binaries*, The Astrophysical Journal **514** 388, ISSN: 0004-637X, (visited on 15/05/2023) (cit. on p. 51).

Wex, N. (2014), *Testing Relativistic Gravity with Radio Pulsars*, arXiv:1402.5594 [gr-qc], arXiv: `1402.5594 [gr-qc]`, (visited on 07/05/2022) (cit. on p. 71).

Wex, N. et al. (2020a), *Gravity Tests with Radio Pulsars*, Universe **6** 156 (cit. on p. 55).

– (2020b), *Gravity Tests with Radio Pulsars*, Universe **6** 156, (visited on 17/04/2023) (cit. on p. 71).

Wharton, R. S. et al. (2012), *Multiwavelength Constraints on Pulsar Populations in the Galactic Center*, **753**, 108 108, arXiv: `1111.4216 [astro-ph.HE]` (cit. on pp. 15, 51, 61).

Wongphechauxsorn, J. et al. (2024), *The High Time Resolution Universe Pulsar survey - XVIII. The reprocessing of the HTRU-S Low Lat survey around the Galactic Centre using a Fast Folding Algorithm pipeline for accelerated pulsars*, Monthly Notices of the Royal Astronomical Society **527** 3208, ADS Bibcode: 2024MNRAS.527.3208W, ISSN: 0035-8711, URL: `https://ui.adsabs.harvard.edu/abs/2024MNRAS.527.3208W` (visited on 14/01/2024) (cit. on p. 51).

Yao, J. M. et al. (2017a), *A New Electron-Density Model for Estimation of Pulsar and FRB Distances*, **835**, 29 29, arXiv: `1610.09448 [astro-ph.GA]` (cit. on p. 52).

– (2017b), *A New Electron-density Model for Estimation of Pulsar and FRB Distances*, The Astrophysical Journal **835** 29, ISSN: 0004-637X, (visited on 28/10/2022) (cit. on pp. 19, 63).

Young, M. D. et al. (1999), *A Radio Pulsar with an 8.5-Second Period That Challenges Emission Models*, Nature **400** 848, ISSN: 0028-0836, (visited on 25/09/2022) (cit. on p. 7).

Zhu, W. et al. (2018), *Tests of Gravitational Symmetries with Pulsar Binary J1713+ 0747*, arXiv preprint arXiv:1802.09206, arXiv: 1802.09206 (cit. on p. 16).

Appendix

The High Time Resolution Universe Pulsar Survey – XVIII. The reprocessing of the HTRU-S Low Lat survey around the Galactic centre using a Fast Folding Algorithm pipeline for accelerated pulsars

The High Time Resolution Universe Pulsar Survey – XVIII. The reprocessing of the HTRU-S Low Lat survey around the Galactic centre using a Fast Folding Algorithm pipeline for accelerated pulsars

J. Wongphechauxsorn ,[1]⋆ D. J. Champion,[1] M. Bailes,[2,3] V. Balakrishnan,[1] E. D. Barr,[1]
M. C. i Bernadich,[1] N. D. R. Bhat,[4] M. Burgay,[5] A. D. Cameron,[2,3] W. Chen,[1] C. M. L. Flynn,[2,3]
A. Jameson,[2,3] S. Johnston,[6] M. J. Keith,[7] M. Kramer,[1,7] C. Ng,[8] A. Possenti,[5,9] R. Sengar,[10,2,3]
R. M. Shannon,[2,3] B. Stappers,[7] W. van Straten[10]

[1]*Max-Planck-Institut für Radioastronomie, Auf dem Hügel 69, D-53121 Bonn, Germany*
[2]*ARC Center of Excellence for Gravitational Wave Discovery (OzGrav), Swinburne University of Technology, Mail H11, PO Box 218, VIC 3122.*
[3]*Centre for Astrophysics and Supercomputer, Swinburne University of Technology, P.O. Box 218, Hawthorn, Victoria 3122, Australia*
[4]*International Centre for Radio Astronomy Research, Curtin University, Bentley, WA 6102, Australia.*
[5] *INAF - Osservatorio Astronomico di Cagliari, Via della Scienza 5, I-09047 Selargius (CA), Italy.*
[6]*CSIRO Astronomy & Space Science, Australia Telescope National Facility, P.O. Box 76, Epping, NSW 1710, Australia.*
[7]*Jodrell Bank Center for Astrophysics, University of Manchester, Alan Turing Building, Oxford Road, Manchester M13 9PL, United Kingdom.*
[8]*Dunlap Institute for Astronomy & Astrophysics, University of Toronto, 50 St. George Street, Toronto, ON M5S 3H4, Canada.*
[9]*Universit ´a di Cagliari, Dept of Physics, S.P. Monserrato-Sestu Km 0,700 - 09042 Monserrato, Italy.*
[10]*Center for Gravitation, Cosmology, and Astrophysics, Department of Physics, University of Wisconsin-Milwaukee, P.O. Box 413, Milwaukee, WI 53201, USA.*
[11]*Institute for Radio Astronomy & Space Research, Auckland University of Technology, Private Bag 92006, Auckland 1142, New Zealand.*

ABSTRACT

The HTRU-S Low Latitude pulsar survey data from 1° around the Galactic Centre (GC) were searched for pulsars using the Fast Folding Algorithm (FFA). Unlike traditional Fast Fourier Transform pipelines, the FFA optimally folds the data for all possible periods over a given range, which is particularly advantageous for slow-rotating, low-duty cycle pulsars. For the first time, a search over acceleration was included in the FFA to improve its sensitivity to binary pulsar. The steps in dispersion measure and accelerations were optimised, resulting in a reduction of the number of trials by 86 per cent. The search resulted in the re-detections of four known pulsars, including PSR J1746−2856, which was missed in previous FFT based processing. This result indicates that the FFA pipeline is more sensitive than the FFT based pipeline used in previous processing of the survey within our parameter range. Additionally, we discovered a slow pulsar, PSR J1746−2829, with a large dispersion measure (1309 ± 2 pc cm^{-3}), located ∼0.5 ° from the GC. Follow-up observations revealed that this pulsar has a flat spectrum ($\alpha = -0.9 \pm 0.1$), is emitting intermittently, and has a period derivative of ∼ 1.5 ×10^{-12} s s^{-1}, implying a surface magnetic field of ∼ 5.2 ×10^{13} G and a characteristic age of ∼ 23000 yr. While the period, spectral index, and surface magnetic filed strength are similar to many radio magnetars, other characteristics such as short-duration profile variation and high linear polarization. Based on the assumption that PSR J1746−2829 is a magnetar, we discussed the possibility of an anomalously high fraction of this kind of object.

Key words: surveys – stars: neutron – pulsars: general

1 INTRODUCTION

The Galactic Centre (GC) is regarded as one of the most interesting regions in our Galaxy, due to the dense environment of matter and relatively large magnetic field around the supermassive black hole, Sgr A* (Eckart & Genzel 1996). Discovering radio pulsars, a subclass of neutron stars whose rotation is visible in pulses of radio emission detectable at Earth, located in the GC can lead to many applications, including studying stellar evolution and the magneto-ionised environment around the GC (e.g. Desvignes et al. 2018). Moreover, the discovery of a typical pulsar orbiting Sgr A* with an orbital period of approximately one year would be sufficient to test two predictions of General Relativity Theory: the No-Hair-Theorem and the Cosmic Censorship Conjecture (Wex & Kopeikin 1999; Kramer et al. 2004; Liu et al. 2012; Liu & Eatough 2017). The No-Hair-Theorem predicts that all stationary black holes can be described by their mass, spin, and electric charge alone, the Cosmic Censorship Conjecture predicts that all black holes must be surrounded by event horizons (Penrose 1979).

The environment around the GC favours the formation of massive

⋆ E-mail: jompoj@mpifr-bonn.mpg.de

stars (see e.g. Figer 2003, for a review). It is predicted that there will be 10^7-10^8 neutron stars, with 10^2 to 10^6 of them being pulsars (Cordes & Lazio 1997). Wharton et al. (2012) estimated that the inner 150 pc of the Galaxy could harbour as many as 1000 active radio pulsars that beam towards Earth, further motivating ongoing searches for pulsars around the GC. However, only six pulsars have thus far been detected within half a degree of angular separation from the GC (Johnston et al. 2006; Deneva et al. 2009; Eatough et al. 2013). One reason for the disparity between the predicted and observed number of pulsars is that the GC environment diminishes pulsar detectability.

The dense environment in the GC affects the pulsar's detectability in two main ways. Firstly, the arrival times of the radio pulses are delayed towards the lower observational frequency as $\Delta t \propto f^{-2}$. This effect is called dispersion, which can be completely mitigated by performing de-dispersion (see Section 2.3.2). Secondly, multi-path propagation caused by scattering in the interstellar medium (ISM) broadens the pulse width with a timescale that scales as $\tau_{ts} \propto f^{-4}$ for a thin screen scenario (see Rickett 1977, for a review). Critically, this effect can only be reduced by observing at higher frequencies. If the broadened pulse width is larger than the pulse period, it is impossible to detect periodicity from the pulsar as the pulses are completely smeared out. At the GC, the scatter broadening time of radio pulses at 1.4 GHz is expected to be as large as 2300 s (e.g. Cordes & Lazio 2002). This is one possible explanation for the lack of pulsar discoveries around the GC from the numerous pulsar surveys to date (e.g. Kramer et al. 1996; Klein et al. 2004; Suresh et al. 2022; Torne et al. 2021; Wharton 2017; Liu et al. 2021; Eatough et al. 2021). However, the scattered broadening of the GC magnetar PSR J1746−2900, the closest pulsar to Sgr A*, with a projected distant of 0.1 pc from the GC (Eatough et al. 2013; Kennea et al. 2013), is still in the order of seconds (Spitler et al. 2014) in stark contrast to the previous prediction. Even this lower scattering time may still be responsible the scarcity of pulsars detected.

Conducted over the last 25 years, most pulsar surveys have used an observing frequency around 1.4 GHz. This balances the negative effect of the scattering at low frequencies with the steep pulsar spectrum (see e.g. Bates et al. 2013; Jankowski et al. 2018). However, the extreme environment around the GC has prompted surveys at higher frequencies. High frequency pulsar surveys at the GC ranges from 4.0-8.0 GHz using the 100-m Effelsberg, 100-m Green bank, and 64-m Parkes (Murriyang) telescopes (Kramer et al. 1996; Klein et al. 2004; Macquart et al. 2010; Suresh et al. 2022) to 84 and 156 GHz (Torne et al. 2021) using the 30-m IRAM telescope. To reduce the effect of red-noise caused by fluctuations in the receiver's electronics of the telescope during long integration observations, GC surveys have also been conducted using interferometers e.g., Atacama Large Millimeter/submillimeter Array (ALMA) and Very Large Array (VLA) (Wharton 2017; Liu et al. 2021). In order to increase the sensitivity of the surveys as the pulsars become weaker at high frequencies, Eatough et al. (2021) made repeated high frequency observations (4.85, 8.35, 14.6, and 18.95 GHz) on a time scale of years. The long duration of the observation meant that the apparent period changes of a potential pulsar due to orbital motion needed to be accounted for not only by including the searches for acceleration (period derivative) but also jerk (the second derivative) (see Section 2.3.3). Despite these numerous higher-frequency pulsar surveys with various observation techniques, no new pulsars have been found.

Rather than competing with the spectral index of the pulsars in the GC, another way to reduce the deleterious effect of scattering is to look for longer period pulsars. Previous surveys were biased toward the fast spinning pulsars through their use of the Fast Fourier

Transform (FFT) algorithm to detect the repeating signal. As the number of pulses in the time-series reduces, so does the sensitivity of the FFT (Cameron et al. 2017; Parent et al. 2018; Morello et al. 2020b), some long-period and narrow-pulse pulsars may be missed. In this work, we searched for long-period pulsars that would not be as strongly affected by a significant scattering of the GC using the Fast Folding Algorithm (FFA) (Staelin 1969) which is more sensitive to long-period pulsars.

The organisation of this paper is as follows. Section 2 describes the methods used in this work, including data selection and the algorithm. The optimisations, the pipeline, and the search parameters are further elaborated. Section 3 reports the re-detection of the known pulsars and a new pulsar discovered in this survey. The discussion of the possible radio image counterpart of the newly found pulsar and the type of newly discovered pulsar is shown in Section 4. Finally, we present our conclusion in Section 5.

2 METHODS

2.1 Data selection

The 64-m Parkes-Murriyang radio telescope, located in New South Wales, Australia, was used for the Southern High Time Resolution Universe Survey (HTRU-S). Observations started in 2008 and ended in 2014 and made use of the Parkes Multibeam receiver which consists of 13 feeds, producing 13 telescope beams into the sky (Staveley-Smith et al. 1996). The HTRU-S survey was divided into three regions based on Galactic latitude. We used only the data set that formed the low-lat survey (LowLat) in this work because it has the longest observation time (4320 s for each pointing) with a sampling time ($t_{samp,0}$) of 64 μs, containing 2^{26} samples per observation and covered the GC (Ng et al. 2015). The central observing frequency f_c is at 1352 MHz with a bandwidth (Δf) of 340 MHz, separated into effective 870 channels (Keith et al. 2010). The long observation time of LowLat also favours the discovery of slow pulsars as it records more pulses. Additional information regarding other HTRU surveys can be found in Keith et al. (2010); Ng et al. (2015) and Cameron et al. (2020).

Because this work is focused on the GC, pointings with one degree of the GC were selected. The data were processed at the Max-Planck Computing and Data Facility in Garching, Germany, using the MPIfR's Hercules cluster.

2.2 The search algorithm

As mentioned in the previous section, the vast majority of pulsars have thus far discovered by performing an FFT on a time-series and searching for signals in the Fourier spectrum, this is due to its computational efficiency. However, the signals become more difficult to detect as the narrower the pulse-width, the more power is distributed to the higher harmonics in the Fourier domain. A fraction of the Fourier power can be recovered by performing "Incoherent harmonic summing" technique (Taylor & Huguenin 1969). This method adds the power of each harmonic to the fundamental frequency, recovering the missing Fourier power. However, it is impossible to recover all of Fourier power if the pulse is sufficiently narrow. Furthermore, as a result, the FFT has some limitations when applied to the detection of long-period (P>1 s) and narrow pulse pulsars (pulse width smaller than 20 per cent of the period for 32 harmonic sums) (see Morello et al. 2020b).

The FFA is an alternative method used to search for periodicity by brute-force folding every possible trial period. These pulse profile

must then analysed to see if a pulsar is present using matched filters. Although the FFA was first implemented in 1969 (Staelin 1969), the algorithm has only been applied to a few pulsar surveys (e.g., Faulkner et al. 2004; Kondratiev et al. 2009) as it is computationally expensive. Recently, Morello et al. (2020b) presented the new FFA implementation (hereafter the Riptide FFA)[1]. This implementation of the FFA has been demonstrated to be faster than the previous implementations and can be used in conjunction with a blind pulsar survey. It has already resulted in several discoveries, including PSR J0043−73 (Titus et al. 2019), a new pulsar in the Small Magellanic Cloud, and PSR J2251−3711, a pulsar from the SUPERB survey (Keane et al. 2018) with a spin period of 12.1s (Morello et al. 2020a). Recently, (Singh et al. 2022, 2023) discovered six new pulsars with the Riptide FFA, one of which has a period of 140-ms using data from the GMRT High Resolution Southern Sky (Bhattacharyya et al. 2016) pulsar survey.

In this work, we searched for periodicity in the selected data using the Riptide FFA implementation. To avoid confusion between a general FFA implementation, the Riptide FFA, and the acceleration search pipeline implemented in this work, we will refer to them as FFA, RFFA, and AFFA, respectively, for the remainder of this paper. We also present a new method to optimise the dispersion and acceleration trials when searching for pulsars in binary systems. Those optimisations could be done due to the fact that the search step size is proportional to the minimum search period, as the period searches in the FFA are independent (unlike the FFT) so that they can be individually tailored.

2.3 Optimisation of dispersion measure and acceleration trials

To improve the sensitivity of a survey to distant pulsars, the effect of dispersion must first be corrected for. While the FFT searches for all possible frequency simultaneously, the FFA only folds a small period range at a time. Since the acceleration and dispersion step size are proportional to the minimum search period, it is thus possible to optimise the search step size for each period range.

2.3.1 Searched period

First, we define the number of bins we want in each profile (N_{bins}). Then we can determine the minimum search period ($P_{\min}$) for a time-series with sampling time t_{samp}:

$$P_{\min} <= N_{bins} \times t_{samp}. \tag{1}$$

As we search for longer periods with the same N_{bins} the time-series can be downsampled. In this work, the RFFA was used to downsample the time-series by the factor of 2 whenever the search period doubles, as illustrated in Figure 1.

2.3.2 Searched dispersion measure

The dispersion measure (DM) of a pulsar describes the quadratic time delay between frequencies. This is given as:

$$\Delta t = 4.15 \times 10^6 \,\mathrm{ms} \times (\mathrm{f(MHz)}_1^{-2} - \mathrm{f(MHz)}_2^{-2}) \times \mathrm{DM}. \tag{2}$$

Dispersion can be mitigated by spitting the bandwidth into channels and progressively shifting each channel in time, before summing them to create a time-series. This method is called the de-dispersion. As the DM is a-prior unknown, a range of DM must be searched.

Folding for a time-series with period of 6s and pulse width of 2s
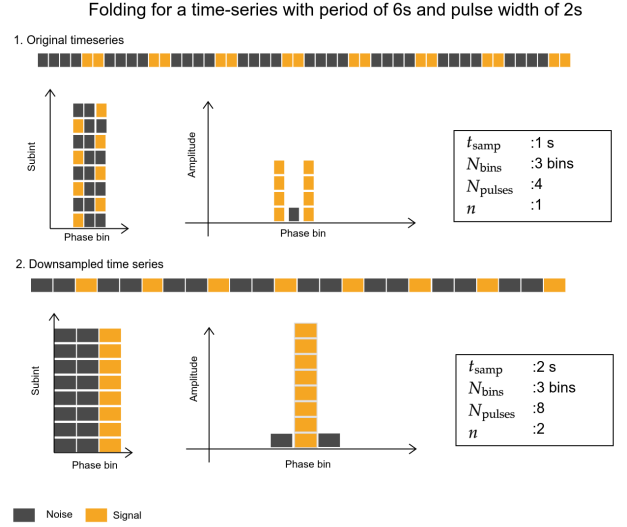
Figure 1. Illustration of how the FFA and the downsampling were implemented for a time-series with t_{samp} of 1 s, carrying a 6 s signal. After downsampling the data by a factor of $n=2$, the signal falls into the same profile bin, creating the pulse profile with the highest S/N. As the search period is twice longer, the number of samples is also halved, making the search for the signal with the longer period less computationally intensive.

The ith dispersion step at central frequency (f_c) at bandwidth (Δf) and sampling time (t_{samp}) in ms is calculated using

$$\mathrm{DM_i} = 1.205 \times 10^{-7} \times (\mathrm{i} - 1) \times \mathrm{t_{samp}} \left(\frac{\mathrm{f_c(MHz)}^3}{\Delta \mathrm{f(MHz)}} \right) \,\mathrm{pc\,cm^{-3}}. \tag{3}$$

As the FFA continuously downsamples the data to maintain the same number of profile bins, the size of the DM steps increases, reducing the total number of trials.

2.3.3 Acceleration search

Any orbital motion will cause an apparent period change in the pulsar during the observation, depending on the relative size of the orbital period and observation length. This will smear and reduce the signal-to-noise ratio (S/N) of the profile and may make the pulsar undetectable. Ideally, a search over all five Keplerian parameters would be performed (e.g. Balakrishnan et al. 2022), however for a large survey this is too computationally expensive. A simpler approach is to assume that the pulsar is moving with a constant acceleration, a, for the duration of the observation. Johnston & Kulkarni (1991) demonstrated that the pulse arrival time during the observation time is modulated as

$$\Delta t = \frac{at^2}{2c} \tag{4}$$

where c is the speed of the light. Ransom et al. (2003) and Ng et al. (2015) demonstrated that this approximation is true only if the observation time is less than 10 per cent of the orbital period.

To correct for the Δt, the time-series was resampled for a range of trial accelerations. The acceleration step size is defined as the value that changes the arrival time by a bin over half the length of the observation T_{obs} (by resampling the data from the middle of the observation), which is written as

$$\delta a = \frac{8 t_{samp} c}{T_{obs}^2}. \tag{5}$$

Table 1. The comparison of processing steps for a search with and without the optimisation demonstrated in this work. N_r is the total number of trials for each range. This optimisation reduced the number of trials for approximately 86 per cent for the selected period range.

$P_{\min}$	Without optimisation			With optimisation		
(s)	N_{DM}	N_{acc}	N_r	N_{DM}	N_{acc}	N_r
0.6	1,000.00	43.00	43,000.00	1,000.00	43.00	43,000.00
1.2	1,000.00	43.00	43,000.00	500.00	22.00	11,000.00
2.4	1,000.00	43.00	43,000.00	250.00	11.00	2,750.00
4.8	1,000.00	43.00	43,000.00	125.00	6.00	750.00
9.6	1,000.00	43.00	43,000.00	63.00	3.00	189.00
19.2	1,000.00	43.00	43,000.00	32.00	2.00	64.00
38.4	1,000.00	43.00	43,000.00	16.00	1.00	16.00
76.8	1,000.00	43.00	43,000.00	8.00	1.00	8.00
153.6	1,000.00	43.00	43,000.00	4.00	1.00	4.00
307.2	1,000.00	43.00	43,000.00	2.00	1.00	2.00
N_{total}			430,000.00			57,783.00

Consequently, the jth acceleration step is written as

$$\delta a_j = (j-1)\frac{8t_{samp}c}{T_{obs}^2}. \tag{6}$$

From the above equation, $\delta a \propto t_{samp}$. As a result, the number of steps can be reduced (similarly to dispersion) as the data are downsampled. The relation between the downsampling factor, n, and the acceleration step is

$$\delta a_{nj} = n \times \delta a_j. \tag{7}$$

The key advantage of this optimisation is when the data are dedispersed at DM_i and resampled it at a_j, these data can be reused when the FFA reaches a fold at twice the period, as shown in Figure 2. As both of the DM and acceleration step are proportional to the minimum period searched, when the searched period range changes by a factor of two, the total number of acceleration and DM trials decreases by a factor of four. As a result, this optimisation reduces the number of trials by approximately 86 per cent for the LowLat survey, as shown in Table 1.

2.4 The search pipeline

The initial stage of the search pipeline involves cleaning radio frequency interference (RFI) from the data. RFIFIND from *PRESTO*[2] was used to remove brightest the RFI bursts. The data were then dedispersed using the PREPSUBBAND routine to generate time-series at the specified DMs. The dedispersed time-series were resampled at each acceleration step using the *resample* routine in SIGPYPROC[3]. Afterwards, the RFFA was used to search in the shortest period range. For the next period range, the acceleration and dispersion steps doubled and half of the time-series generated previously were reused. This process was repeated to cover the whole period range.

Candidates with a S/N lower than a cut-off S/N were filtered out. The cut-off S/N was determined by calculating the false alarm rate (FAR) for the N_{total} number of trials. The FAR was calculated as follows:

$$FAR = 1 - Prob(> S/N) = 1 - \frac{1}{2}\left[1 - erf\left(\frac{S/N}{\sqrt{2}}\right)\right]. \tag{8}$$

[2] https://github.com/scottransom/presto
[3] https://github.com/ewanbarr/sigpyproc
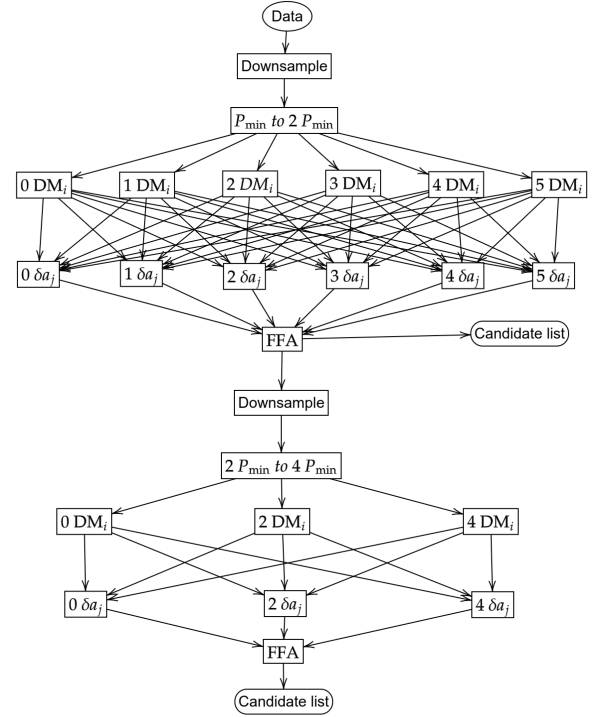
Figure 2. An example of the optimisation of the number of the dispersion and acceleration steps in the pipeline to search in the period range of $P_{\min}$ to $4P_{\min}$, dispersion measure range of 0 to $5DM_i$, and the acceleration range of 0 to $5\delta a_j$. This pipeline is separated into two period ranges. The first part of this pipeline is to search for the period range of $P_{\min}$ to $2P_{\min}$ and to use the dispersion step of DM_i and the acceleration step of δa_j. In the second part, the period range is $2P_{\min}$ to $4P_{\min}$ with the dispersion step and the acceleration step being $2DM_i$ and $2\delta a_j$, respectively. The existing time-series from the first part is reused in the second part of the pipeline.

The error function, $erf(x) = \frac{2}{\sqrt{\pi}}\int_0^x e^{-x^2}dx$, can be solved numerically (e.g. Press et al. 1992). N_{total} was evaluated from

$$N_{total} = N_{FFA} \times N_{acc} \times N_{DM}. \tag{9}$$

N_{DM} and N_{acc} are shown in Table 1, and N_{FFA} was approximated from Morello et al. (2020b) as

$$N_{FFA} = \frac{T_{obs}}{P_{\min}}N_{bin}^2 \log \frac{T_{obs}}{P_{\min}}N_{bin}^2. \tag{10}$$

Applying a limiting S/N to the data reduced the number of candidates greatly. However, the number of candidates observed per observation typically remains in the thousands which is impossible to inspect visually for a blind survey. In this work, we reduce the number of candidates using the kurtosis of the pulse profile's power distribution. Kurtosis is a property that quantifies the "tailiness" of a distribution; for a normal distribution, the kurtosis is 0. The kurtosis filtering has been typically used to detect bright RFI pulses in raw data (for example Nita et al. 2007; Nita & Gary 2010; Purver et al. 2022). However, here we use the kurtosis score as a way to detect a pulsar-like signal but filtering out the low kurtosis profiles which were typically noise or weak RFI. This technique has a negative effect on the survey sensitivity to very broad pulse profiles, but these should have been detected in previous FFT searches. The kurtosis limit was determined by comparing the kurtosis from a random noise profile to a profile containing a Gaussian. The comparison was conducted by simulating 2000 pulse profiles with pure noise and another 2000

Gaussian profiles with noise to represent pulsar pulse profiles. The duty cycle of these Gaussian profiles ranged from 1 per cent to 20 per cent. The kurtosis distribution from the simulation showed that the lowest kurtosis for the pulsar signal was approximately −0.5. We doubled this value to cover some extreme cases. As a result, only the candidates with kurtosis higher than −1.0 were inspected. Such criteria can reduce the number of candidates by 90 per cent.

2.5 Search parameters

The data were searched with the aforementioned pipeline for a total period range of 0.6-s to 432-s. The longest searched period was chosen based on the assumption that the FFA requires at least 10 pulses to obtain more S/N than the single pulse searches (see Keane 2010, for example). The shortest period search was limited by computational resources. As the number of search trials (N_{FFA}) is proportional to N_{samp}^3 for FFA searches (Morello et al. 2020b), processing time increases quickly as the period reduces. We also chose the minimum search period to be 0.6-s, as this period covers a large portion of the known pulsars and still achievable with a reasonable processing time of order 72 h per beam with the available computing facility. The N_{bins} used to create the search profile was set to be 128 bins based on a duty cycle of ∼ 1%, resulting in a 4.6875-ms $t_{samp,1}$ for the first period range according to Equation 1.

For the maximum search DM, we used the YMW16 free electron distribution model (Yao et al. 2017) to estimate the dispersion measure on a line-of-sight directly through the GC to the edge of the Galaxy. This extreme scenario gave a maximum DM of 3946 pc cm^{-3}. Thus, the DM range (DM$_r$) for this search was set to be 4000 pc cm^{-3}. [4] The dispersion step size was calculated from Equation 3 with the HTRU-S LowLat's bandwidth (340 MHz) and central frequency (1352 MHz) with i of 1 and $t_{samp,1}$ of 4.6875 ms at 4.023 pc cm^{-3}.

Because the GC is a dense environment, it is necessary for our acceleration range to be sufficiently wide to cover various kinds of binary companions. The acceleration range was chosen to be ± 128 m s^{-2}, which corresponds to a pulsar (of mass 1.4 M$_\odot$) with a companion up to the mass of a 37$M_\odot$, as e.g. black hole in a 12-hour orbital period (see Ng et al. 2015, for calculations).

For the S/N limit, we used a S/N of 8.0. With this S/N, the number of false candidates is approximately 0.04 candidates per beam, which is exceptionally low.

To test the acceleration part of the pipeline, we generated 5600 artificial pulsars in various binary systems, using *SIGPROC*'s *FAKE* package (Lorimer 2011). The simulated pulsars were selected to have spin periods randomly chosen between 1.0 to 6.0-s, with pulse duty cycles ranging from 1 to 25 per cent.[5] The companion mass was randomly selected between 0 and 37 $M_\odot$ with a fixed orbital period of 12 h at an orbital phase of 0.25, making it the easiest orbital phase to detect for an acceleration search. We then also generated the same pulsars without the binary companions as an isolated realisation. We compared the S/N values resulting from the pipeline from the isolated and accelerated realisations to determine the loss S/N. Our simulations showed that 90 per cent of the acceleration search FFA

---

[4] Note that NE2001 predicts a maximum DM for this line-of-sight to be 3396 pc cm^{-3}.

[5] We chose this period range rather than the full period range (0.6-s to 430-s) because the RFFA downsamples the time-series to the optimal time resolution, making the period range arbitrary.

Table 2. Known pulsars in the HTRU-S LowLat using the FFA pipeline. Note that PSR J1745−2758 was detected at a harmonic of the period.

NAME	P0 (s)	Flux density at 1400 MHz (mJy)	duty cycle $^\diamond$ (%)	S/N_{FFA}	S/N_{FFT}
J1745−2758	0.487528	0.15	6.1	8.8	8.4
J1745−2900 ♣ ♡	3.763733	0.9♣	8.3	-	-
J1745−2910 ♣	0.982	-	8.0	-	-
J1746−2849 ♣	1.47848	0.4	8.2	-	-
J1746−2850 ♣ ♡	1.077101	0.8	5.6	-	-
J1746−2856 ♣	0.945224	0.4	4.8	14	-
J1747−2802	2.780079	0.5	1.0	15.6	14.6
J1750−28	1.300513	0.09	1.3	12.8	8.7

♣Pulsars that are not detected in Ng et al. (2015).
♡Pulsars that shows high flux variation.
$^\diamond$ The duty cycles were calculated from $\frac{W50}{P0}$, using data from *PSRCAT* (Manchester et al. 2005)[6].
♣ For this work, we estimate the L-band flux density from extrapolating the flux and spectral index reported in Torne et al. (2017).

results have S/N greater than 95 per cent of the S/N detected from identical isolated pulsars.

3 RESULTS

3.1 The known pulsars

Of the ten previously known pulsars in the targeted region, two of them are millisecond pulsars, which are outside of our searched period range (PSR J1747−2809 and PSR J1745−2912). Three of them (PSR J1745−2758, PSR J1747−2802, and PSR J1750−28) were detected with the FFT pipeline. We also detected PSR J1746−2856 that was not reported in the previous FFT based survey processing (Ng et al. 2015; Cameron et al. 2020). The GC magnetar PSR J1745−2900, and two pulsars (PSR J1746−2850, PSR J1745−2849, and PSR J1746−2856) were not detected with the FFT or FFA pipelines, while PSR J1745−2910 had never been detected at this observational frequency before. The details about eight pulsars are shown in Table 2.

3.2 PSR J1746−2829: A new discovery

A new pulsar, PSR J1746−2829 was found during the reprocessing of LowLat data with an FFA S/N (S/N$_{FFA}$) of 11.2. Although it is not directly in the GC, its proximity (∼ 0.5°) makes it an interesting source for comparison with the known pulsars in this region. We found that the pulsar has a high DM (∼ 1300 pc cm^{-3}) and a long period (∼ 1.89s). This pulsar was also found in the later reprocessing of the HTRU-S low-lat using FFT based GPU-accelerated pipeline (Sengar et. al., In prep.) with S/N$_{FFT}$ of 8.6.

3.2.1 Follow-up observations

After its discovery, PSR J1746−2829 was observed with the Parkes telescope using the 21-cm Multibeam receiver for seven epochs from April to July 2018. Even the 72-min observations at Parkes were yielding S/N of only approximately 8-9, so observations were also made with the 100-m Effelsberg telescope. While the larger diameter of the Effelsberg telescope leads to higher sensitivity, the beam size (θ_b) is smaller at the same frequency. Hence, the 21-cm receiver[7] was used to make 'gridding' observations (see Cruces et al. 2021, for more details). This technique is performed by observing the pulsar

---

[7] https://eff100mwiki.mpifr-bonn.mpg.de

Table 3. Timing parameters for newly discovered pulsar with 1-σ uncertainty represented in parentheses.

Parameter	
Name	J1746-2829
Right ascension (J2000)$^\heartsuit$	$17^h46^m15^s$(14)
Declination (J2000)$^\heartsuit$	-28° 29′ 32″(38)
Galactic latitude, b (°)	0.117(60)
Galactic longitude, l (°)	0.445(56)
Spin period (s)	1.888928609337(9)
Period derivative (s s^{-1})	1300(30) $\times 10^{-15}$
Epoch of period	58564.0
Dispersion measure (cm^{-3} pc)	1309(2)
Estimated distance$^\spadesuit$ (kpc)	8.2
Rotation measure (rad m^{-2})	-743(14)
Scattering time (ms)	67(3)
Average flux density at 1400 MHz (mJy)	0.55(6)
Inferred B_{field} (G)	5.0×10^{13}
Inferred characteristic age (yr)	23×10^3
Spin-down luminosity (erg s^{-1})	8.4×10^{33}
Flux density spectral index	-0.9(1)

$^\spadesuit$ Estimated with Yao et al. (2017)
$^\heartsuit$ Position obtained from the MeerKAT's detections.
$^\diamond$ This uncertainty considers a contribution from positional uncertainty.

multiple times with a small offset from the central beam to improve the position, narrowing down to the width of the Effelsberg beam at 21-cm (0.163°). The pulsar was subsequently observed for seven epochs using the Effelsberg telescope.

The installation of the Ultra-Wide Band (UWL) (Hobbs et al. 2020) receiver at the Parkes telescope, provided a substantially larger bandwidth of $\sim$ 3 GHz. The pulsar was therefore also observed for 14 epochs from March 2019 to October 2022 and was detected at the upper frequency range of the UWL receiver at $\sim$ 4 GHz, implying that this pulsar might have a flat spectrum.

In order to reduce the positional uncertainty of the pulsar further, observations were scheduled with the MeerKAT interferometer (Jonas & MeerKAT Team 2016). The long baselines between individual dishes reduce the size of the synthesised beam, thus giving an improved localisation of the source of interest. The FBFUSE (Barr 2018) system offers the capability of beamforming (Chen et al. 2021) and recording up to 864 tied array beams and producing SIGPROC format filterbank data. Using the UWL position of PSR J1746−2829 as a reference, 480 beams were tiled around the position with an integration time of 9 min at 1.28 GHz. This covered roughly a 25 arcmin radius. Beams within the UWL positional uncertainty were folded/searched with the pulsar parameters. The only detection was obtained in a beam centred at RA $17^h46^m15^s$.04 and DEC -28°29′32″.40. Since the synthesised beams were elliptical, the positional uncertainties in the major and minor axis were 50 and 80 arcsec respectively.

To acquire an initial timing solution, we found that a simple linear function was sufficient to describe the barycentric spin period evolution, as shown in Figure 3. Consequently, the pulsar's spin period evolution is dominated by a period derivative ($\dot{P}$) which corresponds to 1253(58)$\times 10^{-15}$ s s^{-1}. This initial timing solution was then used to fold all of the observations of this pulsar.

The phase-connected timing solution (where every rotation of the pulsar is modelled from the first observation to the last) was only possible with the UWL observations from MJD 58564 to 59838 due to the combination of a large timing gap, highly contaminated RFI observations. This timing solution is shown in Table 3. Although the timing solution was not fully phase-connected to the other data sets, it confirms the high $\dot{P}$ of this pulsar. The position was not fitted
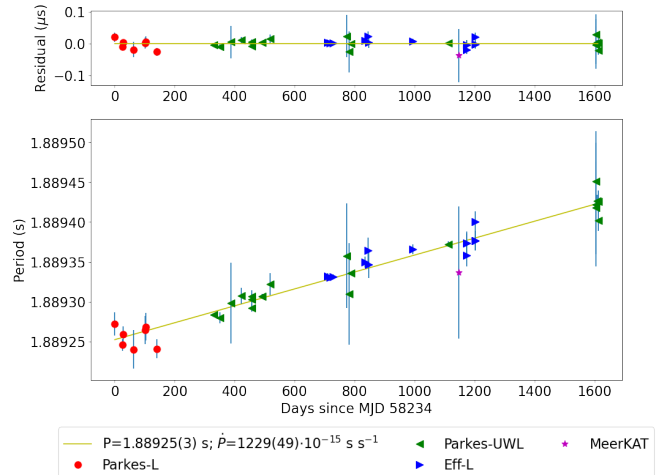
Figure 3. Barycentric spin period evolution of PSR J1746−2829. The spin period of this pulsar can be described by a simple linear function ($P(t) = \dot{P}t + P_0$). The different colours represent the different instruments used.

because it yielded a location outside the MeerKAT beamwidth, suggesting that the current timing position uncertainty is still larger than the position uncertainty derived from the MeerKAT pulsar search observation. Assuming this pulsar to be a magnetic dipole radiator with canonical neutron star mass (1.4$M_\odot$) and radius (10 km), the surface magnetic field (B_{field}) can be estimated: $B_{\text{field}} \sim 5 \times 10^{13}$ G with a characteristic age of $\sim$ 23000 yr. The second-period derivative was found to be highly correlated with the position uncertainty, which makes it less likely to be intrinsic to the pulsar.

To further constrain the position, we modelled the MeerKAT beam as a Gaussian function (see Equation 12). Since this pulsar was detected with an S/N of 12 in only one of the tile-array beams of MeerKAT, and considering that the S/N limit was 7, we used the beam to determine how far the pulsar could be located without being detected in the neighbouring beam with an S/N < 7 (see e.g. Jankowski et al. 2023). The beam and the current position uncertainty are shown in Figure 7.

3.2.2 Polarisation, spectral distribution, pulse profile evolution, and scattering time

The synthesised beam width of the MeerKAT telescope ($\sim$ 1 arcmin) is approximately six times smaller than that of the upper band at UWL receiver ($\sim$ 6.6 arcmin) (Hobbs et al. 2020). As a result, we use the beam position from the MeerKAT observations as this pulsar's position, minimising the impact of a potential position offset on the measured flux density. Now that the angular offset had less effect on the flux of the pulsar, the intrinsic spectrum could be measured. We carried out an observation with UWL receiver to measure the polarization properties, the spectral index, the profile evolution, and the scattering time. Polarisation calibration was done by observing a noise diode at 45° to the receiver dipoles for 90–120s prior to the observation of the pulsar. The data were calibrated for flux using on- and off-source scans of radio sources with known, stable flux densities.

We used the *RMcalc* code (Porayko et al. 2019) to measure the rotation measure (RM). This approach was based on Brentjens & de Bruyn (2005) RM synthesis method and presented the estimates using the Bayesian Generalized Lomb-Scargle Periodogram (BGLSP)
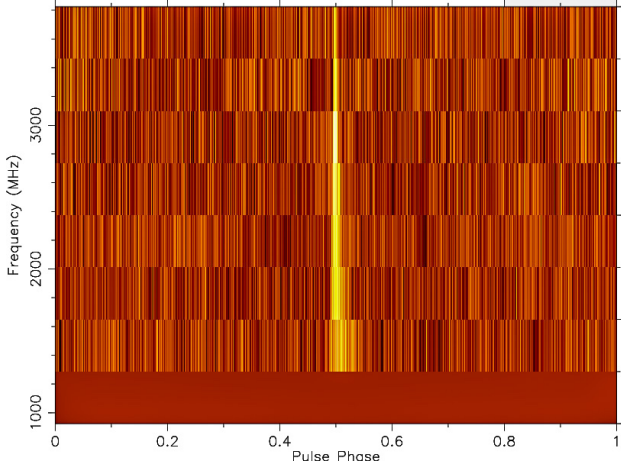
Figure 4. Frequency vs pulse-phase plot for PSR J1746−2829 from an 82-min observation with the UWL receiver, containing 8 channels and 128 pulse phase bins.

Figure 5. Folded pulse profile of PSR J1746-2829 at 3.2GHz showing a narrow pulse profile with a low linear (Red) polarization fraction and no significant circular (Blue) polarisation after correcting for RM.

technique. For consistency, we also used the *RMFIT* routine from *PSRCHIVE* (van Straten et al. 2012), which is based on an optimisation of the linear polarization fraction. The RM range was set according to the analysis by Schnitzeler & Lee (2015), resulting in the RM range of ±78481 rad m^{-2}. *RMcalc* gave a rotation measure of -743 ± 14 rad m^{-2} while *RMFIT* gave −797 ± 39 rad m^{-2}. As the results are consistent, the RM from *RMcalc* with a lower uncertainty has been used. After applying this RM we detected linear polarisation of ∼ 20 per cent without significant circular polarisation. The pulse profile with polarisation is shown in Figure 5.

Subsequently, the observation was split into eight subbands to study the pulse profile evolution over frequency. The pulse profile at the uppermost band (3.84 GHz) showed a profile that could be described by a simple Gaussian function with the full width at half maximum (FWHM) of 10.15±0.07 ms, resulting in a small duty cycle for this pulsar of 0.537 ± 0.04 per cent. The pulse profile shows an increasingly broader tail towards lower frequencies, as shown in Figure 4.

The broadening time is measured by fitting for an exponential decay[8] with a characteristic time defined as:

$$\tau_{ts,f} = \tau_{ts} \left(\frac{f}{1000} \right)^{\alpha_{sc}} \qquad (11)$$

where the reference frequency as 1000 MHz. The frequency-phase pulse profile was modelled as a Gaussian pulse convolved with exponential decay using *Pulse Portraiture* (Pennucci et al. 2014; Pennucci 2019), τ_{ts} was determined through least square minimisation, with α_{sc} at −4.0.[9] The resulting scattering time for this pulsar at 1000 MHz as 67 ± 3 ms.

3.2.3 Radio flux density and spectrum

To study the spectrum, we choose observations with T_{obs} longer than one hour with the UWL receiver, resulting in two observations at MJD 59022 and MJD 59091. The observation at MJD 59091 was made at the current best position. However, the observation from
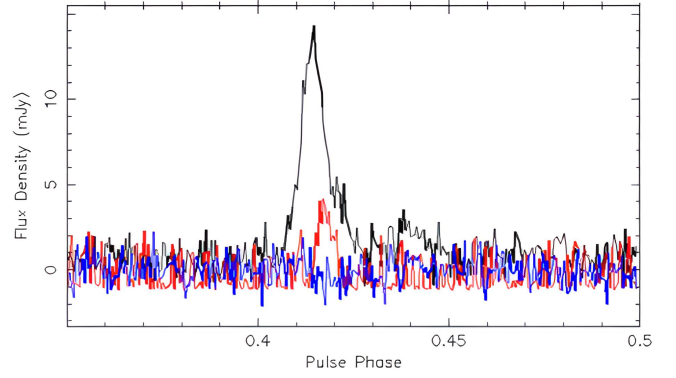
MJD 59022 was made before the current position was determined. It has a position offset (θ) of ∼ 2 arcmin. An offset θ is causing the observed flux density to be reduced as

$$S_{\text{obs}} = S_f e^{\frac{-\theta^2}{2\sigma^2}}, \qquad (12)$$

where S_{obs} is the observed flux density. This equation assumes that the telescope response pattern is a Gaussian, where σ is a Gaussian rms width calculated from

$$\sigma = \frac{\theta_b}{2\sqrt{2\ln 2}}, \qquad (13)$$

using θ_b in each frequency band as published in Hobbs et al. (2020).

The S_{obs} was determined using the *PSRFLUX* routine from *PSRCHIVE* (van Straten et al. 2012) with the 2D pulse profile template from the previous section. After we compensated for the flux density reduction due to the offset using Equation 12 and Equation 13, the spectrum was modeled as a power law with a spectral index (α),

$$S_f = S_{f_{\text{ref}}} \left(\frac{f}{f_{\text{ref}}} \right)^{\alpha}, \qquad (14)$$

where f_{ref} is the reference frequency which is 1400 MHz. We measure the spectral index to be −0.8 ± 0.1 and −0.9 ± 0.2 with a flux density at 1400 MHz of 0.48 ± 0.01 mJy and 0.35 ± 0.01 mJy for MJD 59022 and MJD 59491 respectively, confirming that this pulsar has a relatively flat spectrum compared to the typical pulsar population, which is in range of −1.4 to −1.6 (Bates et al. 2013; Jankowski et al. 2018) and showing no sign of spectral index variation overtime, which has been found in two radio loud magnetars (Torne et al. 2021; Champion et al. 2020).

To explore radio flux distribution and evolution, the radio light curve was calculated using two methods. First, all L-band flux densities were estimated from the radiometer equation using the post cleaning bandwidth, observation time and system equivalent flux density for Parkes (Keith et al. 2010), Effelsberg[10] and MeerKAT (Bailes et al. 2020). In addition, all of the observations before the MeerKAT observation at MJD 59381 had a positional offset which decreases the flux density which can be corrected using Equation 12. The flux density from the MeerKAT observation is still affected by the position offset, which is representing as a large asymmetric

---

[8] $e^{-\frac{t}{\tau_{ts,f}}}$, assuming no pulse profile evolution over frequency.

[9] Depending on the screen and DM.

[10] https://eff100mwiki.mpifr-bonn.mpg.de
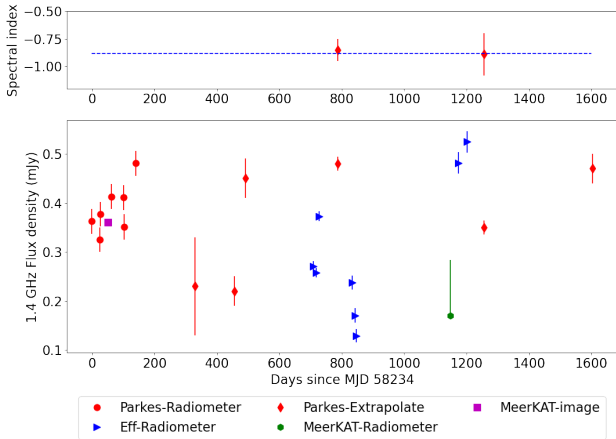
Figure 6. Upper panel: Spectral indexes (α) at two epochs showing no significant α variation, the dashed line represents the average α. Lower panel: Radio light curve of PSR J1746−2829. Red circles represent the flux densities from Parkes L-band observations while the blue triangles represent the L-band fluxes densities from the Effelsberg telescope. The green hexagon represents the flux density calculated using the radiometer equation based on the MeerKAT follow-up observation of this pulsar. The uncertainty here also includes the contribution from any position offset. The magenta square represents the flux density derived from the only source within the position uncertainty (see Section 4). The red diamonds show the 1400 MHz flux densities extrapolated from the UWL observations assuming the spectral index of -0.9.

uncertainty, where the upper limit represents the scenario where the pulsar is located at the edge of the uncertainty. Moreover, we also search for a point source in the GC image mosaic from MeerKAT (Heywood et al. 2022) (see Section 4). Only one point source was found within the positional uncertainty, hence the flux density of this source (0.36 ± 0.04 mJy) was used as an upper limit for epochs that covered this source (MJD 58281,58286 and 58287).

Secondly, since most of the UWL observations at approximately 1400 MHz were heavily polluted by RFI, the channels around 1400 MHz were removed. In this case, the flux density at 1400 MHz is determined by the flux density from the upper frequency data and the spectral index from all available UWL observations with polarisation and flux calibrators, using the average spectral index, $\alpha = -0.9(1)$.

The flux density is plotted against epoch of observation in Figure 6. The radio light curve shows large flux density variations (more than 50 per cent), corresponding to a characteristic of the high B_{field} pulsars and magnetars (see e.g., Dexter et al. 2017). According to NE2001 (Cordes & Lazio 2002), the estimated diffractive scintillation time scale (t_d) at this location is approximately 1.3 s at 1000 MHz. This is significantly shorter than the observation time. NE2001 also predicted the scintillation bandwidth (Δf_d) to be 3×10^{-6} MHz, Stinebring & Condon (1990) demonstrated that the reflective scintillation time scale (t_r) can be estimated from

$$t_r = \frac{4 f_{obs} t_d}{\pi \Delta f_d}.$$ (15)

The t_r at f_{obs} of 1000 MHz is $\sim$ 20 yr, which is significantly longer than the flux density variation timescale ($\sim$ months) as shown in Figure 6. As a result, the observed flux density variation is unlikely dominated by the interstellar scintillation.

Table 4. Results from X-ray archival images. All of them were observed before the start of the timing campaign and showing the minimum X-ray flux of 10^{32} to 10^{33} erg s^{-1} which is approximately 1 to 10 per cent of this pulsar's spin down luminosity.

MJD	Count rate (photons ks^{-1})	$L_x 10^{32}$ (erg s^{-1})	T_{obs} (ks)
54154.30	0.135	1.05	37
54040.59	0.132	1.02	38
52107.89	0.258	2.00	12
57584.33	1.036	8.04	1.9
57584.43	1.036	8.05	1.9

3.3 X-RAY DATA

We searched for X-ray emission by cross-referencing with the sources from GC Chandra X-ray survey. One source was found with an angular separation of 0.441 arcmin from the centre of the MeerKAT radio beam where this pulsar was detected (Muno et al. 2009). The location of this source at the edge of the tile array beam makes it unlikely to be the pulsar as it was not detected in any neighbouring beams.

An upper limit for X-ray emission was estimated from the Chandra composite images[11] that covered the whole positional uncertainty. We searched for the X-ray pixel with the highest count that is not within one pixel from the known X-ray source and used that as the upper limit for the number of photons, which was then converted to a count rate by dividing by the exposure time. *WebPIMMS*[12] was used to convert from the Chandra telescope count rate to X-ray luminosity using the spectrum (blackbody with kT = 1 keV) of the GC magnetar PSR J1745−2900 (Rea et al. 2013) and the column density N_H at the pulsar's position[13] $N_H = 9.42 \times 10^{21}$ cm^{-2}. The upper limit for X-ray flux for each epoch shown in Table 4, is approximately 10^{32} to 10^{33} erg/s, which is 100 times less than the spin-down luminosity, $\sim 10^{34}$ erg/s. In terms of higher-energy emission, specifically gamma-rays, no point source has been reported within 1 arcmin of this source (Abdollahi et al. 2022). This absence is expected due to the considerable distance of the pulsar.

4 DISCUSSION

The FFA pipeline is more sensitive than the FFT pipeline[14] due to the loss of high-spectral frequency information in the FFT. This increased sensitivity can be seen in the S/N of the detection of pulsars as the FFA always has a higher S/N than in the FFT see Table 2, also reported in Cameron et al. (2017); Parent et al. (2018). It should be noted that the FFA pipeline has reduced sensitivity to pulsars with duty cycles of less than $\sim$ 1 per cent, due to the number of bins used in the fold.

The newly discovered pulsar, PSR J1746−2829, has a flat spectrum, long period, and a relatively high $\dot{P}$. These are characteristics that are similar to those of magnetars. However, the degree of linear polarisation is surprisingly low if it is indeed a magnetar (see discussions below). The parameters of this pulsar are shown in Table 3.

Recently, Heywood et al. (2022) published a deep radio image of the GC made with the MeerKAT telescope at 1.28 GHz. The mosaic image also covered the location of PSR J1746−2829. The expected

---

[11] Obs ID:07045,07044,02294,18326,18329

[12] https://heasarc.gsfc.nasa.gov/cgi-bin/Tools/w3pimms/w3pimms.pl

[13] https://heasarc.gsfc.nasa.gov/cgi-bin/Tools/w3nh/w3nh.pl

[14] As long as the duty cycle is larger than the bin width.

flux density of PSR J1746−2829 at the observing frequency of the imaging survey was calculated using Equation 14 with S_{1400} and α reported in Section 3.2.3, resulting in an expected flux density of $0.57^{+0.098}_{-0.070}$ mJy.

As shown in Figure 7, a point source was detected with a peak flux density of 0.3 mJy visible within the position uncertainty of the pulsar. The sensitivity of the imaging survey (Heywood et al. 2022) implies that the pulsar should be visible, and the fact that there is only one point source within the positional uncertainty and the flux density of this pulsar varies between 0.1 mJy to 0.6 mJy suggests that it may indeed be the pulsar. Unfortunately, neither the spectral index nor the polarisation of this point source is reported, which would help to further confirm the association.

Using a kick velocity of 380 km s^{-1} (Faucher-Giguère & Kaspi 2006) and assuming that this pulsar is located 8.2 kpc from Earth, the upper limit for the distance of this pulsar is approximately 4 arcminutes. According to the MeerKAT L-band Mosaic at the GC(Heywood et al. 2022), there are several sources that could be supernova remnants within 4 arcminutes from this pulsar. Consequently, a further proper motion measurement is required to determine if this pulsar is associated with any of these sources.

4.1 Is PSR J1746−2829 a magnetar?

Magnetars are a group of neutron stars characterised by an implied surface magnetic field strength orders of magnitude larger than that of the normal pulsar population. Their large period derivatives ($\dot{P}$) range from 10^{-15} - 10^{-10} s s^{-1} meaning that they quickly spin-down and are detected with relatively long spin periods (≥ 1 s) (e.g. Kaspi & Beloborodov 2017). Magnetars predominately emit X-rays and gamma rays, sometimes with a luminosity that exceeds the spin-down luminosity for a rotating magnetic dipole ($\dot{E} = 4\pi^2 I\dot{P}/P^3$). For this reason, magnetar emission is believed to be powered by the decay of the magnetic field energy, rather than purely by rotation. Most magnetars are radio-quiet; out of the 31 magnetars discovered to-date [15] (Olausen & Kaspi 2014), only six of them are detectable at radio frequencies (Camilo et al. 2006, 2007b; Levin et al. 2010; Livingstone et al. 2011; Levin et al. 2012; Eatough et al. 2013; Shannon & Johnston 2013; Karuppusamy et al. 2020; Lower et al. 2020). The radio-loud magnetars are usually observed to be transient in nature, some magnetars have been known to be in a quiet state for years before becoming active (e.g. Mori et al. 2013; Lyne et al. 2018). Most of these radio loud magnetars show flat radio spectra ($\alpha \leq -1.0$) (Kramer et al. 2007; Camilo et al. 2007b; Shannon & Johnston 2013; Torne et al. 2017; Camilo et al. 2018) and all of the known radio magnetars are intrinsically almost 100 per cent linearly polarised (Camilo et al. 2007a, 2008; Eatough et al. 2013; Camilo et al. 2018; Lower et al. 2020; Champion et al. 2020). In addition, Agar et al. (2021) showed that all magnetars have boarder intrinsic pulse profiles (duty cycle more than 4 per cent) compared to most slow pulsars (duty cycle less than 1 per cent).

However, some magnetars contradict these common properties at least for a period of time. For example, PSR J1846−0258, a young radio magnetar, has a rotation period of 0.3 s (Livingstone et al. 2011), Swift J1818.0-1607 has a steep spectral index of −2.8 (Champion et al. 2020), and some magnetars (PSR J1746−2900, XTE J1810−197, 1E 1547.0−5408, Swift J1818.0−1607) were also reported to have low linear polarisation for some epochs (Camilo et al. 2007a; Torne et al. 2017; Lower et al. 2021, 2023).

[15] http://www.physics.mcgill.ca/~pulsar/magnetar/main.html

Finally, nine magnetars have been reported with X-ray quiescent luminosities approximately 20 times lower than the spin-down luminosities, which is unusual for magnetars (1E 1547.0−5408, PSR 1622−4950, SGR J1745−2900, XTE J1810−197, Swift J1818.0−1607, SGR 1833−0832, Swift J1834.9−0846, SGR 1935+2154, PSR J1846−0258) (see Olausen & Kaspi 2014, for reviews). Interestingly, six of these are radio loud magnetars, suggesting that radio emission from radio magnetars may have lower X-ray quiescent luminosity.

PSR J1746−2829 has some observational features commonly found in radio loud magnetars; The spectrum is flatter than most pulsars and two of the radio magnetars. It has a long rotation period. The measured $\dot{P}$ indicates the magnetic field near the lower-end of the magnetar B_{field} limit ($\sim 4.4 \times 10^{13}$ G) (Rea et al. 2012). This study of the radio flux distribution shows that this pulsar has highly variable flux. However, it also shows some properties that are not in common with radio magnetars, but instead are typical for slow pulsars; a narrow pulse profile and low polarisation fraction at high frequency as shown in Figure 5. Critically, we have not been able to conclude whether PSR J1746−2829 belongs to the family of magnetars or not.

A magnetar or not, this pulsar is the third flat spectrum pulsar out of seven pulsars found around 0.5° from the GC. The other objects are the GC magnetar and a transient flat spectrum pulsar, with a high B_{field}, named PSR J1746−2850 (Dexter et al. 2017). If this pulsar, along with PSR J1746−2850, is a magnetar, then the proportion of recycled pulsars to magnetars in the observed population (40 %) is appeared to be significantly different to that of the GC (0.4 %). This could be explained by a larger intrinsic population of magnetars or the environmental conditions in the GC favour the detection of radio magnetars rather than non-recycled pulsars. This could be explained by a higher intrinsic population of magnetars in the GC, or that the interstellar medium conditions within the GC favour the detection of radio magnetars.

5 CONCLUSIONS

We report on the reprocessing of the HTRU-S LowLat around the GC using the first FFA pipeline with an acceleration search. The survey resulted in the discovery of a new slow pulsar with a very high period derivative, and a flat spectrum, indicating that this pulsar might be a magnetar. The observations showed that this pulsar has a high DM, RM, and τ_{ts}, which is expected for an object found inside a dense magneto-ionic environment such as the GC. As this pulsar is a magnetar or a high B_{field} pulsar, is the third such object out of seven pulsars located less than 0.5° from the GC and may suggest that the GC hosted an anomalously high number of magnetar. All known pulsars detected by the previous FFT processing were detected, as well as a missing pulsar from the FFT based processing of the survey. By comparing the S/N from the FFT to the S/N from the FFA, we found that the FFA pipeline has shown more sensitivity than the FFT pipeline in the searched parameter space.
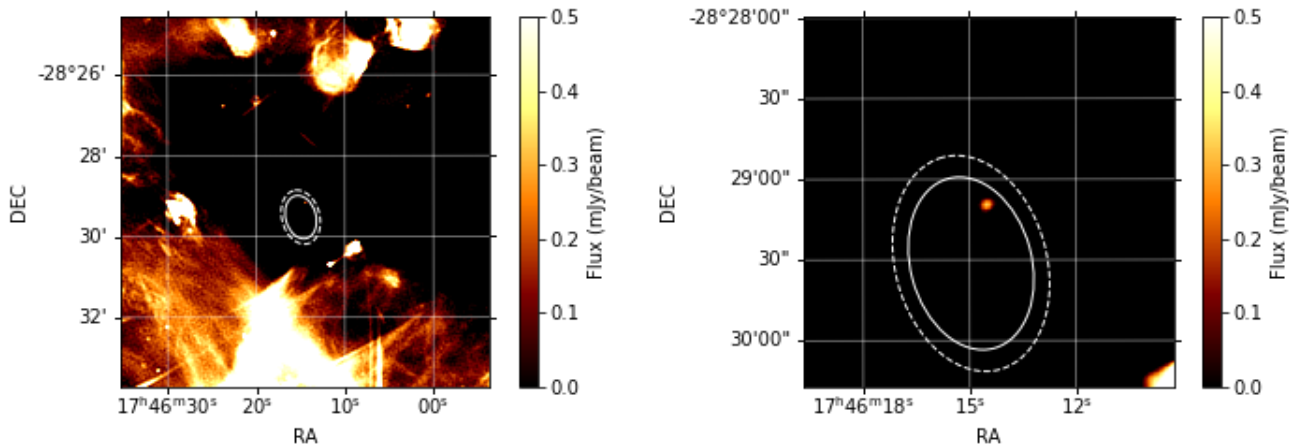
Figure 7. The L-band observations image mosaic obtained at MeerKAT (Heywood et al. 2022). Right: The MeerKAT pulsar search beam of PSR J1746−2829 (white dashed ellipse) reveals a point source with 0.36 mJy flux density and 0.04 mJy rms in the field with a position uncertainty derived from non-detections in the other beams from the follow-up observation with MeerKAT (white ellipse). Left: The magnified version of the image on the left, displaying the location of the point source in the MeerKAT pulsar search beam.

source was completed using the MPIfR FBSUE backend on the 64-dish MeerKAT radio telescope owned and operated by the South African Radio Astronomy Observatory, which is a facility of the National Research Foundation, an agency of the Department of Science and Innovation.

DATA AVAILABILITY

Pulsar data taken for the P860 and P1050 project are made available through the CSIRO's Data Access Portal (https://data.csiro.au) after an 18 month proprietary period. The rest of the data underlying this article will be shared on reasonable request to the corresponding author.

REFERENCES

Abdollahi S., et al., 2022, ApJS, 260, 53
Agar C. H., et al., 2021, MNRAS, 508, 1102
Bailes M., et al., 2020, Publ. Astron. Soc. Australia, 37, e028
Balakrishnan V., Champion D., Barr E., Kramer M., Venkatraman Krishnan V., Eatough R. P., Sengar R., Bailes M., 2022, MNRAS, 511, 1265
Barr E. D., 2018, in Weltevrede P., Perera B. B. P., Preston L. L., Sanidas S., eds, Vol. 337, Pulsar Astrophysics the Next Fifty Years. pp 175–178, doi:10.1017/S1743921317009036
Bates S. D., Lorimer D. R., Verbiest J. P. W., 2013, MNRAS, 431, 1352
Bhattacharyya B., et al., 2016, ApJ, 817, 130
Brentjens M. A., de Bruyn A. G., 2005, A&A, 441, 1217
Cameron A. D., Barr E. D., Champion D. J., Kramer M., Zhu W. W., 2017, MNRAS, 468, 1994
Cameron A. D., et al., 2020, MNRAS, 493, 1063
Camilo F., Ransom S. M., Halpern J. P., Reynolds J., Helfand D. J., Zimmerman N., Sarkissian J., 2006, Nature, 442, 892
Camilo F., Reynolds J., Johnston S., Halpern J. P., Ransom S. M., van Straten W., 2007a, ApJ, 659, L37
Camilo F., Ransom S. M., Halpern J. P., Reynolds J., 2007b, ApJ, 666, L93
Camilo F., Reynolds J., Johnston S., Halpern J. P., Ransom S. M., 2008, ApJ, 679, 681
Camilo F., et al., 2018, ApJ, 856, 180
Champion D., et al., 2020, MNRAS, 498, 6044

Chen W., Barr E., Karuppusamy R., Kramer M., Stappers B., 2021, Journal of Astronomical Instrumentation, 10, 2150013
Cordes J. M., Lazio T. J. W., 1997, ApJ, 475, 557
Cordes J. M., Lazio T. J. W., 2002, arXiv e-prints, pp astro–ph/0207156
Cruces M., et al., 2021, MNRAS, 508, 300
Deneva J. S., Cordes J. M., Lazio T. J. W., 2009, ApJ, 702, L177
Desvignes G., et al., 2018, ApJ, 852, L12
Dexter J., et al., 2017, MNRAS, 468, 1486
Eatough R. P., et al., 2013, Nature, 501, 391
Eatough R. P., et al., 2021, MNRAS, 507, 5053
Eckart A., Genzel R., 1996, Nature, 383, 415
Faucher-Giguère C.-A., Kaspi V. M., 2006, ApJ, 643, 332
Faulkner A. J., et al., 2004, MNRAS, 355, 147
Figer D. F., 2003, Astronomische Nachrichten Supplement, 324, 255
Heywood I., et al., 2022, ApJ, 925, 165
Hobbs G., et al., 2020, Publ. Astron. Soc. Australia, 37, e012
Jankowski F., van Straten W., Keane E. F., Bailes M., Barr E. D., Johnston S., Kerr M., 2018, MNRAS, 473, 4436
Jankowski F., et al., 2023, arXiv e-prints, p. arXiv:2302.10107
Johnston H. M., Kulkarni S. R., 1991, ApJ, 368, 504
Johnston S., Kramer M., Lorimer D. R., Lyne A. G., McLaughlin M., Klein B., Manchester R. N., 2006, MNRAS, 373, L6
Jonas J., MeerKAT Team 2016, in MeerKAT Science: On the Pathway to the SKA. p. 1
Karuppusamy R., et al., 2020, The Astronomer's Telegram, 13553, 1
Kaspi V. M., Beloborodov A. M., 2017, ARA&A, 55, 261
Keane E. F., 2010, PhD thesis, University of Manchester
Keane E. F., et al., 2018, MNRAS, 473, 116
Keith M. J., et al., 2010, MNRAS, 409, 619
Kennea J. A., et al., 2013, ApJ, 770, L24
Klein B., Kramer M., Müller P., Wielebinski R., 2004, in Camilo F., Gaensler B. M., eds, "" Vol. 218, Young Neutron Stars and Their Environments. p. 133
Kondratiev V. I., McLaughlin M. A., Lorimer D. R., Burgay M., Possenti A., Turolla R., Popov S. B., Zane S., 2009, ApJ, 702, 692
Kramer M., Jessner A., Muller P., Wielebinski R., 1996, in Johnston S., Walker M. A., Bailes M., eds, Astronomical Society of the Pacific Conference Series Vol. 105, IAU Colloq. 160: Pulsars: Problems and Progress. p. 13
Kramer M., Backer D. C., Cordes J. M., Lazio T. J. W., Stappers B. W., Johnston S., 2004, New Astron. Rev., 48, 993
Kramer M., Stappers B. W., Jessner A., Lyne A. G., Jordan C. A., 2007, MNRAS, 377, 107

Levin L., et al., 2010, ApJ, 721, L33

Levin L., et al., 2012, MNRAS, 422, 2489

Liu K., Eatough R., 2017, Nature Astronomy, 1, 812

Liu K., Wex N., Kramer M., Cordes J. M., Lazio T. J. W., 2012, ApJ, 747, 1

Liu K., et al., 2021, ApJ, 914, 30

Livingstone M. A., Ng C. Y., Kaspi V. M., Gavriil F. P., Gotthelf E. V., 2011, ApJ, 730, 66

Lorimer D. R., 2011, SIGPROC: Pulsar Signal Processing Programs, Astrophysics Source Code Library, record ascl:1107.016 (ascl:1107.016)

Lower M. E., Shannon R. M., Johnston S., Bailes M., 2020, ApJ, 896, L37

Lower M. E., Johnston S., Shannon R. M., Bailes M., Camilo F., 2021, MNRAS, 502, 127

Lower M. E., et al., 2023, arXiv e-prints, p. arXiv:2302.07397

Lyne A., Levin L., Stappers B., Mickaliger M., Desvignes G., Kramer M., 2018, The Astronomer's Telegram, 12284, 1

Macquart J. P., Kanekar N., Frail D. A., Ransom S. M., 2010, ApJ, 715, 939

Manchester R. N., Hobbs G. B., Teoh A., Hobbs M., 2005, AJ, 129, 1993

Morello V., et al., 2020a, MNRAS, 493, 1165

Morello V., Barr E. D., Stappers B. W., Keane E. F., Lyne A. G., 2020b, MNRAS, 497, 4654

Mori K., Gotthelf E. V., Barriere N. M., Hailey C. J., Harrison F. A., Kaspi V. M., Tomsick J. A., Zhang S., 2013, The Astronomer's Telegram, 5020, 1

Muno M. P., et al., 2009, ApJS, 181, 110

Ng C., et al., 2015, MNRAS, 450, 2922

Nita G. M., Gary D. E., 2010, MNRAS, 406, L60

Nita G. M., Gary D. E., Liu Z., Hurford G. J., White S. M., 2007, PASP, 119, 805

Olausen S. A., Kaspi V. M., 2014, ApJS, 212, 6

Parent E., et al., 2018, ApJ, 861, 44

Pennucci T. T., 2019, ApJ, 871, 34

Pennucci T. T., Demorest P. B., Ransom S. M., 2014, ApJ, 790, 93

Penrose R., 1979, Singularities and time-asymmetry.. pp 581–638

Porayko N. K., et al., 2019, MNRAS, 483, 4100

Press W. H., Teukolsky S. A., Vetterling W. T., Flannery B. P., 1992, Numerical recipies in C.   Vol. 2, Cambridge university press Cambridge

Purver M., et al., 2022, MNRAS, 510, 1597

Ransom S. M., Cordes J. M., Eikenberry S. S., 2003, ApJ, 589, 911

Rea N., Pons J. A., Torres D. F., Turolla R., 2012, ApJ, 748, L12

Rea N., et al., 2013, ApJ, 775, L34

Rickett B. J., 1977, ARA&A, 15, 479

Schnitzeler D. H. F. M., Lee K. J., 2015, MNRAS, 447, L26

Shannon R. M., Johnston S., 2013, MNRAS, 435, L29

Singh S., Roy J., Panda U., Bhattacharyya B., Morello V., Stappers B. W., Ray P. S., McLaughlin M. A., 2022, ApJ, 934, 138

Singh S., Roy J., Bhattacharyya B., Panda U., Stappers B. W., McLaughlin M. A., 2023, ApJ, 944, 54

Spitler L. G., et al., 2014, ApJ, 780, L3

Staelin D. H., 1969, IEEE Proceedings, 57, 724

Staveley-Smith L., et al., 1996, Publ. Astron. Soc. Australia, 13, 243

Stinebring D. R., Condon J. J., 1990, ApJ, 352, 207

Suresh A., et al., 2022, ApJ, 933, 121

Taylor J. H., Huguenin G. R., 1969, Nature, 221, 816

Titus N., et al., 2019, MNRAS, 487, 4332

Torne P., et al., 2017, MNRAS, 465, 242

Torne P., et al., 2021, A&A, 650, A95

Wex N., Kopeikin S. M., 1999, ApJ, 514, 388

Wharton R. S., 2017, PhD thesis, Cornell University

Wharton R. S., Chatterjee S., Cordes J. M., Deneva J. S., Lazio T. J. W., 2012, ApJ, 753, 108

Yao J. M., Manchester R. N., Wang N., 2017, ApJ, 835, 29

van Straten W., Demorest P., Oslowski S., 2012, Astronomical Research and Technology, 9, 237

This paper has been typeset from a TeX/LaTeX file prepared by the author.

List of Figures

List of Tables

Curriculum Vitae

Personal Details

Name	Jompoj Wongphechauxsorn
Email	jompoj@mpifr-bonn.mpg.de

Education

2012– 2016	BSc in Physics, Chiang Mai University, Chiang Mai, Thailand.
2016–2018	MSc in Astrophysics Rheinische Friedrich-Wilhelms-Universität, Bonn, Germany.
2019–2023	PhD in Astrophysics, Rheinische Friedrich-Wilhelms-Universität, Bonn, Germany.

Professional Experience

2014 – 2016	National Astronomical Research Institute of Thailand (NARIT)'s research assistant, Chiang Mai, Thailand.
2016	DESY Summer Student, Zeuthen, Germany.
2019–2023	Doctoral work at the University of Bonn, Germany.

Languages

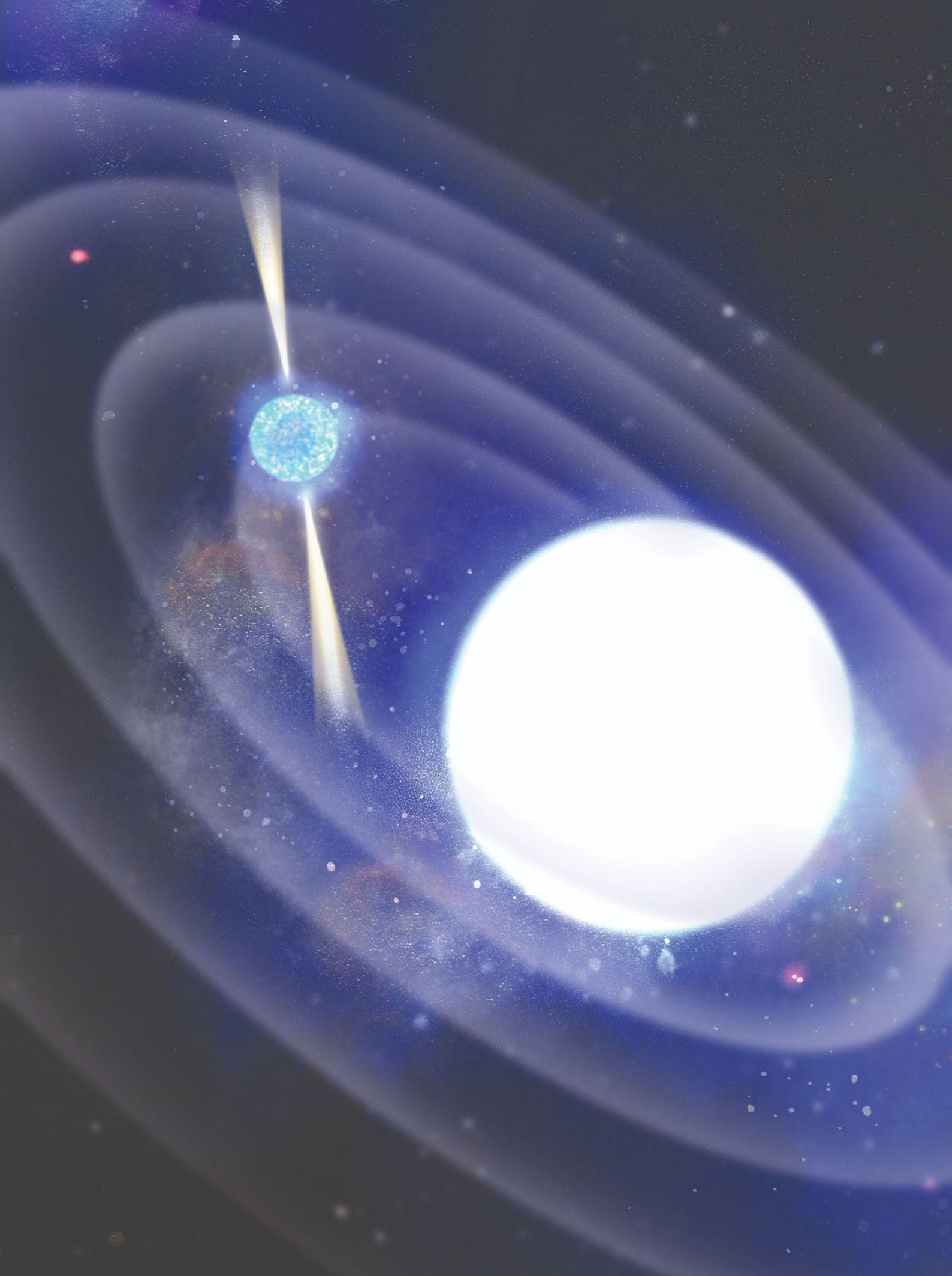|	
Thai	Mother tongue
English	Fluent

List of publications

Peer-reviewed publications

- **J. Wongphechauxsorn**, D. J. Champion, M. Bailes, V. Balakrishnan et al. (2023), MNRAS 527,3208–3219. The High Time Resolution Universe Pulsar Survey – XVIII. The reprocessing of the HTRU-S Low Lat survey around the Galactic centre using an accelerated Fast Folding Algorithm search pipeline

- P. Torne, K. Liu, R. P. Eatough, **J. Wongphechauxsorn** et al. (2023), APJ, 959, 14
  A search for pulsars around Sgr A* in the first Event Horizon Telescope dataset

- R. Sengar, ..., **J. Wongphechauxsorn** et al. (2023), MNRAS, 522, 1071-1090
  Discovery of 37 new pulsars through GPU-accelerated reprocessing of archival data of the Parkes multibeam pulsar survey

- R. Sengar, ..., **J. Wongphechauxsorn** et al. (2022), MNRAS, 512, 5782-5792 The High Time Resolution Universe Pulsar Survey - XVII. PSR J1325-6253, a low eccentricity double neutron star system from an ultra-stripped supernova

- A. Abbate, ..., **J. Wongphechauxsorn** et al. (2023), MNRAS, 524, 2966-2977
  Rotation measure variations in Galactic Centre pulsars

Non peer-reviewed publications

- P. Jaroenjittichai, ..., **J. Wongphechauxsorn** et al.
  Sciences with Thai National Radio Telescope